Numerical simulation of bubble growth in subcooled pool and flow boiling under microgravity conditions

Numerische Simulation des Blasenwachstums bei unterkühltem Behälter- und Strömungssieden in Schwerelosigkeit

Am Fachbereich Maschinenbau der Technischen Universität Darmstadt
zur Erlangung des Grades Doktor-Ingenieur (Dr.-Ing.)
genehmigte Dissertation von M.Sc. Benjamin Franz aus Oelsnitz
Tag der Einreichung: 13.04.2021, Tag der Prüfung: 16.06.2021
Darmstadt 2021 – D 17

1. Gutachten: Prof. Dr.-Ing. Peter Stephan
2. Gutachten: Professor Catherine Colin

TECHNISCHE UNIVERSITÄT DARMSTADT

MASCHINENBAU TTD
We engineer future

Numerical simulation of bubble growth in subcooled pool and flow boiling under microgravity conditions
Numerische Simulation des Blasenwachstums bei unterkühltem Behälter- und Strömungssieden in Schwerelosigkeit

Genehmigte Dissertation von M.Sc. Benjamin Franz aus Oelsnitz

1. Gutachten: Prof. Dr.-Ing. Peter Stephan
2. Gutachten: Professor Catherine Colin

Tag der Einreichung: 13.04.2021
Tag der Prüfung: 16.06.2021

Darmstadt – D 17

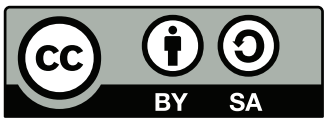

Erklärung zur Dissertation

Hiermit versichere ich, die vorliegende Dissertation ohne Hilfe Dritter nur mit den angegebenen Quellen und Hilfsmitteln angefertigt zu haben. Alle Stellen, die aus Quellen entnommen wurden, sind als solche kenntlich gemacht. Diese Arbeit hat in gleicher oder ähnlicher Form noch keiner Prüfungsbehörde vorgelegen.

Darmstadt, den 13.04.2021

Benjamin Franz

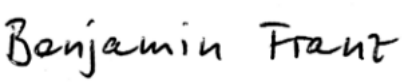

Vorwort

Die vorliegende Arbeit ist während meiner Anstellung als wissenschaftlicher Mitarbeiter am Fachgebiet Technische Thermodynamik der TU Darmstadt entstanden. Ich möchte mich herzlich beim Leiter des Instituts, Prof. Dr.-Ing. Peter Stephan, für die Ermöglichung dieser Arbeit, die Schaffung hervorragender Arbeitsbedingungen am Institut und die fachlich ausgezeichnete Betreuung bedanken. Inhaltlich hatte ich große Freiheiten bei der Ausgestaltung der Arbeit und konnte gleichzeitig bei Herrn Stephan jederzeit fachlichen Rat und hilfreiche Anregungen einholen.

Weiterhin möchte ich mich beim gesamten Kollegium für das gute Arbeitsklima am TTD und die jederzeit anzutreffende Hilfsbereitschaft bedanken. Hervorzuheben sind hier Gabriele Gunkel und Heike Kagerbauer aus dem Sekretariat und ihre effiziente Administration. Besonderer Dank gilt an dieser Stelle auch Dr.-Ing. Axel Sielaff, der mir als mein Gruppenleiter, als Experimentator und als Experte auf dem Feld des Blasensiedens den permanenten Austausch mit der experimentellen Seite meines Forschungsprojektes ermöglicht hat. Auch hier möchte ich mich für detaillierte Beratschlagungen und umfangreiche Anregungen bedanken. Jörn Wassenberg und Alireza Gholijani danke ich für sehr angenehme fünf Jahre als Kollegen im gemeinsamen Büro.

Ebenfalls hervorheben möchte ich die enge Zusammenarbeit in der Entwicklung der OpenFOAM-Bibliotheken und den regen fachlichen Austausch zu Fragestellungen der Numerik mit Christiane Schlawitschek, Achim Bender und Thomas Antritter vom TTD sowie mit Daniel Rettenmaier vom Graduiertenkolleg Computational Engineering, Daniel Deising vom Fachgebiet Mathematische Modellierung und Analysis und Yun Ouedraogo vom Fachgebiet Theorie Elektromagnetischer Felder. Insbesondere danke ich Thomas Antritter, Matthias Zimmermann und Johannes Kind für das Korrekturlesen meiner Arbeit. Ich freue mich, dass Herr Kind als mein Nachfolger das von mir bearbeitete Forschungsprojekt inhaltlich weiterführen und um neue Ergebnisse ergänzen wird.

Ich bedanke mich bei meiner Mutter und bei meinem Vater, die mich während meines Studiums finanziell unterstützt und angespornt haben. Dank gilt außerdem meinen beiden Hauskatzen, die beim Verfassen der Arbeit im Home-Office während der COVID-19-Pandemie für zahlreiche Momente der Aufheiterung gesorgt haben.

Zu guter Letzt bedanke ich mich bei Professor Catherine Colin vom Institut de Mécanique des Fluides de Toulouse für die Übernahme des Korreferats.

Abstract

Abstract

Nucleate boiling is a process, that allows heat transfer characterized by high heat flows at low temperature differences. It is therefore employed in a wide range of industrial applications from the chemical industry over power generation to cooling. It is also a promising method for the cooling e.g. of electronic devices in space applications.

Until today, the design of heat exchangers, which employ nucleate boiling, relies on purely empirical correlations. The heat transfer correlations obtained under 1-g conditions cannot be employed for the design of heat exchangers operating in space. Heat and fluid flow mechanisms under microgravity conditions are not sufficiently understood, e.g. typical time and length scales during boiling in microgravity are larger compared to those under 1-g conditions. The latter is in turn promising for the experimental investigation of the boiling process in general and to draw conclusions for boiling under 1-g conditions. The objective is to find physically based correlations for the boiling process in general and to make the process more predictable.

In order to obtain deeper insight into the mechanisms dominating the boiling process in microgravity, a benchmark experiment was designed for operation aboard the International Space Station ISS. For the present thesis, CFD simulations of the boiling process are performed additional to that experiment. The numerical model employed uses the VOF method to cover the two-phase flow and includes models for the treatment of phase change, contact line evaporation and transient heat transfer between the wall and the fluid. It is further developed to account for specific design features of the reproduced experiment.

Zusammenfassung

Blasensieden ist ein Wärmetransportprozess, der hohe Wärmeströme bei gleichzeitig niedrigen Temperaturdifferenzen ermöglicht. Es kommt daher in einem weiten Spektrum industrieller Anwendungen, von der chemischen Industrie über die Stromerzeugung bis zur Kühlung, zum Einsatz. Es stellt ebenfalls eine vielversprechende Methode z.B. zur Kühlung elektronischer Bauteile in Weltraumanwendungen dar.

Bis heute erfolgt die Auslegung von Wärmeübertragern mit Blasensieden ausschließlich mit empirischen Korrelationen. Die Korrelationen zum Wärmetransport, die unter Erdschwerkraft gewonnen wurden, können für die Auslegung von Wärmeübertragern im Weltall nicht verwendet werden. Wärmetransport und Strömung in Schwerelosigkeit sind dafür noch nicht ausreichend verstanden, z.B. sind typische Zeit- und Längenskalen beim Sieden in Schwerelosigkeit länger im Vergleich zu 1-g-Umgebungen. Letzteres macht man sich wiederum zu Nutze, um den Siedeprozess allgemein experimentell zu untersuchen und Rückschlüsse auf Sieden unter Erdschwerkraft zu ziehen. Ziel ist, physikalisch gestützte Korrelationen zum Siedeprozess allgemein zu finden und den Prozess vorhersagbarer zu machen.

Um einen tieferen Einblick in die Mechanismen zu erhalten, die beim Sieden in Schwerelosigkeit dominieren, wurde ein Experiment zum Einsatz auf der Internationalen Raumstation ISS entwickelt. Für die vorliegende Arbeit werden CFD-Simulationen des Siedeprozesses in Ergänzung zu diesem Experiment durchgeführt. Das numerische Verfahren nutzt die VOF-Methode zur Darstellung der Zweiphasenströmung und enthält Modelle, um Phasenwechsel, Kontaktlinienverdampfung und den transienten Wärmetransport zwischen Wand und Fluid zu berücksichtigen. Es wird weiterentwickelt, um die spezifischen Eigenschaften des Experimentes zur berücksichtigen.

3-D simulations of multiple growing and moving vapor bubbles in a laminar, subcooled shear flow inside the boiling cell are conducted. Parameter studies are performed to investigate the impact of flow velocity, input heat flux, pre-heating time and subcooling on the hydrodynamics and heat transfer around vapor bubbles. Selected material properties of the fluid and the solid are varied, as well. In a second study simulations of bubble growth and detachment at the cavity, which serves as nucleation site in the experiment, are carried out.

For intermediate values of the above mentioned experimental parameters, vapor bubbles grow to an equilibrium volume determined by evaporation at the bubble foot and condensation to the subcooled bulk. Contact line evaporation shows a significantly higher share in the overall evaporation heat flow, than it does in studies conducted under 1-g conditions. A high input heat flux, a long pre-heating time and a low subcooling provoke a highly complex flow pattern of bubbles, which rapidly emerge after one another and coalesce, letting the initial bubble grow beyond its equilibrium volume. This causes a decreasing heat transfer coefficient. A choice of parameters, which causes a high number of small, distant vapor bubbles, appears advantageous for optimized heat transfer.

The cavity simulations show, that the influence of the nucleation process on the flow and temperature field outside the cavity cannot be ignored. Furthermore, for the correlation between detachment diameter of a vapor bubble from a cavity and flow velocity a non-dimensional approach is developed.

The present work shows both the advantages as well as the challenges of the employed numerical model to reproduce the according experimental setup. The impact of system parameters and material properties on bubble growth and heat transfer performance is examined and recommendations on the choice of parameters are given.

Es werden 3-D-Simulationen mehrerer wachsender, bewegter Dampfblasen in einer laminaren, unterkühlten Scherströmung in der Siedezelle durchgeführt. In Parameterstudien wird der Einfluss von Strömungsgeschwindigkeit, Wärmezufuhr, Vorheizzeit und Unterkühlung auf die Hydrodynamik und den Wärmetransport an Dampfblasen untersucht. Ausgewählte Stoffwerte des Fluids und der Wand werden ebenfalls variiert. In einer weiteren Studie werden Simulationen des Blasenwachstums und -abrisses an der Kavität, die im Experiment als Keimstelle dient, durchgeführt.

Für mittlere Werte der o.g. experimentellen Parameter stellt sich bei Dampfblasen ein Gleichgewichtsvolumen durch Verdampfung am Blasenfuß und Kondensation an der Blasenkappe ein. Die Kontaktlinienverdampfung macht einen deutlich größeren Anteil am gesamten Verdampfungswärmestrom aus als unter 1-g-Bedingungen. Hohe Wärmezufuhr, lange Vorheizzeit und geringe Unterkühlung sorgen für ein sehr komplexes Strömungsbild mit schnell hintereinander entstehenden und koaleszierenden Dampfblasen, wodurch die erste Blase über ihr Gleichgewichtsvolumen hinaus anwächst. Das führt zu einem sinkenden Wärmeübergangskoeffizienten. Eine Parameterwahl, die zu einer Vielzahl kleiner, voneinander entfernter Blasen führt, scheint vorteilhaft für einen guten Wärmeübergang.

Die Kavitätssimulationen zeigen, dass der Einfluss des Nukleationsprozesses auf das Strömungs- und Temperaturfeld außerhalb der Kavität nicht vernachlässigt werden kann. Weiterhin wird für den Zusammenhang zwischen dem Abrissdurchmesser einer Blase von einer Kavität und der Strömungsgeschwindigkeit eine dimensionslose Beziehung entwickelt.

Die vorliegende Arbeit zeigt sowohl die Vorteile als auch die Herausforderungen des numerischen Modells beim Nachbilden des dazu gehörenden Experiments. Der Einfluss von Systemparametern und Stoffeigenschaften auf das Blasenwachstum und den Wärmeübergang wird untersucht und Empfehlungen zur Wahl der Parameter werden gegeben.

Contents

Nomenclature

Latin letters		Unit
A	Area	m^2
A	Dispersion constant	J
c	Specific heat capacity	J/(kg K)
C	Constant	various
d	Diameter	m
$\widetilde{D}$	Smearing distance	m
$\vec{e}_x$	Unity vector in x-direction	m
$\vec{e}_z$	Unity vector in z-direction	m
f	Condensation coefficient	-
$f(x,y)$	Probability density funtion	-
$\vec{f}_\sigma$	Volumetric surface tension force	N/m^3
F	Volume-of-Fluid indicator variable	-
F	Force	N
$\vec{g}$	Gravitational acceleration vector	m/s^2
h	Flow channel height	m
Δh_v	Evaporation enthalpy	J/kg
H	Heaviside function	-
K	Curvature	1/m
L	Length	m
$\dot{M}_\mathrm{evap}$	Evaporation or condensation mass flow	kg/s
$\vec{n}$	Unit normal vector	-
N	Normalization coefficient	-
N_p	Number of points	-
p	Pressure	N/m^2
P	Power	W
$\dot{q}$	Heat flux	W/m^2
Q	Heat	J

$\dot{Q}$	Heat flow	W
$\dot{Q}_{\mathrm{cl}}$	Integrated heat flux in the microzone model	W/m
r	Radius	m
R	Thermal resistance	$\mathrm{m^2K/W}$
R_{gas}	Specific gas constant	J/(kg K)
$\vec{S}$	Surface normal vector	$\mathrm{m^2}$
t	Temperature	°C
T	Temperature	K
ΔT	Temperature difference to saturation temperature	K
u	Velocity	m/s
$\vec{u}$	Velocity vector	m/s
$\vec{u}_{\mathrm{r}}$	Compression velocity vector	m/s
V	Volume	$\mathrm{m^3}$
w	Weighting factor	-
$\vec{x}_p$	Position vector of specific point	m
Δx	Cell edge length	m
x, y, z	Cartesian coordinates	m

Greek letters		**Unit**
α	Heat transfer coefficient	$\mathrm{W/(m^2\,K)}$
δ	Film thickness	m
δ_{th}	Thermal boundary layer thickness	m
η	Local coordinate perpendicular to the wall	m
Θ	Contact angle	rad, deg
λ	Thermal conductivity	W/(m K)
μ	Dynamic viscosity	$\mathrm{Ns/m^2}$
ν	Kinematic viscosity	$\mathrm{m^2/s}$
ξ	Local coordinate parallel to the wall	m
ρ	Density	$\mathrm{kg/m^3}$
$\dot{\rho}$	Density source	$\mathrm{kg/(m^3\,s)}$
σ	Surface tension	N/m
σ	Standard deviation	-
Σ_e	Energy source term	$\mathrm{W/m^3}$

Σ_V	Mass source term	1/s
τ	Time	s
ϕ	Distance field	m/s
χ	Material property	-
ψ	Mass source distribution	$kg/(m^3\,s)$

Subscripts

0	Initial
ad	Adsorbed layer
av	Average
B	Bubble
c	Value at cell midpoint
cap	Capillary
cl	Contact line part in one cell
Cl	Whole contact line
cu	Copper
ex	Existing
f	Face
in	input
int	Interface
l	liquid
Laser	Laser
M	Material
max	Maximal
ns	Nucleation site
nucl	Nucleation
p	Pressure
w	Wall
s	solid
R	Roughness
Sens	Sensible heat
sat	Saturation state
trans	Transition region

v	vapor
z	z-direction
σ	Surface tension

Superscripts

i	Current time step
i-1	Last time step
-	Average

Abbreviations

1-g	Earth gravity
2-D	Two-dimensional
3-D	Three-dimensional
ALE	Arbitrary Lagrangian-Eulerian
BW	Black and white
CFD	Computational Fluid Dynamics
CHF	Critical heat flux
Co	Courant-number
CSF	Continuum surface force
DNB	Departure of nucleate boiling
ESA	European Space Agency
FEM	Finite element method
FVM	Finite volume method
GAMG	Geometric algebraic multi grid
IR	Infrared
ISS	International Space Station
LS	Level-set
MAC	Marker and cell
MTCR	Micro thermocouple rack
MULES	Multidimensional universal limiter with explicit solution
ONB	Onset of nucleate boiling
PCG	Preconditioned conjugate gradient
PISO	Pressure implicit split operator

PLIC	Piecewise linear interface calculation
RUBI	Reference multiscale boiling investigation
SLIC	Simple line interface calculation
VOF	Volume-of-Fluid

Dimensionless numbers		**Definition**
Ca	Capillary number	$(\nu \rho u)/\sigma$
Ja	Jacob number	$(\Delta T\, c)/\Delta h_\mathrm{v}$
Nu	Nusselt number	$(\alpha L)/\lambda$
Re	Reynolds number	$(u L)/\nu$

1 Introduction

Nucleate boiling is employed as a method of heat transfer in a wide range of private and industrial applications. It can be found basically in every application, which requires a heat exchanger to transfer high amounts of heat at relatively low temperature differences, or which fundamentally requires the evaporation of a working fluid. Typical areas of applications are e.g. the boiler in a thermal power plant, the evaporator in an air conditioning system, or the cooling of energy dissipating, electronic devices. The main advantage of the nucleate boiling process is, that it allows large heat fluxes at fairly low temperature differences between a heated surface and a working fluid.

Since the 1930s a lot of research was conducted on nucleate boiling in order to gain a deeper insight into the dominating heat and fluid flow processes and the influencing parameters. However, correlations employed for the design of heat exchangers, which use the boiling process, are still of empirical nature. In most cases they are only valid for a specific pairing of wall and fluid materials and a narrow band of process parameters. Phenomenologically based correlations, which allow the prediction of the process in general, are still not available. The main problem in deducing such correlations is, that boiling is a highly complex process with manifold influencing parameters, which are strongly entangled with one another. Still a lot of research on the underlying heat and fluid flow phenomena has to be done.

Obviously, gravitational forces play an important role in nucleate boiling heat transfer. Therefore, one specific approach in boiling research is the conduction of experiments at different gravity levels and especially in weightlessness, respectively. Because vapor bubbles grow larger and for a longer period of time, experimental measurements can be performed at larger time and length scales. Secondly, under microgravity conditions the process gets disentangled from buoyancy, which, under earth gravity conditions, can dominate the process. Influencing quantities apart from buoyancy can be investigated in regard to their impact on the process.

Furthermore, experiments under microgravity conditions provide results, which can later be used in applications for astronautics. It appears promising to employ the boiling process for the cooling of electronic, heat dissipating devices used in space. Since several aspects of the boiling process change due to the lack of gravity, it is unfortunately not possible to employ empirical correlations, which have been obtained in experiments under normal gravity conditions, for the design of heat exchangers that are used in space. For a proper design, the influence of gravity on local transport phenomena has to be investigated. A current overview over boiling research in microgravity during the last 50 years is given by Colin and co-workers [11].

In order to obtain deeper insight into boiling under microgravity conditions, the european collaborative reference experiment "Multiscale Boiling" has been planned and designed in recent years to conduct microgravity boiling experiments aboard the International Space Station (ISS) [99]. In this experiment the behavior of single vapor bubbles in a boiling cell is investigated both in pool boiling and under the influence of a laminar shear flow. After a series of preliminary studies performed with the experimental setup on ground and during parabolic flight campaigns, the Multiscale Boiling experiment eventually launched aboard ISS in July 2019, while the present thesis was written. A sketch of the experimental setup of shear flow experiments of this campaign is given in figure 1.1.

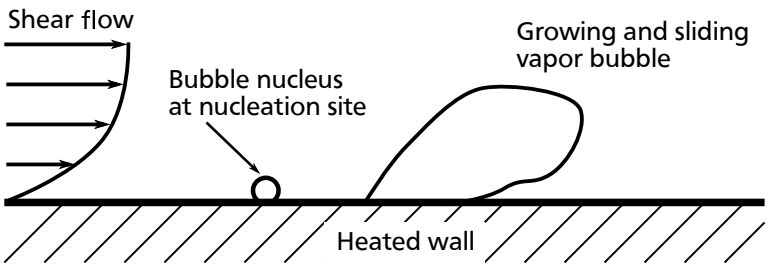

Figure 1.1: Scheme of a flow boiling run in the Multiscale Boiling experiment aboard the International Space Station

The experiments aboard the ISS are supported by numerical simulations in order to resolve all desired spatial and time scales, as well as the ability to provide results at locations, which are not accessible with experimental equipment. Numerical simulations have become an important tool in the research of multiphase flows including phase change such as boiling or evaporation. It is nowadays used as an equal important method as experiments and both approaches are often used in a collaborative way. The researcher is free in the variation of process parameters as well as of material properties, which cannot be varied that easily in experiments. Therefore numerical studies are often conducted in addition to experiments in order to benefit from the advantages of both approaches.

The present work deals with the numerical studies, which have been conducted to accompany the Multiscale Boiling experimental campaign. Different length scales of the experiment were modeled for different simulation campaigns. Chapter 2 presents the recent research status on nucleate boiling from both experimental and numerical works. The scope of the present work is clarified. Chapter 3 briefly outlines the experimental campaign for the sake of better understanding of the numerical simulations. Chapter 4 introduces the numerical model, which is developed and employed in the present work. In chapters 5 and 6 the simulation setup and results of the numerical campaigns regarding two different length scales of the experiment are discussed in detail. Finally, a summary of and conclusions from the simulations in the present work are given in chapter 7, and a choice of system parameters for an optimized heat transfer coefficient is suggested. Finally, an outlook to possible future research is given.

2 State of the art

2.1 Boiling phenomena

Boiling heat transfer has been subject of research for almost a century. A detailed description of the fundamental physical basics of phase change phenomena is given e.g. by Carey [9]. In this section boiling phenomena will be briefly discussed before an overview over scientific literature on experimental and numerical work on boiling will be given in the next sections.

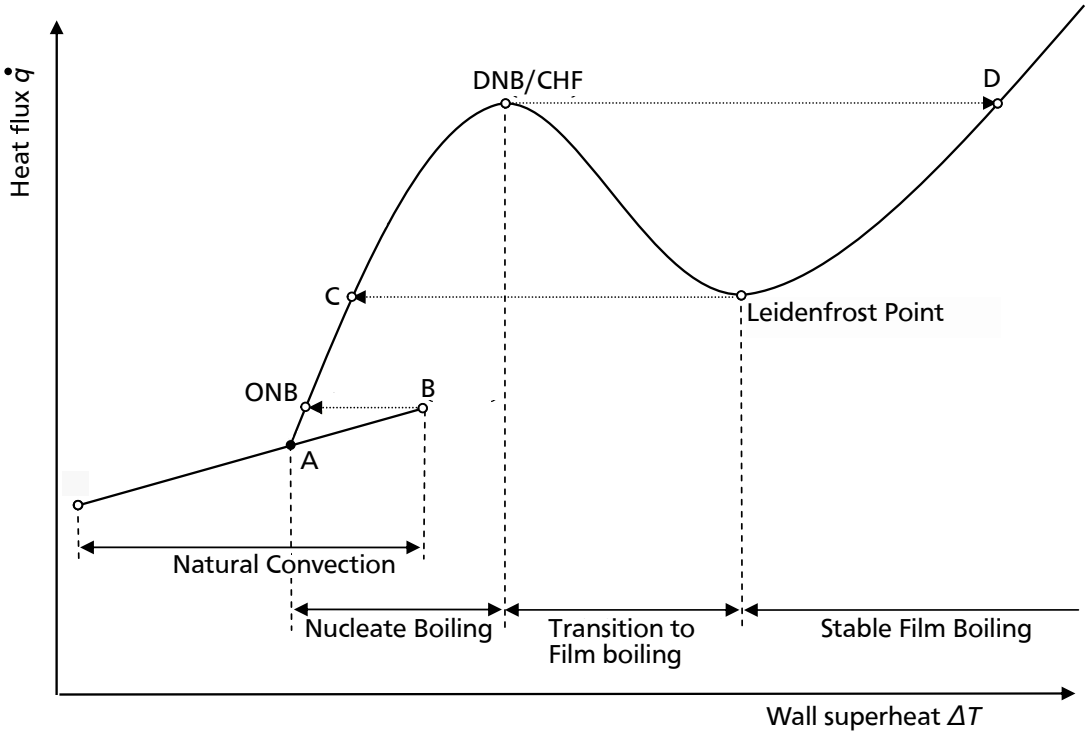

Figure 2.1: Pool boiling curve according to Nukiyama [76]

Heat transfer between a superheated wall and a fluid can be calculated by

$$\dot{Q} = \alpha A (T_{\mathrm{w}} - T_{\mathrm{fluid}}) \tag{2.1}$$

with the heat flow $\dot{Q}$, the heat transfer coefficient between solid and fluid α, the surface of the heated wall A and the temperatures of wall and fluid T_{w} and T_{fluid}, respectively.

One of the earliest works, which had a lot of impact on following research, is the work from Nukiyama [76]. He introduced the concept of a specific boiling curve for each experimental setup. An example of such a boiling curve is shown qualitatively in figure 2.1. It relates the heat flow per surface area or the heat flux $\dot{q}$, respectively, to the wall superheat ΔT compared to the saturation temperature of

the bulk fluid. At the origin of the curve the fluid is at saturation temperature. When the heat flux is increased, firstly heat is transferred from the wall to the fluid by natural convection only. At the same time the wall superheat increases and a thermal boundary layer above the wall develops. The moment when the first nucleation site is activated represents point B. Once the first bubble appears and grows, the heat transfer coefficient increases, resulting in a decrease of the wall superheat to the point ONB (onset of nucleate boiling), and nucleate boiling begins. Increasing the heat flux further, additional nucleation sites are activated. Usually in technical applications the nucleation sites are distributed heterogeneously over the heated wall as they are situated at small cavities or scratches due to imperfections of the surface or at spots of contamination. The increase in nucleation site density results in an increase of the heat transfer coefficient. If the heat flux is increased even further, bubble density gets high enough that bubble coalescence occurs. More and more area is covered by vapor, which has an insulating effect, and the heat transfer coefficient reaches its maximum right before the point CHF.

Increasing the heat flux even higher, CHF (critical heat flux) or DNB (departure of nucleate boiling) is reached eventually. At this point, bubbles merge to a vapor film covering the whole heater surface. The wall superheat increases suddenly and drastically to point D as the heat transfer coefficient decreases due to the insulating effect of the vapor film. This rapid increase in wall superheat has the potential to destroy heater surfaces in many technical applications and is therefore often avoided.

Point D is situated in the film boiling regime and decreasing the heat flux slightly will not get the wall superheat back to point DNB. If the heat flux is decreased from point D, stable film boiling regime is maintained until the Leidenfrost point is reached, where the wall superheat suddenly decreases to point C as the film collapses and the process is back in nucleate boiling regime.

Decreasing the heat flux even further will not lead to a transition back to pure convection at point ONB. Instead the nucleate boiling regime is maintained below the heat flux which was required to activate the nucleation sites until point A is reached where the nucleate boiling regime is left and heat transfer is again occurring only by natural convection. The triangle between the points A, B and ONB is referred to as boiling hysteresis; the region between points A and DNB is referred to as the nucleate boiling regime.

Accurately predicting the boiling curve for a specific fluid and surface from a general correlation is impossible, instead every special curve has to be determined by experiments.

In the present thesis, the heat transfer regime of interest is nucleate boiling at moderate heat flux, given in figure 2.1 as the range between point A and C. According to Stephan and Kern [104] as well as Kim [53] three mechanisms of heat transfer from the heater surface to the fluid can be observed in this boiling regime:

1. Convective heat transfer, which is enhanced compared to pure natural convection, since it includes forced convection induced by bubble motion and thermocapillary convection.

2. Transient conduction: The superheated thermal boundary layer above the heater is consumed by the vapor bubble during its growth. During bubble detachment and rise colder bulk liquid flows into the emerging void and the thermal boundary layer is restored until the next bubble emerges at the nucleation site.

3. Latent heat transfer by evaporation or condensation at the bubble hull and evaporation at the three-phase contact line. The relative contribution of contact line evaporation to the overall evaporation process is very large compared to the relatively small share that the micro region has on the whole

liquid-vapor interface. According to Stephan and Kern [104] and Kim [53] contact line evaporation has a share of 20 to 30 % of the overall heat transfer at a vapor bubble.

Regarding evaporation in the vicinity of the three-phase contact line, two distinct models have been proposed throughout literature: On the one hand, the microzone or contact line model assumes evaporation in a microscopic area directly at the contact line. An adsorbed liquid layer of few nanometers thickness is situated underneath a vapor bubble. Within that layer adhesive forces are dominating, preventing the liquid layer from evaporation. In a transition region between the adsorbed layer and the macroscopically visible liquid-vapor interface the film grows in thickness, causing a high curvature at the interface, until the latter reaches the apparent macroscopic contact angle. In this microzone, very high relative evaporation rates can be observed. On the other hand, the microlayer model assumes a liquid film of several micrometers thickness and length underneath a bubble between the three phase contact line and the bulk liquid. At this film, again very high evaporation rates are observed.

Both models appear to be valid depending on the parameters: Sielaff [93] found, that for fast receding contact lines and high contact line velocities a microlayer forms, while for advancing and slowly receding contact lines evaporation in the microzone dominates. Furthermore, the formation of a microlayer appears to be more likely in case of liquids, which show worse wetting characteristics and larger contact angles at the bubble foot, e.g. water, in opposition to highly wetting liquids with low contact angles, e.g. FC-72. Schweikert et al. ([85], [86]) confirmed the findings on the impact of the receding contact line velocity. They showed, that both evaporation regimes are sharply distinguished by a critical dewetting velocity, which in turn depends on the wall temperature and the heat flux.

Urbano et al. [111] found, that in pool boiling a microlayer forms, if the bubble growth rate and thus the interface velocity is higher than the maximal contact line velocity. This is correlated to the Jacob number as a measure of the evaporation rate on the one hand, and on thermophysical properties of the fluid on the other hand. They state, that a low contact angle, low surface tension and high viscosity of the liquid promote the formation of a microlayer.

In the following two sections an overview of publications about boiling research is given. For the sake of clarity it is divided into experimental and numerical work, in each case with a subsection that focuses on boiling research in variable gravity environments, which is of special interest in this work. An overview of both experimental and numerical research throughout the last decades is given by Stephan et al. [105].

2.2 Experimental investigations of nucleate boiling

The earliest experimental investigations of nucleate boiling date back to the 1930s. In 1931, Jakob and Fritz [45] studied the effect of surface roughness and heat flux on the wall temperature during boiling of water and gave an empirical correlation for the bubble frequency. In a following publication Fritz [27] derived a correlation for the departure diameter of vapor bubbles in dependence of the contact angle and thus in dependence of the properties of the boiling fluid and its wetting behavior on the heating surface. Around the same time Nukiyama's boiling curve (figure 2.1) was published [76].

During the following decades several more correlations have been deduced for the departure diameter, e.g. [10, 124], the bubble frequency, e.g. [10, 67], and the heat transfer coefficient, e.g. [101]. All these correlations have been determined empirically and thus rely on empirical parameters. They are actually only valid for a narrow band of parameters and for certain combinations of fluids and substrate materials. However, due to the lack of general correlations they are still used for the design of heat

exchangers. The given references represent only a small selection. A detailed overview of correlations of boiling processes is given by Carey [9].

During the last years measurement technology has improved rapidly and has enabled researchers to investigate parameters such as temperature or heat flux at very small spatial and temporal resolutions. Especially the local wall temperature underneath a bubble and the instantaneous heat flux at the bubble foot are quantities of big interest throughout literature.

Contemplating the detailed temperature measurements at the heater surface, it has to be distinguished between contact and non-contact measurement. The most common contact measurement techniques are those based on the Seebeck effect (e.g. thermocouples) and those based on the temperature-dependent electrical resistance. Microheater arrays, consisting of several resistance heaters and integrated micro-thermocouples or resistance thermometers, are used in several publications [12, 13, 35, 53, 70, 71]. Microthermocouples, which have diameters of only a few microns, are used to measure the temperature of the liquid near the three-phase contact line with a sufficiently high resolution [114].

The most popular optical methods are high speed infrared thermometry [24, 23, 88, 93, 114] and the use of thermochromic liquid crystals [48, 49, 94, 113], which are used in particular to study the transient heat transfer between solid and fluid.

A major outcome of the experimental investigations is the importance of heat transfer in the region of the three-phase contact line. The heat transfer reaches a maximum there and can be several orders of magnitude higher than the mean input heat flux [88, 114]. Most publications state that contact line heat transfer accounts for a relative amount of 20 to 30 % of the overall heat transfer. Not only the timewise integrated contact line heat transfer itself is of interest, but its evolution over time because its value changes depending on the velocity and the direction of the contact line motion [12, 24, 70, 71, 74, 87].
The investigations show, that for a receding contact line during bubble growth the heat transfer is less pronounced and almost independent of the contact line velocity while the heat transfer gets stronger and highly velocity dependent for an advancing contact line in the detachment phase. Ibrahem and co-Workers [41, 42] as well as Fischer [23] performed experiments on a single moving meniscus observing the temperature at the heated wall by infrared thermometry. In contrast to nucleate boiling experiments this setup allows a very precise control of the boundary conditions at the contact line and of the contact line velocity. Both confirmed the strong dependency of contact line heat transfer on the contact line motion at advancing contact lines, while Fischer additionally studied the influence of system pressure on contact line evaporation. He shows that with increasing system pressure the heat flux peak at the contact line decreases. Schweikert and co-workers [85] performed experiments of a superheated substrate being withdrawn from a pool of volatile liquid and investigated the heat transfer to the emerging liquid film and to the receding contact line. They confirm the weak dependency of the contact line heat transfer on the contact line velocity, apart from the case, when the velocity exceeds the critical velocity for the transition to microlayer evaporation. In this case, a sharp increase in the contact line heat transfer can be observed.

Experiments in Microgravity

A series of experiments on pool boiling were performed under microgravity or variable gravity conditions in order to gain a deeper understanding of the boiling process by varying or switching off buoyancy.

Siegel [92] summarized the boiling experiments in microgravity from the 1950s and 1960s. He evaluated the different forces on a vapor bubble and their dependency on gravity: Surface tension and drag

forces are attaching forces while buoyancy force, pressure force and the inertial force act as detaching forces. He evaluated the development of the forces during bubble growth and stated that the inertial force reaches its maximum in an early stage. In the case of fast bubble growth the inertial force is high enough to detach the bubble so that bubble growth time and departure diameter are independent of gravity. In contrast, in the case of slow bubble growth, buoyancy and surface tension dominate the process and the departure diameter is proportional to $g^{-1/2}$, as can be derived from the force balance. That means that at higher heat fluxes and higher wall superheats the boiling behaviour becomes independent of gravity because of the domination of the inertial force. Siegel draws several more conclusions, some of which are confirmed by other authors and newer experiments. A detailed overview about these conclusions and the literature supporting them is given by Schweizer [87].

Ervin and co-workers [18] conducted multiple bubble pool boiling experiments under different gravity conditions, ranging from earth gravity over microgravity to negative gravity. They combined it with different subcoolings and superheats of the bulk fluid, respectively, and with different wall superheats. The authors stress the strong impact of buoyancy on the boiling process and point out heat transfer and bubble propagation phenomena only observable under microgravity conditions.

Lee and Merte [60] performed experiments of subcooled boiling in 0-g, varying input heat flux and subcooling, and compared the results to according 1-g experiments. In case of steady state boiling at a stationary bubble, where evaporation at the bubble foot and condensation at the bubble cap are in equilibrium, an increase in the heat transfer coefficient up to 32 % compared to 1-g conditions was observed. The authors concluded, that subcooling is an important matter in microgravity pool boiling and that it is possible to enhance the heat transfer coefficient in the case of small and medium heat fluxes, while the value of critical heat flux always decreases.

Schweizer and Stephan [88] studied the dependency of contact line heat transfer on subcooling and gravity level. They found that in an early stage of bubble growth, subcooling and gravity have no impact on the ratio between heat flow at the contact line and the overall heat flow. However, at later stages of bubble growth the ratio is strongly increased by subcooling and decreased by gravity. Furthermore, they observed that as soon as a bubble slides away from the nucleation site, new bubbles nucleate and merge with the first one. The authors state that the frequency of this process is higher than the bubble frequency under earth gravity conditions.

Dhir et al. [15] conducted single bubble nucleate boiling and lateral bubble coalescence experiments on the ISS and found that at high superheats the larger coalescent tends to detach and hover closely above the wall while sucking smaller bubbles into it.

Some works focus on the influence of external force fields other than the earth gravity field that have an effect on the boiling process, particularly on electric fields. An overview of those works is given by Di Marco [16]. It could be shown, that under microgravity conditions an electric field can substitute the missing gravitational force field. Furthermore, under the influence of an electric field the differences that are found between boiling phenomena under normal gravity conditions and those under microgravity conditions, diminish. Schweizer [87] conducted nucleate boiling experiments during parabolic flights and activated a 10 kV electrode above the nucleation site right after reaching the microgravity phase. He found that the charging of the electrode immediately stabilized the previously chaotic boiling process. The vapor bubbles are completely removed from the heater surface so that a steady re-wetting of the surface was ensured and a fully developed, stable boiling process was maintained.

Colin et al. [11] provide an overview of experimental research on boiling in microgravity over the last 50 years. The existing correlations for the influence of the gravity level on heat transfer as well as correlations for the different forces acting on an isolated bubble in a shear flow under microgravity conditions are summarized. The authors point out, that at low heat flux heat transfer is enhanced in microgravity compared to 1-g, because of rapid bubble detachment under earth gravity conditions. However, at high heat flux the effect is opposite and under microgravity conditions partial dry-out of the heater surface can be observed.

2.3 Numerical simulations of nucleate boiling

During the recent decades computational resources on the one hand and numerical models on the other hand have been enhanced significantly. Nowadays it is possible to conduct numerical simulations of nucleate boiling producing high quality results. The most challenging part of the numerical simulation of flow boiling is the accurate modeling of the two-phase flow. In literature four methods are commonly used to detect the position of the interface between the two phases:

- The **Front Tracking** or **Marker and Cell method (MAC)** [34]: Either one of the two phases or the interface itself is marked by weightless particles, which are convectively transported with the velocity field in order to reconstruct the interface.
- **Moving mesh based methods** of which the **Arbitrary Lagrangian-Eulerian method (ALE)** is the most commonly used [37]. Each phase has its separate mesh, which is deformable. Thus, the interface always coincides with the boundary between the two meshes.
- In the **Level-Set method (LS)** [78] a signed distance field is defined, which contains the distance of each cell to the interface and which is convectively transported with the velocity field. The zero isoline of this field represents the interface.
- In the **Volume-of-Fluid method (VOF)** [38] a field that contains the volume fraction of one of the phases in each cell is transported convectively with the velocity field. If there is no need to know the exact location of the interface, the interface normal is determined by the gradient of the volume fraction field. If the exact interface position is required, the interface can be explicitly reconstructed from this field.

The original marker-and-cell method has been continuously developed by the group of Tryggvason [19, 108, 109] to a method, which they call front-tracking method. They used it mainly to perform simulations of film boiling [20, 21, 46, 47]. The authors state, that the method is advantageous in particular in terms of curvature calculation at the interface, which is crucial in terms of eliminating parasitic currents. However, the method only works with structured meshes and does not include contact line evaporation and transient heat conduction in the solid wall.

The great advantage of the ALE method is that the computational domain boundaries of the two meshes always coincide with the interface, which makes it easy to calculate the heat flux at the interface and therefore the evaporation rate. It has been used combined with the Finite-Element-Method (FEM) by the group of Stephan to simulate nucleate boiling of binary mixtures [50, 52, 51, 28, 29]. Contact line heat transfer is included by using the model of Stephan and Hammer [103] and transient heat conduction in the solid wall is taken into account.

Welch [117, 118] employed a combination of ALE and the Finite-Volume-Method (FVM) to perform 2-D-simulations of nucleate boiling. He takes transient heat conduction in the wall into account but no

contact line evaporation.

The level-set method has been extensively employed by the group of Dhir for the simulation of different boiling phenomena and boiling regimes. Son and Dhir performed simulations of film boiling near the critical pressure [95, 96] and on immersed surfaces [97]. In the field of nucleate boiling the group has conducted numerous studies e.g. on the influence of contact angle dynamics and different contact angle models [98, 73], on bubble coalescence [1, 72], on the influence of contaminants [4] and structured surfaces [61, 62] and on the influence of gravity [2, 3, 63]. Wu and co-workers developed a combined level-set and moving-mesh method to simulate subcooled pool boiling [122, 123]. In all publications from this group contact line evaporation is taken into account, however, in older works the temperature of the heated wall is assumed to be constant and therefore the transient heat conduction within the wall is not calculated. This changed in works published in 2012 and later on. An overview of the numerical work of Dhir's group is given in [14].

The group of Colin employed the level set approach combined with a ghost-fluid method ([22]) to calculate the velocity jump at the sharp interface and simulated pool boiling. Tanguy and co-workers [106] validated the method with different variants of the ghost-fluid approach against analytical solutions of test cases of static and rising bubbles growing in a superheated liquid. The method was then employed in several following works on pool boiling ([40], [111], [110]). Huber and co-workers showed, that in case of a partially wetting liquid such as water in a configuration with moderate Jacob number, large contact angle and large density ratio the influence of wall superheat on contact angle and on heat transfer is small. They conclude, that the inclusion of a microzone model is expandable in such a configuration.

The VOF method is the method which is used in the current thesis. Since its development in the late seventies [38] it has continuously been improved by several groups and has been employed to simulate very different phenomena of two-phase flow with and without phase change. There have been investigations e.g. on film boiling [119, 120], the physics of droplets on walls, e.g. [5, 7, 36, 80], pool boiling from flat surfaces [30, 54, 55, 56, 57, 58] and from reentrant cavities and subsurface tunnels [17].

Any evaporation model, independent of the method of interface tracking employed, depends on information about the exact position of the interface in order to properly calculate temperature gradients. If VOF is employed, the method alone does not provide this information. Thus, the geometric reconstruction of the interface out of the volume fraction field is needed. Shu [91] combined the advantages of VOF and the Level-Set method by calculating the signed distance field for the LS method from the VOF method's volume fraction field and conducted simulations of nucleate boiling. Unfortunately his method is limited to structured, fully orthogonal, two-dimensional grids. Kunkelmann [54, 55, 56, 57, 58] developed a method to reconstruct the interface from iso-surfaces which hold a value of 0.5 for the volume fraction field and implemented it in the open source framework OpenFOAM. This method works for unstructured, three-dimensional meshes regardless of their topology.

Hardt and Wondra [33] developed an evaporation model, which can be combined with any method of interface tracking. Within this method, the evaporation rate at the interface is calculated from the interface temperature and the thermal resistance of the interface.

In one of his early works Kunkelmann [56] combined the evaporation model from Hardt and Wondra [33] with his method of explicit interface reconstruction from iso-surfaces within a VOF approach. This approach suffers from the need of information on the exact temperature of the interface, such that a very fine grid resolution in the vicinity of the interface is needed. Hence, the evaporation model has been modified in a following work [58] such that it relies on the temperature difference between the

interface, which is assumed to hold saturation temperature, and arbitrary cells in its vicinity, and now works on coarser grids. Furthermore, Kunkelmann implemented a parametric subgrid-scale model in his framework to account for contact line evaporation. He validated his numeric results against several experimental results from the literature and found them to be in good agreement.

Batzdorf [5] improved Kunkelmann's evaporation model further by introducing an implicit approach to solve the emerging system of equations. That way, the interaction between heat flow towards the interface and the temperature of the regarding grid cells is accounted for and an iterative solution is avoided. Kunkelmann's OpenFOAM based solver with its modifications by Batzdorf [5] and Dietl [17] is employed in the present thesis. A detailed outline of the solver will be given in chapter 4.

Using the VOF method, Georgoulas and Marengo [30] showed a linear relationship between the thickness of the thermal boundary layer on the one hand and the bubble departure diameter and the bubble departure time on the other hand. Furthermore they showed, that the influence of the contact angle on bubble departure diameter or bubble departure time, respectively, becomes significant above a certain threshold value of the contact angle.

Okajima and Stephan [77] used the VOF approach developed by Kunkelmann to perform simulations of superheated boiling of a single bubble in a microchannel. They found, that a liquid film is developing between the elongated bubble and the wall, which prevents the bubble from touching the wall. Heat transfer between the wall and the bubble takes places in three distinct regions, which is in accordance with Thome's three-zone model [107]. The liquid film thickens at higher fluid superheats so that the share of heat transfer from the wall contributing to bubble expansion decreases.

Pattamatta, Freystein and Stephan [79] simulated coalescing Taylor-Bubbles in a minichannel using Kunkelmanns model and analysed the heat transfer from the wall to the liquid. They found that from all studied parameters the Reynolds number and the wall superheat have the strongest impact on the time averaged Nusselt number. Furthermore, they stressed the influence of the Capillary number on the structure of coalescence and that different bubble sizes lead to faster coalescence.

Mikic and Rohsenow [69] derived a correlation for the heat transfer during pool boiling in relation to the wall superheat and the cavity size distribution on the heated wall, assuming that only transient conduction and the subsequent replacement of the thermal boundary layer around a bubble contribute to the overall heat transfer. A comparison with experimental data on pool boiling of water and three organic liquids shows good agreement.

Dietl [17] performed numerous simulations of pool boiling out of single reentrant cavities of different geometry and out of subsurface tunnels. For circular reentrant cavities he found, that the cavity completely dries out and the processes inside the cavity have no influence on the heat transfer, if the size of the pore on top of the cavity is significantly smaller than the bubble departure diameter. If the pore diameter is in the scale of the bubble departure diameter, thin liquid films form in the corners of the cavity, which leads to a significantly enhanced heat transfer. Also complete flooding of the cavity with liquid and no remaining vapor and thus no further boiling from the cavity can occur, though. In contrast to Mikic and Rohsenow [69] he found, that the thermal boundary layer outside a pore of a reentrant cavity is almost not disturbed by a bubble growing from the cavity and departing. He concludes, that the subsequent replacement of the thermal boundary layer is a considerable mechanism only in case of a bubble growing on a flat surface, but not, if the bubble foot is pinned at the pore. Nevertheless he states, that there is indeed a convective flow removing a considerable amount of sensible heat in boiling from several pores close to each other.

Besides the aforementioned experiments, a series of numerical works investigate boiling in variable gravity in order to either accompany experimental investigations, or to study the influence of gravity.

Aktinol and Dhir [2] performed 2-D simulations of subsequent bubble cycles in pool boiling of water under variable gravity conditions using the Level-Set method, taking contact line evaporation and transient heat conduction from the solid wall into account. They used a wall superheat criterion to determine when to place a new bubble nucleus at the nucleation site and used the experimental results of Wang and Dhir [115] to estimate the necessary wall superheat. They found that the waiting time between subsequent bubbles strongly depends on the thickness and on the thermal conductivity of the heater because both variables influence the recovery of the substrate surface temperature. For the influence of gravity they found a strong impact on the growth period, but a less pronounced impact on the waiting time. However, they did not assume total weightlessness, but they reduced gravity to a level of 1 % of earth gravity, ensuring that the bubble would still detach from the wall eventually. Furthermore they observed a high variation of heat flux distribution along the wall and a significant temperature fluctuation at any location on the wall, which is traversed by the three-phase contact line.

Aktinol and co-workers [3] used the experimental results from [15] for validation and as a source of boundary conditions and performed 2-D simulations of nucleate boiling in microgravity in the presence of a noncondensable, dissolved gas using the Level-Set method. They found that noncondensables enrich at the top of the bubble, lowering the local vapor pressure and thus reducing the effect of subcooling.

Abarajith et al. [1] performed numerical investigations of bubble coalescence under reduced gravity conditions using the Level-Set method and validated the results with experimental results from parabolic flight campaigns. They found, that on a plane surface bubble coalescence in reduced gravity leads to early lift off and smaller departure diameters compared to single bubble boiling. The cause for the early lift off is found to be an additional drag force due to fluid motion during the coalescence process.

Kunkelmann and co-workers [55] performed numerical and experimental investigations of pool boiling in reduced gravity and of meniscus evaporation with different fluids. In spite of the two different processes and in spite of different fluids they found the same characteristic behavior regarding heat transfer in the contact line region. They confirmed a strong heat transfer peak near the contact line as well as the dependence of contact line evaporation on contact line velocity in case of a an advancing contact line, but a nearly independence in case of a receding contact line.

Urbano and co-workers [110] employed a level-set approach to perform simulations of subcooled pool boiling of water under microgravity conditions, focusing on a single bubble. They studied the steady state, when evaporation at the wall and condensation to the subcooled bulk are in equilibrium, and used the results to develop an analytical correlation of the equilibrium radius. The authors defined the ratio of the condensation Jacob number and the evaporation Jacob number as a measure between bulk subcooling and wall superheat. They performed parametric studies, varying this Jacob number ratio as well as the static contact angle. They showed, that the equilibrium radius is inversely proportional to the temperature gradient between the superheated wall and the subcooled bulk fluid. Additionally, the equilibrium radius decreased, if the bulk subcooling increased relative to the wall superheat, and it increased for an increasing contact angle. Moreover, they analyzed the Nusselt number in the vicinity of the bubble and found a complex dependency on both contact angle and Jacob number ratio. Transient heat transfer at the wall was included and the strong influence of the wall's heat transfer capacity on the evaporation mass flow rate and hence the equilibrium radius was highlighted.

2.4 Summary of state of the art, methodological approach and scope of this work

A lot of experimental and numerical research on nucleate boiling has been conducted during the recent decades. Some of the works examine the process on the scale of a single or a few bubbles, in contrast to phenomena on a molecular scale on the one hand and to heat transfer characteristics on an industrial scale on the other hand. In the majority of works boiling is investigated under earth gravity conditions, leaving every sub-process strongly connected with buoyancy.

In experimental works three main heat transfer mechanisms have been identified: Transient heat conduction to the thermal boundary layer and replacement of the latter in the vicinity of the bubble foot, evaporation or condensation at the bubble hull and microlayer or contact line evaporation, respectively. The importance of evaporation at the three-phase contact line for the overall boiling process has been emphasized. Experiments in microgravity showed, that the critical heat flux always decreases compared to earth gravity, but that the heat transfer coefficient can be enhanced significantly in the case of subcooled boiling.

Numerical simulations have proved to be an important complement to experiments in boiling research, since they are able to resolve arbitrarily small time and length scales and provide information at locations, which are not accessible in experiments. Furthermore, in simulations it is possible to vary and investigate the influence of single material properties and process parameters. Numerical works in literature support the findings of experimental works of different heat transfer mechanisms and their changing contribution to the overall heat transfer over the growth and detachment process.

Numerical works, which take contact line evaporation into account, support the experimental finding of its big share in overall heat transfer. The direction of contact line motion and its velocity appear to have a big influence on heat transfer in the microregion.
The thickness of the thermal boundary layer prior to nucleation appears to have an impact on the departure diameter and departure time under earth gravity conditions [30]. It will be examined, if this boundary layer thickness, which is influenced by system parameters as well as material properties, impacts the bubble growth rate and frequency under microgravity conditions, as well.

The vast majority of numerical works researching nucleate boiling focus on pool boiling and employ 2-D models. Except from simulations of taylor bubbles in microchannels, there are very few works simulating bubbles in a shear flow combined with microgravity conditions. The advantage of employing rotational-symmetric 2-D simulations is a lot lower requirement of computational resources. However, if the influence of a shear flow around a bubble shall be examined, it is not longer possible to employ rotational symmetry in the mid-axis of the bubble as it is conducted in most numerical works. Therefore, all simulations in the present thesis are conducted as 3-D simulations employing parallelization in the numerical solver.

In order to gain a deeper insight into boiling phenomena in microgravity, both for application in aerospace technology and for a fundamental understanding of the underlying mechanisms, the benchmark experiment "Reference mUltiscale Boiling Investigation" (RUBI) has been designed for operation aboard ISS starting in July 2019 [99]. In the present thesis the Multiscale Boiling experiment is reproduced numerically in order to take advantage of the aforementioned combination of experiment and simulation.

Prior to the ISS experimental campaign, the Multiscale Boiling experimental setup was used for preparatory studies in several parabolic flight campaigns. Results from those preliminary studies show,

that the impact of the process parameter input heat flux on bubble growth is a lot more pronounced than the impact of pre-heating time. A possible explanation for this different impact might be the relatively low thermal conductivity of the evaporating fluid [59]. However, this theory is not verified and analyzing the impact of specific material properties on a process by experiments is challenging. Hence, the thermal conductivity of liquid FC-72 is varied in the simulations conducted for the present thesis. Additionally, thermal conductivity and heat capacity of the heater substrate is varied in order to verify the applicability of an existing correlation from literature on the impact of those two material properties on the heat transfer coefficient.

Preliminary simulations conducted for the present thesis showed, that the numerical reproduction of the boiling experiments in parabolic flight campaigns is not straightforward. In the experiments the process suffered from g-jitter, fluctuations in gravitational acceleration, which often causes a bubble to detach mostly or complete and to hover closely above the surface without developing a three-phase contact line. This phenomenon is difficult to reproduce numerically, since the exact fluctuation of the acceleration field must be implemented into the simulation, which is often not known exactly. In contrast it is a lot more straightforward to reproduce space station experiments with perfect long-term weightlessness. Hence, validation simulations, which aim to reproduce specific experimental runs, focus on the Multiscale Boiling experiment aboard ISS in the present work. A detailed description of the experimental setup during the ESA 70th parabolic flight campaign in 2018 can be found in a work from Nejati et al. [75]. Information on and results of the 71st ESA parabolic flight campaign conducted in May 2019 are available in the master's thesis of Kühnemund [59].

In the experiment the only nucleation site is a cavity, which was manufactured by laser technology in the surface of the heater. The length scales of the boiling process in the boiling cell are several orders of magnitude higher than that of the evaporation process inside the cavity. This makes it challenging to cover both processes in one and the same simulation. Therefore the simulations of the nucleation process and of the bubble growth and movement inside the test cell are conducted separately.

The first set of the investigations are 3-D simulations of laminar flow boiling of FC-72 in microgravity in the Multiscale Boiling cell, neglecting the cavity and assuming a perfectly smooth wall in the nucleation site area. Several successively nucleating, growing and moving bubbles are simulated in each run. The nucleation process is modeled by artificially creating a bubble nucleus on the flat wall. This modeling of the nucleation process depends on several assumptions and simplifications. It will be discussed, which modeling errors and deviations between simulation and experiment are caused by those assumptions and if the physics of the boiling process is still displayed correctly by the numerical approach.

The process of nucleation inside a cavity and bubble detachment from the latter is investigated in a second set of simulations. Generic investigations of the nucleation process out of simple cavities with a circular cross section and different depths are carried out in order to examine the detachment process off the cavity in microgravity. It will be shown, that the specific geometry of the cavity either causes complete flooding of the cavity, disabling the nucleation site, or remaining of vapor inside the cavity. This question is discussed in the context of microgravity, because in the existing literature a bubble detaches from a cavity due to buoyancy, whereas in the discussed setup a bubble can only detach due to the shear flow. The relation between flow velocity and the bubble diameter at detachment will be expressed by a dimensionless correlation.

Furthermore, the nucleation process in the Multiscale Boiling experiment is investigated numerically taking the very deep, L-shaped geometry of the cavity into account. The impact of system parameters on the nucleation process is discussed as well as the impacts of the nucleation process on subsequent bubble

growth outside the cavity.

For the two different strategies and length scales, several key questions are addressed by the simulations. For the boiling cell simulations the following questions emerge:

1. Does the numerical model developed in the present thesis, including assumptions and simplifications compared to the according experiment, cover the physics of the boiling process sufficiently?
2. How do the process parameters input heat flux, pre-heating time, flow velocity and subcooling influence heat and fluid flow of the boiling process?
3. What is the impact of the thermal conductivity of the evaporating fluid as well as the thermal conductivity and the heat capacity of the solid substrate on bubble growth and heat transfer coefficient?

For the cavity simulations, the following questions shall be adressed:

4. When a bubble grows out of a cavity under microgravity conditions, what is the influence of cavity depth and flow velocity on the bubble detachment diameter and on flooding of the cavity?
5. Which impact do system parameters and the position of the nucleus inside the L-shaped cavity of the Multiscale Boiling experiment have on the nucleation process?
6. Does the growth process of the bubble out of the cavity effect the following bubble growth in a way, which is not covered by the boiling cell simulations?

The simulations are conducted on the "Lichtenberg" High Performance Cluster of the Hessian State.

3 The Multiscale Boiling experiment on the International Space Station

The numerical work of the present thesis is a subproject of the Multiscale Boiling experimental project, also known as RUBI (Reference mUltiscale Boiling Investigation), which is coordinated and supported by the European Space Agency (ESA) [99]. Since the numerical simulations are heavily entangled with the Multiscale Boiling experiments, a brief outline of the experiments will be given in this chapter.

Single bubble boiling of FC-72 is carried out under microgravity conditions in form of pool boiling as well as under the influence of a laminar shear flow and/or of an electrical field. The design of the experiment allows for implementation on the International Space Station, which enables to perform experiments under permanent, stable microgravity conditions without temporal limitation or disturbances e.g. by g-jitter. In preparation of the ISS experiments, components of the experimental setup were tested during several parabolic flight campaigns beforehand.

3.1 Experimental design and scope

The central component of the experimental setup is a boiling cell made of stainless steel, illustrated in figure 3.1 (a) with external dimensions of 117 x 90 x 91 mm ([75]). It has two optical accesses opposite of each other designed as transparent synthetic windows, which enable the observation of the boiling phenomena by a black and white camera and a corresponding light source.

A substrate heater is situated below the fluid volume inside the test cell, its assembly is depicted in figure 3.1 (b). Its core element is a barium-fluoride crystal of 25 mm diameter and a 45° chamfer at its top, resulting in a 20 mm diameter at its top boundary to the fluid. Its height is 9 mm. It is sputtered with a thin chromium layer on its top surface. This layer is contacted by two copper electrodes and serves as an electrical resistance heater. The barium-fluoride is transparent for infrared radiation, so that 2-D infrared images of the top heater surface can be taken from below the heater. In the numerical simulations, only the BaF2 crystal is taken into account. A detailed description of the manifacturing process of the substrate heater can be found in [75].

Vapor bubbles are supposed to solely nucleate at an artificial nucleation site in the middle of the top surface of the barium-fluoride crystal. The nucleation site is an L-shaped cavity with a circular cross-section of 30 μm diameter, which was lasered into the center of the crystal substrate beforehand. In order to activate this nucleation site at the end of the pre-heating time in an experimental run, a laser beam is focused on the cavity for several milliseconds in order to create the necessary superheat. The depth and the L-shape of the cavity ensure, that enough residual vapor is left in the cavity, ensuring the nucleation of subsequent bubbles after a bubble has detached from the cavity.

A high voltage electrode is inside the boiling cell, which can be moved to a position above the substrate heater to perform boiling experiments within an electrical field. However, those experiments are not reproduced by the simulations of the present thesis. Additionally, a rack of 4 micro-thermocouples ("MTCR") can be moved closely towards the nucleation site in order to measure the fluid temperature.

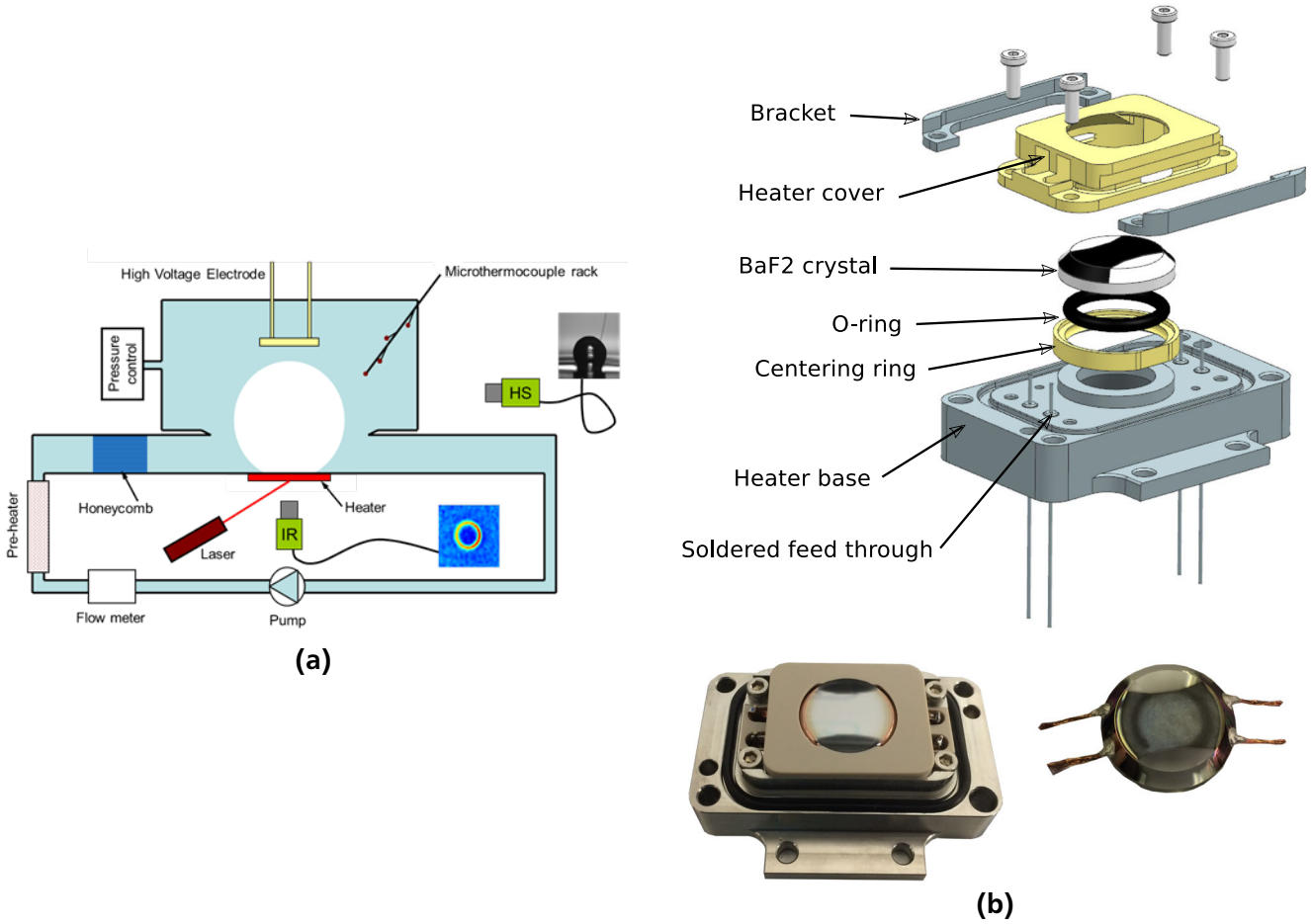

Figure 3.1: Illustration (a) of the boiling cell assembly and (b) of the heater assembly [75]

Both the high voltage electrode and the MTCR are situated at the top of the cell by default and only one of them at a time can be moved in their active position if needed.

The boiling cell has an inlet and an outlet port for a shear flow. Upstream of the inlet port there is a honeycomb structure, which serves to freeing the shear flow of turbulences and to straighten it. The resulting laminar shear flow in the rectangular flow channel of the boiling cell then passes the heater substrate and gets heated by the latter. Downstream of the outlet port a collecting unit of constricting cross section follows. The FC-72 shear flow is driven by a pump and tempered by an additional heater inside this cycle.

Detailed information on the technical requirements, parameter ranges and experiment conduction on the International Space Station since July 2019, as well as on the motivation and the physical background is provided in the "Experimental Scientific Requirements" document provided by ESA [99].

3.2 ISS Experiments

Beginning in July 2019, the Multiscale Boiling experiment has been carried out aboard the ISS. Figures 3.2 and 3.3 show black and white images of experiments aboard the ISS, the first of a pool boiling case, the second of a flow boiling case. The images were recorded with a framerate of 500 frames per second. From the black and white images, the volume of vapor and thus the size of the bubbles in the

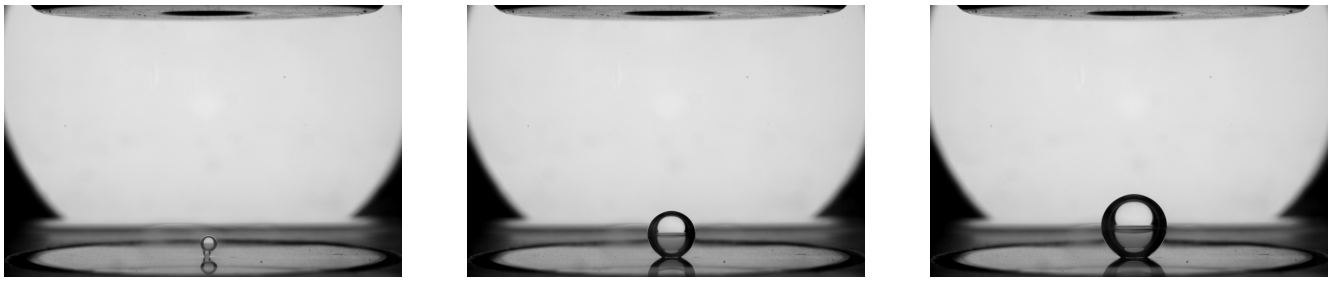

(a) (b) (c)

Figure 3.2: Sequence of black and white images from a pool boiling case of the Multiscale Boiling experiment aboard the ISS with $p = 0.5\,\text{bar}$ / $t_{\text{sat}} = 37.7\,°\text{C}$, 5 K subcooling, $\dot{q}_{\text{in}} = 1.23\,\text{W/cm}^2$, 5 s pre-heating time, (a) 20 ms, (b) 1 s, (c) 2 s after nucleation. The very first bubble detaches due to inertia forces caused by rapid nucleation inside the cavity, merges with the succeeding bubble and attaches to the wall again

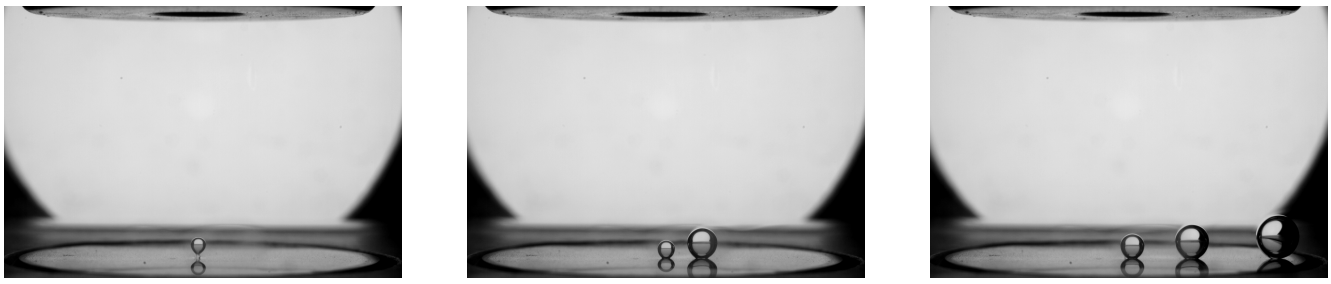

(a) (b) (c)

Figure 3.3: Sequence of black and white images from a shear flow boiling case of the Multiscale Boiling experiment aboard the ISS (the right side of the pictures is the downstream side) with $p = 0.5\,\text{bar}$, 5 K subcooling, $\dot{q}_{\text{in}} = 1.23\,\text{W/cm}^2$, 5 s pre-heating time, 0.3 l/min volume flow, (a) 20 ms, (b) 0.4 s, (c) 1.2 s after nucleation. The very first bubble detaches due to inertia forces caused by rapid nucleation inside the cavity, coalesces with several succeeding bubbles until it attaches again downstream. See also figure 5.37

corresponding time step is deduced by an algorithm: In Matlab, all pixels in a picture, which apply for a minimum level of brightness, and which are located within a prescribed area, where a bubble is assumed, are counted. The summed up area of all those pixels represents the cross-section of the bubble. It is assumed, that the bubble is a perfect sphere, thus from the cross section the equivalent diameter of a single, spherical bubble can be deduced.

This approach is applied in the present thesis in section 5.3, when numerical results are compared to experiments for validation. Since the search for bright pixels is relatively imprecise, this approach comes with a uncertainty and the high-frequent fluctuations in the resulting diameters can lead up to over 45 . Therefore, when black and white images from the Multiscale Boiling experiments are evaluated, the evaluated cross-section is filtered employing a low-pass filter with a cutoff frequency of 25 Hz in Matlab. The resulting diameters gained from the evaluated black and white images of a flow boiling case are shown in figure 3.4.

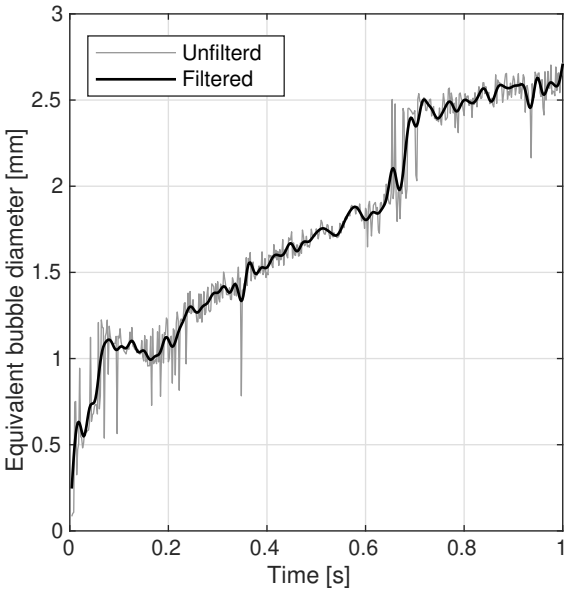

Figure 3.4: Bubble equivalent diameters in the flow boiling case presented in figure 3.3 before and after application of a low-pass filter with a cutoff frequency of 25 Hz. The diameters are gained by evaluation of the black and white images

4 Numerical model

The numerical solver utilized in the present thesis is based on the interFoam solver from the OpenFOAM framework [121], which has been significantly enhanced by Kunkelmann [54], Batzdorf [5], Dietl [17] and Rettenmaier [81]. The solver uses the Finite-Volume-Method (see e.g. [89]) to solve the conservation equations of continuum mechanics and the Volume-of-Fluid method [38] to capture the liquid-vapor interface. Heat and mass transfer in the vicinity of the three-phase contact line (see figure 4.1) are calculated by a subgrid model. The basic functionality of the numerical solver as well as modifications, which have been made to address specific demands of the present work, are outlined in the following chapter. A detailed step-by-step description of the simulation procedure in one transient time step in the solver in use is given by Batzdorf [5], p. 85, and Rettenmaier [81], pp. 60, in form of a program flow chart. All simulations presented in the present thesis have been conducted with OpenFOAM version 5.

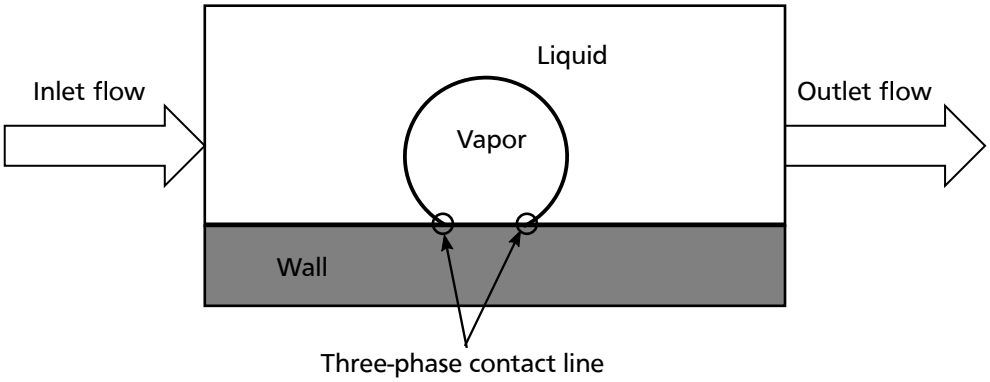

Figure 4.1: Scheme of relevant regions, the liquid-vapor interface and the position of the three-phase contact line in the considered numerical setup

4.1 Governing equations

The fluid flow can be described by the set of extended Navier-Stokes-Equations, i.e. the conservation equations of mass, momentum and energy within the theory of continuum mechanics. Following assumptions are made throughout all simulations of the present thesis:

- The fluid properties are constant,
- the fluid is newtonian,
- the work of pressure and of viscous dissipation can be neglected,
- Fourier's law can be applied for the heat flux,
- the fluid in each of the two phases is incompressible.

The latter is justified due to the very low Mach-numbers throughout the flow field, although part of the fluid consists of vapor. The conservation equations of mass, momentum and energy are then:

$$\nabla \cdot \vec{u} = \Sigma_V, \tag{4.1}$$

$$\rho\left(\frac{\partial\vec{u}}{\partial\tau}+(\vec{u}\cdot\nabla)\vec{u}\right)=-\nabla p+\nabla\left(-\frac{2}{3}\mu\nabla\cdot\vec{u}\right)+\nabla\cdot\left(\mu(\nabla\vec{u}+(\nabla\vec{u})^{\mathrm{T}})\right)+\vec{f}_{\sigma}+\rho\vec{g}, \tag{4.2}$$

$$\frac{\partial\rho cT}{\partial\tau}+\nabla\cdot(\vec{u}\rho cT)=\nabla\cdot(\lambda\nabla T)+\Sigma_{\mathrm{e}}. \tag{4.3}$$

The terms Σ_{V} and Σ_{e} on the right hand side of equation (4.1) and (4.3), respectively, account for mass and energy sources due to evaporation or condensation. Their calculation is described in detail in section 4.3. The terms $\vec{f}_{\sigma}$ and $\rho\vec{g}$ on the right hand side of equation (4.2) account for volumetric forces due to surface tension and gravity, respectively.

In the computational domain of the solid wall, the energy equation simplifies to three-dimensional heat conduction:

$$\frac{\partial\rho cT}{\partial\tau}=\nabla\cdot(\lambda\nabla T). \tag{4.4}$$

Multiphase flow is captured by the Volume-of-Fluid method of Hirts and Nichols [38], which uses an indicator variable F to distinguish between the liquid and the vapor phase. This volume fraction field F is zero for cells completely filled with vapor and unity for cell completely filled with liquid. In cells containing part of the interface, F has values between zero and unity. In OpenFOAM, the advection of the volume fraction field is solved by the MULES algorithm:

$$\frac{\partial F}{\partial\tau}+\nabla\cdot(\vec{u}F)+\nabla\cdot(\vec{u}_{\mathrm{r}}F(1-F))=\Sigma_{\mathrm{V}}. \tag{4.5}$$

Again, the term on the right hand side of equation 4.5 accounts for phase change. In order to prevent diffusion of the interface, the compression term $\nabla\cdot(\vec{u}_{\mathrm{r}}F(1-F))$ is introduced, which only acts in cells containing the interface. The compression parameter $\vec{u}_{\mathrm{r}}$ points orthogonal to the interface and scales with the flow velocity in the standard framework of interFoam. Due to very small flow velocities in the simulations conducted for the present thesis, it turned out to be necessary to modify this method and use a fixed value independent of the flow velocity for $\vec{u}_{\mathrm{r}}$, because otherwise an extreme smearing orthogonal to the interface over the range of several 10 cells occured in some of the simulations. In all calculations presented in the following chapters, the compression velocity is set to $\vec{u}_{\mathrm{r}}$=0.1 m/s.

The material properties χ of the fluid are calculated by linear averaging of the liquid and the vapor properties χ_{l} and χ_{v}:

$$\chi=F\chi_{\mathrm{l}}+(1-F)\chi_{\mathrm{v}}. \tag{4.6}$$

For the sake of simplicity, the fluid properties are assumed to be constant at saturation temperature of the system pressure.

When the continuity equation 4.1 and the momentum equation 4.2 are discretized using the finite volume method, velocity and pressure show a linear dependence of one another. In transient OpenFOAM solvers this problem is addressed by employing the PISO loop, which was developed by Issa et al. [44] and which solves both quantities in an iterative loop.

The systems of linear equations originating from the finite volume discretization are solved employing a *Preconditioned Conjugate Gradient (PCG)* solver combined with a *Geometric Algebraic Multi Grid (GAMG)* preconditioner. A detailed description of the PISO algorithm, the employed solvers and the finite volume method in general can be found in relevant literature, e.g. [89].

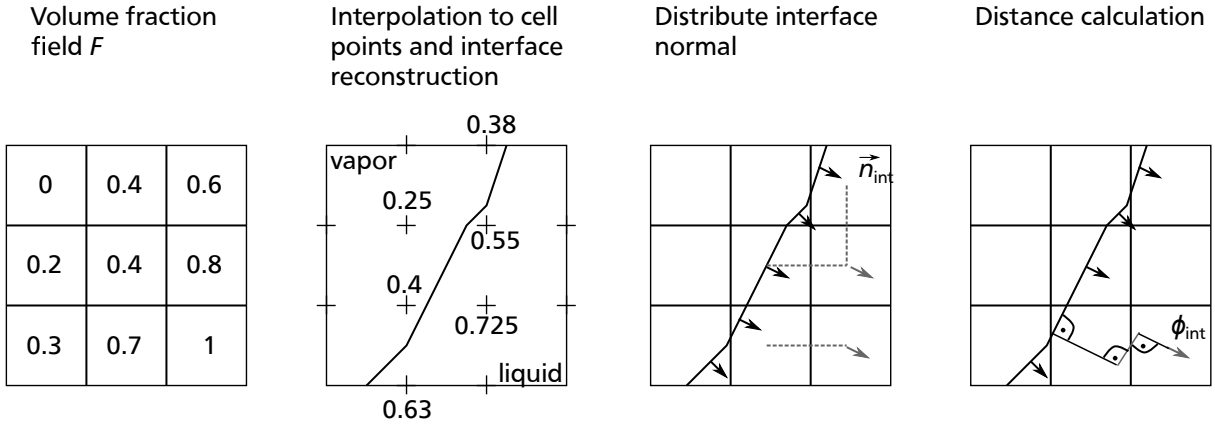

Figure 4.2: Illustration of the interface reconstruction following [17]

4.2 Interface capturing method

As introduced above, the position of the liquid-vapor interface is represented indirectly by the volume fraction field of the Volume-of-Fluid method. The robustness, applicability to unstructered meshes and mass conservative characteristic are the reasons for the popularity of the VOF approach. Within OpenFOAM, the volume fraction advection equation 4.5 is solved explicitly bounding the values for F between 0 and 1.

In the pure algebraic VOF-method, the exact position of the interface is not explicitly given. Nevertheless, this information is needed for the evaporation model in order to accurately calculate the temperature gradient between a cell and the interface. Furthermore, the curvature calculation from the volume fraction field itself turns out to cause strong spurious currents, as shown in section 4.2. Therefore the interface is reconstructed explicitly in every time step by a method called isosurface reconstruction, which is presented schematically in figure 4.2.

In the first step, all cells, which contain a part of the interface, have to be marked. Two methods are available for this step, the first selecting cells by their direct value of F,

$$C_1 < F < C_2, \tag{4.7}$$

where C_1 and C_2 should be in the magnitude of 10^{-9} or $1-10^{-9}$, respectively. The second method selects cells by their gradient of F:

$$|\nabla F| > C. \tag{4.8}$$

C is usually in the magnitude of $10^{-2}\,1/\mathrm{m}$. Rettenmaier [81] strongly advises the use of the gradient method for long simulation times, because over time small amounts of the volume fraction $F < 10^{-6} \vee F > (1-10^{-6})$ smear out over the whole computational domain, despite the counter gradient compression scheme of the MULES algorithm. Hence, in all simulations presented in the present theses the gradient method has been chosen with $C = 10^{-2}\,1/\mathrm{m}$.

After the necessary cells are marked, the steps of interface reconstruction are as followed:

- The cell centered values of F are interpolated to the cell points (Figure 4.2 (b)).
- Between these cell points, all values of $F = 0.5$ are marked on the cell edges.

- Those points are connected by planes, which then represent the piecewise reconstructed interface.
- In each cell the interface normal $\vec{n}_{\text{int}}$ and the interface area A_{int} are calculated.
- Both these values are distributed to neighboring cells and a distance field ϕ_{int} from these cells to the interface is calculated (Figure 4.2 (c) and (d)).
- In boundary cells the value for $\vec{n}_{\text{int}}$ is corrected to comply with the contact angle from the employed contact angle boundary condition.
- The curvature is calculated and smoothed.

The obtained interface is continuous, but opposed to geometric VOF representations like SLIC or PLIC it is not strictly mass conserving due to its piecewise linearity. Therefore, it is not possible to reset the volume fraction field using the reconstructed interface in order to prevent interface diffusion.

After the values of F have been interpolated from the cell centers to the cell points (for the methods of interpolation, see [5]), the reconstruction of each interface segment in form of a polygon between the points of $F = 0.5$ on the cell edges is carried out following the geometrical considerations of López and Hernández [66]. Because the resulting polygon is not always exactly planar, the center $\vec{x}_{\text{int}}$ of the segment is calculated via triangulation. The surface normal vector is calculated as:

$$\vec{S}_{\text{int}} = \sum_{\text{i}=1}^{N_p} \frac{1}{2} (\vec{x}_{\text{p,i}} \times \vec{x}_{\text{p,i+1}}). \tag{4.9}$$

$\vec{x}_{\text{p,i}}$ are the polygon corner points ordered clockwise. The area of the segment then reads

$$A_{\text{int}} = |\vec{S}_{\text{int}}| \tag{4.10}$$

and the unit normal vector

$$\vec{n}_{\text{int}} = \frac{\vec{S}_{\text{int}}}{|\vec{S}_{\text{int}}|} \tag{4.11}$$

points into the denser fluid. The interface normal information is then distributed to a band of cells around the interface, as described in [5], pp.68. The calculation of the distance field, which is necessary to calculate the gradients of the temperature field next to the interface, is done in one step with the distribution of the interface normals by:

$$\phi_{\text{int}} = (\vec{x}_{\text{c}} - \vec{x}_{\text{int}}) \cdot \vec{n}_{\text{int}}. \tag{4.12}$$

Here, ϕ_{int} is positive in the denser fluid and negative in the less dense phase. During pre-processing, one can define a threshhold for interface normal distribution and distance calculation, such that those steps are only performed in a limited band of cells around the interface, in order to reduce computational costs.

At wall boundaries, the values of the volume fraction field at the cell points have to be adjusted in a way such that the gradient of F at the boundary face matches the contact angle given by a contact angle model discussed later. This is needed in order to accurately determine the position of the three-phase contact line. For a detailed description of the correction method see [5] and [81].

Treatment of surface tension

An accurate calculation of surface tension is crucial for the simulation of vapor bubbles, where surface tension has a strong influence on hydrodynamics. Even a slightly wrongly calculated surface tension leads to strong numerical induced flows at the liquid-vapor interface, called spurious currents. Rettenmaier [81] gives an overview over different approaches of the calculation of surface tension. In this section only a short presentation of the method implemented in interFoam and the enhancements made in the code used for the simulations of this work is given.

Brackbill et al. [8] introduced the Continuum Surface Force method (CSF), which converts the surface tension force into a volumetric force as it appears in 4.2. This way, the method overcomes the problem, that within a VOF approach the pressure jump across the interface cannot be implemented, since the exact interface position is not known:

$$\vec{f}_\sigma = \sigma K \nabla F. \tag{4.13}$$

Herein, K represents the curvature of the interface, which Brackbill et al. [8] suggest to calculate as

$$K = -\nabla \cdot \frac{\nabla F}{|\nabla F|}. \tag{4.14}$$

This formulation is the implementation of surface tension used in original interFoam. However, it has been shown, that with this formulation the curvature error increases with a finer mesh resolution, leading to strong parasitic currents, if the grid near the interface is refined [81]. This occurs because the gradient of F only provides an approximation of the normal direction of the interface within a grid cell. Only a small inaccuracy causes a force component tangential to the interface, which results in parasitic currents. Therefore, the curvature is calculated from the unit normal vector $\vec{n}_{\text{int}}$ of the reconstructed interface (see equation 4.11).

First, the information about the interface normal, which has only been calculated for interface containing cells, is propagated to a band of neighboring cells around the interface (see [5] for the distribution algorithm). The curvature is then calculated as

$$K = -\nabla \cdot \vec{n}_{\text{int}}. \tag{4.15}$$

In order to reduce spurious currents even more, the curvature field is then smoothed in multiple cycles. Initially, the curvature field is only present in interface containing cells. A median filtering of the curvature field is applied among the interface cells. Next, the filtered curvature values are distributed from interface cells to a narrow band of neighboring cells and again filtered. Both averaging operations can be conducted a pre-defined number of times; in this work both averaging operations have been conducted two times following the suggestions of Kunkelmann [54] and Batzdorf [5].

Rettenmaier [81] compared the quality of curvature calculation between the interface reconstruction method outlined above, the standard CSF method and three other methods for a static droplet testcase and a capillary rise testcase. He showed, that the maximum domain velocity, which serves as a measure of parasitic currents in case of an otherwise completely static droplet, is about one order of magnitude lower for the iso-surface reconstruction method compared to the standard CSF method. For the capillary rise test case an improved accuracy in the calculation of the meniscus height is shown compared to standard CSF, however, the best results have been achieved with a combined VOF-Level Set approach.

4.3 Evaporation model

Phase change is included in the simulation code by the source terms in equations 4.1, 4.3 and 4.5. To calculate these source terms, an evaporation model is required. Batzdorf [5] developed an evaporation model with an implicit approach based on explicit models by Hardt and Wondra [33] and Kunkelmann and Stephan [58]. Solving the implicit formulation of the heat flow from a cell to the interface overcomes the problem of mutual dependency between the temperature of a cell and the heat flow from this cell towards the interface. This way it avoids the need for iteration loops and temperature undershoots below saturation temperature. Throughout the present thesis, Batzdorf's model is employed to calculate the phase change source terms and will briefly be outlined in in the following.

The liquid-vapor interface is assumed to be always at saturation temperature. In order to determine the heat flow from the liquid and vapor bulk towards the interface, it is calculated for a band of cells on each side of the interface, which contain pure liquid or pure vapor, respectively, and which share at least one cell point with an interface containing cell. The heat flow from one of those cells to the interface is calculated based on the local temperature gradient and distance field. An additional weighting factor is introduced depending on the angle between the interface normal and the distance vector between the cell center and the interface (see [5], pp. 71). To avoid heat conduction over the interface, the thermal conductivity is set to zero at the cell faces of interface containing cells. The energy source term for a liquid cell i and all adjacent interface cells j then reads

$$\Sigma_{\mathrm{e,i}} = -\frac{\dot{Q}_{\mathrm{i,int}}}{V_{\mathrm{i}}} = -\frac{1}{V_{\mathrm{i}}} \sum_{\mathrm{j}} w_{\mathrm{i,j}} A_{\mathrm{int,j}} \frac{\lambda_{\mathrm{l}}}{\phi_{\mathrm{int,i}}} (T_{\mathrm{i}} - T_{\mathrm{sat}}) \tag{4.16}$$

with the weighting factor $w_{\mathrm{i,j}}$. For the pure vapor cells adjacent to the interface cells the procedure is performed accordingly. Note, that the value for Σ_{e} becomes positive for a heat flow from a liquid cell to the interface and negative for a heat flow from a vapor cell to the interface because of the orientation of ϕ_{int}. For the numerical implementation of the implicit solution procedure, as for the detailed calculation of the weighting factors, see Batzdorf [5], pp. 71.

The mass transfer due to phase change inside a single interface containing cell is defined as

$$\dot{M}_{\mathrm{evap}} = -\frac{(\dot{Q}_{\mathrm{l,int}} + \dot{Q}_{\mathrm{v,int}})}{\Delta h_{\mathrm{v}}}. \tag{4.17}$$

Here, Δh_{v} is the specific evaporation enthalpy of the fluid and $\dot{Q}_{\mathrm{l,int}}$ and $\dot{Q}_{\mathrm{v,int}}$ are the heat flows from all adjacent liquid and vapor phase cells towards the regarding interface cell. Note, that $\dot{M}_{evap}$ becomes negative in case of condensation. To avoid issues regarding a continuously further smearing of the F-field, the mass source terms are not implemented directly in interface containing cells, but instead separate source terms for the liquid and the vapor bulk are defined according to a method proposed by Hardt and Wondra [33]. This way phase change is modeled as extinction of mass on one side of the interface and its re-appearance on the other side, outside the actual interfacial region. The initial mass source term is

$$\psi_0 = \frac{\dot{M}_{\mathrm{evap}}}{V_{\mathrm{c}}} + \frac{\dot{Q}_{\mathrm{cl,f}}}{\Delta h_{\mathrm{v}} V_{\mathrm{c}}}. \tag{4.18}$$

In equation 4.18 the mass source term due to contact line evaporation has been added for contact line containing cells. For its determination, see section 4.5.

Since large local mass sources can lead to stability problems, this source term is smeared out over several cells. The smooth distribution ψ is given by the solution of the inhomogeneous Helmholtz equation

$$\widetilde{D}\Delta\psi = \psi - \psi_0. \tag{4.19}$$

The constant $\widetilde{D}$ is set at pre-processing and determines the width over which ψ_0 gets smeared out. If Δx is the width of one cubic cell, a choice of $\widetilde{D} = (4\Delta x)^2$ leads to a distribution of the source term over a range of three to four cells in each direction, which is the value chosen throughout the present thesis. The mass source term in each cell around the observed interface cell is then

$$\dot{\rho} = [N_\mathrm{v}(1-F)H(F_0-F) - N_\mathrm{l}FH(F_0-1+F)]\psi. \tag{4.20}$$

Here, F_0 is a cutoff value and H is the Heaviside function, which ensures, that the smeared liquid and vapor sources do not spatially overlap. F_0 is set to 0.1 throughout the present thesis. N_v and N_l, respectively, represent normalization coefficients, which ensure global mass conservation. They are defined such that the source terms integrated over the computational domain are constant:

$$N_\mathrm{v} = \frac{\iiint_V \psi_0 dV}{\iiint_V (1-F)H(F_0-F)\psi dV}, \tag{4.21}$$

$$N_\mathrm{l} = \frac{\iiint_V \psi_0 dV}{\iiint_V FH(F_0-1+F)\psi dV}. \tag{4.22}$$

The mass source term in the continuity equation and the volume fraction equation results to

$$\Sigma_\mathrm{V} = \dot{\rho}\left(H(F_0-F)\frac{1}{\rho_\mathrm{v}} - H(F_0-1+F)\frac{1}{\rho_\mathrm{l}}\right). \tag{4.23}$$

4.4 Hydrodynamics and evaporation at three-phase contact lines

As pointed out in section 2.2 the evaporation at the three-phase contact line makes for a large relative amount of the evaporation heat transfer during nucleate boiling. However, simulating the heat and mass transfer within the contact line region with the numerical solver by resolving the length scales by the numerical grid would demand unacceptable computational resources. Based on the work of Stephan and Busse [102] Kunkelmann [54] developed a subgrid model to determine the heat transfer through the microzone, which was later enhanced by Batzdorf [5]. This model provides a solution for contact line heat transfer, contact angle and film thickness for any desired combination of the two input variables wall superheat and contact line velocity. The solutions are passed to the CFD-solver in parameterized form prior to a simulation such that the solver can determine contact line heat flow and contact angle from the wall temperature and contact line velocity in each time step. Hence, those two variables must be determined by the solver before the solution from the subgrid model can be employed. The temperature field at the wall is a solution of the coupled conjugate heat transfer solution algorithm outlined in section 4.5. In the following section, a short outline will be given on the challenges of contact line velocity within the numerical solver. The solution algorithm of the subgrid model itself are outlined in section 4.4.2.

4.4.1 Determination of the contact line velocity

At the development status, when the present thesis was written, the numerical solver offered a selection of three different approaches of contact line velocity calculation. The easiest way is to take the velocity in the cell center of a contact line containing cell and define its component parallel to the wall as contact line velocity. This approach is implemented in original interFoam but it is quite imprecise. Linder et al. [65] argue, that setting the contact line propagation velocity equal to the velocity of the next material point is not physical and only holds for contact angles close to 90°.

Instead, the authors propose a contact line velocity model based on geometrical considerations. For a velocity in the nearest cell midpoint $\vec{u}_c$ and the vector normal to the wall $\vec{n}_w$, the contact line velocity reads:

$$u_{\mathrm{cl}} = \frac{\vec{u}_{\mathrm{c}} \cdot \vec{n}_{\mathrm{int}}}{\sqrt{1-(\vec{n}_{\mathrm{w}} \cdot \vec{n}_{\mathrm{int}})^2}}. \tag{4.24}$$

A detailed derivation of 4.24 can be found in [65] and [64]; the square in the denominator has been added by Rettenmaier [81].

Batzdorf [5] proposes a method, which determines the contact line velocity from the contact line position in the current and the last time step. In order for this approach to work, the exact position of the contact line in every time step must be known from the iso-surface reconstruction. However, the iso-surface reconstruction at the boundary is not as straightforward as it is at faces between grid cells, because the volume fraction is a cell centered field and not properly defined at boundaries. In order to determine the position of the contact line, a correction of the volume fraction field at the boundary is necessary. The correction algorithm uses a prescribed contact angle to derive the face centered value of the volume fraction from its value at the cell center. The procedure and its derivation are described in detail in the works of Batzdorf [5], pp. 64, and Rettenmaier [81], pp. 38. The so corrected boundary values are interpolated to the edges at the boundary and the contact line is reconstructed accordingly to the iso-surface reconstruction.

The contact line velocity is then calculated as the temporal derivative between the contact line position vectors at the current and the last timestep projected onto the component of the interface normal tangential to the wall:

$$u_{\mathrm{cl}} = -\frac{1}{\Delta\tau}(\vec{x}_{\mathrm{cl}}^{(i)} - \vec{x}_{\mathrm{cl}}^{(i-1)}) \cdot \left(\frac{\vec{n}_{\mathrm{int}} - (\vec{n}_{\mathrm{int}} \cdot \vec{n}_{\mathrm{f}})\vec{n}_{\mathrm{f}}}{|\vec{n}_{\mathrm{int}} - (\vec{n}_{\mathrm{int}} \cdot \vec{n}_{\mathrm{f}})\vec{n}_{\mathrm{f}}|} \right). \tag{4.25}$$

It has to be noted, that the contact angle is dependent on the contact line velocity, whereas in this approach the prescribed contact angle is used to correct the boundary volume fraction field. This counter-dependency is solved by a fixpoint-iteration, in which the solution for the contact angle is under-relaxed in order to support convergence [5].

When selecting one of the above methods for the calculation of contact line velocity, the specific demands of the simulations conducted for the present thesis as well as the combination with other numerical methods have to be considered. Rettenmaier [81] showed, that the model, which determines the contact line velocity from its position as proposed by Batzdorf, provides the results best matching with experimental data, but fails in combination with contact line pinning models. However, in the present thesis no pinning model is involved since no stick-slip effect is expected in boiling FC-72. Additionally, in section 4.5 it will be shown, that the position of the contact line in every time-step has to be determined anyway for the proper simulation of coupled conjugate heat transfer between wall and fluid. Hence, the

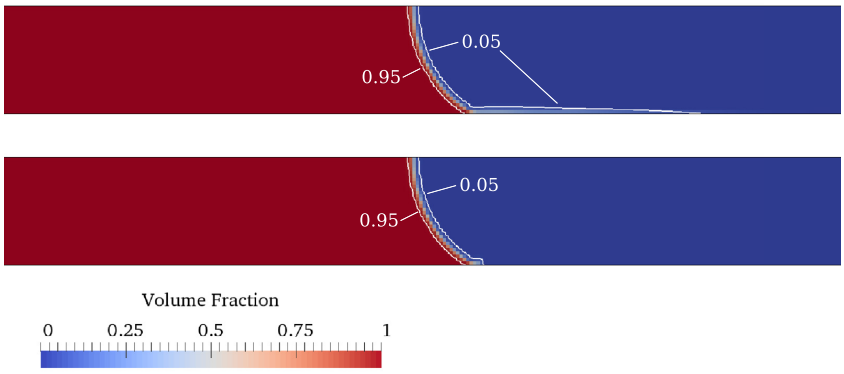

Figure 4.3: Volume fraction field in case of the original (top) and modified (bottom) boundary correction approach from [32]. 0.05 and 0.95 iso-lines of the volume fraction field are displayed in white. ©The authors ([32]), available under Creative Commons BY 4.0 license: http://creativecommons.org/licenses/by/4.0/

contact line position approach is selected to calculate the contact line velocity, with one modification:

In the original version of this approach as introduced by Batzdorf [5] the correction of the volume fraction field at the boundary employing a prescribed contact angle is imposed at the entire wall boundary, regardless if a face actually contains part of the contact line. This can cause an extreme smearing of the liquid-vapor interface in the first cell layer above the wall due to non-physical values of the surface tension force, depicted in figure 4.3. In order to avoid this problem, Gründing et al. [32] introduced a modification of the boundary correction. Here, the prescribed contact angle is used only to correct the volume fraction field at boundary faces in a band of approximately eight cells around the $F = 0.5$ iso-surface, whereas a contact angle of 90° is imposed at the rest of the boundary faces. The authors showed a significant reduction of the smearing issue, which could be confirmed during the simulations conducted for the present thesis. Therefore in all simulations presented in this work, the modification of the boundary correction by Gründing et al. has been employed.

4.4.2 Evaporation at the three-phase contact line

As outlined in section 2.2, the heat transfer at the three-phase contact line has a high share in the overall evaporation heat transfer. Proper modeling of the evaporation in this region is crucial for computational results of high accuracy. In section 2.1 the co-existence of the contact line and the microlayer model has been discussed. Since in the present thesis boiling of FC-72 with very slow contact line velocities is simulated, the contact line evaporation model is more suitable to cover the underlying physics and it is employed in all conducted simulations.

Since the length of the microzone is usually smaller than one micrometer, it is not efficient to resolve it with the numerical grid and cover the hydrodynamic and heat transfer phenomena inside it with a direct numerical simulation. Instead, the physics inside the microzone are covered by a subgrid model, which is solved once before the CFD simulation. The first work to introduce the concept of evaporating thin films to model contact line evaporation was Wayner et al. [116]. Based on this work Stephan and Busse [102] derived a model for contact line evaporation founded on a dimensional analysis to simplify the governing equations in the microzone. They stated the following assumptions:

- The lubrication theory is valid, i.e. the liquid layer is thin and the Reynolds-number is low.

- Heat conduction is one-dimensional.
- The wall temperature within the whole microzone is uniform.
- The thermal inertia of the system is small, therefore the system can be assumed to be at steady state.

Governing equations in the microzone

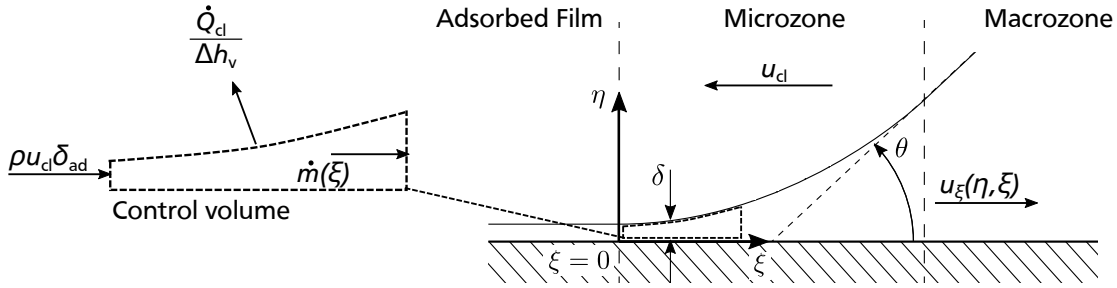

Figure 4.4: Microzone region with control volume following [17]

Figure 4.4 shows a sketch of the microzone. Beginning with the adsorbed layer, a liquid film forms, which shows a rapidly increasing slope, until it reaches the macroscopic contact angle Θ. This thin film has a low thermal resistance, resulting in high heat fluxes. The equations below are derived for a reference frame moving with the contact line velocity u_{cl}. In between, the film thickness δ depends on the coordinate ξ. It is assumed, that the film thickness is always smaller than the length of the microzone $\delta << L$. In the microzone, the conservation of mass, momentum and energy applies.

The momentum equation in ξ-direction reads

$$\frac{\partial p_l}{\partial \xi} = \rho_l \nu_l \frac{\partial^2 u_\xi}{\partial \eta^2}, \tag{4.26}$$

and in η-direction

$$\frac{\partial p_l}{\partial \eta} = \rho_l \nu_l \frac{\partial}{\partial \eta}\left(\frac{A}{\eta^3}\right). \tag{4.27}$$

Here, ν_l is the kinematic viscosity of the liquid and A is the dispersion constant, which quantifies Van-der-Waals-forces between the molecules of the wall and of the liquid film. The dispersion constant for a fluid interacting with a solid can be approximated with an equation given by Israelachvili [43]

$$A_{ls} = \sqrt{A_{ll} A_{ss}} \tag{4.28}$$

with the dispersion constants A_{ll} and A_{ss} for the fluid and the solid interacting with themselves. Batzdorf [5] calculates the dispersion constant of FC-72 to $A_{ll,FC72} \approx 1.7/(6\pi) \cdot 10^{-20}$ J from the surface energy of the liquid, which is permitted for non-polar liquids. The dispersion constant of barium fluoride is difficult to estimate, but it is in the order of magnitude of $A_{ss,BaF2} \approx 1/(6\pi) \cdot 10^{-19}$ J. However, Batzdorf [5] showed, that the variation of the dispersion constant even by the factor of 5 leads to an variation in contact line heat flow of under 10 %. This influence is considerably lower than the impact of the condensation coefficient, which will be introduced later, on contact line heat flow. Therefore, for the

dispersion constant between the liquid and the wall a rough estimate of $A = \sqrt{A_{\mathrm{ll,FC72}} A_{\mathrm{ss,BaF2}}} \approx 2 \cdot 10^{-21}$ J is considered sufficiently exact and is chosen throughout all simulations performed in the present thesis.

Applying the assumptions, that the kinetic energy in the microzone is small compared to the evaporation enthalpy and that the temperature within the microzone is constant, the mass balance in the control volume shown in figure 4.4 leads to

$$0 = \dot{m}(\xi) + \frac{\dot{Q}_{\mathrm{cl}}}{\Delta h_{\mathrm{v}}} - \rho_l u_{\mathrm{cl}} \delta_{\mathrm{ad}} \tag{4.29}$$

with the heat flow $\dot{Q}_{\mathrm{cl}}$ presenting the heat flux at the interface integrated between $\xi = 0$ to ξ. The mass flow over the outer boundary in ξ-direction is given by

$$\dot{m}(\xi) = \int_0^{\delta} \rho_{\mathrm{l}} u_{\xi} d\eta. \tag{4.30}$$

Integrating the momentum equation in η-direction (4.27) one obtains the liquid pressure:

$$p_l(\xi, \eta) = \frac{A}{\eta^3} + C(\xi, \eta). \tag{4.31}$$

In order to obtain the integration constant $C(\xi, \eta)$, the pressure difference at the liquid-vapor interface is taken into account:

$$\Delta p_{\mathrm{v,l}} = p_{\mathrm{v}} - p_{\mathrm{l}}(\eta = \delta) = \sigma K \rho_{\mathrm{l}} + u_{\mathrm{n,l}}^2 - u_{\mathrm{n,v}}^2. \tag{4.32}$$

In equation 4.32 K is the curvature of the interface and $u_{n,l}$ and $u_{n,v}$ are the molecule velocities normal to the interface on the liquid and the vapor side, respectively. The curvature at a specific coordinate ξ can be expressed using the first and second derivative of the corresponding layer thickness $\delta(\xi)$:

$$K = \frac{\delta''}{(1 + \delta')^{1.5}}. \tag{4.33}$$

The molecule velocities normal to the interface emerge from phase change and can be obtained from the evaporating mass flow:

$$\dot{m}_{\mathrm{cl}} = \frac{\dot{Q}_{\mathrm{cl}}}{\Delta h_{\mathrm{v}}} = \rho_l u_{\mathrm{n,l}} = \rho_v u_{\mathrm{n,v}}. \tag{4.34}$$

With the integration constant obtained, equation 4.31 reads:

$$p_{\mathrm{l}}(\xi, \eta) = p_{\mathrm{v}}(\xi) - \Delta p_{\mathrm{v,l}} - \frac{A}{\delta^3} + \frac{A}{\eta^3}. \tag{4.35}$$

This equation is simplified in the following introducing an augmented capillary pressure

$$p_{\mathrm{cap}} = \Delta p_{\mathrm{v,l}} + \frac{A}{\delta^3}. \tag{4.36}$$

Deriving equation 4.35 in ξ leads to

$$\frac{\partial p_{\mathrm{l}}}{\partial \xi} = \frac{\partial p_{\mathrm{v}}}{\partial \xi} - \frac{\partial p_{\mathrm{cap}}}{\partial \xi} \tag{4.37}$$

which can be simplified with $|\frac{\partial p_v}{\partial \xi}| << |\frac{\partial p_{cap}}{\partial \xi}|$ to

$$\frac{\partial p_l}{\partial \xi} = -\frac{\partial p_{cap}}{\partial \xi}. \tag{4.38}$$

Integrating equation 4.26 twice in η leads to

$$u_\xi = \frac{\eta^2}{2\nu_l \rho_l}\frac{\partial p_l}{\partial \xi} + C_1\eta + C_2. \tag{4.39}$$

Eliminating the integration constants with the boundary conditions $u_\xi(\eta = 0) = u_{cl}$ and $(\partial u_\xi/\partial \eta)|_{\eta=\delta} = 0$ and incorporating equation 4.38, one obtains

$$u_\xi = -\frac{1}{\nu_l \rho_l}\left(\frac{\partial p_{cap}}{\partial \xi}\right)\left(\frac{\eta^2}{2} - \eta\delta\right) + u_{cl}. \tag{4.40}$$

Combining equations 4.29, 4.30 and 4.40, one obtains an equation for the augmented capillary pressure in dependence of the contact line heat flow:

$$\frac{\partial p_{cap}}{\partial \xi} = -\frac{3\nu_l}{\delta^3 \Delta h_v}\left(\dot{Q}_{cl} + \rho_l \Delta h_v u_{cl}(\delta - \delta_{ad})\right). \tag{4.41}$$

The last unknown variable is now the contact line heat flow $\dot{Q}_{cl}$. As heat transfer is one-dimensional, the heat flux at the wall can be calculated by

$$\dot{q}_{ad} = \frac{\lambda_l}{\delta}(T_w - T_{int}). \tag{4.42}$$

The heat flux at the liquid-vapor interface can be calculated as follows:

$$\dot{q}_{int} = \frac{T_{int} - T_{sat}\left(1 + \frac{p_{cap}}{\Delta h_v \rho_l}\right)}{R_{int}}. \tag{4.43}$$

The term in brackets accounts for the increase in saturation temperature due to the pressure jump across the interface. R_{int} describes the thermal resistance at the interface itself. Usually, for phase change at the bubble hull surrounded by bulk fluid, R_{int} can be neglected since it is much smaller than the thermal resistance of the liquid in the thermal boundary layer. However, when the liquid film approaches the thickness of the adsorbed layer, which is only a few molecule layers, R_{int} is in the same order of magnitude as the thermal resistance of the liquid film. Schrage [84] analyzed the mass flux across the interface and deduced an equation for the thermal resistance of the interface

$$R_{int} = \frac{2-f}{f}\frac{T_{sat}\sqrt{2\pi R_{gas} T_{sat}}}{\Delta h_v^2 \rho_v} \tag{4.44}$$

under the assumptions, that

- the vapor is at saturation temperature,
- the vapor is an ideal gas,
- the vapor has a much lower density than the liquid,

- the vapor consists of only one component and
- the velocity of the vapor molecules is much smaller than the speed of sound.

In equation 4.44 R_{gas} is the ideal gas constant of the vapor, which can be obtained by the ideal gas law:

$$R_{gas} = p_{sat}/(\rho_v T_{sat}). \tag{4.45}$$

The evaporation or condensation coefficient f is a measure of the effectiveness of phase change at the interface and is in the range between 0 and 1. It has a strong influence on the contact angle and on the contact line heat flow calculated by the subgrid model: Batzdorf [5] showed for FC-72, that for small wall superheats doubling the evaporation coefficient can lead to an increase of the integrated heat flux in the microzone up to 60 %, while for wall superheats of 20 K the increase can still be 20 %. Dietl showed for the fluid R134a and a small wall superheat of 1 K, that the integrated heat flux is still increased by almost 20 %, if f is increased from 0.6 to unity. However, in the same work Dietl showed, that the effect is less severe for an entire CFD simulation of the boiling process. In his evaluated case the share of contact line heat flow in the overall heat flow $\dot{Q}_{Cl}/\dot{Q}$ increases by 13 %, if f is increased from 0.6 to unity.

f is an empirical value and depends on the material properties of both evaporating fluid and of the wall, on the wall roughness, and on several more system parameters. If the surface temperature and contact angle are known from experiments, f can be adjusted such that the numerical results fit the contact angle obtained by the experiment. Since no experimental contact angle data was available for the simulations of the present thesis, f had to be estimated. Marek and Straub [68] point out, that f is generally higher for permanently rewetting surfaces than for surfaces with a quasi static state of wetting. This finding suggests a relatively low value for f in a system with slowly moving contact lines, as in the majority of cases investigated in the present thesis. On the other hand, values are higher for non-polar substances like FC-72 in contrast e.g. to water. For the lack of information about the evaporation coefficient, its value is set to $f = 0.5$ in the present work.

The energy balance in the microzone ($\dot{Q}_{cl} = \dot{Q}_{int}$) and the area difference between the wall and the interface result in

$$\dot{q}_{cl} = \dot{q}_{int}\sqrt{1+\delta'^2}. \tag{4.46}$$

Combining equations 4.42, 4.43 and 4.46 gives an equation for the heat flux at the wall, eliminating T_{int} and q_{int}:

$$\dot{q}_{cl} = \frac{d\dot{Q}_{cl}}{d\xi} = \frac{T_w - T_{sat}\left(1+\frac{p_{cap}}{\Delta h_v \rho_l}\right)}{\frac{\delta}{\lambda_l} + \frac{R_{int}}{\sqrt{1+\delta'^2}}}. \tag{4.47}$$

Below the full, rearranged system of ordinary differential equations in the microzone is given:

$$\begin{aligned}
\frac{d\delta}{d\xi} &= \delta' \\
\frac{d\delta'}{d\xi} &= \frac{(1+\delta'^2)^{1.5}}{\sigma}\left(p_{\mathrm{cap}} - \frac{A}{\delta^3} + \frac{1}{\Delta h_{\mathrm{v}}^2}\left(\frac{T_{\mathrm{w}} - T_{\mathrm{sat}}\left(1+\frac{p_{\mathrm{cap}}}{\Delta h_{\mathrm{v}}\rho_{\mathrm{l}}}\right)}{\sqrt{1+\delta'^2}\frac{\delta}{\lambda_{\mathrm{l}}} + R_{\mathrm{int}}}\right)^2\left(\frac{1}{\rho_{\mathrm{v}}} - \frac{1}{\rho_{\mathrm{l}}}\right)\right) \\
\frac{dp_{\mathrm{cap}}}{d\xi} &= -\frac{3\nu_{\mathrm{l}}}{\delta^3\Delta h_{\mathrm{v}}}\left(\dot{Q}_{\mathrm{cl}} + \rho_{\mathrm{l}}\Delta h_{\mathrm{v}} u_{\mathrm{cl}}(\delta - \delta_{\mathrm{ad}})\right) \\
\frac{d\dot{Q}_{\mathrm{cl}}}{d\xi} &= \frac{T_{\mathrm{w}} - T_{\mathrm{sat}}\left(1+\frac{p_{\mathrm{cap}}}{\Delta h_{\mathrm{v}}\rho_{\mathrm{l}}}\right)}{\frac{\delta}{\lambda_{\mathrm{l}}} + \frac{R_{\mathrm{int}}}{\sqrt{1+\delta'^2}}}
\end{aligned} \tag{4.48}$$

This system of equations is solved within the boundaries $\xi = 0$ at the adsorbed film and $\xi = \xi_{\mathrm{end}}$ at the end of the microzone. The thickness of the adsorbed film is given by $\delta_{\mathrm{ad}} = \sqrt[3]{A/p_{\mathrm{cap}}(\xi = 0)}$ with the augmented capillary pressure in the adsorbed film being $p_{\mathrm{cap}}(\xi = 0) = (T_{\mathrm{w}}/T_{\mathrm{sat}} - 1)\Delta h_{\mathrm{v}}\rho_{\mathrm{l}}$.

The system of equations is solved in non-dimensional form employing Matlab's ode45-solver and a shooting method. The length of the microzone is divided in intervals and the equations 4.48 are integrated along ξ within each interval. After the solution has converged at the end on one interval, the process is started at the beginning of the next interval with the solution of the prior one. If the solution does not converge within an interval, a shorter interval is taken and the solution process with the solution of the prior interval as start condition is repeated. In order not to obtain a trivial solution (both δ and $\dot{Q}_{\mathrm{cl}}$ are zero at the adsorbed film), the film thickness and the integrated heat flow do not start with a value of zero, but with a small perturbation at the beginning of the microzone. The overall solution process ends, when the curvature of the interface is small and when the thermal resistance of the liquid film is much higher than of the interface. The length of the microzone is set to $\xi_{\mathrm{end}} = 0.5\mu\mathrm{m}$. For a detailed description of the solution process in Matlab, see Batzdorf [5] pp. 34 ff.

The system is solved for a set of combinations of wall superheats and contact line velocities. The results for film thickness at the end of the microzone, integrated heat flow and contact angle for each wall supherheat / contact line combination, are curve fitted, such that the relation between superheat, contact line velocity and each of those three quantities can be expressed by a polynomial. The coefficients of those polynomials are passed to the macroscopic CFD-simulation in order to incorporate the solution of the subgrid model. For details of this parameterization process, see [5] pp. 55 ff. The coefficients of the regression polynomial used in the present work are given in appendix B.

It must be stressed that, since the microzone model is two-dimensional, the resulting contact line heat flow $\dot{Q}_{\mathrm{cl}}$ comes with the unit [W/m] or Watt per meter contact line.

4.5 Conjugate heat transfer and coupling of micro scale and macro scale heat transfer

The conjugate heat transfer between the fluid and the solid numerical domain is implemented by an alternating, iterative solution of the energy equation in the fluid and the solid domain (eqs. 4.3 and 4.4). The algorithm is depicted in figure 4.5. In a first step, the energy equation in the fluid domain is solved with the temperature at the fluid-solid interface given as a Dirichlet boundary condition. In cells containing part of the three-phase contact line, the boundary is taken to be adiabatic in order to prevent sensible heat

transfer, as it is assumed, that the contact line heat flow is completely consumed by evaporation. The wall superheat in contact line containing faces and the contact line velocity at the same face are taken as input for the polynomials obtained by the subgrid model (see 4.4.2). For all faces, which do not contain part of the contact line, the heat flux orthogonal to the wall is obtained from the solution of the energy equation.

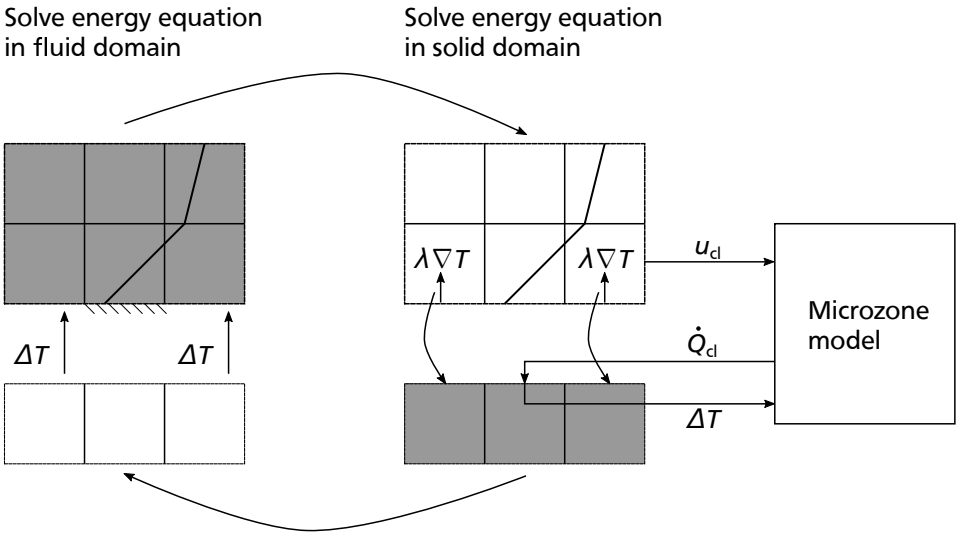

Figure 4.5: Scheme of iterative conjugate heat transfer calculation, alternating in the fluid and solid domain, including the microzone model, following [17]

In the next step, the energy equation in the solid domain is solved for with the heat flux obtained in the prior step as a Neumann boundary condition. For solid faces matching contact line containing faces of the fluid domain, the heat flux is calculated from heat flow provided by the subgrid polynomial. However, the subgrid model only provides a solution for up to a distance of 0.5 µm from the contact line, which leaves the heat flux at the rest of the affected cell face to be calculated. Heat transfer on the vapor side of the contact line is neglected at those faces due to the thermal conductivity of the vapor being considerably lower than that of the liquid. On the liquid side of the contact line, a transition region is defined in the remaining part of the face. In this region, the interface is assumed to be a plane starting with the height of the liquid film at the end of the microzone and an inclination angle identical to the contact angle, both which are provided as results of the microzone model. The lubrication model with one-dimensional heat transfer is still considered valid, however, outside the microzone the influence of curvature and dispersion forces on thermal equilibrium get small. Equation 4.47 then simplifies to

$$\dot{q}_{\mathrm{trans}} = \frac{T_{\mathrm{w}} - T_{\mathrm{sat}}}{\frac{\delta}{\lambda_{\mathrm{l}}} + \frac{R_{\mathrm{int}}}{cos\Theta}}. \tag{4.49}$$

The heat flow in the transition region then reads

$$\dot{Q}_{\mathrm{trans}} = \iint_{A_{\mathrm{trans}}} \dot{q}_{\mathrm{trans}} dA. \tag{4.50}$$

Further details on the determination of the heat flux in the transition zone are given by [5].

The combined heat flow at a contact line containing face, as it is added to the mass source term in equation 4.18, can be calculated as

$$\dot{Q}_{\mathrm{cl,f}} = \dot{Q}_{\mathrm{cl}} L_{\mathrm{cl}} + \dot{Q}_{\mathrm{trans}} \tag{4.51}$$

and the heat flux at a solid face matching a contact line face results to

$$\dot{q}_{\mathrm{cl,f}} = \frac{\dot{Q}_{\mathrm{cl,f}}}{A_{\mathrm{f}}}. \tag{4.52}$$

After the energy equation in the solid region is solved, the obtained temperature at the fluid-solid boundary is imposed as Dirichlet boundary condition in the fluid region again and the process starts all over. This alternating solution is performed until the temperature change between iterations is smaller than a pre-defined threshhold, which is set to 10^{-4} throughout all simulations performed for the present thesis.

4.6 Acceleration techniques

Since 3-D simulations of physically complex boiling phenomena are performed for the present study, several acceleration techniques are employed in order to reduce computational cost and simulation time. The tools used for this purpose are an adaptive time step, adaptive mesh refinement and parallel computing combined with load balancing.

4.6.1 Adaptive time step

All simulations conducted in the present study are transient simulations, hence additionally to the spatial discretization defined by the numerical grid a temporal discretization is employed in order to cover transient phenomena. It is obvious, that simulation time can be reduced by selecting a relatively large time step. In an explicit discretization scheme, as it is used for solving the advection of the volume fraction field (eq. 4.5), the Courant- or CFL-number

$$Co = \frac{|\vec{u}|\Delta\tau}{\Delta x} \tag{4.53}$$

shall not exceed unity in order to maintain numeric stability. However, for multiphase flows an even lower limit of $Co \leq 0.4$ are recommended in order to minimize discretization erros ([81]). In the present work, a limit of $Co \leq 0.4$ in pure liquid or vapor cells and a limit of $Co \leq 0.2$ in cells containing part of the interface is imposed. Additionally, if surface tension has a significant influence, Brackbill et al. [8] give a time constraint for the stability of capillary waves:

$$\Delta\tau \leq \frac{\sqrt{(\rho_{\mathrm{l}} + \rho_{\mathrm{v}})\,\Delta x^3}}{\sqrt{4\pi\sigma}}. \tag{4.54}$$

For the smallest cell width in the simulations presented in chapter 5, equation 4.54 yields to a limit of $\Delta\tau \leq 2.4 \cdot 10^{-6}$ s.

Instead of specifying a fixed time step prior to a simulation, at the end of every time step throughout the simulation the following timestep is adapted in a way that it is as large as possible and still both constraints are fulfilled.

4.6.2 Adaptive mesh refinement

Multiphase simulations of boiling flows are characterized by moving regions of interest, which migrate through the computational domain and require a high resolution of the numerical grid. The most prominent example for such a region of interest is the liquid-vapor interface, which changes its position due to bubble growth and movement. Adaptive mesh refinement is a tool, which allows the user to impose a high mesh resolution wherever needed throughout the simulation, while keeping the mesh relatively coarse, wherever no high mesh resolution is required. All cells of the computational domain are checked every few timesteps, if they meet one of the pre-defined refinement criteria. If so, a three-dimensional cell is split into eight child cells. It is possible to refine a cell several times implementing a high number of refinement levels. If all child cells of one parent cell do not meet the refinement criteria anymore, unrefinement is conducted and the cells are getting merged again.

OpenFOAM comes with an adaptive mesh refinement functionality readily implemented. Rettenmaier and co-workers [82] significantly enhanced the available refinement tool by fixing several major bugs. This way the computational cost of the refinement step could be severely reduced.

Additional to bug-fixes, Rettenmaier and co-workers extended the abilities of the corresponding C++ class by adding a wide list of refinement criteria, such as values and gradients of fields or quasi-static refinement inside geometrical shapes as boxes, cylinders or spheres. Those criteria can be arbitrarily combined and the desired refinement level for each criterion can be defined. All improvements implemented by Rettenmaier are employed in the simulations for the present thesis. For details on bugfixes and enhanced functionality, the reader is referred to [81] and [82].

4.6.3 Parallelization and load balancing

Nowadays, all medium and large scale CFD computations rely on the parallel execution of the flow solver on several cores or processors. In finite volume approaches the typical way to parallelize the computational task is to decompose the numerical mesh and let each processor run the solver only on a part of the computational domain. Because an increasing number of employed processors causes an increase of in-out-operations between the processors, the speed-up is not linear and decreases with an increasing processor number. Beyond a specific processor number, which depends on the problem size and on the specific flow solver used, the simulation gets slower as inter-processor communication outweighs the advantage of smaller problem size per processor. Stechowsky [100] showed for the interFoam solver with the specific modifications utilized in the present thesis, that a speed-up can be observed until a cell number of 9000 per processor. However, the compuational efficiency shows an almost linear decrease with increasing processor number.

As the liquid-vapor interface migrates through the computational domain, the load of a single processor can vary significantly over simulation time due to adaptive mesh refinement in the vicinity of the interface. A strong imbalance between the load of the different processors in use can reduce the efficiency of computational resources drastically, because the processor with the highest load becomes a bottleneck and other processors wait for processed data.

Figure 4.6 shows the principle to overcome this problem. After a refinement step, the load between two processors is imbalanced and after a re-distribution of cells to the processors the load balance is almost even again. The load imbalance is defined as the ratio of the difference between the highest and the average load and the average load itself. Several algorithms of load balancing have been implemented in different versions of the OpenFOAM framework yet, e.g. by Batzdorf [5] and Voskuilen [112]. Retten-

maier et al. [82] implemented the first stable load balancing algorithm based on the work of Voskuilen overcoming relevant stability problems, which can be traced back to insufficient mapping of boundary values at Dirichlet or Neumann boundary conditions. Rettenmaiers load balancing implementation is employed throughout the present thesis.

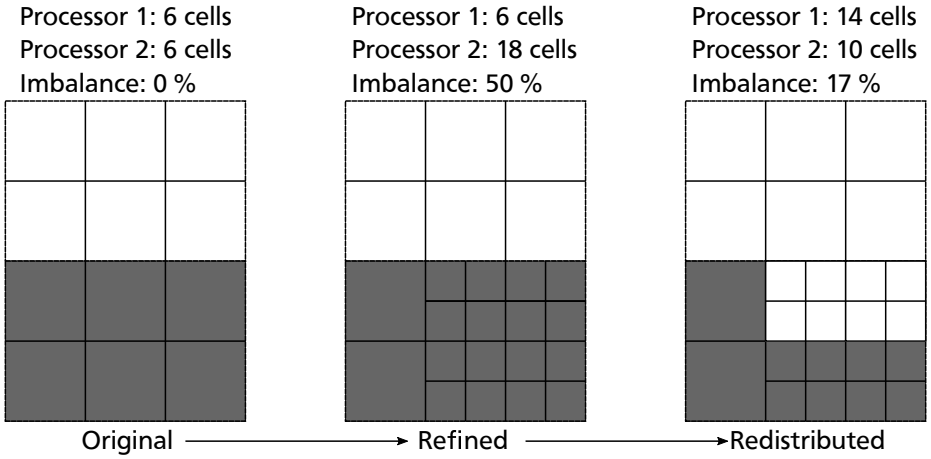

Figure 4.6: Principle of load balancing following [81]. After a refinement step processor 2 holds a higher number of cells than processor 1. After a redistribution of cells between the processors, the load is balanced more evenly again.

It must be noted that load balancing can not be employed to an arbitrary extent in the current framework. All child cells of a common parent cell have to be distributed to the same processor in order to maintain the possibility of unrefinement. The descent of every cell is stored in a refinement history. Thus, for n refinement levels in adaptive mesh refinement, every cell of the base mesh can be disassembled into 8^n child cells, which all have to stay on the same processor and a relatively high imbalance must be accepted. This limits the possibility to maintain a balanced processor load even with the employment of a load balancing algorithm, and there is a trade-off between a high level of adaptive mesh refinement on the one hand and a base mesh, which is relatively fine from the beginning.

4.7 Validation

The original solver from Kunkelmann [54] was validated with analytical solutions of a sucking interface problem, spherical bubble growth and an evaporating meniscus. Additionally, numerical results were compared to single bubble experiments and found to be in good agreement. Batzdorf [5] validated the implicit evaporation model with the analytical solution of bubble growth in a superheated liquid bulk by Scriven [90] and numerical solutions of drop impingement on a superheated wall with experimental results and found them to be in good agreement. Dietl [17] validated the solver with experimental results of a capillary rise experiment and points out the significance of incorporating a dynamic contact angle treatment in order to obtain high quality results.

In the present thesis the solver is applied to flow boiling on a flat wall including several bubble cycles and coalescence, as well as to bubble growth out of cavities, which is mainly driven by capillary forces. For the latter type of problem the solver has been validated by Dietl [17], who employed the solver to simulate bubble growth out of reentrant type cavities. The simulations of boiling on a flat wall are compared with the according experiments conducted on ISS during the Multiscale Boiling project. The results of those validation simulations are outlined in section 5.3.

5 Numerical simulations of boiling in the Multiscale Boiling test cell

In order to gain a deeper understanding of heat and fluid flow mechanisms during subcooled flow boiling in microgravity, simulations of successively nucleating, growing and moving bubbles have been performed following the experimental setup of the Multiscale Boiling project. The numerical domains in the simulations represent the fluid inside the boiling cell and the solid substrate from the experiment, respectively.

Some features specific to the according experimental setup have been reproduced by the numerical model as detailed as possible with acceptable numerical effort. The modeling of the experiment in the simulation framework is presented and inevitable discrepancies between the simulation and the experiment are discussed. Subsequently, general observations in heat and fluid flow are presented through the example of a flow boiling reference case, which uses intermediate values of input parameters from the Multiscale Boiling experiment. Based on this reference case, the results of several parameter studies on the sensitivity of the boiling process to input parameters, to the thermal conductivity of the liquid and to material properties of the substrate are presented.

5.1 Setup and procedure

5.1.1 Creation of the numerical grids

For the simulations of flow boiling in the Multiscale Boiling test cell two numerical grids were used, which represent the fluid volume inside the boiling cell and the solid heater substrate in the Multiscale Boiling experiment. Figure 5.1 (a) shows a CAD model of the boiling cell. Three-dimensional simulations are conducted in order to correctly cover the hydrodynamics of non-spherical bubbles affected by a shear flow. It is taken advantage of the plane symmetry in the middle of the boiling cell and the heater, respectively. The cavity inside the substrate, which serves as nucleation site in the experiment, is not part of the numerical mesh. In order to study the nucleation process out of the cavity, a number of simulations specially designed for this purpose have been performed. The results of those simulations will be presented in chapter 6.

The two grids are created employing the hexa-mesh approach of the software ANSYS® ICEM CFD™, which makes it possible to create structured hexahedral meshes of high quality even in complex geometries. This structured meshing approach proofs advantageous for interface reconstruction and adaptive mesh refinement, because the mesh topology is characterized by high orthogonality and low aspect ratios: In a large area around the supposed nucleation site the grid cells have the shape of an ideal cube.

In order to include the whole boiling cell on the one hand and to address the need for high mesh resolution in the vicinity of the liquid-vapor interface on the other hand, while keeping the computational effort acceptable, adaptive mesh refinement as presented in section 4.6.2 is employed in an extensive manner. The cross section of the basic meshes as they are created in ICEM CFD™ are shown in figure 5.1 (b). The visible plane is the symmetry plane, which is used as a boundary in the simulations. The

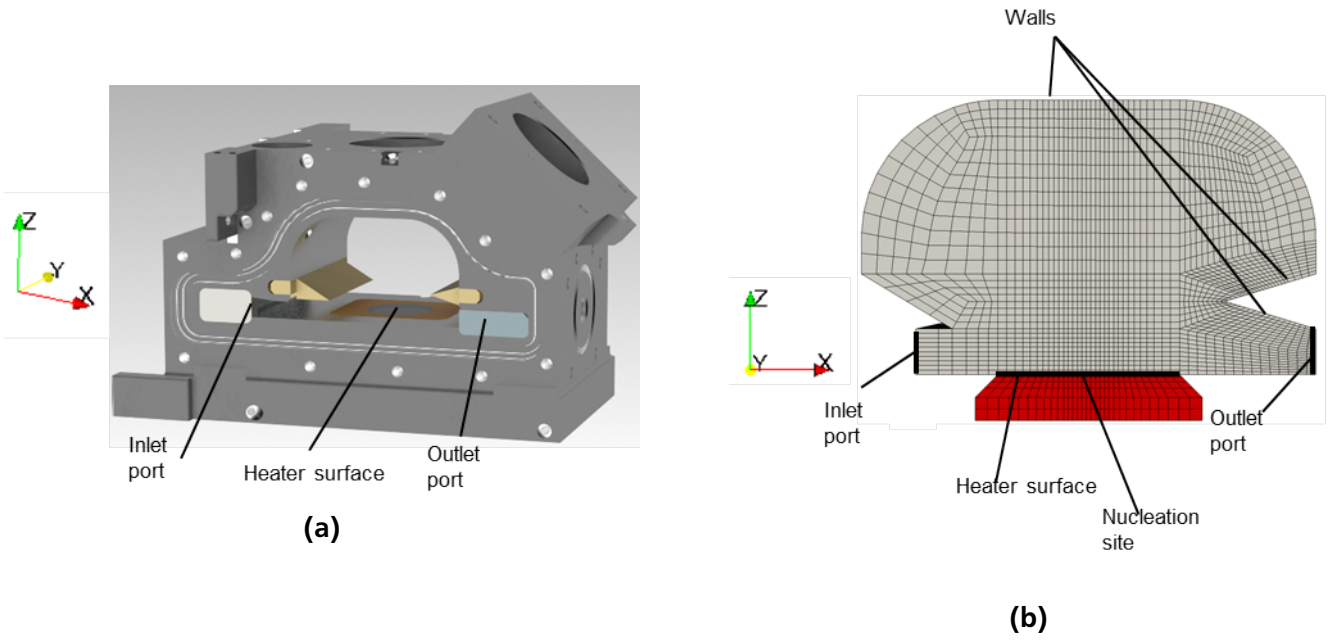

Figure 5.1: (a) CAD model of the boiling cell, (b) Cross section of 3-D computational domain with boundary conditions as defined in table 5.1

grids hold around 32000 cells in the fluid and 2500 cells in the solid domain and show an edge length of 480 µm in the vicinity of the defined nucleation site spot. Batzdorf [5] showed, that the evaporation model is in excellent agreement with the analytical solution of Scriven [90], if the temperature gradient between the liquid-vapor interface and the bulk liquid is resolved with at least four cell layers in case of a 10 K temperature difference. Based on this finding, adaptive mesh refinement in the presented simulations is implemented with a total of six levels in the vicinity of the moving interface, which results in a minimum edge length of 7.5 µm. With this resolution, the condition of at least four cells per 10 K temperature difference is fulfilled during the vast majority of the simulation time in all conducted cases.

In order to verify, if this resolution is indeed sufficient for the specific application of the solver in the present work, a mesh study is conducted. Figure 5.2 shows the results, comparing the chosen resolution of 7.5 µm edge length with one of 3.75 µm in a simulation of the main growth phase of a vapor bubble in the reference case during the first 20 ms after nucleation. It will be shown later, that this time span is characterized by the highest temperature gradients and the fastest bubble growth throughout each simulation. Figure 5.2 shows, that the estimation of the bubble volume matches well for both resolutions, with a slight deviation during the first few milliseconds after nucleation. This deviation is caused by very high temperature gradients in the vicinity of the bubble foot due to the laser power (the implementation of the laser power in the simulation will be outlined in detail in section 5.1.3). Nevertheless, those deviations have a maximum of only 8.5 % and the bubble diameters start to converge again after approximately 5 ms. Due to this relatively small deviation over a very short period of the simulation time, a minimum edge length of 7.5 µm is considered to be the best compromise between precision and computational effort, considering the overall mesh size and simulation time.

The overall cell number in each simulation depends strongly on the size of the interfacial area and thus on size and number of vapor bubbles in the fluid domain. Dependent on the parameters and the progress of the simulation, the number of cells in the fluid domain ranges from 300 000 to 2.5 million, if

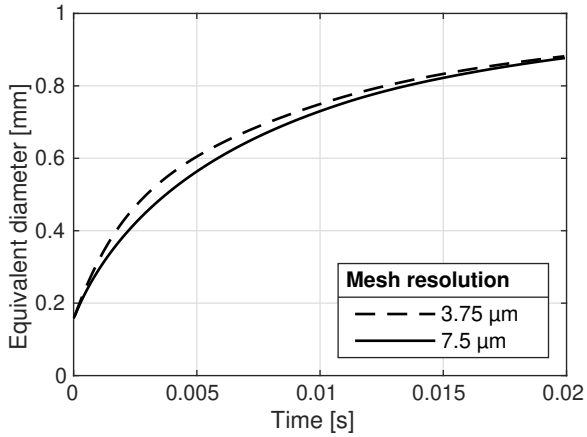

Figure 5.2: Impact of mesh resolution on bubble growth immediately after the very first nucleation

a finest mesh resolution of 7.5 µm is chosen. Since all simulations start with the same very low number of cells and gain their maximum cell number during run-time, it is not possible to increase the number of processors arbitrarily for those simulations with a very high maximum cell number from the very beginning of the simulation. The distribution algorithm has trouble to distribute the small cell number in the beginning to a large number of processors. Therefore, the majority of simulations is conducted on 24 processors. Some simulations, which develop a very large number of cells over time, are conducted on 36 processors. Under those conditions, the clock time needed for the simulation of the first 0.5 s after the initial nucleation varies between four days and over four weeks depending on the parameters.

Due to the high number of adaptive refinement levels and distribution restrictions, dynamic load balancing (see section 4.6.3) can only be employed to a limited degree. In order to maintain the possibility to unrefine prior refined cells, all children cells from the same parent cell have to stay on one common processor. Since in 3-D one refinement step of a cell produces 8 children cells, a refinement level of 6 theoretically produces up to 8^6 cells from one single cell, which have to be distributed to the same processor. This constraint limits the possibility of distributing the mesh on a large number of processors as well as imposing a tight imbalance restriction in the load balancing algorithm. A rather high load imbalance $>100\,\%$ has to be accepted in order to prevent the solver from crashing during the attempt to redistribute cells. Between different simulation runs, the maximum cell load per processor spans from 30 thousand up to 250 thousand. Nevertheless, given the need of a sufficiently fine mesh resolution in the vicinity of the interface on one hand and a large spatial expansion of the computational domain on the other hand, employing adaptive mesh refinement to such a large extent and accepting a high load imbalance is still advantageous compared to starting with a finer basic mesh and employing less refinement levels. Sparing only one level of adaptive refinement would demand an increase in cell number of the basic mesh by the factor of 8, sparing two levels would increase the cell number in the basic mesh by the factor of 64. However, in both cases still a relatively large load imbalance must be accepted.

5.1.2 Boundary conditions and simulation procedure

The formulation of the boundary conditions is given in detail in table 5.1. The working fluid in the experiment and all presented simulations is perflourhexane, also known as FC-72, the substrate material is bariumfluoride. The properties of both materials are given in appendix A. All investigations presented are conducted for a system pressure of 0.54 bar, or a saturation temperature of 39.7 °C, respectively. The

Fluid domain	p	$\vec{u}$	T	F
Inlet port	$\nabla p \cdot \vec{n} = 0$	Given Profile	$\nabla T_\mathrm{f} \cdot \vec{n} = 0$	$\nabla F \cdot \vec{n} = 0$
Outlet port	0	$\nabla \vec{u} \cdot \vec{n} = 0$	$\nabla T_\mathrm{f} \cdot \vec{n} = 0$	$\nabla F \cdot \vec{n} = 0$
Symmetry plane	Symmetry	Symmetry	Symmetry	Symmetry
Far field plane	$\nabla p \cdot \vec{n} = 0$	$\nabla \vec{u} \cdot \vec{n} = 0$	$\nabla T_\mathrm{f} \cdot \vec{n} = 0$	$\nabla F \cdot \vec{n} = 0$
Adiabatic walls	$\nabla p \cdot \vec{n} = 0$	(0,0,0)	$\nabla T_\mathrm{f} \cdot \vec{n} = 0$	$\nabla F \cdot \vec{n} = 0$
Heater surface	$\nabla p \cdot \vec{n} = 0$	(0,0,0)	$T_\mathrm{f} = T_\mathrm{s}$	$\Theta = \Theta_{cl}$
Solid domain	T			
Heater surface	$\lambda_\mathrm{s}(\nabla T_\mathrm{s} \cdot \vec{n}) = \dot{q}_\mathrm{in} + \dot{q}_\mathrm{cl,f}$ at contact line $\lambda_\mathrm{s}(\nabla T_\mathrm{s} \cdot \vec{n}) = \dot{q}_\mathrm{in} + \lambda_\mathrm{f}(\nabla T_\mathrm{f} \cdot \vec{n})$ elsewhere			
Other surfaces	$\nabla T \cdot \vec{n} = 0$			

Table 5.1: Boundary conditions in the fluid and the solid domain

liquid streams in form of a laminar shear flow from the inlet port towards the outlet port in the indicated x-direction. The flow is assumed to be an ideal Poiseuille flow (i.e. a laminar flow with a parabolic velocity profile) with the maximal flow velocity in the middle of the channel and zero at walls:

$$\vec{u} = 4u_\mathrm{max}\left(1 - \frac{z}{h}\right)\frac{z}{h}\vec{e_x} \tag{5.1}$$

In equation 5.1 h is the height of the flow channel at the inlet, z is the space coordinate normal to the lower confining wall, u_max is the maximum flow velocity at half channel height and $\vec{e_x}$ is the unit vector in flow direction. In y-direction, the limiting boundaries are the symmetry plane at $y = 0$ and a far field plane in the test cell at $y = 15\,\mathrm{mm}$, which is sufficiently distant from the center of the boiling cell, that the flow is not affected by any bubbles. Since the boiling cell has a y-wise expansion of 40 mm, that way the size of the numerical domain could be significantly reduced.

At the boundary between the two domains coupled temperature and heat flux boundary conditions are employed as described in section 4.5. Additionally, on the solid side of the coupled boundary conditions an input heat flux $\dot{q}_\mathrm{in}$ is implemented as a source term. This way, the electrical resistance heater from the experiment, which consists of a sputtered layer of chromium on top of the substrate, is modeled. This sputtered layer has a constriction in the direction of space of the channel width (referred to as the y-direction throughout the present thesis) in the vicinity of the nucleation site and a y-wise expansion towards the inlet and the outlet. This way, the input heat flux is smaller towards the boundaries and higher at the nucleation site, since the electrical current is constant, but the resulting heat flow is distributed to a smaller area in the constriction zone. This was introduced to the experiment in order to prevent parasitic boiling in areas distant from the nucleation site. The variable input heat flux is modeled in the simulation as the imposed heat flux per cell face at the wall boundary scales inversely with the width of the sputtered area in y-direction, as shown in figure 5.3. Furthermore, in cells containing part of the three-phase contact line, the contact line evaporation heat flux obtained from the subgrid model is added on the solid side (see section 4.4.2).

In the corresponding experiments a specific pre-heating time is defined prior to the very first nucleation, during which a thermal boundary layer can develop inside the flowing liquid above the heater. At the end of this pre-heating time, the nucleation site is activated and the first nucleation is enforced by a laser beam.

Accordingly, the simulations start with a flow of single phase, liquid FC-72. The velocity field from equation 5.1 for the inlet boundary condition is imposed as initial condition throughout the whole flow channel, as well. In order to display the nucleation of a new vapor bubble during a running simulation,

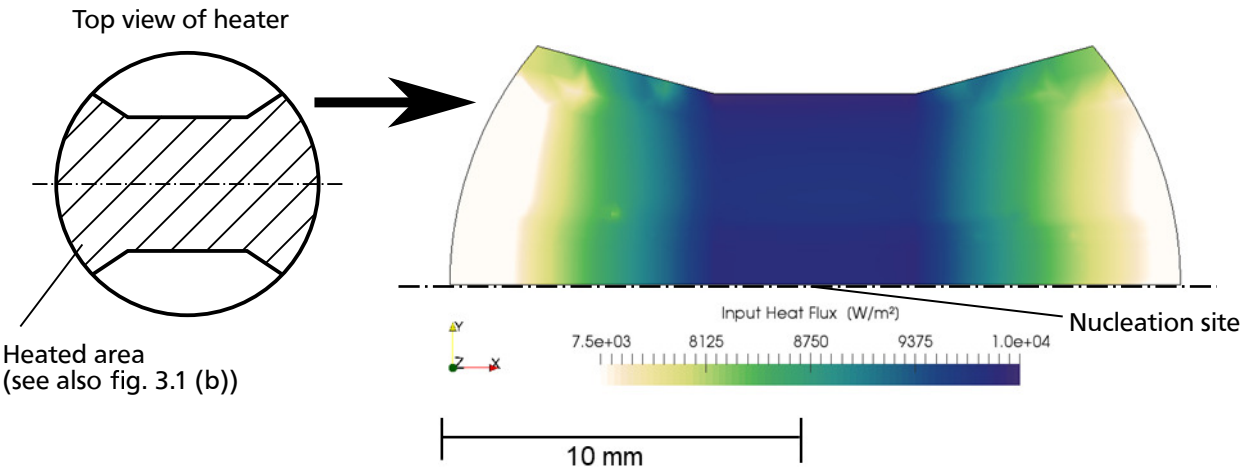

Figure 5.3: Input heat flux source term on top of the solid domain with $1\,\mathrm{W/cm^2}$ in the middle of the area

a bubble nucleus is set inside the liquid at the location of the nucleation site by manipulating the volume fraction field. This method is discussed in detail in the following section.

5.1.3 Nucleation of successive bubbles during a running simulation

In the simulations presented in this chapter a perfectly smooth wall is assumed at the solid-liquid boundary. Since the cavity, which serves as nucleation site in the according experiment, is neglected by the numerical mesh, the physical nucleation process cannot be covered by the simulation. A special focus needs to be set on the workaround to model the appearance of new bubbles throughout a simulation.

As soon as a defined nucleation criterion is met during a running simulation, a new vapor bubble instantly appears above the spot at the boundary, which has been defined at nucleation site. This is done by manipulating the volume fraction field F. In the affected cells the value of F is changed from unity to zero. Since a new vapor bubble is likely to be created in an area of the mesh, which is not refined with the highest refinement level, the manipulation of the volume fraction field has to be followed by a reconstruction of the interface and a mesh refinement loop. This sequence has to be conducted iteratively until the highest refinement level is reached in the vicinity of the newly created liquid-vapor interface. After every loop of the iteration but the last one, F is set back to unity in all affected cells in order to prevent artifacts of the F-field in the coarse mesh in the following timesteps.

The criteria to create a new bubble during the simulation are the end of the defined pre-heating time and, after the very first nucleation, a defined superheat of the wall at the nucleation site, analogous to the approach by Aktinol and Dhir [2].

Heat distribution by the laser beam

The pre-heating time in both the experiments and the simulations are in the range of several seconds. In the experiment, at the end of the pre-heating time the nucleation site is activated by a laser beam. It is focused on the cavity, increasing the temperature of the liquid inside the cavity as well as the temperature of the surrounding wall. However, it is not possible to determine exactly the three-dimensional distribution of the imposed power and the resulting temperature field. Additionally, in the simulations discussed in this chapter the cavity and the liquid, which it contains, are neglected. Thus, it is not straightforward

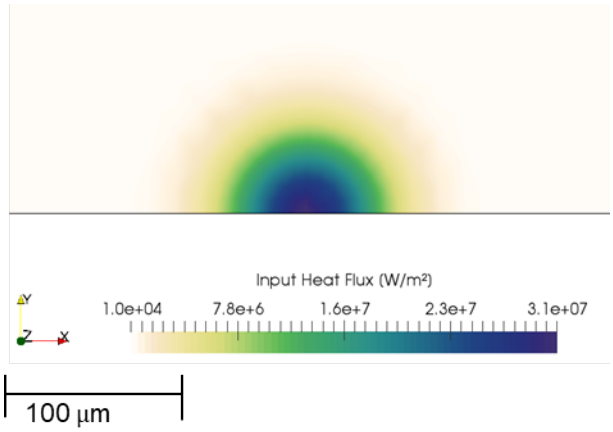

Figure 5.4: Strongly increased input heat flux source term in the vicinity of the nucleation site during activated laser

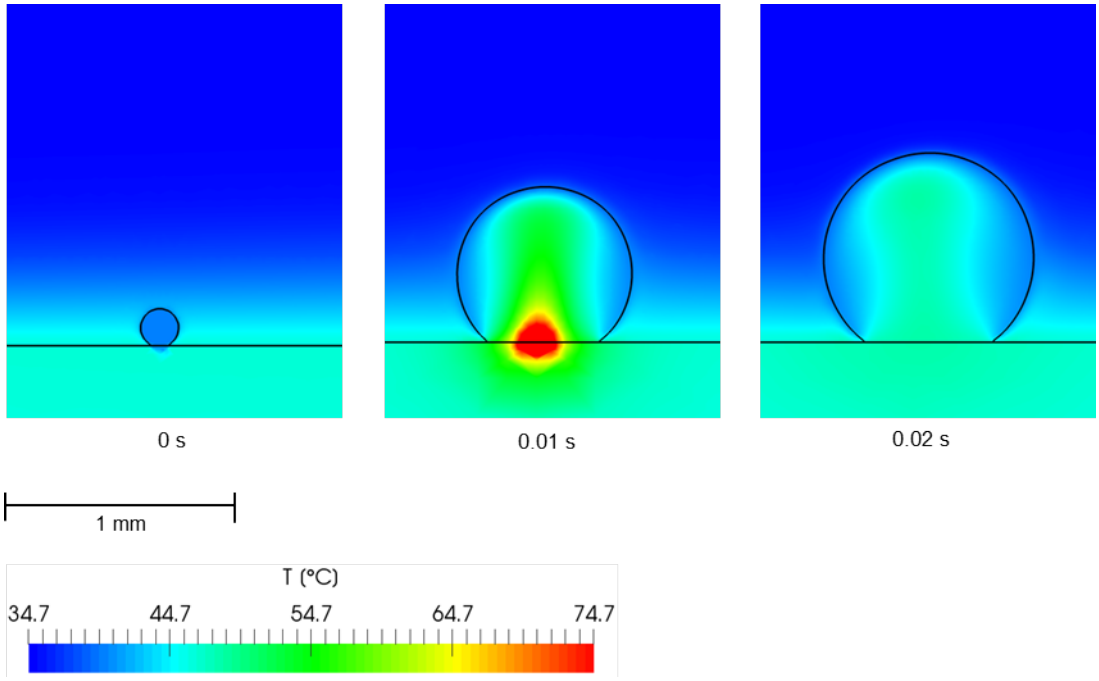

Figure 5.5: Temperature field around the very first bubble of a simulation, laser active for the first 0.01 s. The maximum temperature at 0.01 s exceeds the scale and reaches 119 °C. The black line represents the bubble hull and the solid-liquid interface, respectively

to implement the heat input resulting from the laser power in the simulations with exact accordance to the experiment.

Since the heat flux source term $\dot{q}_{\text{in}}$ is already implemented on the solid side of the solid-fluid interface, it seems promising to account for the power of the laser beam by increasing the existing input heat flux during the time span, when the laser is activated, and decreasing it again afterwards. Infrared temperature measurements from preliminary experiments show, that the increase in temperature during the activated laser time follows a two-dimensional Gaussian distribution around the center of the cavity with equal standard deviations $\sigma_{\text{x}} = \sigma_{\text{y}} = \sigma = 30\,\mu\text{m}$ at the solid-liquid boundary. It is concluded, that the laser power is distributed in the same way as the resulting rise in temperature, and the increase in

input heat flux is implemented with a circular Gaussian distribution around the nucleation site in the simulation. If the origin of coordinates matches with the defined nucleation site spot and the x-y-plane represents the solid-fluid boundary, the probability density function of the laser power is

$$f(x,y) = \frac{e^{-\frac{x^2+y^2}{2\sigma^2}}}{2\pi\sigma^2} \tag{5.2}$$

and the additional source heat flux on each cell face due to the laser beam

$$\dot{q}_{\text{Laser}} = f(x,y) P_{\text{Laser}} \tag{5.3}$$

The total laser power is set to $P_{\text{Laser}} = 177\,\text{mW}$ in all presented simulations. Figure 5.4 shows the resulting heat supply on top of the solid domain during the on-time of the laser. The resulting increase in temperature both in the solid and the liquid and the following decrease after the laser is turned off can be observed in figure 5.5.

Superheat criterion for successive bubbles

Successive bubbles are created, as soon as the wall temperature at the nucleation site exceeds a defined superheat criterion. The superheat necessary for subsequent nucleations must be estimated. Hsu [39] developed a model for the necessary wall superheat for incipience of boiling in case of known material properties and cavity features:

$$\Delta T_{\text{nucl}} = \frac{2BC}{\delta_{\text{th}}} + \sqrt{\left(2T_{\text{sat}} + \frac{2BC}{\delta_{\text{th}}}\right)\left(\frac{2BC}{\delta_{\text{th}}}\right)} \tag{5.4}$$

with

$$B = \frac{2\sigma T_{\text{sat}}}{\Delta h_{\text{v}} \rho_{\text{v}}}$$

The model is based on the assumption, that a bubble nucleus sitting in a cavity will start to grow, as soon as the surrounding liquid reaches the saturation temperature of the vapor inside the cavity. In equation 5.4 the constant C depends upon both the contact angle and the angle of the cavity mouth, which both are usually unknown. Therefore the author states it to be $C = 1.6$ based on a series of assumptions. δ_{th} is the thickness of the thermal boundary layer, which for the sake of simplicity the author assumes to have a maximum limit due to turbulence in the bulk fluid. Since in the present work a pure laminar flow is assumed, the actual thickness of the thermal boundary layer is taken to estimate the needed superheat from equation 5.4. Preliminary studies showed, that δ varies over a range between 0.2 mm and 1 mm, depending on flow velocity, input heat flux, pre-heating time and subcooling. Values for ΔT_{nucl} are then in the range between 4 K and 10 K. Since it would have been too complex to detect the thermal boundary layer thickness in each time-step and to implement the superheat nucleation criterion dependent on δ, and since equation 5.4 serves as a fairly rough approximation anyway, an intermediate value of 7 K has been set as nucleation criterion for successive bubbles for all simulations presented throughout this chapter. It will be shown in section 5.2.3, that cases characterized by low input heat flux or high subcooling are sensitive to the chosen wall superheat criterion: With the chosen value of 7 K no successive bubbles are created in the affected cases. In case of a moderately lowered input heat flux a superheat criterion of 5 K would still be sufficient for subsequent nucleations. For a very low input heat flux and high subcooling, however, the criterion must be lowered to 3 K, which is outside the range calculated with equation 5.4.

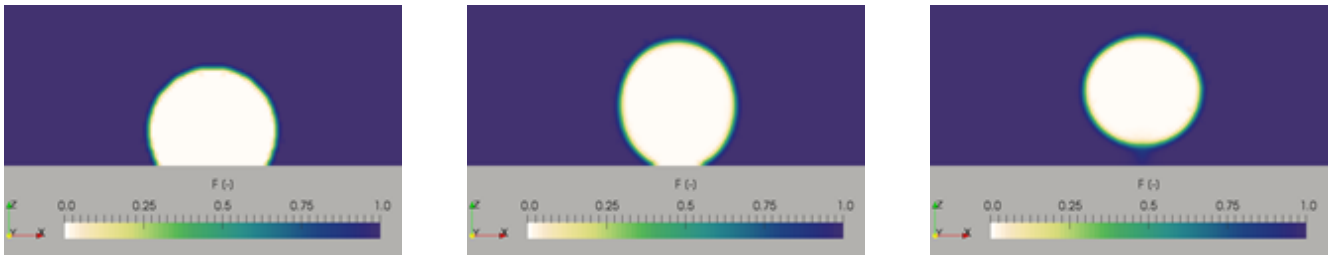

(a) (b) (c)

Figure 5.6: Newly created bubble with the sphere center too low and the contact angle too large at (a) 0 s, (b) 1 ms and (c) 2 ms after nucleation. The capillary forces cause a rapid contraction of the bubble foot as the bubble strives to an equilibrium contact angle and the resulting momentum causes non-physical detachment

Influence of bubble height above the wall

Each bubble is created with the shape of a sphere, which is cut off at the bubble foot. Attention has to be paid to the correct height of the sphere center above the wall and the resulting apparent contact angle. Figure 5.6 shows an example of a newly created bubble with the sphere center too low above the wall. The resulting contact angle is too large, causing the bubble foot to shrink rapidly as the capillary forces act towards an equilibrium contact angle. The resulting momentum from that contraction then causes a detachment of the bubble shortly after its creation despite the absence of gravity. In order to avoid such non-physical detachments, the height of the sphere center has to be chosen such that the resulting contact angle is in the range of the physical equilibrium contact angle. Preliminary simulations showed that for FC-72 on a barium fluoride substrate and the considered wall superheats and contact line velocities, contact angles are typically in the range of $20° - 30°$. In order to match this value range, the height of the sphere center above the wall z_0 should be approximately 94 % of the sphere radius r_B, or $z_0 = 0.94\, r_B$, following the nomenclature of figure 5.9. Hence, for all simulations presented in the current chapter, the sphere radius is chosen to $r_B = 40\,\mu m$ and the height of the sphere center to $z_0 = 37.5\,\mu m$. The resulting diameter of the bubble foot is then approximately 28 µm, which matches sufficiently well the diameter of the cavity in the experiment. Thus the modeling of the nucleation process in the simulation can be considered as producing a state, when a bubble has just grown out of the cavity in the experiment, and skipping the growth process inside the cavity.

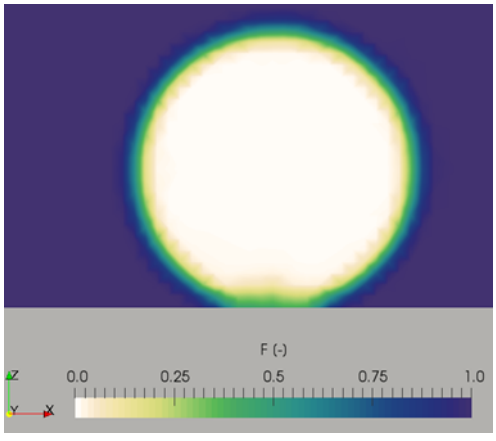

Figure 5.7: Smearing of the interface at the bubble foot and numerical caused detachment 8 ms after bubble creation due to improperly defined contact angle correction

Another cause for non-physical detachment is the smearing of the interface at the wall, if the modified contact angle correction by Gründing et al. [32] (see section 4.4.1) is applied with a too large distance from the contact line. In this case the prescribed contact angle is imposed in a distance too far from the contact line. Figure 5.7 shows a liquid-vapor interface completely smeared out throughout the whole bubble foot. The smearing is caused by a wrongly calculated surface tension force in cells, which do not contain part of the contact line, but nevertheless are imposed with a contact angle smaller than 90°. Since the interface reconstruction algorithm searches for the 0.5 iso-surface in the volume fraction field, in the worst case this behavior causes the reconstructed interface being completely out of contact with the wall. Gruending et al. suggest a distance of approximately 8 cells from the contact line, beyond which a 90° contact angle should be imposed, for their capillary rise test case. However, for the creation of bubble nuclei in the presented simulations, a much stricter distance of two cells around the contact line proofs necessary to avoid numerical bubble detachment.

Safety distance between new and existing bubbles

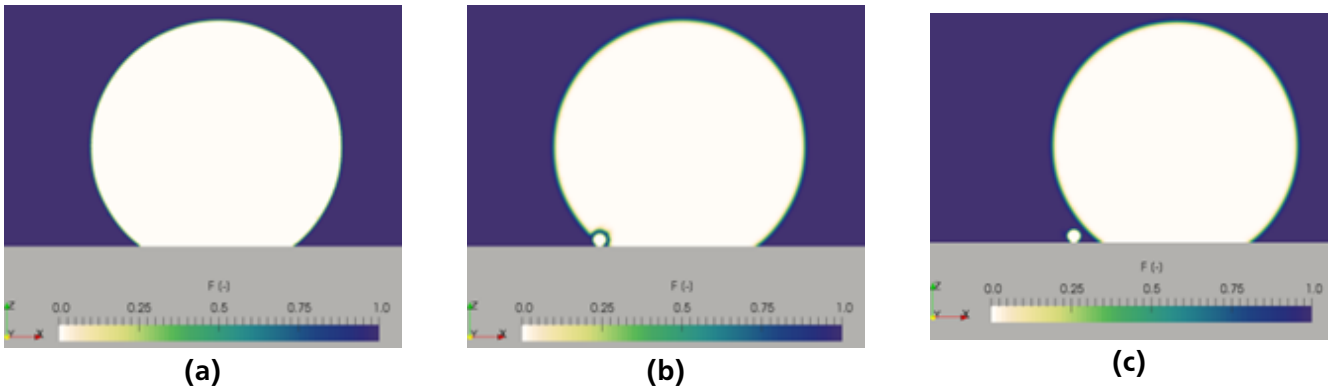

Figure 5.8: Creation of a succeeding bubble at the nucleation site next to the large initial bubble during a running simulation after the superheat criterion is met: (a) Shortly before the bubble creation, (b) with interference and unphysical cutout of the initial bubble, (c) without interference after implementation of additional distance condition

A second, restrictive condition for the creation of successive bubbles is a minimum distance of all other bubbles, which are already present in the fluid domain, to the nucleation site. Because a new bubble is created artificially by manipulating the volume fraction field inside a sphere of finite radius, it has to be ensured that other bubbles are not affected by the creation process of a successor. Figure 5.8 (a) and (b) show, how the creation of a successive bubble cuts out a part of the larger initial bubble because the distance between the old bubble and the nucleation site is too small compared to the radius of the new bubble. It is obvious, that the resulting shape of the old bubble is not physical anymore and will lead to non-physical, surface tension induced flows. Therefore, as additional condition for the creation of a succeeding bubble, the volume fraction field in the first cell layer above the wall has to be unity within a defined radius, hence the affected cells have to be completely filled with liquid. The result can be observed in figure 5.8 (c), as the initial bubble has moved downstream sufficiently, before the next bubble can nucleate.

Figure 5.9 shows, how this safety radius r_{ns} around the nucleation site is calculated by the example of one existing bubble next to a freshly nucleated one. In a conservative approach, it is ensured that the newly created bubble is situated completely beyond the tangent formed by the contact angle of the

existing bubble. The minimum radius around the nucleation site, which has to be filled with liquid, then calculates to

$$r_{ns} = x_1 + x_2 = \frac{r_B}{sin\Theta_{ex}} + \frac{z_0}{tan\Theta_{ex}} \tag{5.5}$$

with the new bubble's radius r_B, the height of the new bubble's sphere center above the wall z_0 and the contact angle Θ_{ex} of the existing bubble at the symmetry plane. As a conservative estimate, the contact angle for this safety distance calculation is assumed $\Theta_{ex} = 30°$ throughout the present thesis. With a radius of a newly created bubble $r_B = 40\,\mu m$ and $z_0 = 37.5\,\mu m$ throughout the simulations presented in this chapter, a safety radius of $r_{ns} = 145\,\mu m$ around the nucleation site must be completely covered by liquid for a successive bubble to be created.

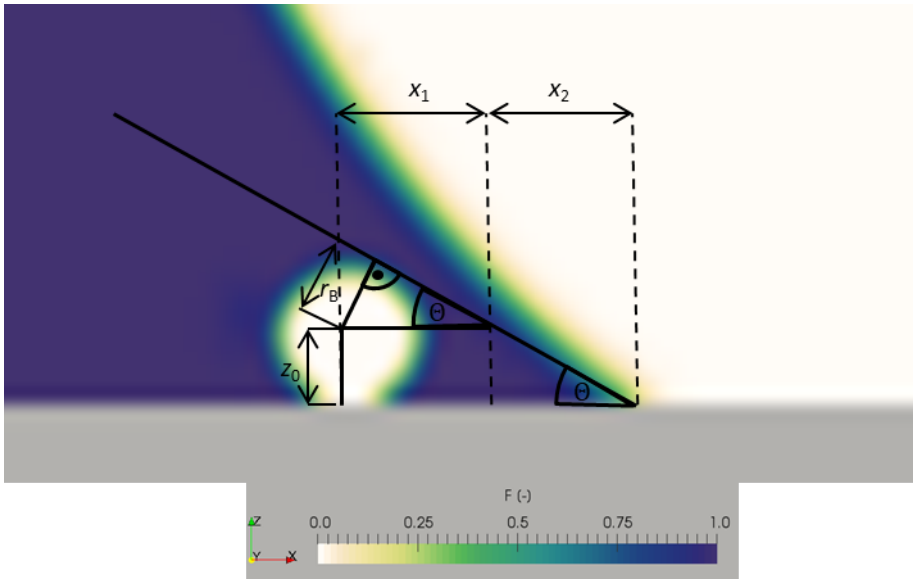

Figure 5.9: Calculation of the radius around the nucleation site, within which $F = 1$ has to be valid at boundary faces before a new bubble can be created

Waiting for sufficient space in the liquid before the nucleation of a new bubble is a key deviation from the hydrodynamics of the nucleation process, as it can be observed in any boiling experiment. In an experiment, a new bubble of significantly smaller size continuously grows out of a cavity. In case that it gets in contact with another bubble during this process, it will either merge and be sucked up by the larger bubble or push the larger bubble away. However, without taking the geometry of the experimental cavity into account by the numerical mesh, this behavior cannot completely be reproduced in the simulation. Nevertheless, the safety distance r_{ns} obviously depends on the radius of the nucleus, in the sense that smaller nuclei need smaller distances. As the possible smallest size of the nuclei created by this method depends on the resolution of the numerical mesh, a finer mesh can serve to reduce the discussed modeling error.

Cooling down the wall underneath a new bubble

Each time, when a bubble is created in the simulation, the temperature in the wall cells below the nucleus is reduced in a way that energy conservation is fulfilled in respect to the evaporation enthalpy and to the superheat of the evaporating fluid. In reality, the superheated liquid surrounding the nucleation site also contributes sensible heat to the nucleation process. For the sake of simplicity, this contribution is neglected in the simulations and the sensible heat needed for the forming of a vapor nucleus from liquid is completely withdrawn from wall cells. Nevertheless, it will be shown, that the temperature drop in

the wall cells at the nucleation site is immediately balanced out by heat conduction, since the volume and the absolute heat capacity of the cooled area is very small compared to that of the heated substrate (see e.g. figure 5.12 (b)). The sensible heat Q_s, which is withdrawn from the wall, is calculated as

$$Q_s = V_B \rho_v (\Delta h_v - c_l \Delta T_l) \tag{5.6}$$

with V_B being the volume of the created bubble, ρ_v the vapor density, Δh_v the evaporation enthalpy, c_l the heat capacity of the liquid and ΔT_l the superheat of the liquid before nucleation. Since the volume of the liquid evaporating to become the bubble nucleus is very small compared to the nucleus volume, it is assumed, that solely liquid in close vicinity to the wall is evaporating, hence $\Delta T_l = T_w - T_{sat}$. The vapor temperature inside the created nucleus is set to saturation temperature. If $Q_s > 0$, the temperature in the first layer of solid cells underneath the bubble foot is decreased to saturation temperature and the difference in sensible heat is subtracted from Q_s. If Q_s is still greater than zero, the next cell layer underneath is cooled down to saturation temperature and so on, until enough sensible heat is withdrawn from the substrate. If eventually Q_s gets negative, the temperature in all solid cells affected so far is increased again to an extent, that Q_s is exactly zero.

5.2 Results

In this section the results of an extensive parameter study will be presented and discussed. The sensitivity of the subcooled flow boiling process of the Multiscale Boiling experiment to process parameters as well as to material properties is studied numerically. First, a reference case is defined applying intermediate values from the experimental parameter range. Striking hydrodynamic and heat transfer related phenomena will be discussed through the example of that reference case. Secondly, based on the reference case, the impact of parameter variation will be outlined in detail. The variation of input parameters is presented in table 5.2. Parts of the results on the reference case and the variation of process parameters are published in [26]. At last, the influence of the thermal conductivity of the liquid as well as the thermal conductivity and the heat capacity of the solid substrate on bubble growth and heat transfer coefficient will be discussed in section 5.2.4.

	Reference	Variation
Max. flow velocity [m/s]	0.0375	0 - 0.0625
Input heat flux [W/cm^2]	1	0.5 - 2
Pre-heating time [s]	10	20, 30
Subcooling [K]	-5	0 - -10

Table 5.2: Parameter variation. The maximal flow velocity is the velocity at half channel height, i.e. u_{max} in eq. 5.1

5.2.1 Two-Phase flow behaviour in reference case

Figure 5.10 (a) exemplarily depicts the state of bubble evolution in the reference case 1.7 s after the very first nucleation, (b) displays the bubble growth process during the first two seconds after activation of the nucleation site in the reference case and the influence of the laser pulse on this process. In both cases an overshoot in bubble growth can be observed due to the large amount of sensible heat stored in the wall and in the thermal boundary layer prior to the activation of the nucleation site. Later the bubble partly condensates again and strives towards an equilibrium state of evaporation at the bubble foot

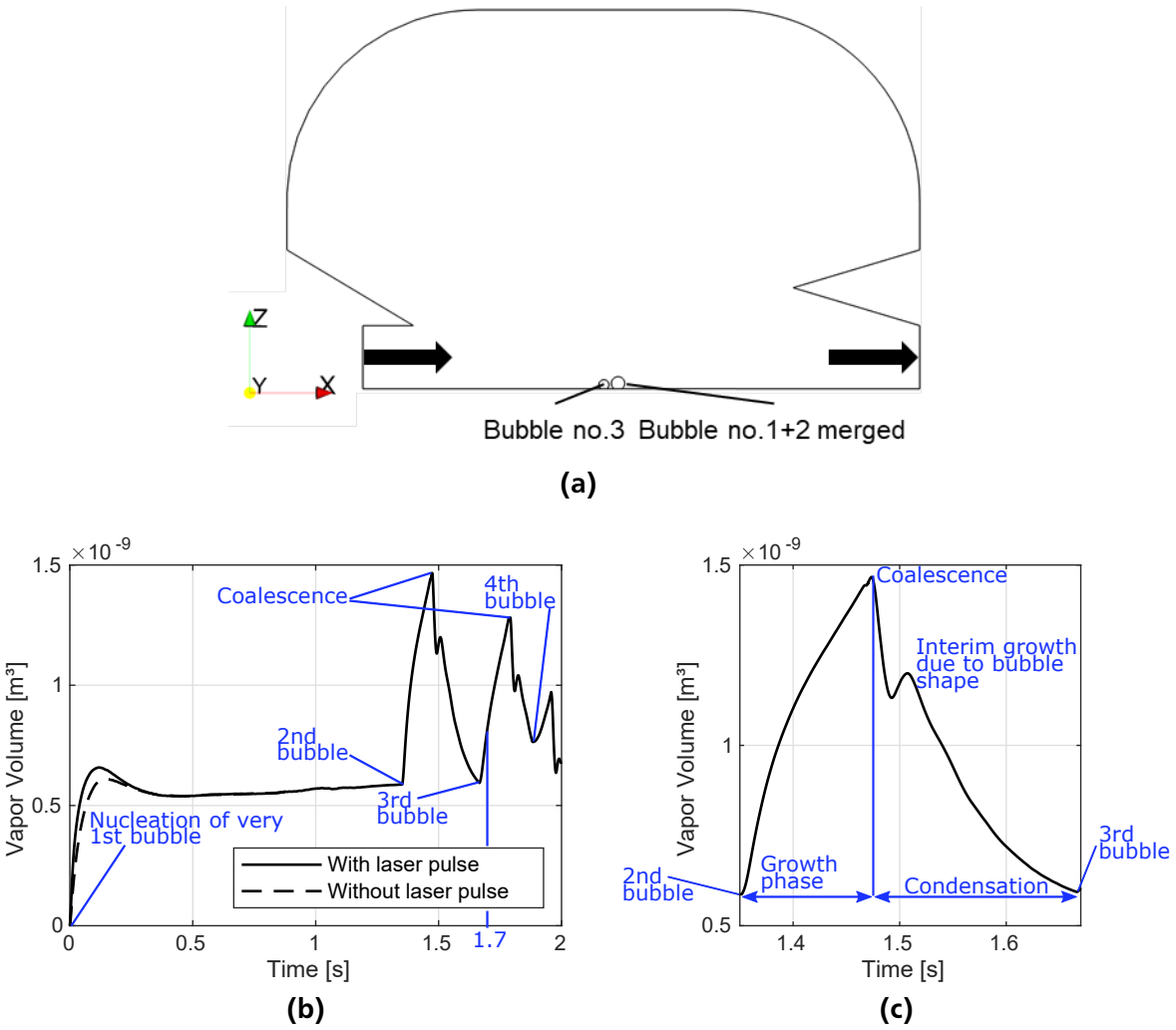

Figure 5.10: (a) Fluid domain and bubble contours at 1.7 s after the very first nucleation. The second bubble has already merged with the very first one, the third bubble is right before coalescence, (b) Vapor volume with and without consideration of laser power for the first two seconds after activation of the nucleation site in the reference case, (c) detailed depiction of the second bubble cycle with growth phase, coalescence with the initial bubble and following condensation

and condensation at the bubble cap. The overshoot right after nucleation is considerably higher, if the laser power is taken into account, however, after approximately 300 ms no difference can be observed between the two cases.

The shear flow drags the initial bubble downstream and a second bubble is created as soon as the wall temperature reaches the defined superheat. This second bubble grows until it gets in contact with the first bubble and coalescence occurs approximately 1.3 s after the very first nucleation. Figure 5.11 shows the life cycle of the second bubble in the reference case from nucleation till the end of the coalescence with the first bubble. After the merger, the resulting bubble is larger and rises higher into the subcooled bulk. Consequently, condensation dominates and the bubble shrinks until it reaches the equilibrium state again. Nevertheless, due to the momentum of the merger an alternating spreading and receding of the contact line sets in, which can be observed in figure 5.11 at 1.477 s and 1.523 s. In consequence, phases of a short contact line and a bubble cap rising highly into the bulk alternate with a short phase of a

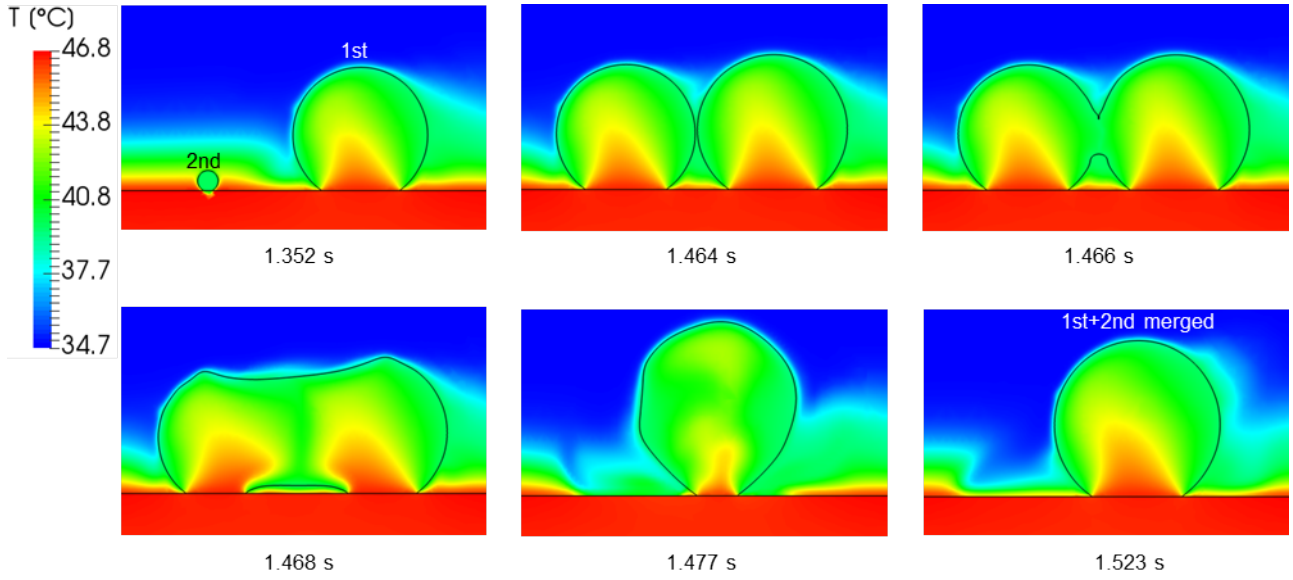

Figure 5.11: Temperature field and phase boundaries during merger of the first two bubbles in reference case

flatter bubble with a longer contact line. This phase shortly interrupts the shrinking process by a stage of evaporation dominance, which is visualized in detail in figure 5.10 (c). Due to the merger, the second bubble rapidly gives space at the nucleation site, in contrast to the initial bubble, which was slowly driven downstream by the shear flow. The waiting time between nucleations reduces significantly after the second bubble. A continuous process of nucleation of successive bubbles and following coalescence with the very first bubble begins, while the growth phase and thus the end volume of the bubbles before coalescence decrease.

5.2.2 Heat transfer characteristics

Figure 5.12(a) shows the evaporation and condensation heat transfer, respectively. The hydrodynamic phenomena discussed in the prior section can clearly be followed in the evolution of the two heat flows. While both heat flows are equal during the equilibrium stage of the initial bubble, evaporation dominates during phases of bubble growth and condensation dominates in the phase right after a merger, shortly interrupted of evaporation dominance, when the bubble is relatively flat.

Figure 5.12(b) shows the evolution of the wall temperature at the nucleation site. After a strong increase and following decrease during the first milliseconds after the very first nucleation due to the laser pulse, a slow and continuous increase in wall temperature can be observed until the nucleation criterion for the second bubble is reached. Each time, when the nucleation temperature of 46.7°C is reached and a new bubble is created, a steep decrease in wall temperature can be observed. This is due to the feature of manipulating the wall temperature in a way that the energy balance is fulfilled, as presented in section 5.1.3. However, due to the very small solid volume, which is cooled down compared to the volume of the whole heater substrate, the temperature at the nucleation site almost fully recovers in an extremely short time span. Furthermore, a reversible decrease in wall temperature can be observed each time, when the contact line of the sliding bubble passes the location, where the temperature is monitored.

Figure 5.12(c) shows the contact line evaporation heat transfer. Relating the values of heat transfer due to contact line evaporation to the overall evaporation heat transfer from figure 5.12(a), it is striking,

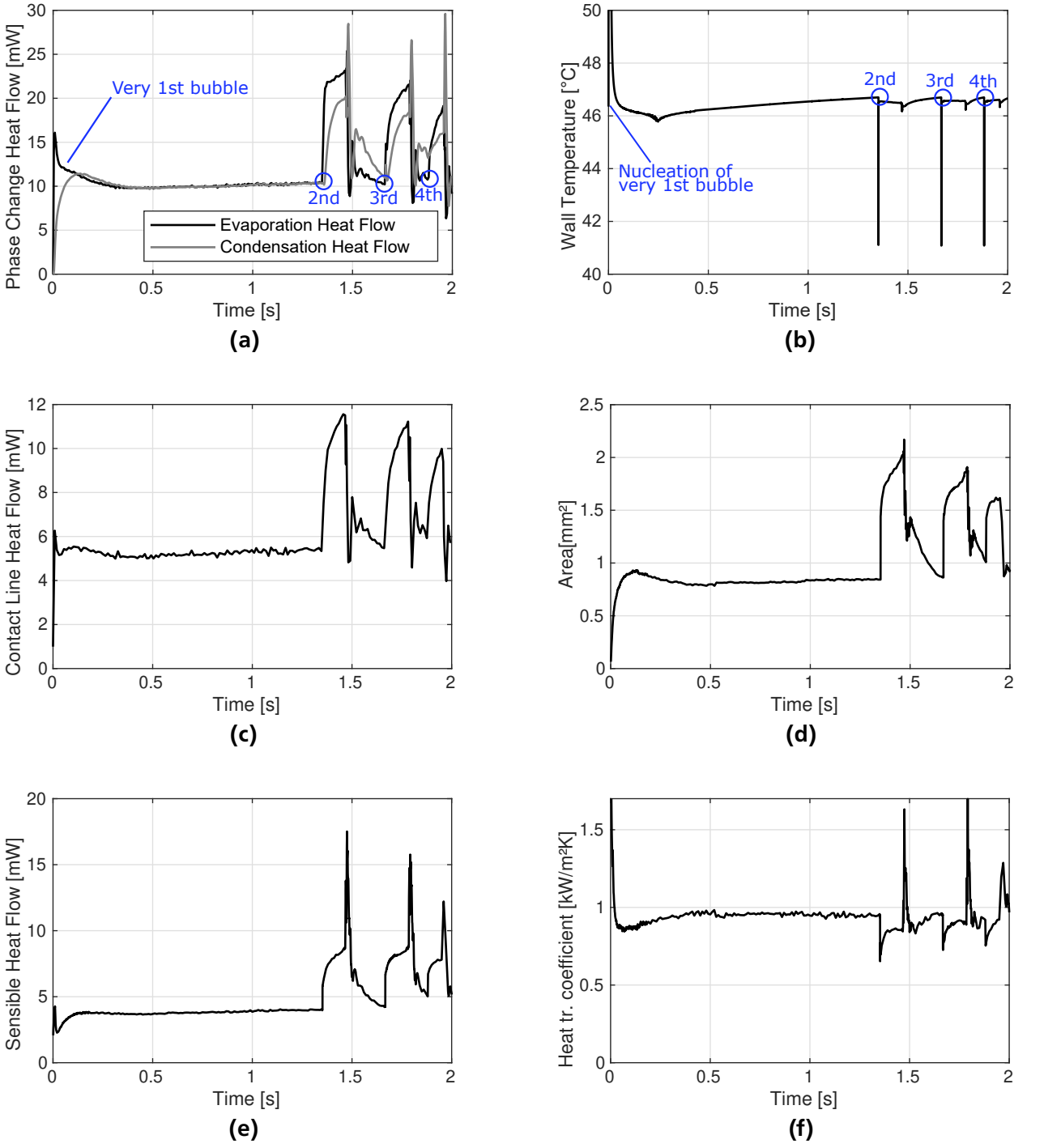

Figure 5.12: Heat transfer characteristics in the reference case: (a) evaporation and condensation heat flow, (b) wall temperature at the position of the nucleation site, (c) contact line heat flow, (d) area taken into account for sensible heat flow, (e) Sensible heat flow, (f) heat transfer coefficient

that the contact line share is considerably high. During the equilibrium state it is constantly higher than 50 %, while during merger the share of contact line evaporation temporarily grows up to almost 60 % due to the alternating expanding and contracting bubble foot. Those values are significantly higher than estimations for the share of contact line heat transfer given in literature for boiling under earth gravity conditions. Those are usually in the range of 20 % to 30 % ([53] and [104]). The reason for this deviation is the relatively higher evaporation rates at the bubble hull under earth gravity conditions due to the presence of natural convection as well as enhanced bubble growth dynamics compared to microgravity.

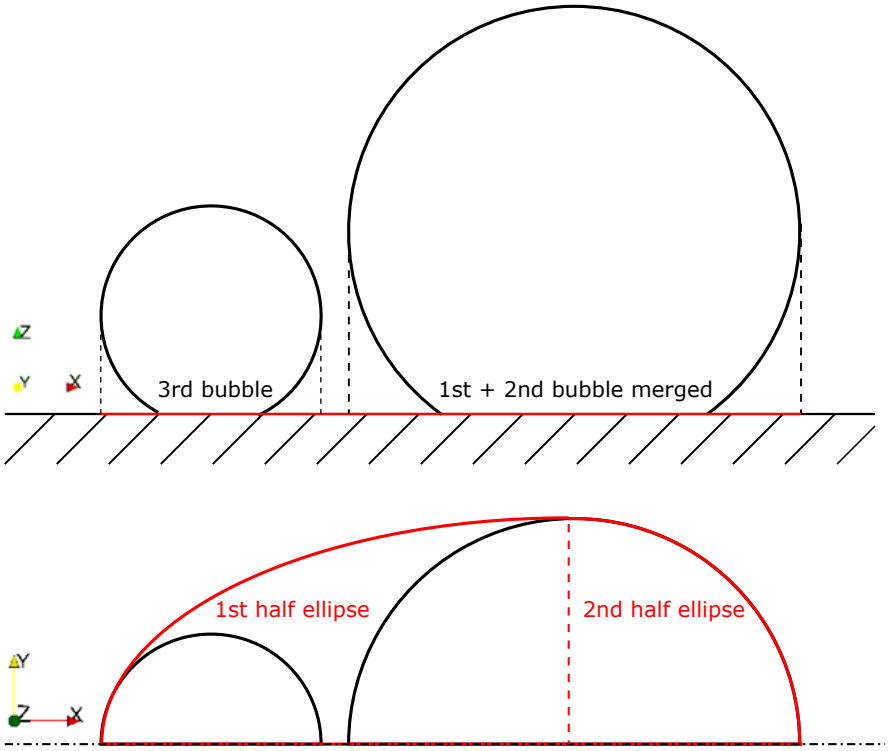

Figure 5.13: Schematic visualization of the area evaluated to determine the heat transfer coefficient for the example of 1.7 s in the reference case. The 3-D interface of every bubble is projected to the heater surface and an area consisting of two half ellipses is formed, which completely includes the projected interfaces (red boundary line). This area changes in every time step. Sensible heat flow, the area averaged wall temperature and the heat transfer coefficient are determined within this area

In order to determine the heat transfer coefficient of the boiling process, a representative area on the heater surface has to be defined, where sensible heat flow to the fluid contributing to the heat transfer coefficient is evaluated. Since most of the time the majority of the heater surface is not populated by any bubble and because the aim is to quantify the impact of bubble growth and movement on heat transfer, integrating the sensible heat flux over the whole surface would distort the results. Therefore, the 3-D phase interface of each bubble is projected onto the heater surface. This approach is depicted schematically in figure 5.13. The area of the projected bubble hull is considered a legitimate region of influence of a single bubble and therefore the sensible heat flux on the heater surface is integrated over that area. In case of multiple bubbles an area enclosed by two half ellipses, which just includes all existing bubbles, is taken into account for the evaluation of sensible heat flow. Because the number, size and position of bubbles change over time, this region of interest is determined anew for every evaluated time step. The

resulting evolution of this representative area is depicted in figure 5.12 (d) for the reference case.

Figure 5.12(d) shows the evolution of sensible heat flow in the reference case at the described area of interest. At the very first nucleation, the heat flow increases steeply due to the power of the laser beam and decreases rapidly as soon as the laser is turned off. After that, sensible heat flow increases constantly during bubble growth. One reason for this correlation is obviously, that a growing bubble causes an increase in the evaluated area per se. A second reason is, that the growing contact line does not only cause an increase in contact line heat flow, but also enhances the sensible heat flow: Figure 5.14 shows an increase of sensible heat flux to the liquid phase in the vicinity of the contact line. Note, that the sensible heat flux next to the contact line is one order of magnitude lower than the contact line heat flux itself, nevertheless a larger contact line is correlated to an increase in sensible heat flow, as well. This observation can be explained by the effect that the evaporating contact line consumes superheated liquid from the thermal boundary layer, which is replaced by colder liquid.

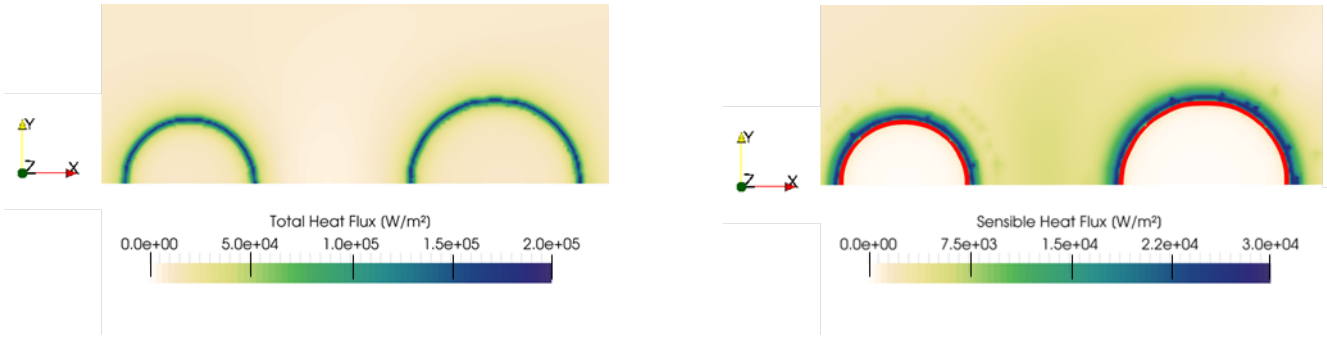

(a) (b)

Figure 5.14: (a) Total heat flux and (b) sensible heat flux (excluding contact line heat flux) with the position of the contact line in red, on the liquid-solid interface in the reference case at 1.704 s after the very first nucleation, view from above

In the aftermath of every successive nucleation, a rapid increase in sensible heat flow can be observed. This is caused by a jump in the size of the area evaluated to obtain the sensible heat flow, as depicted in 5.12(e). The very first bubble has already moved relatively far downstream from the nucleation site. During the existence of only the very first bubble the evaluated area is the 3-D interface of the bubble projected onto the heater surface. In the timestep of a new bubble creation the evaluated area changes to two half ellipses, which contain the projected interfaces of both bubbles, causing the aforementioned size jump (see figure 5.13). Additional to this methodological caused jump, the sensible heat flow shows a strong and short increase every time, when two bubbles coalesce. In this moment contact line heat flow and and the overall evaporation heat flow already begin to strongly decrease. During coalescence the successive bubble is promptly being sucked up by the initial bubble and the emerging space is filled with colder bulk liquid, as can be observed in figure 5.11. This increases the local temperature gradient from the wall to the liquid, causing a pronounced increase in sensible heat flow.

From the sensible and contact line heat flow, the area averaged temperature on the evaluated bi-elliptic area and the size of the area itself the heat transfer coefficient for the boiling process is determined:

$$\alpha_{\mathrm{sl,B}} = \frac{\dot{Q}_{\mathrm{Sens,elliptic}} + \dot{Q}_{\mathrm{Cl}}}{(T_{\mathrm{av,elliptic}} - T_{\mathrm{bulk}})A_{\mathrm{elliptic}}} \tag{5.7}$$

This definition of the heat transfer coefficient has specific advantages and disadvantages. On the one hand, it only takes the influence zone of vapor bubbles on the heater surface into account, which is where heat transfer is largely influenced by phase change. A large area, where heat transfer is achieved through forced convection only is cut out. The definition is therefore appropriate to study the effect of few, isolated vapor bubbles on heat transfer at a large area. If one took the whole heater surface into account, the effect of the two-phase flow on heat transfer would vanish behind forced convection to the pure liquid, which dominates the global heat transfer. On the other hand, since the area, at which the heat transfer coefficient is evaluated, is changing in every time-step, the results for the heat transfer coefficient are hardly comparable between different simulation runs and even in a single run over the simulated time span. This will be discussed in detail in the following.

Figure 5.12(f) shows the evolution of the heat transfer coefficient over time in the reference case: The trend follows basically that of the combined sensible and contact line heat flow, with the main difference, that in the moment of the emergence of a new bubble at the nucleation site, a rapid decrease occurs. The reason for this behaviour is the sudden change in the area evaluated for the determination of the heat transfer coefficient. Until the nucleation of the second bubble, the heat transfer coefficient is evaluated for an area directly impacted by the first bubble only. Beginning with the the second nucleation, at a large share of the evaluated area convective heat transfer dominates, causing a lower heat transfer coefficient. Therefore, for methodological reasons the heat transfer coefficient right after the nucleation of a successive bubble is barely comparable to the heat transfer coefficient before, if the successive bubble has a relatively large distance to the existing one. However, it is shown, that in the vicinity of a bubble heat transfer is largely enhanced compared to areas with little impact of bubbles. After this methodologically caused decrease, the heat transfer coefficient increases during the growth of the second bubble. Additionally, a steep and short increase can be observed for the heat transfer coefficient during merger due to the pronounced increase in sensible heat flow.

5.2.3 Influence of process parameters

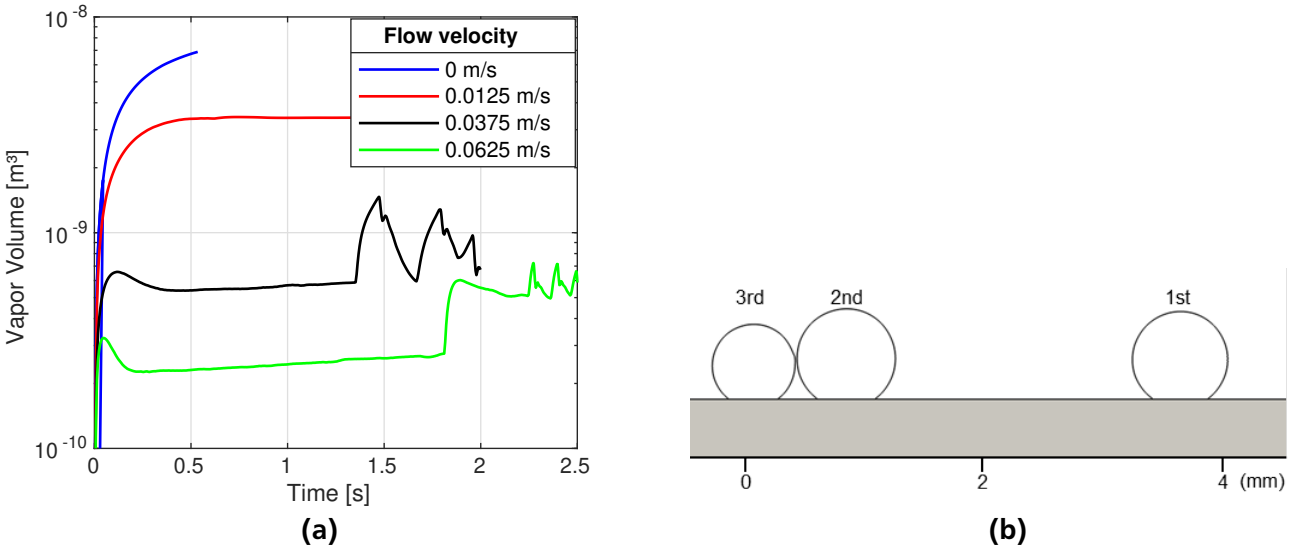

Figure 5.15: (a) Bubble growth for different flow velocities, (b) Interface for $u_{max} = 0.0625\,m/s$ 2.27 s after first nucleation, shortly before the second and the third bubble merge

Flow velocity

Figure 5.15 (a) shows the bubble volume evolution for maximum flow velocities lower and higher than in the reference case (0.0375 m/s, black line). Apparently, an increasing flow rate correlates with a decreasing volume of each bubble. This can be explained by the thermal boundary layer between the superheated wall and the subcooled bulk fluid, which is thinner in case of higher flow rates. Next the maximal wall temperature is lower for higher flow velocities due to the increased convective heat transfer. This also causes prolonged waiting periods between nucleations during the first three bubble cycles in the 0.0625 m/s case. Hence, the first two bubbles do not merge in this case, as indicated in figure 5.15 (b), and the bubble volumes of the first two bubbles permanently add up in figure 5.15 (a). For flow velocities lower than in the reference case, the very first bubble grows larger and blocks the nucleation site for a longer period of time than in the reference case, such that no subsequent nucleation occurs

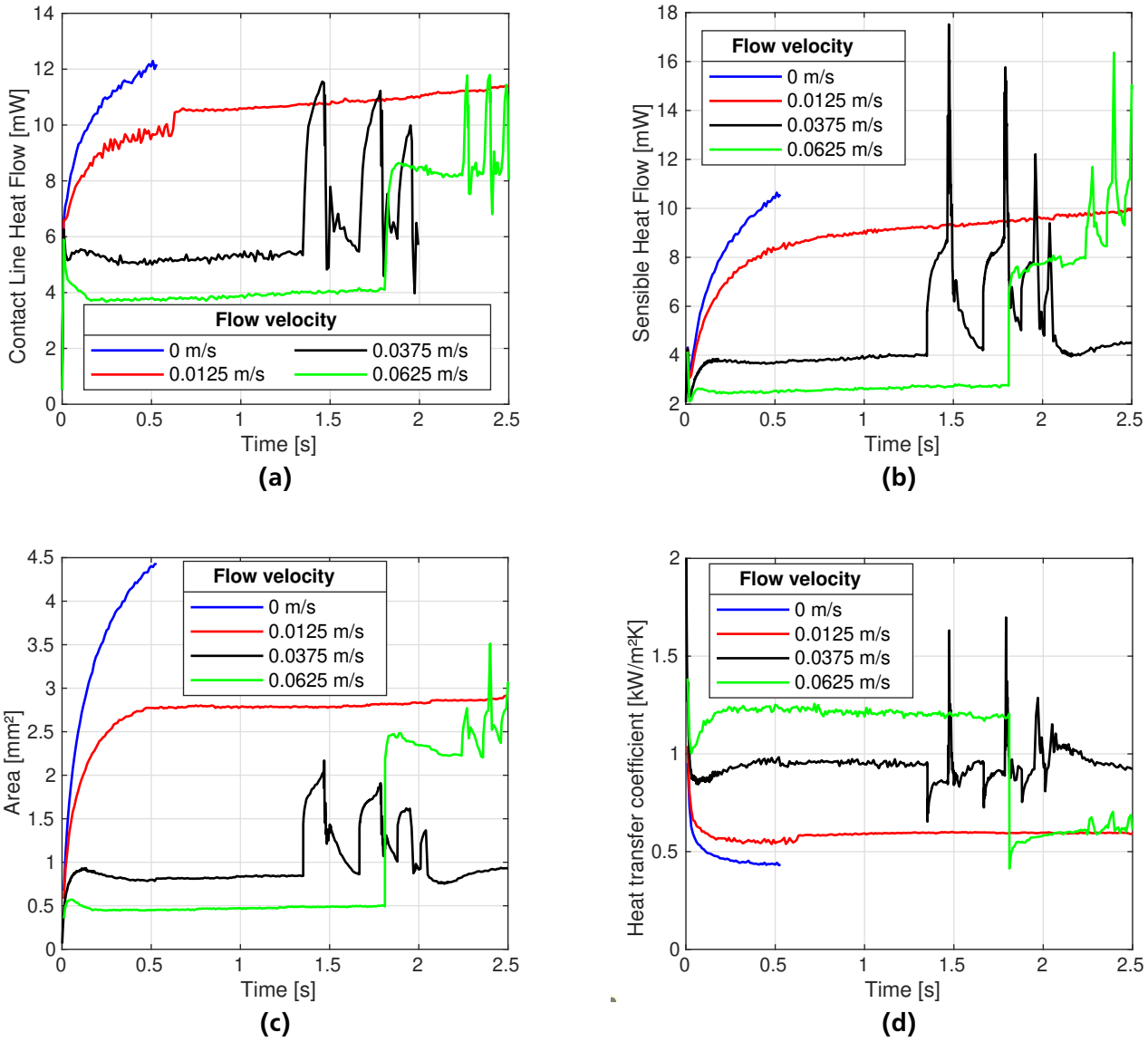

Figure 5.16: Heat transfer characteristics for different flow velocities: (a) Contact line heat flow, (b) Sensible heat flow at the evaluated bi-elliptic area, (c) size of the evaluated bi-elliptic area, (d) Heat transfer coefficient at the evaluated bi-elliptic area

during the conducted simulation time.

Figure 5.16 (a) shows the heat transfer due to evaporation at the contact line. It indicates, that the contact line heat transfer in case of a single bubble is higher for lower flow velocities due to larger bubble volumes and therefore longer contact lines. The sensible heat flow is evaluated in the same way as in section 5.2.2 within two half ellipses containing the projection of all bubble interfaces onto the heater surface. Figures 5.16 (b) - (d) show, that during the presence of only the very first bubble on the heater surface, the absolute sensible heat flow as well as the evaluated area decrease for increasing flow velocities due to smaller bubble size. However, the heat transfer coefficient in the effective area of the bubble increases significantly for increasing flow velocities. This is due to the very low heat transfer coefficient from the solid to the vapor phase of the bubble, which has a high share in case of large bubbles.

In the $u_{max} = 0.0625$ m/s case the spatial distance between the first two bubbles is sufficiently large, so that the two bubbles do not coalesce. Therefore, contact line and sensible heat flow add up permanently and are higher during the equilibrium phase than in the reference case. The heat transfer coefficient shows a steep decrease in the moment of the nucleation of the second bubble in the $u_{max} = 0.0625$ m/s case and from then on remains on the same low level as in the $u_{max} = 0.0125$ m/s case. Again, the reason for this development is the sudden change of the evaluated area, which in case of two small bubbles with great spatial distance causes the inclusion of a large area between the two bubbles. In this area, heat transfer is achieved by forced convection to the liquid only. In the reference case this effect is balanced out as soon as the first two bubbles approximate sufficiently and eventually merge; if the bubbles stay apart in case of higher flow velocities, the effect persists. Again, the values for the heat transfer coefficient before and after the nucleation of an additional bubble are hardly comparable. Apparently, in case of several bubbles with large spatial distance the method for the evaluation of sensible heat flow and heat transfer coefficient has to be enhanced for better comparability. It can be assumed, that if only the

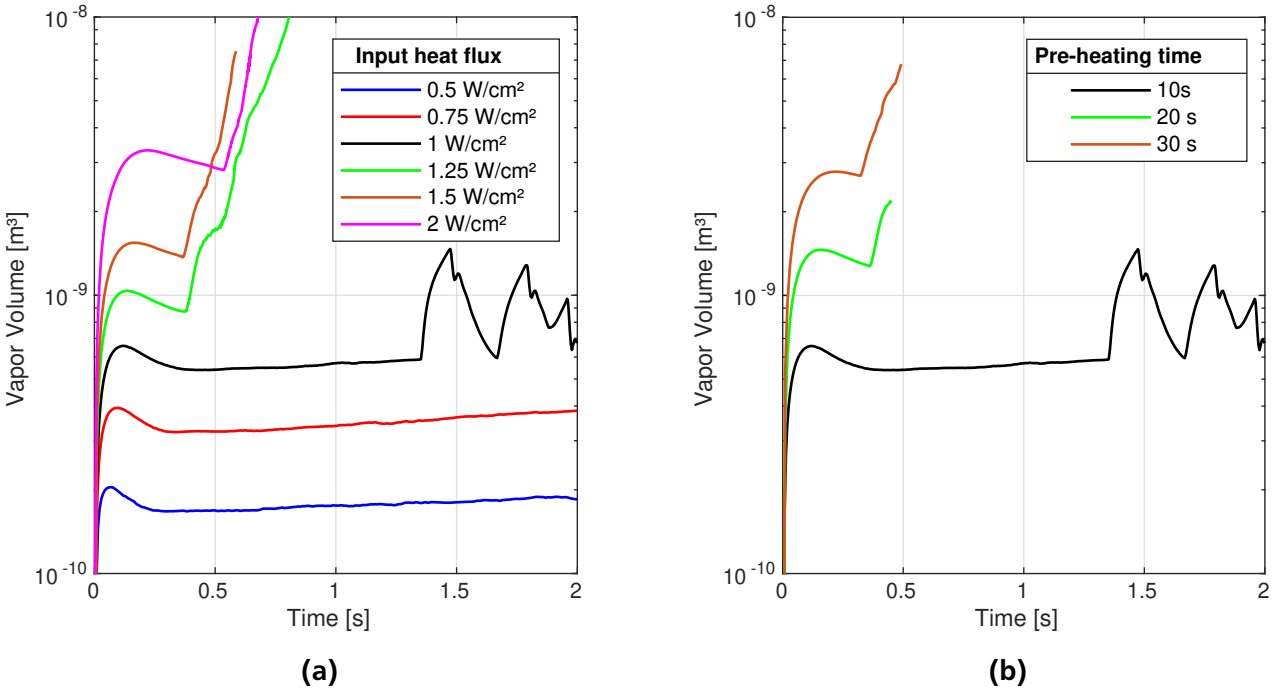

Figure 5.17: Bubble growth for (a) different input heat fluxes, (b) different pre-heating times

actual effective area of the bubbles are taken into account, the enhanced heat transfer coefficient of a single bubble in the $u_{max} = 0.0625\,m/s$ case will add up for two bubbles with large spatial distance.

The results indicate, that a high flow velocity can contribute to optimized heat transfer during flow boiling in microgravity. It causes lower wall temperatures and bubbles of smaller volume, which are dragged downstream of the nucleation site sufficiently fast. If a high flow velocity is chosen, ideally the other parameters should be adjusted in a way, that the nucleation frequency of successive bubbles is low enough for bubbles not to coalesce. That way, a high number of relatively small bubbles on the heater surface can be established.

Input heat flux and pre-heating time

High input heat fluxes (figure 5.17 (a)) as well as increased pre-heating times (see 5.17 (b)) cause a faster growth and a larger equilibrium size of the very first bubble. This is intuitive, since in both cases more sensible heat is provided for bubble growth from the wall as well as from the liquid thermal boundary layer. However, as soon as the very first bubble is dragged downstream sufficiently to give space at the nucleation site for successive bubbles, a cycle of rapidly nucleating and coalescing bubbles begins.

That high frequent nucleation cycle causes repeated coalescence between bubbles of very different size and thus strongly diverging pressures of the vapor phase inside the two merging bubbles. The result of this pressure difference at the beginning of the merging process is a pressure driven flow of vapor from the small to the large bubble (see figure 5.18), resulting in the small bubble being sucked up by the large one. Please note, that the pressures depicted in figure 5.18 is not the absolute pressure inside the bubbles as it would be measured in the corresponding experiment, but the pressure difference towards the outlet port of the flow channel. The pressure driven flow is counteracted by the surface tension force at the bubble foot, which causes the bubble to stay attached to the heater surface. Schweizer [87] derived a simple correlation for the surface tension force at the bubble foot of a spherical bubble, taking into account the bubble diameter d_B and the apparent contact angle Θ. With the coordinate z orthogonal to the solid-fluid boundary pointing into the fluid, the surface tension force, which drags the bubble towards the wall, reads:

$$F_{\sigma,z} = -\pi \cdot d_B \cdot \sigma \cdot (sin\Theta)^2 \tag{5.8}$$

Inside a single fluid grid cell, with the pressure gradient in all three directions ∇p and the cell volume V_c, the pressure force, which drags the fluid upwards and away from the wall, can be defined as:

$$F_{p,z,c} = (\nabla p \cdot \vec{e}_z)\, V_c \tag{5.9}$$

The combined pressure force at the whole bubble is then $F_{p,z,c}$ summed over all fluid cells containing part of the bubble:

$$F_{p,z} = \sum_B F_{p,z,c} \tag{5.10}$$

In case that $|F_{\sigma,z}| > |F_{p,z}|$ for the smaller bubble, the pressure driven force does not detach the small bubble completely from the wall during the merger with the large bubble. Instead, the small bubble is torn apart during this process. Part of the smaller bubble's vapor volume coalesces with the major bubble, while the rest stays attached to the wall and forms an additional bubble in the vicinity of the nucleation site, which grows and eventually coalesces with the major bubble again. This happens repeatedly during a fast sequence of nucleating and coalescing bubbles in the high input heat flux and high pre-heating time cases. Figure 5.19 shows a sequence of this phenomenon with high temporal resolution in the

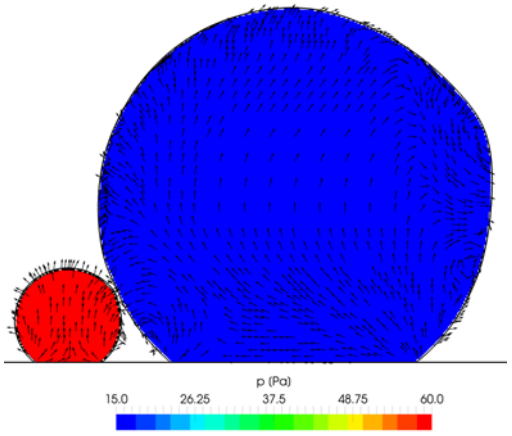

(a) 0.58741 s

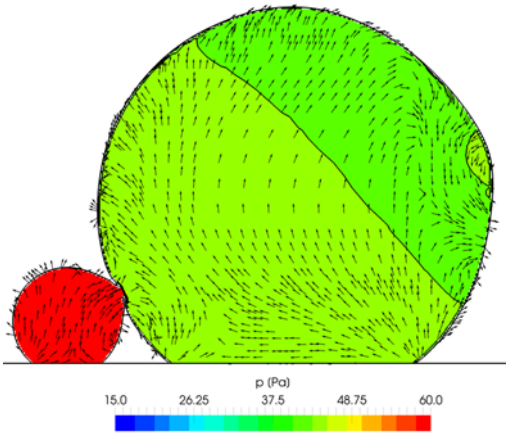

(b) 0.58791 s

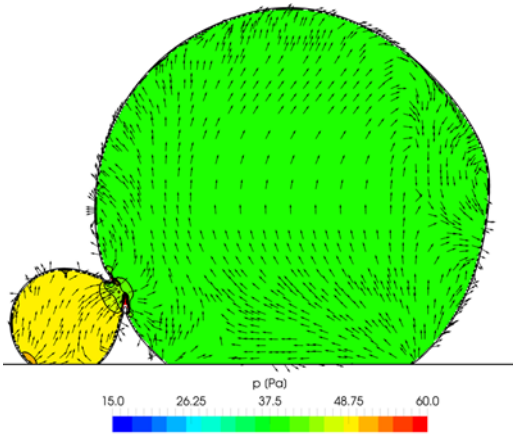

(c) 0.58801 s

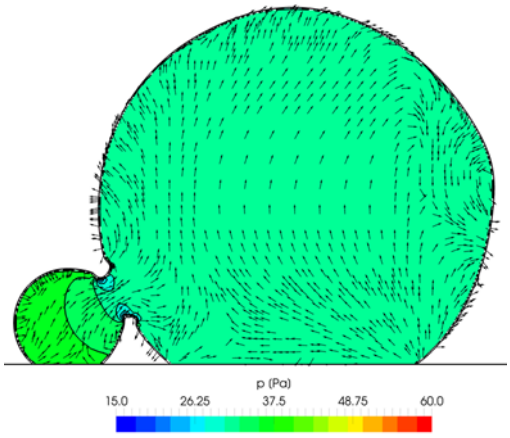

(d) 0.58811 s

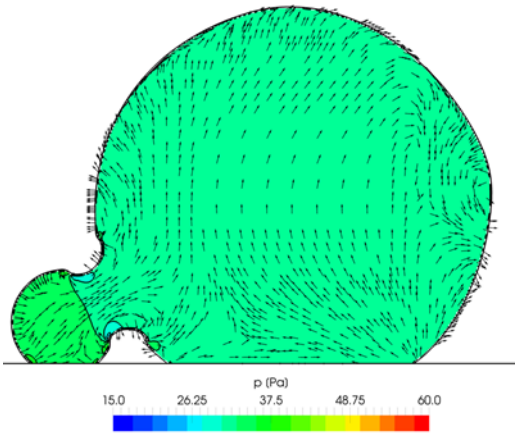

(e) 0.58831 s

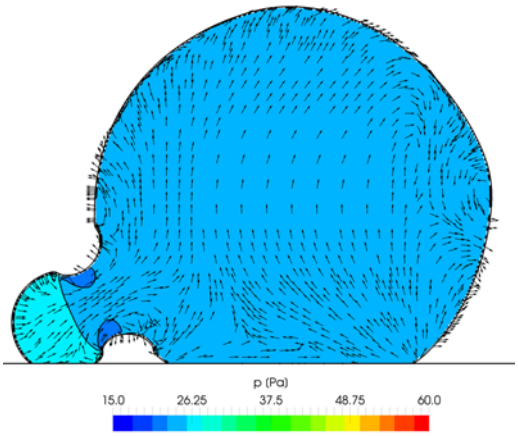

(f) 0.58841 s

Figure 5.18: Pressure difference and pressure driven flow during the coalescence between bubbles of different size in the 2 $\mathrm{W/cm^2}$ case

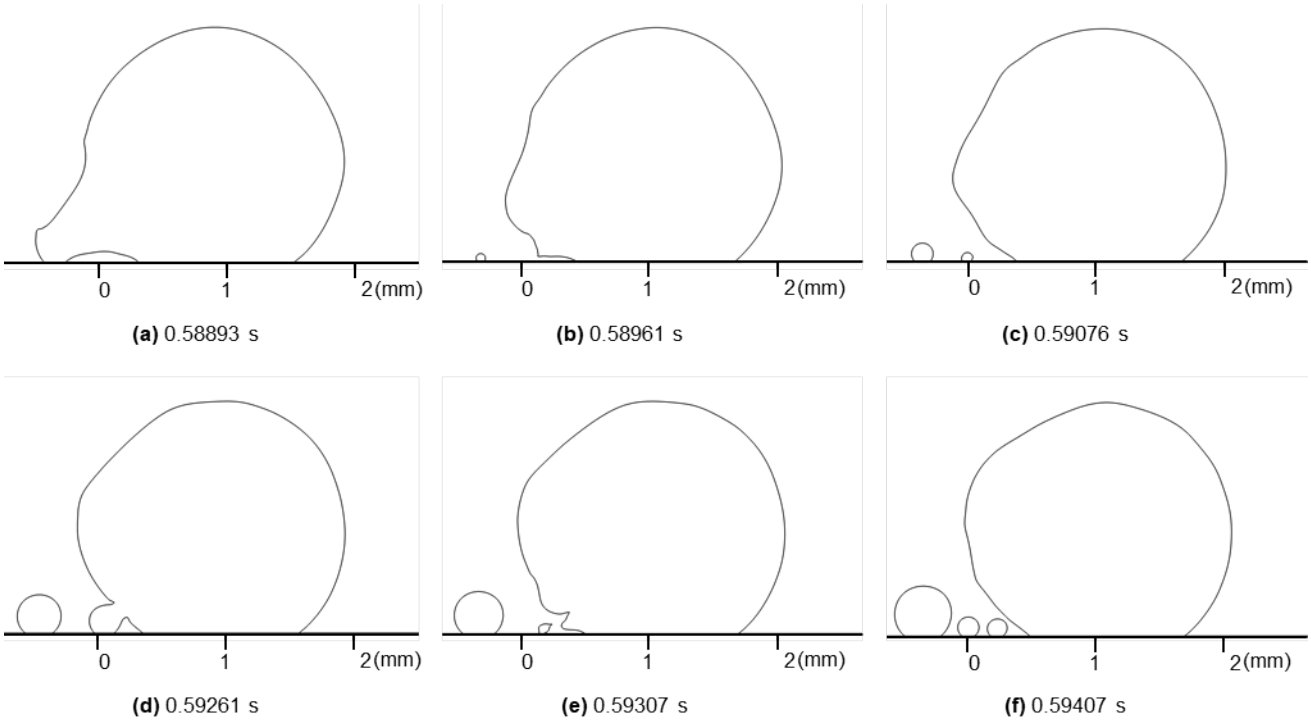

Figure 5.19: Process of coalescence with following detachment of vapor and forming of new bubbles in the $2\,\mathrm{W/cm^2}$ case, which is typically occurring in a rapid sequence in high heat flux and high pre-heating time cases, time starting from first nucleation: (a) a successive bubble from the nucleation site is coalescing with the first bubble, (b) part of the vapor volume detaches during the merger process and forms a new bubble upstream of the nucleation site, (c) while the latter bubble is growing, the next successive bubble nucleates at the defined nucleation site due to the superheat criterion, (d) this bubble again coalesces with the first bubble, (e) again vapor detaches during the merger process, forming another bubble between the nucleation site and the major bubble, (f) another bubble nucleates at the nucleation site due to superheat

$2\,\mathrm{W/cm^2}$ case.

In consequence of this process of "feeding" the very first bubble by the succeeding ones, the volume of the initial bubble grows above its equilibrium size determined by evaporation at the bubble foot and condensation at the bubble cap, because the growth due to coalescence runs faster than shrinkage due to condensation. Figure 5.17 depicts, that in every case of input heat fluxes or pre-heating times higher than in the reference case, the vapor volume begins to grow without limit during the conducted simulation time, as soon as the very first bubble gives space at the nucleation site. Interestingly, if the input heat flux is increased above $1.5\,\mathrm{W/cm^2}$, the very first bubble grows larger isolated, but after the "feeding" pattern starts, the overall vapor volume gets smaller than in lower input heat flux cases. In the $2\,\mathrm{W/cm^2}$ case the very first bubble grows larger in the beginning and blocks the nucleation site for a longer time, thus the described growing process beyond the equilibrium size begins later.

Comparing the effect of an increased input heat flux and an increased pre-heating time compared to the reference case, the same qualitative effect can be observed but with stronger expression for increased input heat flux: Increasing the heat flux by the factor 1.5 has the same effect on bubble growth as dou-

bling the pre-heating time to 20 s. Doubling the heat flux has even a slightly stronger effect on the growth of the first bubble than tripling the pre-heating time. This observation confirms prior observations from experiments.

For heat fluxes lower than in the reference case (0.5 W/cm^2 and 0.75 W/cm^2) no nucleation of subsequent bubbles occurs for the prescribed wall superheat criterion of 7 K. However, the criterion as deducted in section 5.1.3 is only an estimate. At the very deep cavity of the Multiscale Boiling experiment a lower superheat might be sufficient for the nucleation of successive bubbles. Figure 5.20 shows the temporal evolution of the wall temperature at the nucleation site for the reference case and lower heat fluxes, indicating, that decreasing that criterion to appr. 5 K in the case of 0.75 W/cm^2 or 3 K in the case of 0.5 W/cm^2 would be sufficient for a stable cycle of successive bubbles.

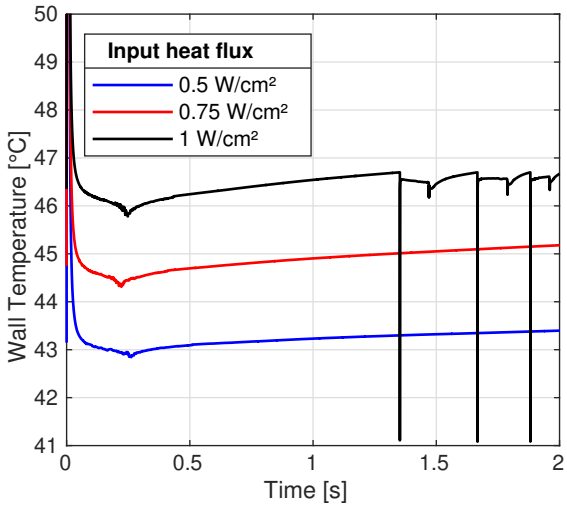

Figure 5.20: Wall temperature at the nucleation site for input heat fluxes lower than in the reference case

Figure 5.21 shows the contact line heat flow, the sensible heat flow within the bi-elliptic influence zone of the bubbles, the area of that zone and the heat transfer coefficient, respectively. Note, that for input heat fluxes >1 W/cm^2 the results have been filtered with a MATLAB fir1-lowpass filter with a cutoff frequency at 0.2 of the Nyquist frequency due to the values fluctuating at high frequencies with large amplitudes. The absolute values of contact line and sensible heat flow increase for increasing input heat flux as long as there is only the very first bubble present on the heater surface. However, as soon as the discussed "feeding" pattern begins, the mean values of both contact line and sensible heat flow do not differ significantly between 1.5 W/cm^2 and 2 W/cm^2, despite very large fluctuations due to bubble growth and coalescence. Heat transfer to the fluid appears to depend more on bubble size and length of the contact line than on the actual input heat flux. This effect can be well explained by the thermal conductivity, which is much higher in the solid substrate than in the fluid.

Furthermore, for high input heat fluxes an increase in input heat flux is correlated with a decrease in heat transfer coefficient during the presence of only the very first bubble, which is caused by a large part of the evaluated area being covered with vapor. For input heat fluxes up to 1 W/cm^2 the heat transfer coefficient stays almost constant. When the feeding pattern begins for the high input heat flux cases, the lower heat transfer coefficient deteriorates even further, correlating with the size of the main bubble and the evaluated area.

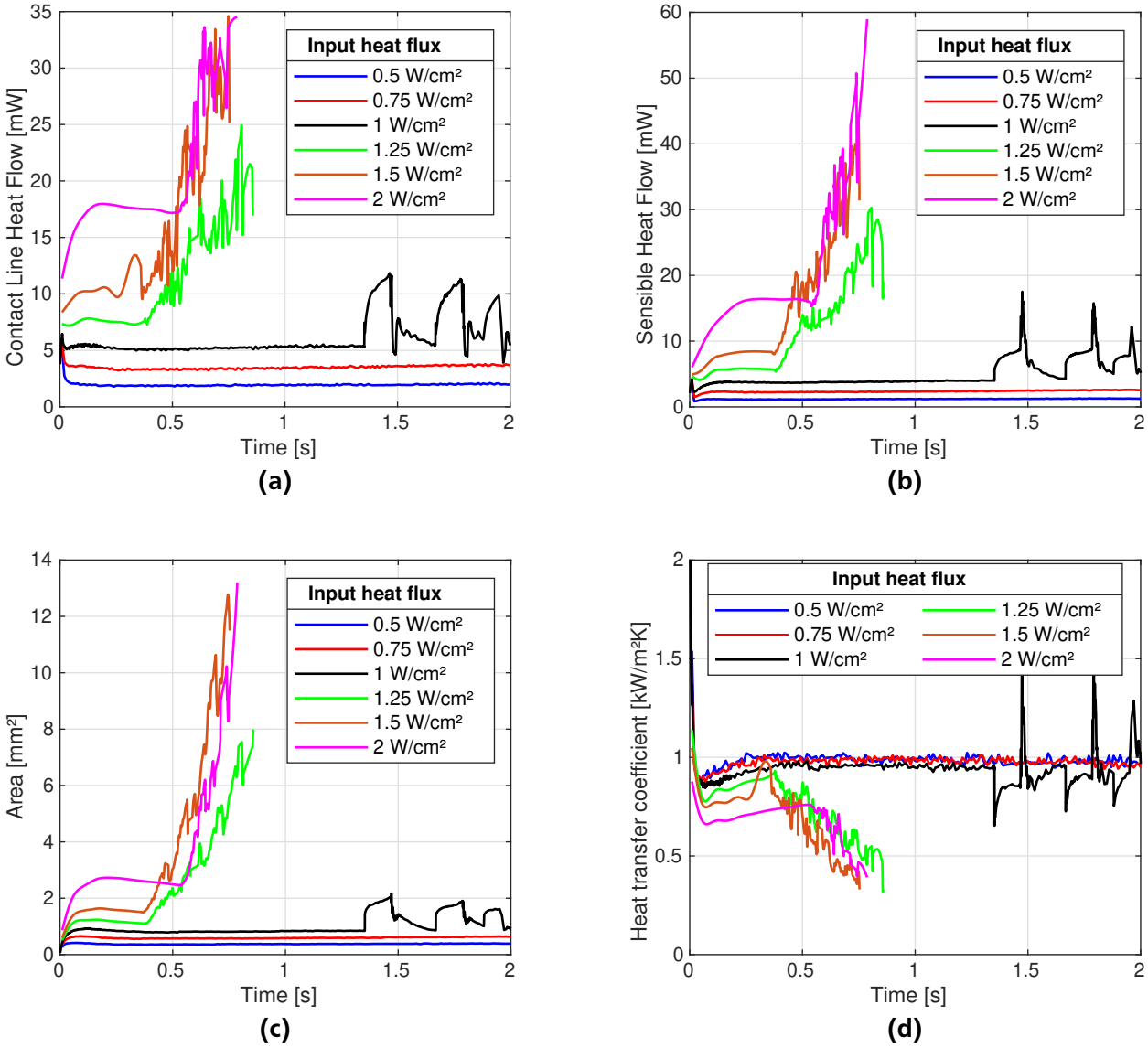

Figure 5.21: Heat transfer characteristics for different input heat fluxes: (a) Contact line heat flow, (b) Sensible heat flow at the evaluated bi-elliptic area, (c) size of the evaluated bi-elliptic area, (d) heat transfer coefficient at the evaluated bi-elliptic area

The heat transfer in case of increased pre-heating times (see figure 5.22) shows a qualitatively similar behavior to increased input heat flux. In correlation to the quantitative differences in bubble growth (figure 5.17), the effects of an increased pre-heating time are less pronounced than those of an increased input heat flux.

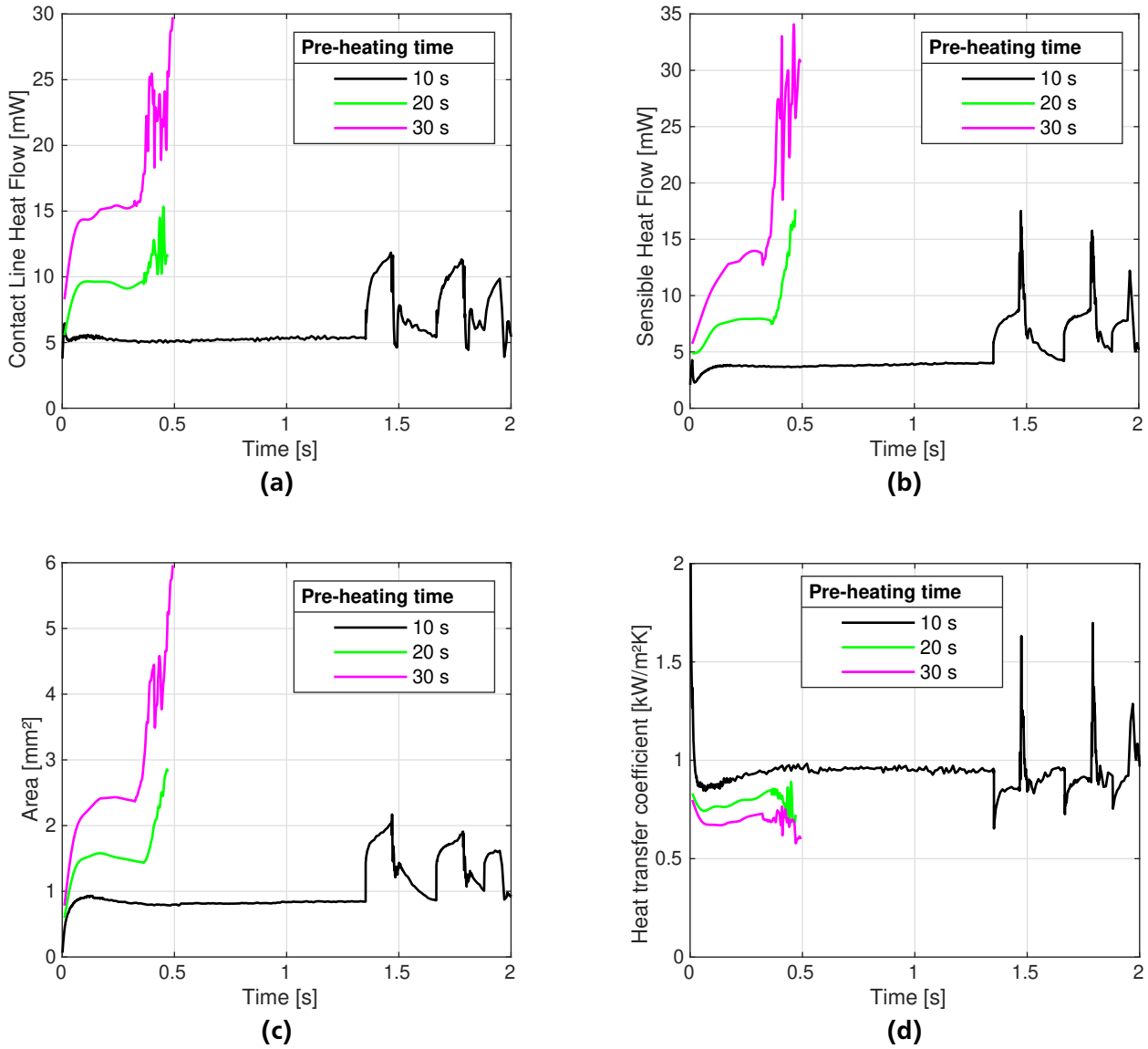

Figure 5.22: Heat transfer characteristics for different pre-heating times: (a) Contact line heat flow, (b) Sensible heat flow at the evaluated bi-elliptic area, (c) size of the evaluated bi-elliptic area, (d) Heat transfer coefficient at the evaluated bi-elliptic area

Subcooling

Figure 5.23 (a) shows an increase in bubble volume for a decreasing level of subcooling in the bulk fluid. For a very high subcooling of -10 K no successive bubbles appear after the very first, laser induced nucleation for the nucleation criterion of 7 K. Again, the superheat needed for successive nucleations might be lower for the cavity in the Multiscale Boiling experiment. Successive nucleations would be possible, if the criterion was decreased to approximately 3 K. In case of a subcooling of only -2 K, a stable sequence of nucleating bubbles merging with the very first one begins after approximately 0.9 s.

For saturated boiling (0 K subcooling) successively nucleating bubbles at the nucleation site and additional bubbles originating from vapor torn off in prior mergers can be observed, as shown in figure 5.23 (b). This behavior is similar to the cases of increased input heat flux, but the sequence of nucleation

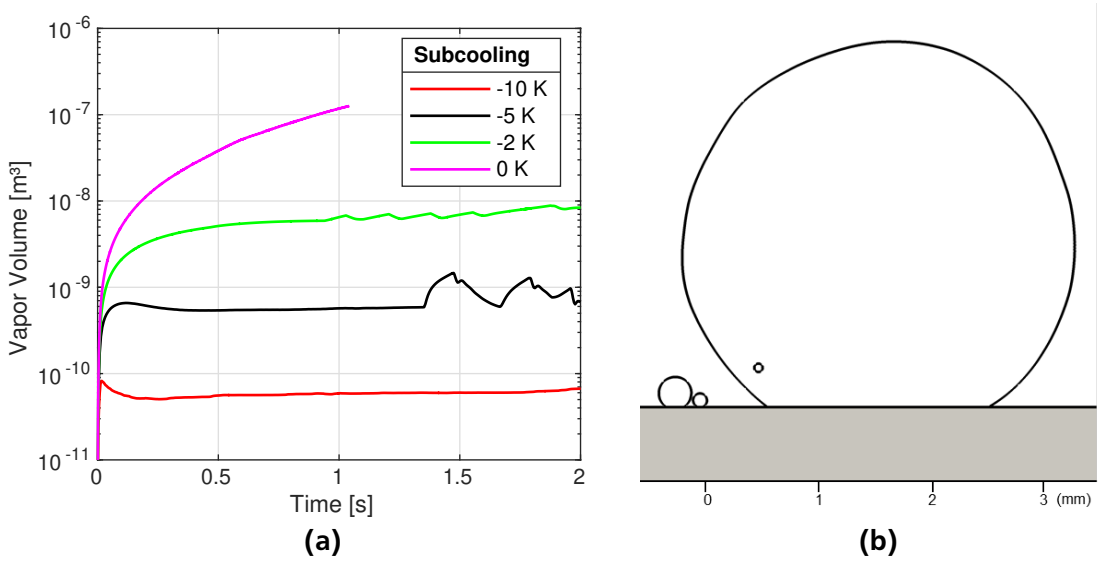

Figure 5.23: (a) Bubble growth for different subcoolings, (b) Phase interfaces for saturated boiling 0.356 s after first nucleation. Left of the major bubble a subsequent bubble has nucleated, on the most left another bubble has been formed from vapor detached during coalescence. Additionally, a liquid droplet has formed inside the major bubble during a merger

and merger is less rapid. The wall temperature is lower compared to the cases of high input heat flux, resulting in longer waiting times between subsequent nucleations. Additionally the very first bubble grows to a volume even larger than in the $2\,W/cm^2$ case, resulting in a faster bubble movement and larger distance to the nucleation site, giving successive or torn off bubbles more space and time to grow until coalescence. In consequence, fewer mergers of larger bubbles can be observed compared to the "feeding" pattern of the high input heat flux cases. Strikingly, during those incomplete mergers liquid can be sucked into the major bubble, forming small droplets, which is depicted in figure 5.23 (b) as an additional interface in the lower left of the larger bubble. The growth and merger of successive bubbles in the saturated boiling case cannot be explicitly noticed in the representation of vapor volume in figure 5.23 (a), because the very first bubble itself never reaches an equilibrium state and grows infinitely. However, the mergers can be observed in the evolution of both contact line and sensible heat flow in figure 5.24 (a) and (b). Every merger results in a rapid decrease of contact line heat flow (e.g. at 0.6 s) due to the disappearance of a relatively large bubble. In the same moment, a steep increase in sensible heat flow can be observed, because right before the merger most part of the evaluated area is covered by the vapor phase of large bubbles, but a relevant part of the evaluated area immediately gets covered by liquid in the moment of coalescence. This effect results in a slight increase of the heat transfer coefficient during mergers in the saturated boiling case (5.24 (d)).

The absolute heat transfer depicted in 5.24 (a) and (b) is of course considerably smaller for high levels of subcooling, because the contact line is shorter and the evaluated area for sensible heat flow is smaller in case of a smaller bubble. However, the heat transfer coefficient clearly increases within the influence zone of a bubble with increasing subcooling. An increase in subcooling appears advantageous for the optimization of heat transfer. Ideally, it should be combined with parameters, which ensure a fast downstream movement of bubbles such as high flow velocity. At the same time, input heat flux or pre-heating time should be adapted in a way, that the wall superheat is sufficient for stable nucleation of successive bubbles. The pursued target must be a high number of small bubbles with sufficient distance to one another not to coalesce.

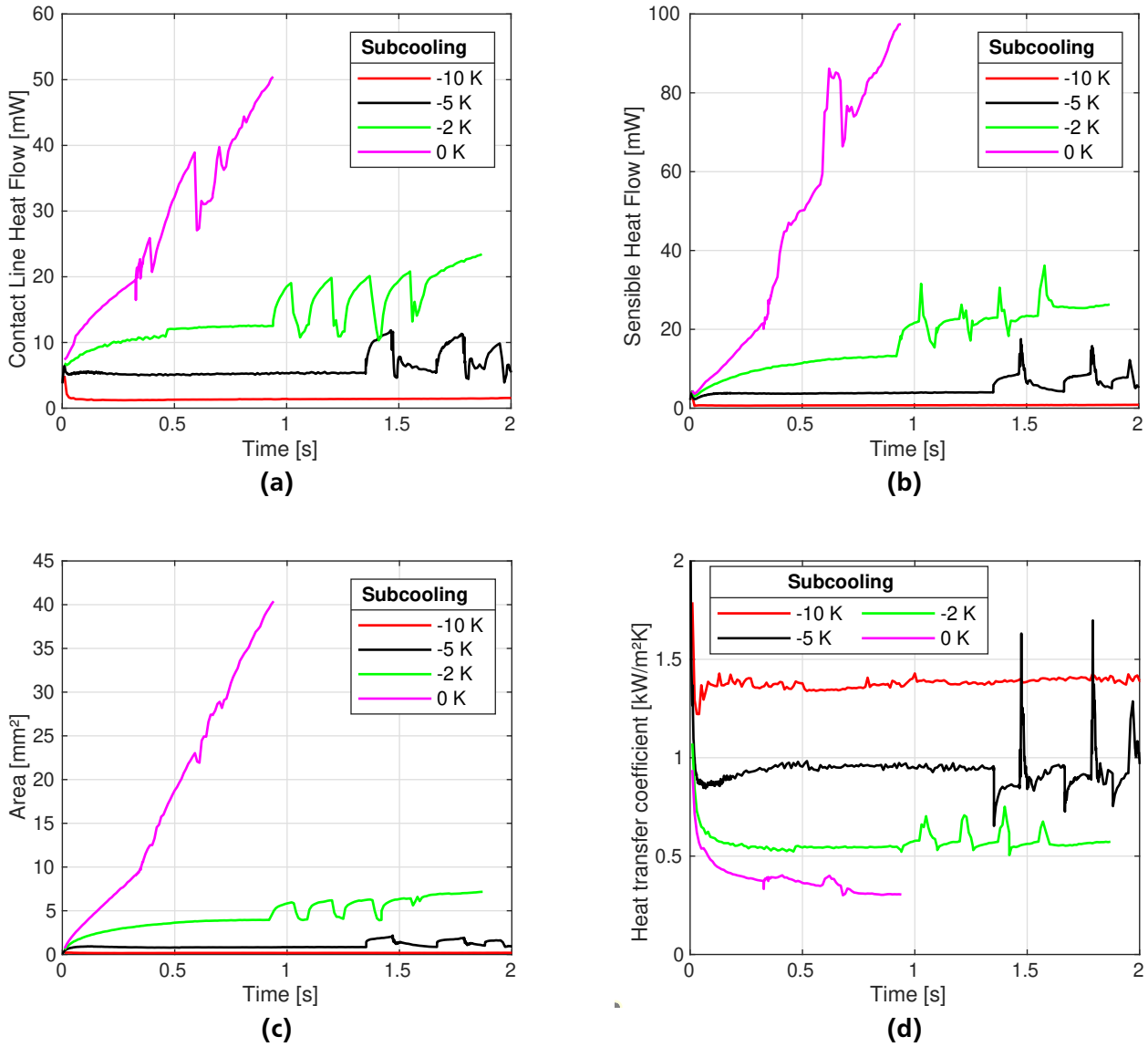

Figure 5.24: Heat transfer characteristics for different subcoolings: (a) Contact line heat flow, (b) Sensible heat flow at the evaluated bi-elliptic area, (c) size of the evaluated bi-elliptic area, (d) Heat transfer coefficient at the evaluated bi-elliptic area

5.2.4 Influence of material properties

In the research of boiling in microgravity the impact of material properties of the boiling fluid as well as those of the solid substrate on the process are of special interest. During the parabolic flight experiments of the Multiscale Boiling project, the low thermal conductivity of the working fluid FC-72 in particular was suspected to be responsible for the different quantitative impact of input heat flux and pre-heating time (see figure 5.17). The impact of the thermal conductivity of the liquid on the boiling process will be discussed in the following section.

Concerning the material properties of the substrate, a series of experiments were carried out in order to determine their impact on the boiling process. Gorenflo evaluated those experiments and derived a

correlation in VDI Wärmeatlas [31], which relates heat capacity and thermal conductivity of the heater material to the heat transfer coefficient. This correlation will be compared to numerical results obtained with the Multiscale Boiling setup in the section after the following one.

An advantage of numerical simulations is their ability to study processes with arbitrary material properties, which do not necessarily have to match those of a real material. This way, a single material property can be varied in order to study its impact on the process while fixing all other properties. It will be shown, that in the framework of the present thesis this advantage is valid only for the finite volume CFD solver, but comes up against borders in the microzone subgrid model used for the determination of contact line heat flow.

Influence of the thermal conductivity of liquid FC-72

In order to verify, if an increased thermal conductivity of the working fluid would reduce the measurable impact between pre-heating time and input heat flux on bubble growth and heat transfer, the thermal conductivity of the liquid phase was varied by the factors 2, 5 and 10 compared to the physical value. This variation was conducted isolated and combined with a variation of input heat flux and pre-heating time, in order to study their interrelation. The variation of parameters is shown in detail in table 5.3. Properties of the vapor phase have not been varied since the thermal conductivity of gaseous FC-72 is around one order of magnitude lower than that of the liquid phase.

	Reference	Variation cases				
$\lambda_{\text{liquid}}[\text{W/(m K)}]$	0.0541	0.1082	0.2705	0.2705	0.541	0.541
$\dot{q}_{\text{in}}[\text{W/cm}^2]$	1	1	1, 1.5, 2	1	1, 1.5, 2	1
Pre-heating time [s]	10	10	10	20	10	20

Table 5.3: Combined variation of the thermal conductivity of the liquid, input heat flux and pre-heating time

Isolated influence of liquid thermal conductivity

Figure 5.25 shows the evolution of bubble growth, heat flow and heat transfer coefficient, respectively, for the isolated variation of liquid thermal conductivity, thus at an input heat flux of $1\,\text{W/cm}^2$ and a pre-heating time of 10 s. The evolution of the evaluated bi-elliptic area will not be presented explicitly in this section, since the boiling process will always be characterized either by a single bubble or by the "feeding" behavior with small bubbles very close to one major bubble, as it is known from the cases of increased input heat flux. Therefore, the evaluated area always strongly correlates with the vapor volume and does not need to be depicted separately. Figure 5.25 (a) shows an increase in bubble growth for an increasing liquid thermal conductivity up to a factor of 5 compared to the actual physical value of $0.0541\,\text{W/(mK)}$. This evolution seems intuitive, since an higher thermal conductivity causes more sensible heat being transferred from the heater to the liquid, which then serves for more evaporation at the bubble hull. Remarkably, if the thermal conductivity is increased further up to ten times the physical value, this evolution reverts and bubble growth gets weaker again. The explanation for this development can be deduced from an analysis of the temperature field around the bubble as shown in figure 5.26. The enhanced heat conduction in the liquid normal to the wall causes the thermal boundary layer between the wall and the subcooled bulk liquid to be thicker, but with a lower gradient normal to the wall. The maximal temperature at the wall and in the vicinity of the bubble foot is therefore lower. If the thermal conductivity is increased, the effect of a thicker thermal boundary layer dominates bubble growth up to

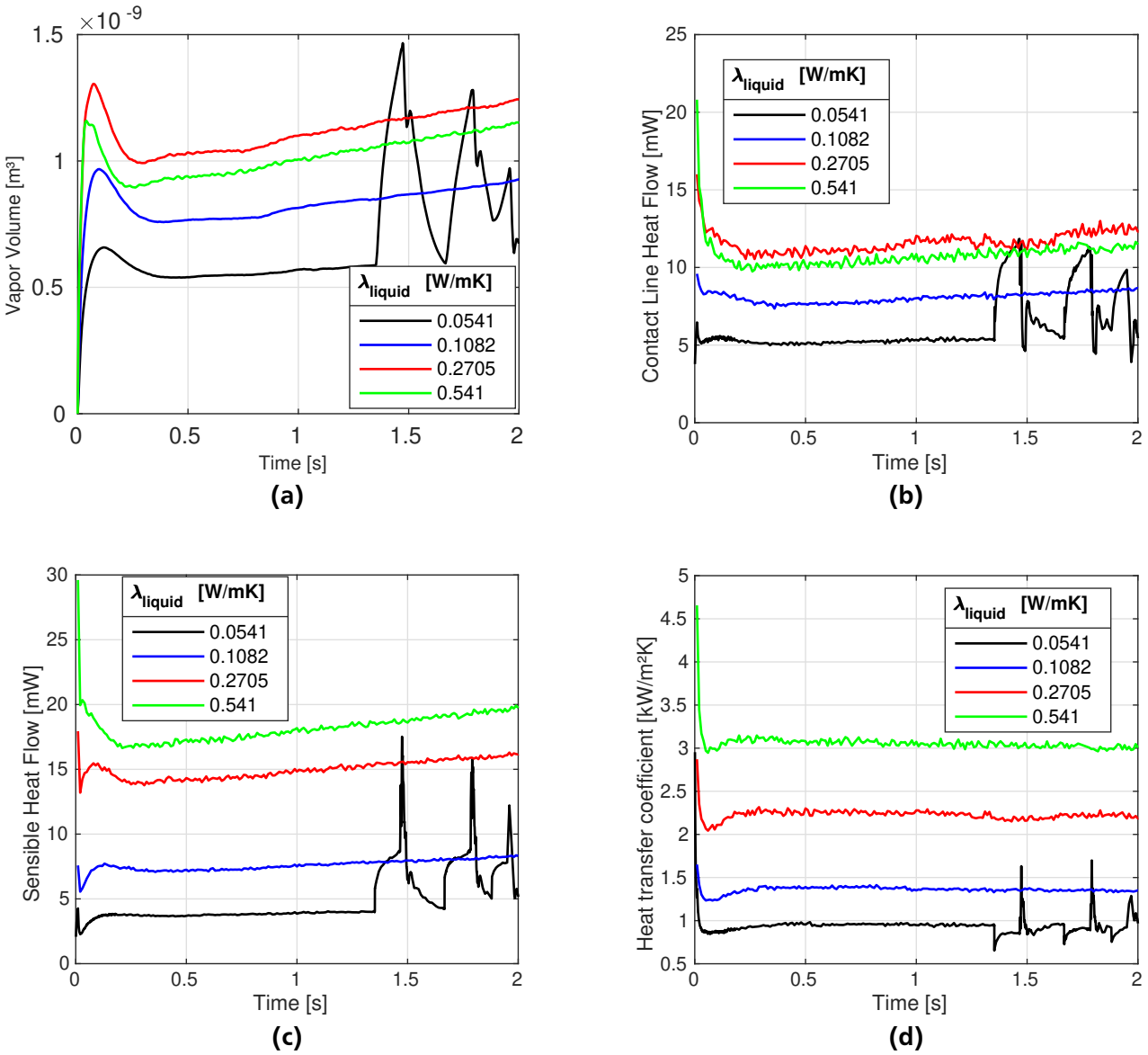

Figure 5.25: Evolution of (a) bubble volume, (b) contact line heat flow, (c) sensible heat flow in the bi-elliptic evaluated area and (d) heat transfer coefficient for the original, double, fivefold and tenfold thermal conductivity in the liquid FC-72 at $\dot{q}_{\mathrm{in}} = 1\,W/cm^2$ and 10 s pre-heating time

a specific level, because a bubble can grow higher until its cap reaches the subcooled zone of the liquid, where condensation at the bubble cap begins. However, above a specific level the lower temperatures within the thermal boundary layer more than counteract this effect and evaporation slows down again. It will be shown, that the quantity of this turning level is not a constant for the working fluid, but is strongly interdependent with other parameters, e.g. input heat flux. Additionally, the overshoot in bubble growth due to the laser power right after the very first nucleation and the following shrinkage of the bubble takes less time for increasing liquid thermal conductivity; a turning level cannot be observed here. This effect can be explained by the temperature field, which reacts more dynamically on a change in input heat flux in case of high thermal conductivity.

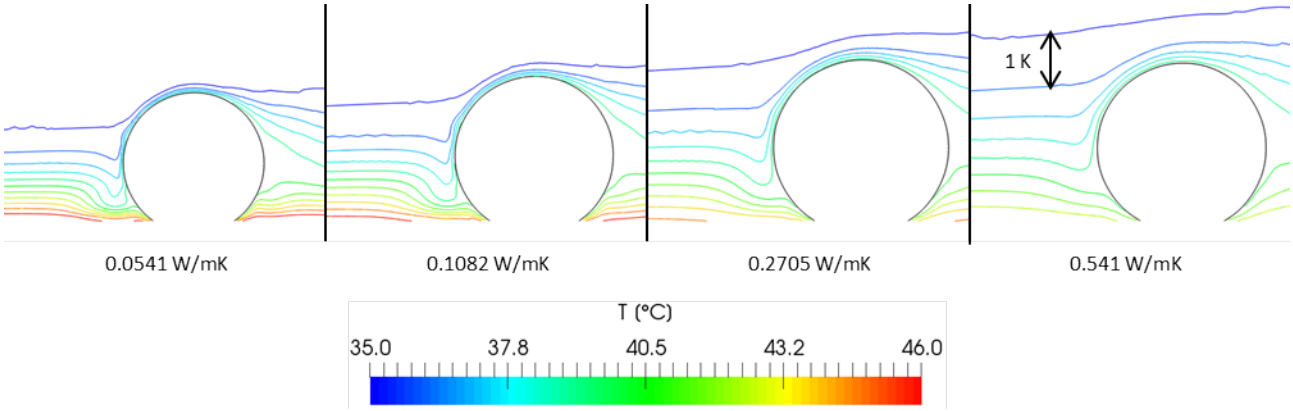

Figure 5.26: Isothermes and liquid-vapor interface for different liquid conductivities at 0.5 s after the very first nucleation

Additionally, for all studied levels of increased conductivity the specified wall superheat criterion necessary for the nucleation of successive bubbles is not reached within the conducted simulation time. Thus, all effects discussed in the following, regarding heat flow and heat transfer coefficient, are only stated for a single bubble populating the heated surface.

Contact line heat transfer (figure 5.25 (b)) shows a strong correlation to the bubble volume and therefore to the length of the contact line. Contact line heat transfer increases for increasing levels of thermal conductivity up to a level of five times the physical conductivity and decreases again for tenfold conductivity due to shorter contact lines and lower wall temperatures. However, the solution of the microzone model is obtained with the unchanged, physical thermal conductivity in all shown cases, because the

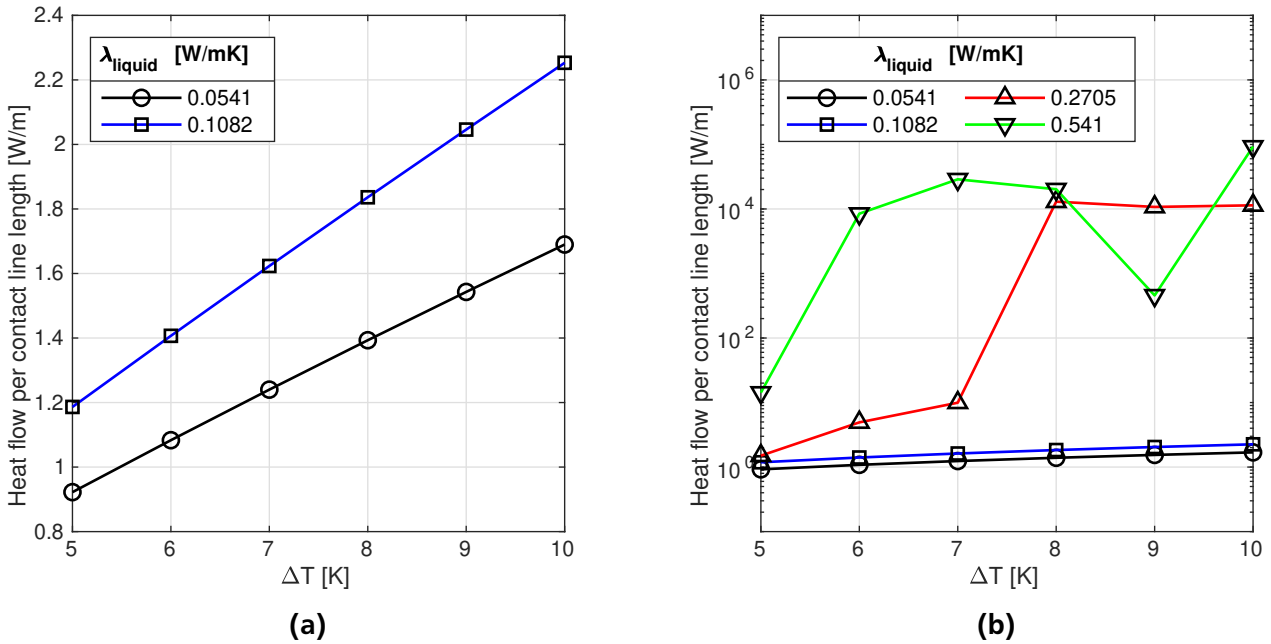

Figure 5.27: Microzone solution for heat flow per contact line length at static contact lines for different liquid thermal conductivities

model does not provide physical solutions, if the thermal conductivity is varied by a factor of 5 or above. As outlined in section 4.4.2, the contact line heat flow is calculated prior to the actual CFD simulations within a subgrid model for a number of wall superheats and contact line velocities. The model reacts considerably sensitive to a change in thermal conductivity alone; i.e. the model does not converge for most evaluated wall superheats and contact line velocities. Figure 5.27 shows the heat transfer results in the microzone for different wall superheats and thermal conductivities. For the sake of simplicity, only results for static contact lines are shown. For an increase in thermal conductivity by a factor of two the model still converges and returns an average increase in heat flow per length unit of contact line by approximately 30 % (figure 5.27 (a)). For a thermal conductivity varied by the factors 5 and 10, the model does not converge for most wall superheats and returns non-physical results for the contact line heat flow. For the sake of comparability, in the CFD calculations the results of the subgrid model for an unchanged thermal conductivity are used for all varied conductivities. Hence, the results shown in 5.25 (b) have a relatively high uncertainty.

In contrast to contact line heat flow, sensible heat flow (figure 5.25 (c)) within the evaluated area does not correlate with bubble volume alone, since no level of increased thermal conductivity shows the discussed turnaround effect. Although the increase in sensible heat flow slows down with increasing levels of thermal conductivity, an increase can be observed until the highest level evaluated. Obviously, for sensible heat flow the higher thermal conductivity weighs out the smaller area on which the heat flow is evaluated. The increase in sensible heat flow results in a higher heat transfer coefficient for an increasing thermal conductivity (see figure 5.25 (d)). It is noticable, that both bubble growth and heat flow do not reach an equilibrium state during the evaluated simulation time of two seconds after the very first nucleation for all cases of increased thermal conductivity. Both are still growing after those two seconds. Nevertheless, in all three cases the heat transfer coefficient on the evaluated area stays almost perfectly constant, which means that the growing heat flows almost exactly outweigh the growing evaluated area at any time.

Combined influence of liquid thermal conductivity, input heat flux and pre-heating time

Following, the influence of increased input heat flux or increased pre-heating time, respectively, at thermal conductivity levels five and ten times the physical value of FC-72 are discussed and compared. Figure 5.28 (a) shows the evolution of bubble growth for different input heat fluxes and pre-heating times at a liquid thermal conductivity five times the physical value. Comparing it to figure 5.17 it is apparent, that for all input heat fluxes and pre-heating times the volume of the very first bubble is increased compared to the original thermal conductivity of the liquid. However, the relative difference in impact of input heat flux on the one hand and pre-heating time on the other hand on bubble growth increases for the higher conductivity: In case of the original liquid thermal conductivity, increasing the input heat flux by factor 1.5 (1.5 W/cm^2) compared to the reference case and increasing the pre-heating time by factor 2 (20 s) have almost the same effect. In case of a thermal conductivity five times higher, the equilibrium volume of the very first bubble is approximately 50 % higher for an input heat flux of 1.5 W/cm^2 compared to 20 s pre-heating time.

For the prolonged pre-heating time, the wall superheat does not reach the set criterion for additional nucleations and no successive bubbles appear. In case of the intermediate input heat flux of 1.5 W/cm^2, successive bubbles start to nucleate and merge with the very first bubble after around 0.6 s. Strikingly, this pattern is not the same to the "feeding" pattern of rapidly nucleating and merging bubbles as it can be observed for 1.5 W/cm^2 at physical liquid conductivity. Instead, the waiting time in between nucleations is longer. After coalescence, the emerged bubble has time to condensate to its equilibrium size. This makes the nucleation and coalescence-pattern more similar to that of the reference case at physical conductivity. However, if the input heat flux is increased even further (2 W/cm^2), the known "feeding"

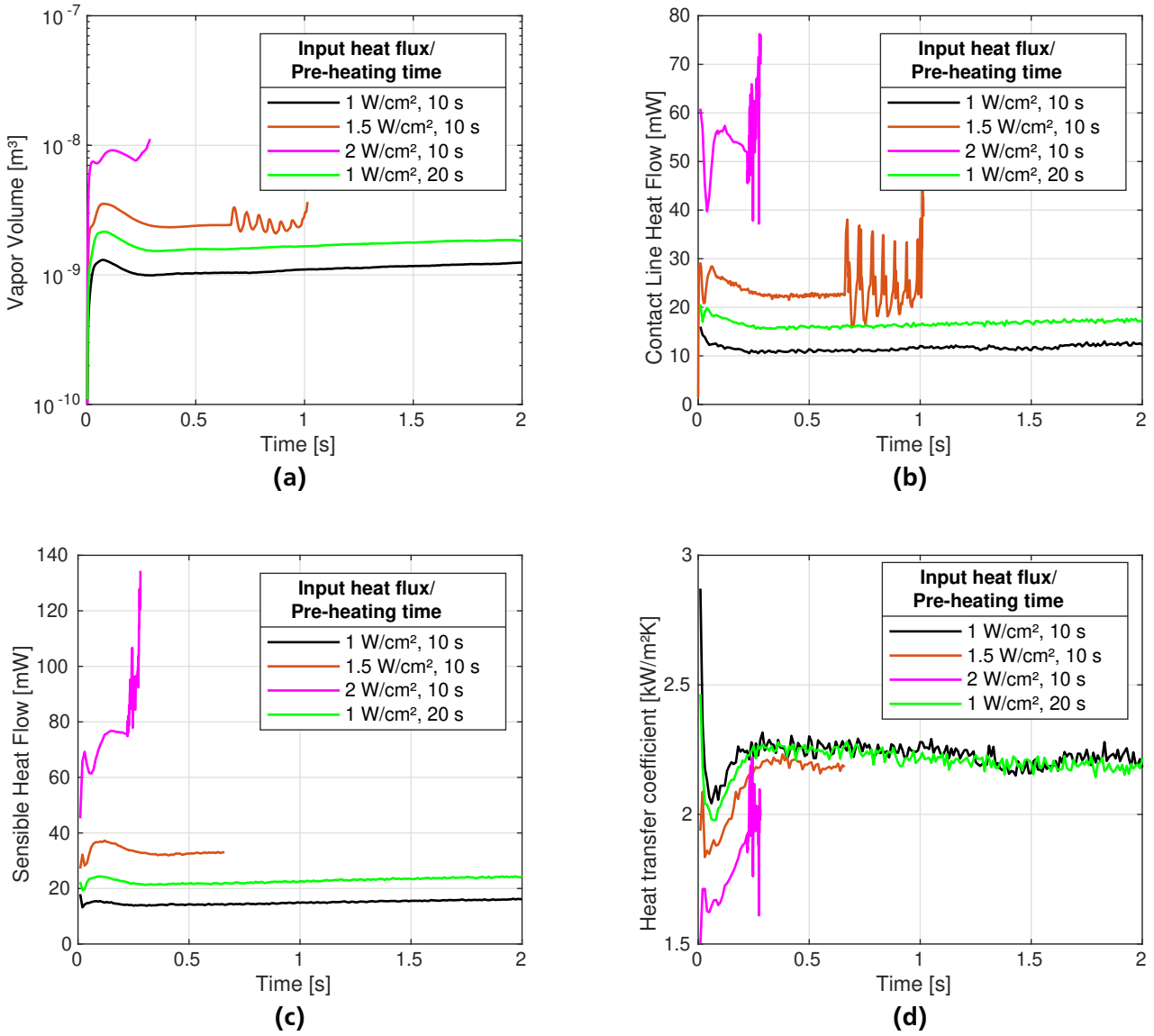

Figure 5.28: Evolution of (a) bubble volume, (b) contact line heat flow, (c) sensible heat flow in the bi-elliptic evaluated area and (d) heat transfer coefficient for thermal conductivity in the liquid FC-72 of 0.2705 W/m K (5 times the physical value) for different input heat fluxes and pre-heating times

process begins and the initial bubble starts to grow above its equilibrium size after approximately 0.3 s.

The evolution of contact line heat flow again correlates strongly with the evolution of bubble size, which in case of the $1.5\,\mathrm{W/cm^2}$ case means that a continuous cycle of increase and decrease can be observed in connection with the steady nucleation and merger of successive bubbles, similar to the observations in the reference case. In the $2\,\mathrm{W/cm^2}$ case, as soon as the cycle of small bubbles feeding the major bubble begins, the oscillations in contact line heat flow due to changing contact line length show a very high frequency and amplitude. However, contact line heat flow in this case is always higher than for cases with lower input heat flux.

A similar tendency can be observed for sensible heat flow. A striking difference between high input heat flux cases with physical liquid conductivity (see figure 5.21) and high input heat flux cases with the increased liquid conductivity is a clear correlation between input heat flux and heat transfer. For physical liquid conductivity no clear difference in contact line or sensible heat transfer between the $1.5\,\mathrm{W/cm^2}$ case and the $2\,\mathrm{W/cm^2}$ case could be observed after the beginning of the rapid nucleation and merging cycle. In case of liquid thermal conductivity five times the physical value, the sensitivity even on a high input heat flux is still observable. With the physical thermal conductivity of the liquid, the larger part of the input heat goes to the substrate due to the strongly deviating thermal conductivity between solid and fluid. In case of the increased liquid conductivity a higher input heat flux causes a significant part of that heat going to the fluid.

The heat transfer coefficient in the influence zone of bubbles does not show a high sensitivity at least for moderate increases of input heat flux or pre-heating time during the phase of only a single bubble present on the heater. Only for the highest input heat flux of $2\,\mathrm{W/cm^2}$ a significantly lower heat transfer coefficient in the vicinity of the very first bubble can be observed due to the large size of that bubble and the low heat transfer below its vapor phase. In this case, strong fluctuations in heat transfer coefficient can be observed as soon as the nucleation of successive bubbles starts.

Figure 5.29 (a) shows the evolution of bubble growth for different input heat fluxes and pre-heating times in case of the thermal conductivity of the liquid being ten times as high as the physical value. In case of the increased pre-heating time, bubble growth is less pronounced than for the combination of prolonged pre-heating time and the liquid thermal conductivity only five times the physical value. In case of the moderately increased input heat flux ($1.5\,\mathrm{W/cm^2}$) no difference in the equilibrium volume of the first bubble can be observed compared to $1.5\,\mathrm{W/cm^2}$ combined with the fivefold liquid thermal conductivity. However, in contrast to the latter no subsequent bubbles nucleate due to a lower wall temperature.

The results on bubble growth show, that an increase in thermal conductivity of the working fluid does not reduce the difference in impact between input heat flux and pre-heating time, as suspected. Quite the contrary, this difference even increases with higher thermal conductivity. Among the examined values for liquid thermal conductivity, up to a factor of five compared to the physical value, bubble growth is enhanced for all studied input heat fluxes and pre-heating times. However, the influence of input heat flux and pre-heating time on bubble growth is even more different than for the physical thermal conductivity. For a very high thermal conductivity of ten times of the physical value, bubble growth even gets weaker again in case of a doubled pre-heating time, while it stays at least constant in case of a moderately increased input heat flux.

For the $1.5\,\mathrm{W/cm^2}$ and tenfold conductivity case, the overshoot in bubble growth due to the power of the laser beam in the very beginning of the observed time period is interrupted by a short phase of bubble shrinkage with a local minimum at around 50 ms. This phenomenon can also be observed for some of the fivefold conductivity cases in figure 5.28, but less pronounced. It is caused by an explosive growth of the initial bubble caused by the combination of high thermal conductivity and high input heat flux. The inertia of the explosive growth drags the bubble upwards, forcing it almost (in case of $1.5\,\mathrm{W/cm^2}$) to detach from the wall, as depicted in figure 5.30. If the bubble does not detach eventually, it strives back towards a spherical shape causing the contact line to grow larger again. This contraction and spreading of the bubble foot can also be retraced in the evolution of contact line heat transfer, see figure 5.29 (b).

For the combination of tenfold thermal conductivity in the liquid and the highest input heat flux of $2\,\mathrm{W/cm^2}$, the explosive bubble growth actually causes detachment from the surface. This confirms prior findings e.g. of Siegel [92], that for a sufficiently fast bubble growth detachment can occur even under

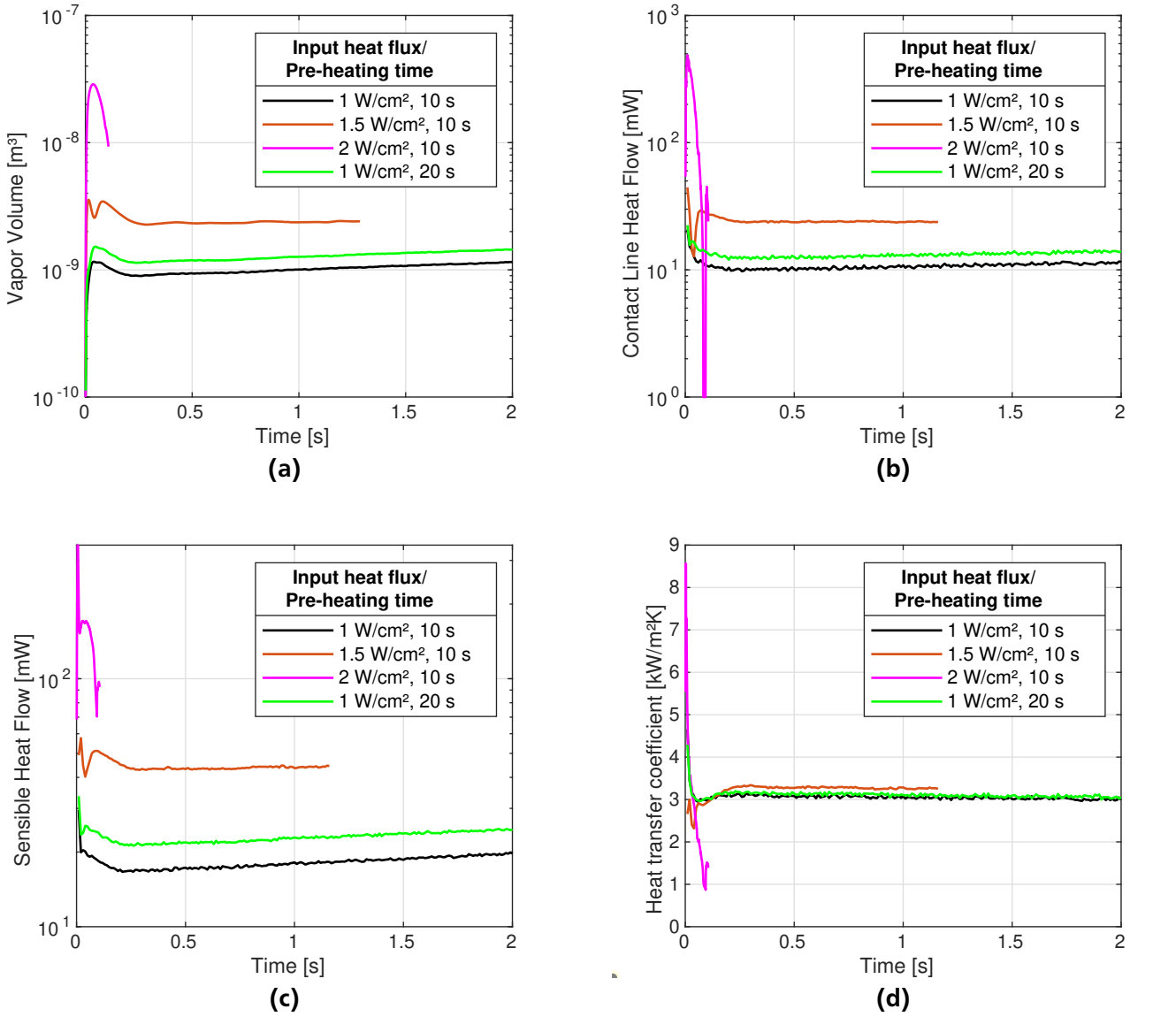

Figure 5.29: Evolution of (a) bubble volume, (b) contact line heat flow, (c) sensible heat flow in the bi-elliptic evaluated area and (d) heat transfer coefficient for thermal conductivity in the liquid FC-72 of 0.541 W/m K (10 times the physical value) for different input heat fluxes and pre-heating times

microgravity conditions purely due to inertial forces. Figure 5.31 shows, how in a first stage of around 10 ms the bubble grows explosively and mostly sidewards and far less upwards. This imbalance in the bubble shape and surface tension force at the interface is then balanced out by a strong upwards impetus, causing the bubble to eventually detach after a little more than 80 ms. After detachment, the very first bubble immediately starts condensating inside the subcooled bulk liquid and a second bubble nucleates. This second bubble shows an explosive growth similar to that of the first bubble and eventually coalesces with the initial bubble detached from the surface. Due to the very high bubble growth rate and the correlated massive increase in cell number caused by the size of the interface, only a short simulation time of few more than 100 ms after the very first nucleation could be established for this case. In future investiga-

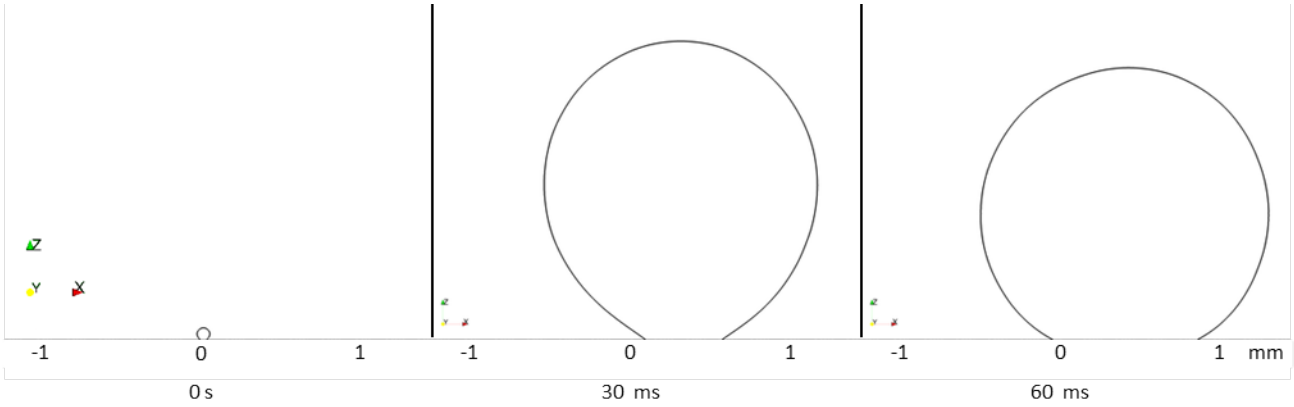

Figure 5.30: Liquid-vapor interface for liquid thermal conductivity of 0.541 W/m K (10 times the physical value) and 1.5 W/cm^2 input heat flux at 0 ms, 30 ms and 60 ms after the very first nucleation

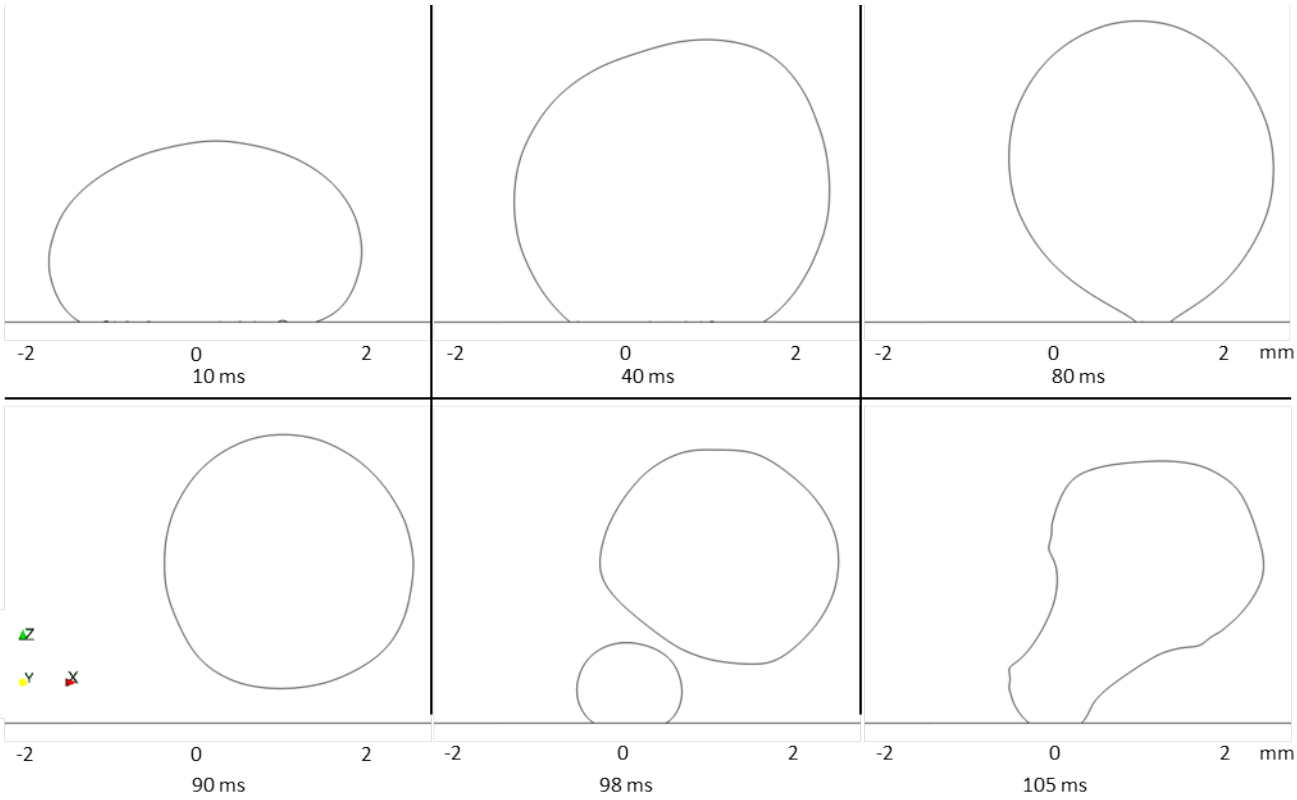

Figure 5.31: Liquid-vapor interface for liquid thermal conductivity of 0.541 W/m K (10 times the physical value) and 2 W/cm^2 input heat flux at the indicated time steps after the very first nucleation

tions it will be very interesting, how similar cases further develop in terms of nucleation and coalescence.

The explosive bubble growth as well as the detachment have a strong impact on contact line heat transfer: Figure 5.29 (b) shows an extraordinary growth in contact line heat transfer in the 0.541 W/m K and 2 W/cm^2 case during the stage of explosive bubble growth. After this very short period, contact line heat transfer decreases to 0 during the detachment period. It then shows a strong increase during the growth period of the second bubble and again a decrease during coalescence. The increase of contact line heat transfer in the growth period of the very first bubble, however, is extremely high even for the

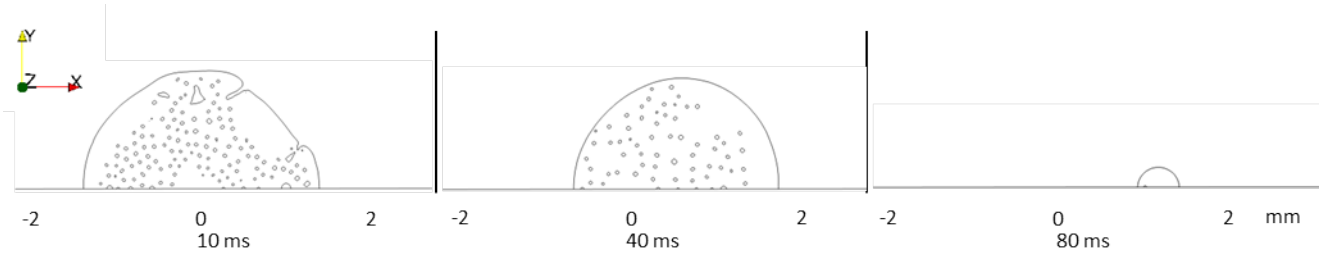

Figure 5.32: Three phase contact line on the heater surface (view from above) for liquid thermal conductivity of 0.541 W/m K (10 times the physical value) and 2 W/cm^2 input heat flux at the indicated time steps after the very first nucleation. Explosive bubble growth causes smearing of the volume fraction field at the wall and extra three-phase contact lines from a numerical artifact

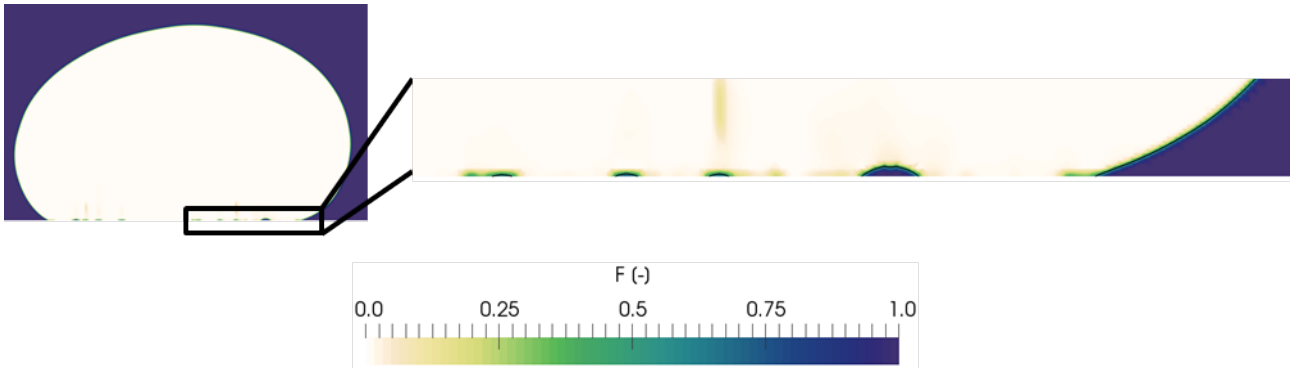

Figure 5.33: Liquid-vapor interface and volume fraction field for liquid thermal conductivity of 0.541 W/m K (10 times the physical value) and 2 W/cm^2 input heat flux at 10 ms after the very first nucleation

observed volume of the bubble and the length of its contact line. This is caused by a numerical issue arising from explosive bubble growth: Figure 5.32 shows the heater surface from above and the contact line during the initial growth period of the bubble. Within the bubble foot several 0.5 iso-lines of the volume fraction field appear on the surface, which the numerical solver interprets as three-phase contact lines of liquid droplets sitting on the heater surface inside the bubble. All of those extra contact lines contribute to the overall contact line heat transfer shown in figure 5.29 (b). The emergence of those extra contact lines is caused by the rapid sidewards growth of the bubble, as depicted in figure 5.31 at 10 ms. Due to the high lateral expansion of the interface, the volume fraction field in the first cell layer above the wall is strongly smeared parallel to the surface, because the contact line does not move with the same velocity. The smeared interface and the resulting 0.5 iso-surface is depicted in figure 5.33. Hence, the extremely high contact line heat flow during the initial 20 ms of that case in figure 5.29 (b) must be considered overrated.

It shall be noted, that a reduction in size and density of those artificial droplets on the surface can be observed between their emergence until bubble detachment. However, the droplets do not completely evaporate. Since the volume fraction is smeared, it is $0.5 < F < 1$ inside the reconstructed interfaces in the vast majority of grid cells. The cutoff value $F_0 = 0.1$ in equation 4.20 causes, that the mass sources and sinks resulting from phase change in an interface cell are distributed only to liquid cells of $F > 0.9$. This means, that in most of the artificial droplets no mass sink term resulting from the contact line heat flow can be imposed. Nevertheless, global liquid and vapor mass conservation is ensured by the normal-

ization coefficients determined in equations 4.21 and 4.22, meaning that the lack of liquid mass sink in an area of strongly smeared F-field is compensated by a larger liquid mass sink in the vicinity of other interface containing cells, e.g. at the hull of the major bubble. However, several artificial droplets do not perish by evaporation alone, but only during the detachment phase of the major bubble, and therefore contribute to the overall contact line heat flow longer, than they should actually exist.

Furthermore, the sensible heat flow 5.29 (c) during the first 20 ms has a large uncertainty, as well, due to the increased sensible heat flow from the wall to the liquid droplets, which represent a numerical artifact. Therefore, the resulting heat transfer coefficient 5.29 (d) of the $2\,\mathrm{W/cm^2}$ case must be considered overrated during the initial growth phase. However, its strong decrease connected to the detachment process of the initial bubble and the following increase due to the emergence of a successive bubble appear physical.

Apart from this case, which is an exception due to the detachment of the initial bubble, the heat transfer coefficient in case of the tenfold liquid thermal conductivity strives towards similar values during the equilibrium stage of the initial bubble for all investigated input heat fluxes or pre-heating times.

Influence of solid thermal conductivity and heat capacity

After the impact of the thermal conductivity of the working fluid on bubble growth and heat transfer has been studied, the influence of the substrate's material properties are investigated, as well. Analyzing a vast set of pool boiling experiments, Gorenflo [31] has deducted an empirical formulation to predict the heat transfer coefficient of an arbitrary fluid/wall material pair in relation to a reference:

$$\frac{\alpha}{\alpha_0} = C_\mathrm{q}\, C_\mathrm{p}\, C_\mathrm{w} \tag{5.11}$$

α_0 is the heat transfer coefficient of a specific fluid at a reference state, which theoretically can be chosen freely. On the right hand side there are three dimensionless numbers, which quantify the impact of input heat flux, system pressure and wall properties, respectively, on the heat transfer coefficient α relative to the reference state. This reference state is characterized by an input heat flux of $2\,\mathrm{W/cm^2}$, a system pressure 0.1 times the critical pressure of the working fluid, and a copper pipe with arithmetic mean deviation of 0.4 µm as boiling substrate. The majority of experimental results on pool boiling, which Gorenflo analyzed, were obtained with copper as boiling substrate, which is why it serves as reference material in his formulation. Regarding the influence factor of the wall, C_w is further split into

$$C_\mathrm{w} = C_\mathrm{w,R}\, C_\mathrm{w,M}, \tag{5.12}$$

with $C_\mathrm{w,R}$ representing the influence of surface roughness and $C_\mathrm{w,M}$ that of the material. The latter is further formulated as:

$$C_\mathrm{w,M} = \left(\frac{\lambda\rho c}{(\lambda\rho c)_\mathrm{cu}}\right)^{0.25} \tag{5.13}$$

$(\lambda\rho c)_\mathrm{cu}$ represent the thermal conductivity, the density and the specific heat capacity of the copper pipe of the reference state. The relationship between the heat transfer coefficient and the material properties of the substrate can thus be reformulated as:

$$\alpha \propto (\lambda_\mathrm{s}\rho_\mathrm{s}c_\mathrm{s})^{0.25} \tag{5.14}$$

	Reference	Variation cases			
λ_s [W/(m K)]	10.9	5.45	2.18	1.09	10.9
c_s [J/(kg K)]	410	410	410	410	205

Table 5.4: Variation of the thermal conductivity and heat capacity of the solid substrate

In the following section, the impact of the thermal conductivity of the heater substrate in the Multiscale Boiling framework on bubble growth and heat transfer will be studied in detail by reducing it to 50 %, 20 % and 10 % of its original physical value (see table 5.4). Furthermore, the impact of the specific heat capacity reduced to 50 % will be evaluated in order to check, if thermal conductivity and heat capacity really have the exactly same impact, as predicted by equation 5.14. Since the volumetric heat capacity of a material is represented by ρc, studying the impact of density would be redundant and is therefore not executed. The results of this study will be compared to Gorenflo's prediction outlined above. Beforehands it must be noted that in the present study the method used to determine the heat transfer coefficient is different from that in Gorenflo's meta-study:

- In the experiments evaluated by Gorenflo, the heater surface is covered by multiple bubbles, thus the heat transfer coefficient is evaluated for the whole surface.
- Contrarily, in the present study the heat transfer coefficient in the vicinity of few, isolated bubbles is determined. The evaluated area changes over time.
- Gorenflo averages the heat transfer coefficient over a long time span and obtains a result for a quasi steady-state.
- Contrarily, in the present study the heat transfer coefficient is obtained in specific time steps, when the system is still heating up and not yet in a steady state.

Another crucial difference between the experimental setups is, of course, that the Multiscale Boiling experiments take place in a microgravity environment. Hence, any change, which causes e.g. an increase in bubble growth, will most probably lead to a lower heat transfer coefficient underneath the bubbles, because a higher share of the evaluated area is covered by the vapor phase. In contrast, a change leading to enhanced bubble growth in experiments under earth gravity conditions will cause faster detachment of a single bubble, a higher bubble frequency and perhaps a higher density of bubbles on the heated surface. The consequence for the heat transfer coefficient is hard to predict in this case.

Figure 5.34 (a) shows the bubble growth for all varied thermal conductivities and heat capacities of the substrate. It is apparent, that with decreasing solid thermal conductivity, the volume of the very first bubble increases significantly. This phenomenon is caused by a more uneven temperature distribution throughout the substrate and a higher temperature gradient normal to the heated surface. This causes higher temperatures near the solid-fluid boundary and within the thermal boundary layer in the liquid, as depicted in figure 5.35. Furthermore, a higher share of the input heat flux goes towards the fluid due to lower thermal conductivity in the solid. As soon as the very first bubble gives space at the nucleation site, the known "feeding"-pattern of bubbles rapidly nucleating and merging with the very first one begins and the bubble volume grows beyond its equilibrium size.

For solid heat capacity decreased to 50 %, an increase in bubble volume even higher than in the 50 % solid thermal conductivity case can be observed. Apparently, the impact of heat capacity and thermal conductivity of the solid on bubble growth is not the same. For reduced solid heat capacity, the temperature distribution in the substrate is very uniform, similar to the reference case, but with higher

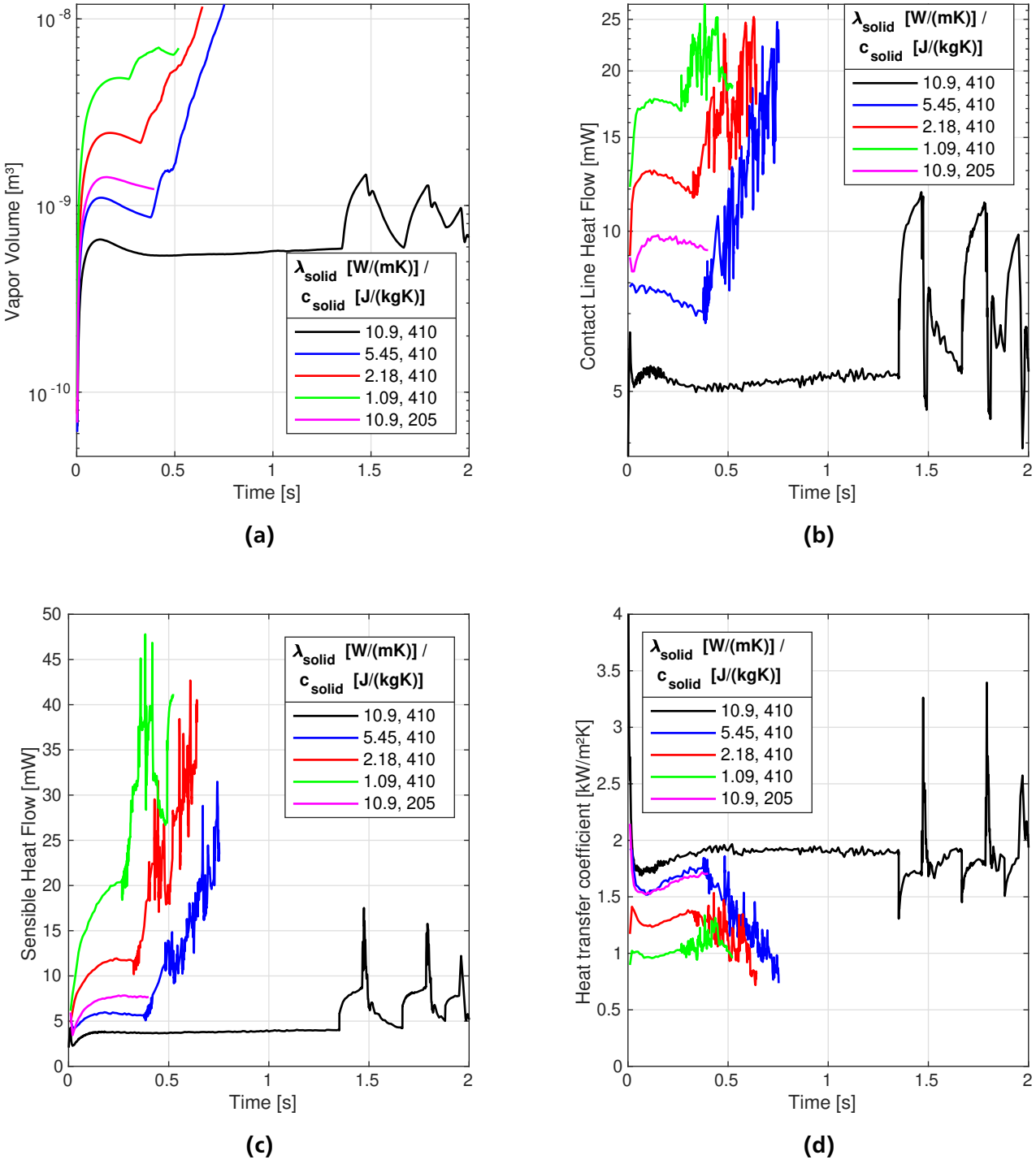

Figure 5.34: Evolution of (a) bubble volume, (b) contact line heat flow, (c) sensible heat flow in the bi-elliptic evaluated area and (d) heat transfer coefficient for the original, 50 %, 20 % and 10 % thermal conductivity and 50 % heat capacity of the solid substrate

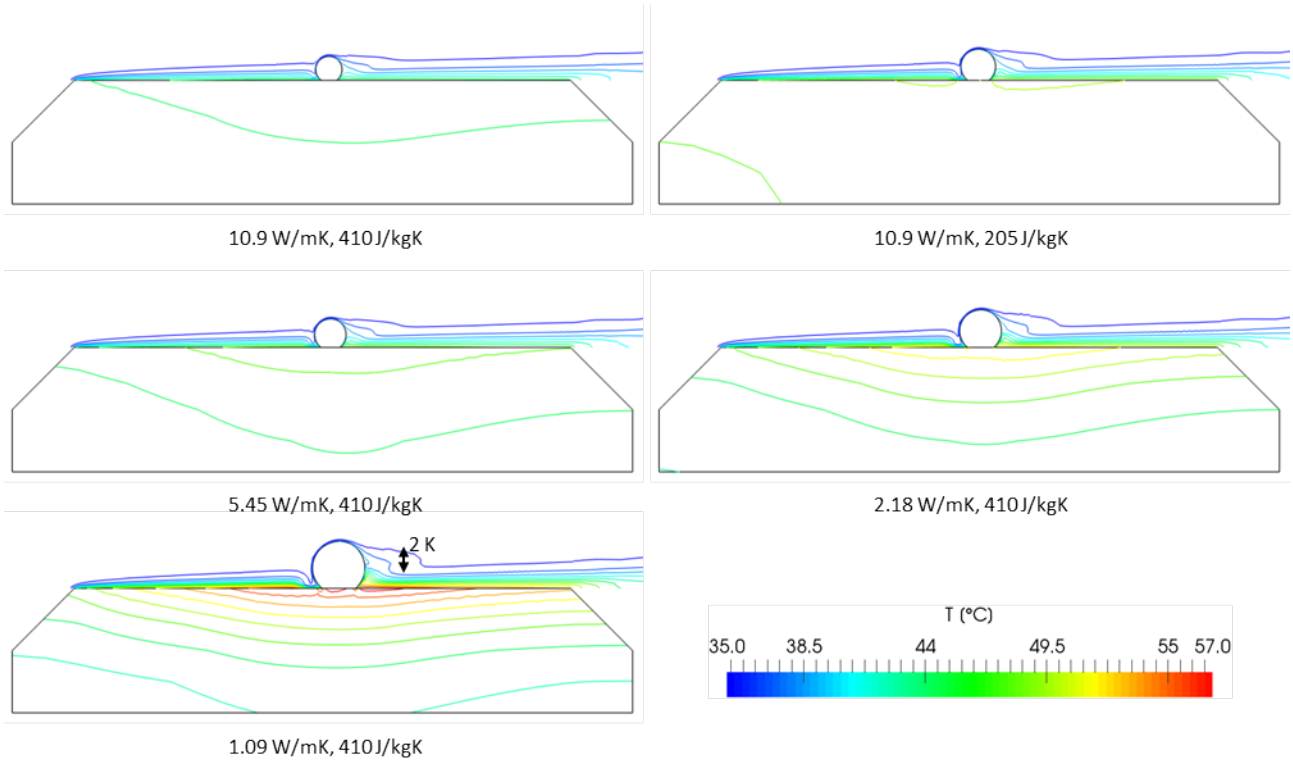

Figure 5.35: Isothermes, liquid-vapor interface and outline of the solid substrate for different thermal conductivities and heat capacities of the substrate at 0.2 s after the very first nucleation

temperatures throughout the whole substrate (see figure 5.35). At the solid-fluid boundary and in the thermal boundary layer higher temperatures can be observed than in the 50 % solid thermal conductivity case. Since the temperature gradient between the solid-fluid boundary and the subcooled bulk liquid is higher than the gradient to the substrate, a higher share of the input heat flux goes to the fluid than in the reference case, causing enhanced bubble growth.

Both contact line and sensible heat transfer (figure 5.34 (b) and (c)) show a strong correlation to the bubble size during the presence of a single bubble. As soon as the pattern of rapid nucleation and coalescence begins, in all cases both types of heat flow show a growing tendency with very strong fluctuations due to the strong bubble dynamics due to growth and coalescence.

The resulting heat transfer coefficient deserves a special evaluation. Figure 5.34 (d) shows a decreasing heat transfer coefficient for a decreasing thermal conductivity of the substrate during the presence of a single bubble. Qualitatively, this matches the prediction of equation 5.14. Furthermore, despite strong differences in bubble growth, heat transfer and temperature field, the cases of halved thermal conductivity and heat capacity show almost exactly the same development, which is a good qualitative agreement with equation 5.14, as well. Table 5.5 shows the quantitative deviation of the heat transfer coefficients at 0.2 s after the very first nucleation from its prediction. The predicted values α_{predict} are given by $\alpha_{\text{reference}} \cdot 0.5^{0.25}$, $\alpha_{\text{reference}} \cdot 0.2^{0.25}$, $\alpha_{\text{reference}} \cdot 0.1^{0.25}$ for one of the material properties reduced by the factors 0.5, 0.2 and 0.1, respectively. In all studied cases the deviation of the heat transfer coefficient from its prediction is not more than 8 %. At least for a system with a single bubble in the first phase after the very first nucleation, the simulation results match very well with the empirical approach by Gorenflo [31] on the impact of solid material properties on the heat transfer coefficient.

	α[kW/(m^2 K)]	α_{predict}[kW/(m^2 K)]	Deviation
Reference	1.79		
$c_{\text{solid}} \cdot 0.5$	1.59	1.51	5 %
$\lambda_{\text{solid}} \cdot 0.5$	1.63	1.51	8 %
$\lambda_{\text{solid}} \cdot 0.2$	1.29	1.2	7.5 %
$\lambda_{\text{solid}} \cdot 0.1$	1	1.01	1 %

Table 5.5: Heat transfer coefficient at 0.2 s after the very first nucleation for different thermal conductivities and heat capacities of the solid substrate and its deviation from the prediction given by equation 5.14

In the following nucleation and coalescence mode, the difference in heat transfer coefficient between the different reduced thermal conductivities blurs and is not that distinct anymore. In the 50 % and 20 % cases, the heat transfer coefficient shows a decreasing tendency with increasing bubble volume, which is in agreement with other cases of this work showing extensive bubble growth. However, due to the large fluctuations caused by the hydrodynamics of coalescence and torn off vapor, the curves coincide partly and the difference between the cases is not that clear anymore.

5.3 Comparison of simulations with the experiments

Two of the experiments, which were conducted throughout the Multiscale Boiling project on the ISS, have been picked out to be reproduced numerically in order to compare experimental and numerical results. One pool boiling experiment and one flow boiling experiment were chosen. The numerical setup follows the steps outlined in section 5.1. At the time, when the present thesis was written, no reliable experimental data of the temperature field at the heater surface was available. The IR camera must have had a calibration shift and provided non-physically low temperatures. Therefore no temperature data is compared and the validation focuses on the comparison of the bubble diameter between simulation and experiment. The evaluation of the bubble diameter in the experiments is conducted from the black-and-white images as explained in section 3.2.

Figure 5.36 (b) shows a black and white image from a pool boiling experiment, figure 5.36 (a) shows the experimental and numerical results on the bubble equivalent diameter. The system pressure in this run is $p = 0.5$ bar, the corresponding saturation temperature is $t_{\text{sat}} = 37.7\,°\text{C}$, the subcooling is -5 K, the input heat flux in the vicinity of the nucleation site is $\dot{q}_{\text{in}} = 1.23\,\text{W/m}^2$ and the pre-heating time is 5 s. The laser beam is turned on for 20 ms with a laser power of 177 mW.

From figure 5.36 (a) it is apparent, that the bubble diameters are matching for a short time span after nucleation but diverge strongly afterwards. In the experiment the bubble grows continuously even after the laser is turned off. Until the end of the investigated time period, no equilibrium between evaporation at the bubble foot and condensation at the bubble cap is achieved in the experiment.

In the simulation the bubble shrinks after the laser beam is turned off, stays at an equilibrium size for almost a second and eventually starts growing again, when the wall temperature has further increased. Apparently, the temperature of the wall and the thermal boundary layer in the fluid is not sufficiently high at the end of the pre-heating time to serve for stable bubble growth in the simulation. At least additional 1 s of pre-heating time or a higher input heat flux are needed for a temperature distribution in the wall and in the thermal boundary layer to serve for additional bubble growth. In contrast, in the experiment the temperature distribution in the liquid thermal boundary layer and in the wall must be

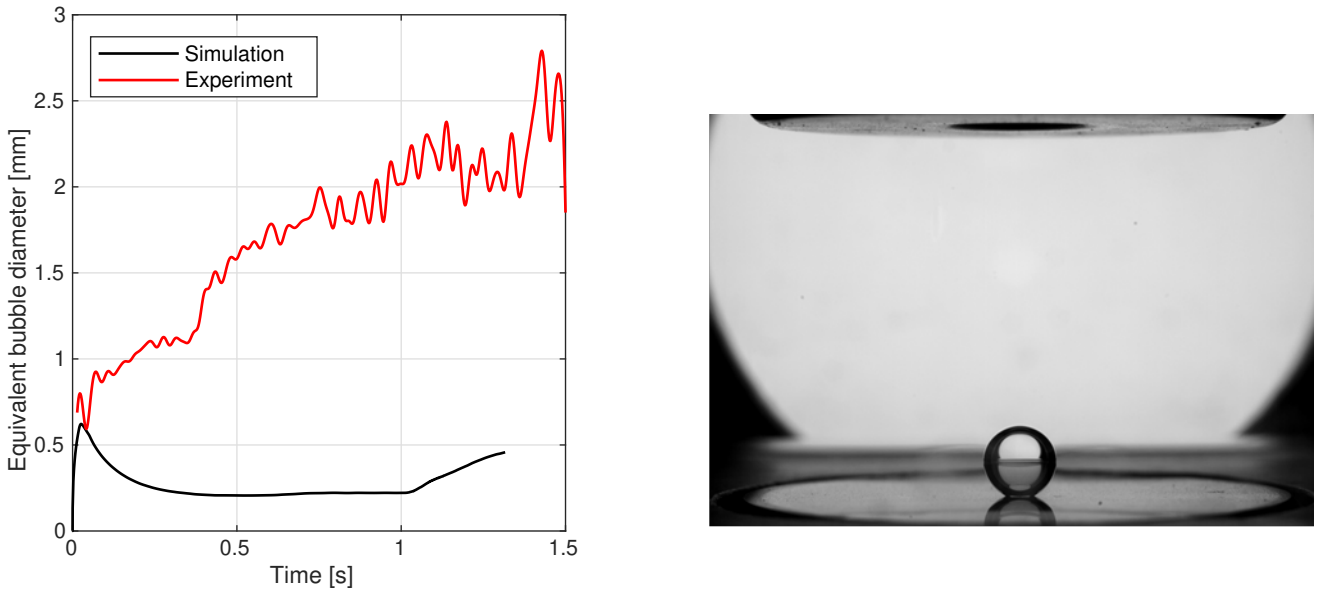

(a) (b)

Figure 5.36: (a) Numerical and experimental results of a pool boiling case with $p = 0.5$ bar / t_{sat} = 37.7 °C, -5 K subcooling, $\dot{q}_{in}$ = 1.23 W/m^2, 5 s pre-heating time, (b) black and white image from experiment 1 s after nucleation

sufficient for constant bubble growth after the set 5 s of pre-heating time.

Figure 5.37 shows the black and white image and the experimental and numerical results of the bubble equivalent diameter of a flow boiling run with an additional sensitivity study in the numerical investigation. The varied parameters of the sensitivity study are the flow velocity, the input heat flux and the wall temperature $\Delta T_{w,0}$ at the beginning of the pre-heating time. The latter variation is based on the assumption, that during the waiting time in between experimental runs the wall temperature might not completely decrease to the temperature of the subcooled bulk again, leaving the wall temperature higher than the bulk temperature at the beginning of a run. Due to the lack of experimental temperature data at the heater surface, the validity of this assumption could not be finally assessed. The varied parameters are given in table 5.6. In the unvaried numerical simulation based on the nominal parameters of the experimental run, the system pressure is $p = 0.5$ bar, the corresponding saturation temperature is set to $t_{sat} = 37.7$ °C, the subcooling is -5 K, the input heat flux in the vicinity of the nucleation site is $\dot{q}_{in} = 1.23$ W/m^2 and the pre-heating time is 5 s. The volume flow through the boiling cell is 0.3 l/min.

	u_{max} [m/s]	$\dot{q}_{in}$[W/cm^2]	$\Delta T_{w,0}$ [K]
Unvaried	0.03	1.23	-5
High velocity	0.037	1.23	-5
Low velocity	0.022	1.23	-5
High heat flux	0.03	1.5	-5
$\Delta T_{w,0} = 1$ K	0.03	1.23	1
$\Delta T_{w,0} = 3$ K	0.03	1.23	3

Table 5.6: Parameter variation in simulation of flow boiling experiment with $p = 0.5$ bar / t_{sat} = 37.7 °C, -5 K subcooling, $\dot{q}_{in} = 1.23$ W/cm^2, 5 s pre-heating time, 0.3 l/min volume flow

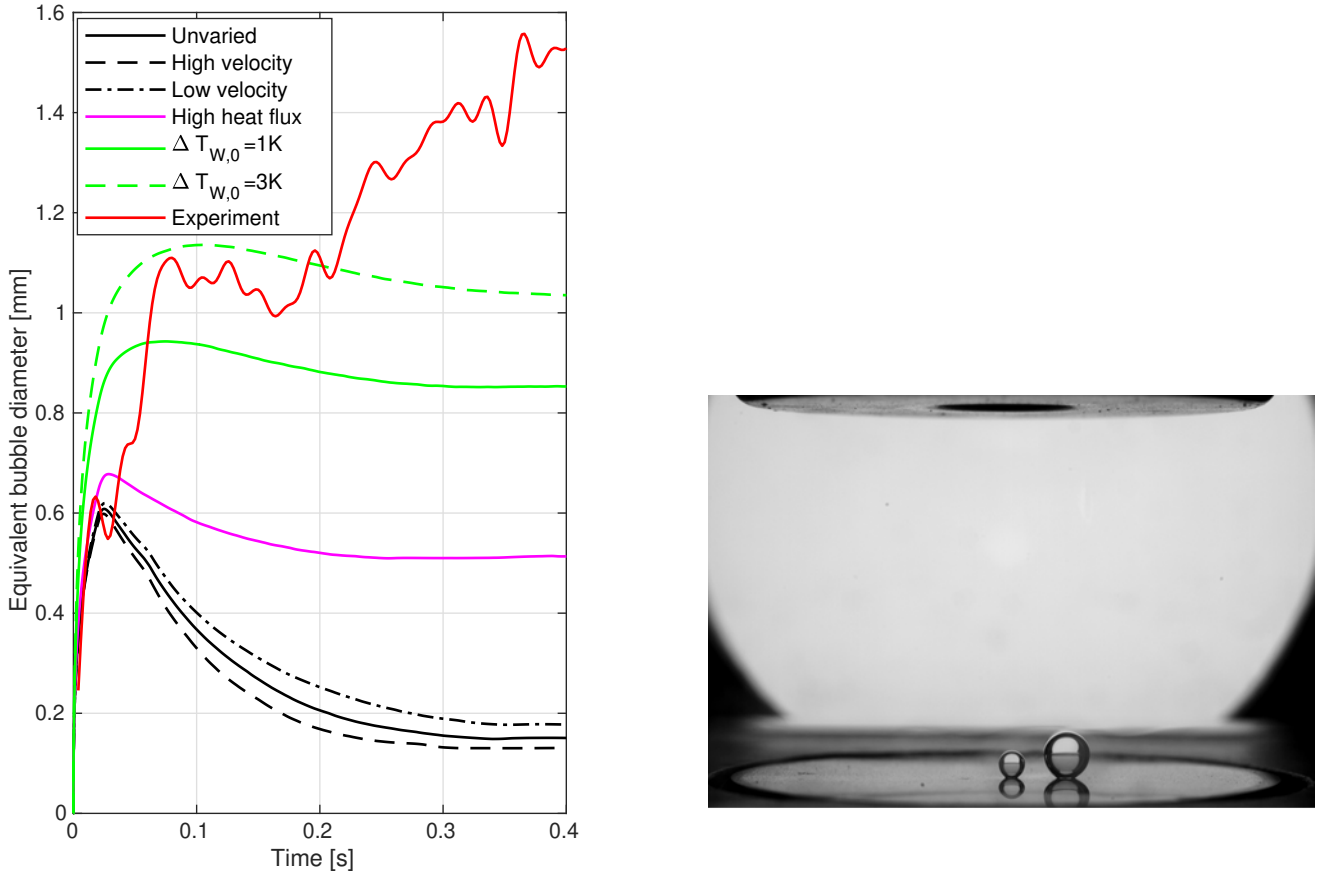

(a) **(b)**

Figure 5.37: (a) Numerical and experimental results of a flow boiling case with $p = 0.5$ bar, -5 K subcooling, $\dot{q}_{\text{in}} = 1.23\,\text{W/m}^2$, 5 s pre-heating time, 0.3 l/min volume flow, parameter variation in simulation according to table 5.6, (b) black and white image from experiment 400 ms after nucleation

Again, the laser beam is turned on for 20 ms with a laser power of 177 mW. Apparently, in the unvaried simulation case, represented by the black line, the deviation to the experimental result is very large again.

There are a number of possible reasons for the divergence of the experimental and numerical results in both the pool boiling and the flow boiling case, some of which will be discussed in the following:

- Non-condensable gases might be solved in the fluid, lowering its saturation temperature.
- The form of the flow profile inside the channel is not clear. The thermal boundary layer above the heater could be altered by a velocity profile deviating from the assumed profile in the simulations, leaving a larger part of the bubble surrounded superheated liquid.
- The maximum velocitiy in the vicinity of the nucleation site has an uncertainty of approximately 20 %.
- The growth of the bubble out of the cavity during nucleation may impact the thermal boundary layer above the wall, as well.

- The system might not be isothermal at the beginning of the pre-heating time, meaning the wall might have a higher temperature than the subcooled bulk liquid.
- The heat flux produced by the electrical resistance heater has an uncertainty of approximately 20 %.
- The wall superheat criterion for subsequent bubbles in the simulation might be too high or other reasons might cause additional bubbles in the experiment, which do not appear in the simulation.
- The wall temperature at the end of the pre-heating time might be underestimated in the simulation.

Besides the listed unpredictabilities, it has been shown in section 5.2.3, that a lowering of the subcooling level causes larger bubble volumes and and earlier nucleations of subsequent bubbles in the simulations. However, the temperature of the bulk fluid and thus the subcooling level does not appear to come with a considerable uncertainty in the experiment.

The presence of non-condensables cannot be investigated numerically within the present work and must be examined experimentally in the future. The liquid flow in the boiling cell was investigated by Behle [6], who showed, that the flow profile over the channel height $u(z)$ is in very good agreement with the analytical prediction of an ideal Poiseuille flow in a rectangular channel (see eq. 5.1). However, he also found, that the velocity in main flow direction is not uniform over the channel width, but instead an oscillating velocity profile $u(y)$ exists. The reason for this behavior is found in the presence of a Dean vortex in the flow channel, caused by the design of the preheater before the inlet port of the boiling cell. It has to be further investigated, in which way the thermal boundary layer is affected by this uneven velocity profile. The growth of the bubble out of the cavity and its impact on the thermal boundary layer have been examined numerically and will be discussed in section 6.1, see figure 6.8. It will be shown, that the flow caused by the rapid bubble growth inside the cavity at least influences the shape of the strongly superheated thermal boundary layer caused by the laser beam within the first few milliseconds after nucleation. Most probably, further bubble growth also impacts the rest of the thermal boundary layer originated during pre-heating time. Modeling the nucleation process in the boiling cell simulations by manipulating the volume fraction field proofs disadvantageous, since the impact of nucleation on the thermal boundary layer is neglected this way.

In order to study the sensitivity of the process to the parameters flow velocity, input heat flux and initial wall superheat, those parameters are varied in the simulation of the flow boiling experiment (table 5.6). The results of that sensitivity study are depicted in figure 5.37 (a).

The influence of the flow velocity on the process is apparently small. Increasing the heat flux causes a significantly larger diameter of the initial bubble, but the discrepancy to the experiment is still large. An increase in initial temperature of the wall has a bigger impact and in case of 3 K superheat at the beginning of the simulation the bubble diameters are in relatively good agreement during the first 200 ms after nucleation. However, in all simulations no successive bubbles appear, which is a significant qualitative difference to the experiment and suggests, that the superheat criterion for the nucleation of successive bubbles in the simulation might be too large. Additionally, the sequence of black and white images in figure 5.38 shows an interesting phenomenon occurring in the experiment. The very first bubble detaches from the wall due to inertia after rapid evaporation inside the cavity. This effect has been observed multiple times in the simulations of the nucleation process from the Multiscale Boiling cavity (see section 6.1), as well. The detached bubble then coalesces with a cycle of 19 subsequent bubbles immediately nucleating at the cavity and moves downstream. When it finally attaches to the wall again after approximately 140 ms, it has moved sufficiently downstream to give space for stable growth of a second

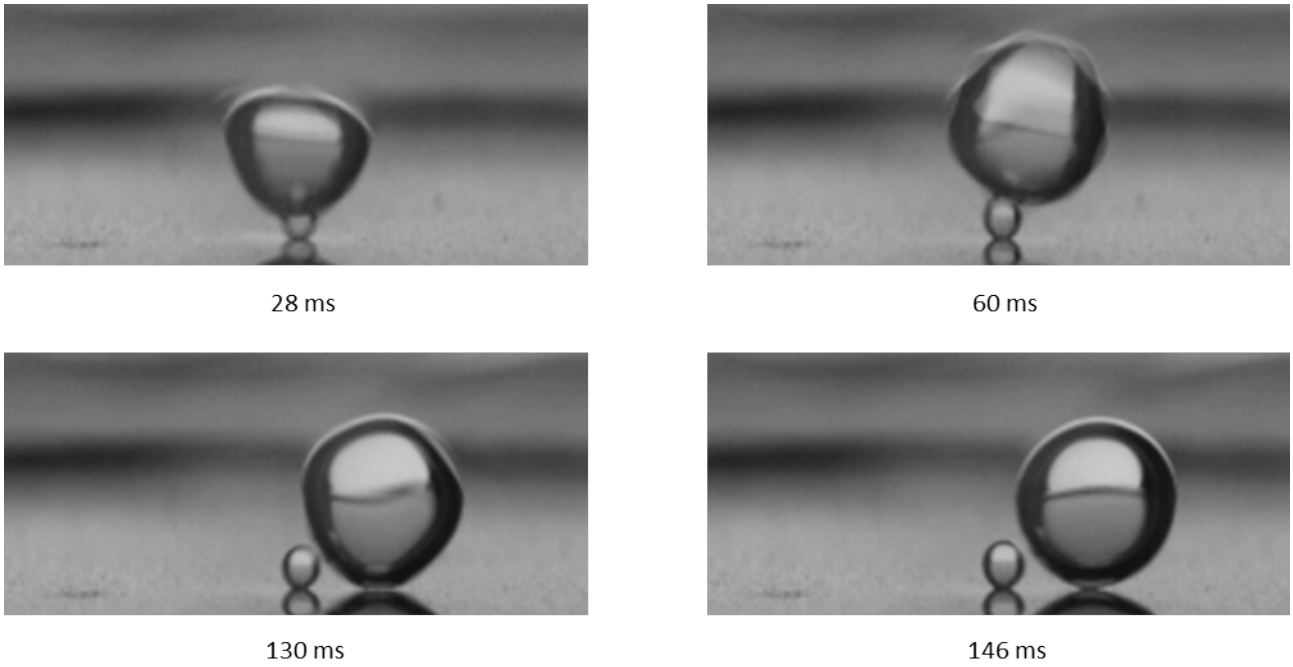

Figure 5.38: Nucleation in the experiment of the investigated flow boiling case. The very first bubble detaches from the wall due to inertia after rapid evaporation inside the cavity and gets fed by a series of 19 successive bubbles nucleating from the cavity while hovering above the surface. During this growth process, the first bubble moves downstream and when it attaches to the wall again after 140 ms, it has a sufficient distance for a second bubble to stably grow at the nucleation site

bubble. Thus, the equivalent diameter of the experimental bubble shown in figure 5.37 actually combines the volume of two bubbles still present on the heater surface after 140 ms. This effect cannot be reproduced in the simulation as long as the cavity and the evaporation process inside it remain neglected.

Nevertheless, the analysis of the black and white pictures show, that not only the presence of subsequent bubbles contributes to the growing vapor volume in the experiment. Additionally, the initial bubble itself does not reach the equilibrium between evaporation and condensation until it leaves the boiling cell, similar to the pool boiling case discussed at the beginning of this section. In contrast, in the simulations the initial bubble always grows until it reaches its maximum volume dictated by said equilibrium. This discrepancy shows that it is probable, that additionally one or more of the discussed reasons cause the difference between experiment and simulation.

The calculation of the wall temperature during the pre-heating time in the simulation of the flow boiling case was verified by comparing it to the data obtained by simulating the pre-heating phase with another simulation software. The parameters for the simulation are those of the "Unvaried"-case from table 5.6. A simulation on forced convection of the pure liquid during the pre-heating time is conducted in the OpenFOAM based solver, which was employed for the present thesis, and in COMSOL Multiphysics. Figure 5.39 shows the temperature increase at the nucleation site during the 5 s pre-heating time for both softwares. Despite a small discrepancy in the beginning, the development is very similar and the deviation after 5 seconds is only about 7.5 %. Since two different numerical solvers, which even employ different numerical approaches (Finite element method in the case of COMSOL Multiphysics and Finite volume method in case of OpenFOAM) and different numerical meshes, provide

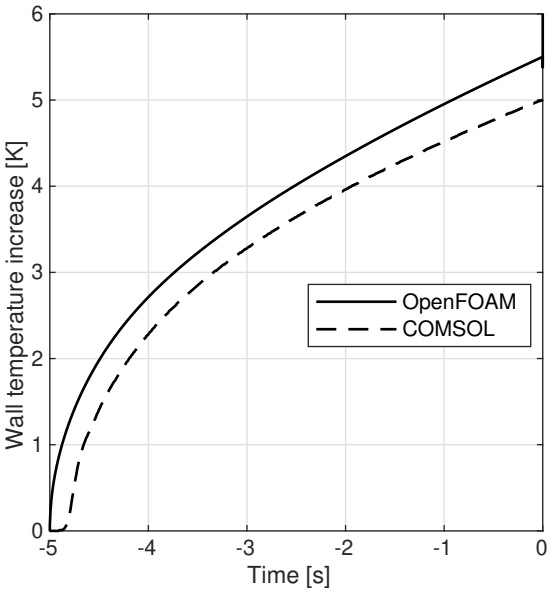

Figure 5.39: Temperature increase at the nucleation site within the pre-heating time span of 5 s for the flow boiling reference case investigated for validation with the modified OpenFOAM solver used throughout this thesis and with COMSOL Multiphysics

very similar results, it is assumed that heat transfer during pre-heating time is calculated with sufficient accuracy throughout the simulation.

6 Numerical simulations of nucleation and detachment from cavities in microgravity

Additional to the simulations of the boiling process in the Multiscale Boiling test cell with the assumption of a flat heater surface, simulations of the nucleation and detachment process at different cavities under microgravity conditions are performed. The investigations are divided in two parts:

In the first part, the process of nucleation inside the rather deep, L-shaped cavity of the Multiscale Boiling experiment and the growth of vapor out of the cavity until the formation of a bubble on its top is simulated (section 6.1). The motivation is to investigate the influence of process parameters specific to the corresponding experiment on the nucleation process, both of the initial bubble and of subsequent bubbles. The underlying data of section 6.1 was obtained within the scope of the bachelor's thesis of Schommartz [83].

Although the numerical domain in those cavity studies is much smaller than in the simulations of the whole boiling cell, it still proves numerically expensive to study a complete cycle of the bubble growth out of the cavity, further growth outside the cavity and eventual detachment from the cavity. Due to the lack of buoyancy under microgravity conditions, a bubble only detaches as a result of a shear flow above the cavity. It was often observed, that a bubble tends to stay attached at the sharp edge at the opening of a cavity even in a highly deformed state. In case of slow, laminar flows as in the Multiscale Boiling experiments, very long simulation times are necessary until bubble detachment.

Therefore in a second approach the detachment process of a bubble from a cavity is studied with flow velocities several orders of magnitude higher than in the Multiscale Boiling experiment (section 6.2). A dimensionless correlation between flow velocity, the size of a bubble and the moment of its detachment is proposed in order to transfer the results to cases with lower flow velocities. Additionally it is investigated, under which conditions residual vapor stays inside the cavity after detachment and provides for the growth of a subsequent bubble, and when a cavity is washed out and stays inactive afterwards. Since one focus of these investigations is the influence of cavity depth on the detachment process and the activation state of the cavity, cavities of circular cross section and of different depths, without the L-shape characteristic for the Multiscale Boiling cavity, are examined. The underlying data of section 6.2 was obtained within the scope of the bachelor's thesis of Stechowsky [100].

6.1 Investigations of the nucleation process inside the Multiscale Boiling cavity

The nucleation process inside the cavity specific to the Multiscale Boiling experiment was investigated in detail. Both the nucleation of initial bubbles, starting from a micro nucleus inside the cavity, and of successive bubbles, growing from a cavity filled with vapor up to a certain level, were examined. In case of initial bubbles the impact of the position of the starting nucleus was studied; in case of successive bubbles, the impact of the height of the vapor column inside the cavity was investigated. Furthermore, the impact of initial wall temperature, input heat flux and inclusion of the laser beam power was examined.

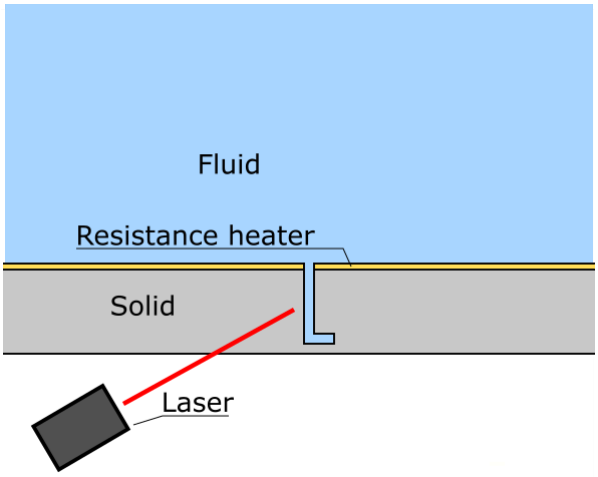

Figure 6.1: (a) Schematic of the Multiscale Boiling cutout around the L-shaped cavity

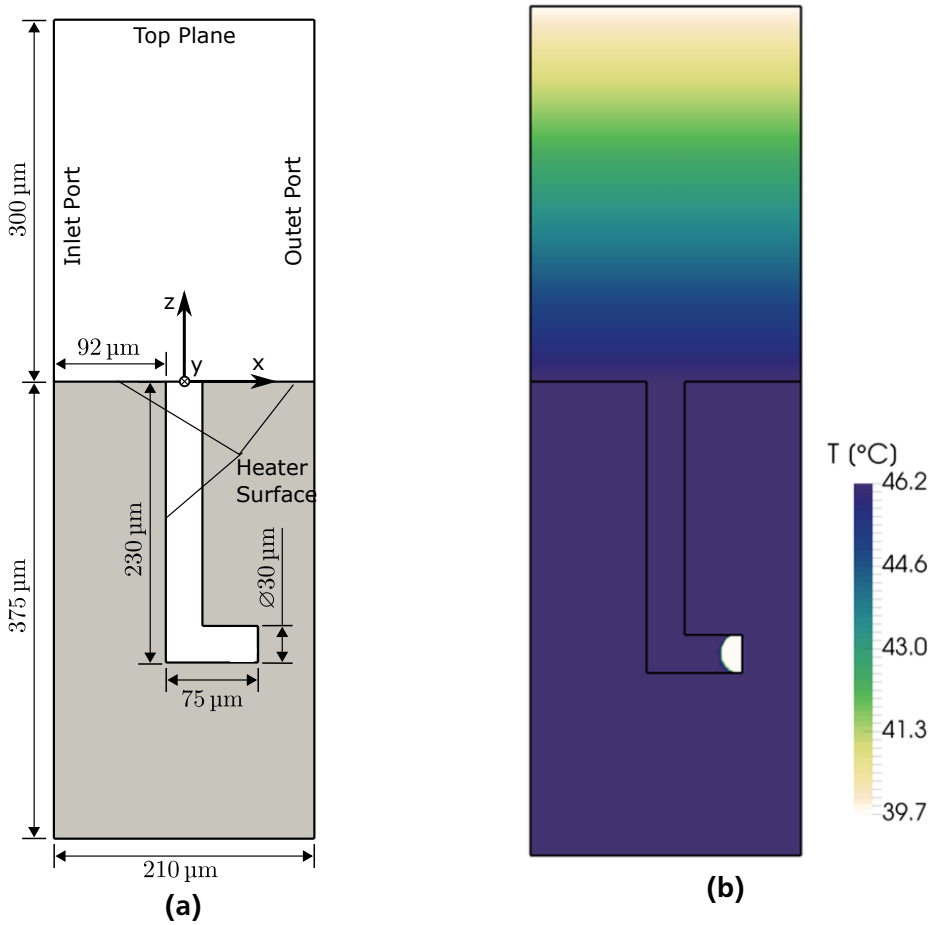

Figure 6.2: (a) Dimensions of the fluid and solid numerical domains, (b) initial temperature profile in fluid and solid for a saturation temperature of 39.7 °C and 6.5 K superheat

The numerical setup complies with that outlined in chapter 5, though with the two numerical meshes representing only a small cutout of the Multiscale Boiling test cell in the vicinity of the nucleation site. Figure 6.1 sketches the experimental setup around the cavity; figure 6.2 (a) shows the two numerical domains with their dimensions and boundaries. The boundary conditions are outlined in detail in table 6.1. They comply with those of the boiling cell simulations with the difference, that the velocity profile at the inlet port is set to zero. Since only the pure growth process out of the cavity is studied, the influence of the very low velocity near the wall can be neglected. The shape of the cavity follows that of the Multiscale Boiling experiments and is characterized by a depth of 230 µm and a 90 degree bend.

Fluid domain	p	$\vec{u}$	T	F
Inlet port	$\nabla p \cdot \vec{n} = 0$	0	$\nabla T_\mathrm{f} \cdot \vec{n} = 0$	$\nabla F \cdot \vec{n} = 0$
Outlet port	0	$\nabla \vec{u} \cdot \vec{n} = 0$	$\nabla T_\mathrm{f} \cdot \vec{n} = 0$	$\nabla F \cdot \vec{n} = 0$
Symmetry plane	Symmetry	Symmetry	Symmetry	Symmetry
Far field plane	$\nabla p \cdot \vec{n} = 0$	$\nabla \vec{u} \cdot \vec{n} = 0$	$\nabla T_\mathrm{f} \cdot \vec{n} = 0$	$\nabla F \cdot \vec{n} = 0$
Top plane	$\nabla p \cdot \vec{n} = 0$	$\nabla \vec{u} \cdot \vec{n} = 0$	$\nabla T_\mathrm{f} \cdot \vec{n} = 0$	$\nabla F \cdot \vec{n} = 0$
Heater surface	$\nabla p \cdot \vec{n} = 0$	(0,0,0)	$T_\mathrm{f} = T_\mathrm{s}$	$\Theta = \Theta_{cl}$
Solid domain	T			
Heater surface	$\lambda_\mathrm{s}(\nabla T_\mathrm{s} \cdot \vec{n}) = \dot{q}_\mathrm{in} + \dot{q}_\mathrm{cl,f}$ at contact line $\lambda_\mathrm{s}(\nabla T_\mathrm{s} \cdot \vec{n}) = \dot{q}_\mathrm{in} + \lambda_\mathrm{f}(\nabla T_\mathrm{f} \cdot \vec{n})$ elsewhere			
Other surfaces	$\nabla T \cdot \vec{n} = 0$			

Table 6.1: Boundary conditions in the fluid and the solid domain for the cavity detachment investigations

The unrefined base mesh has a resolution of 2 µm inside the cavity and up to 4 µm outside the cavity and in the solid domain. Two levels of adaptive mesh refinement are employed, which results in a finest mesh resolution of 0.5 µm at the liquid-vapor interface inside the cavity. Dietl [17] showed the necessity to pay special attention to the meshing of corners or edges in a way, that every fluid cell sharing a point or a line with a wall must also share a face with the wall in order to avoid singularities when the contact line moves through those cells. In the present study the smooth transition of the contact line at the edge of the cavity is ensured by a small chamfer, as depicted in figure 6.3.

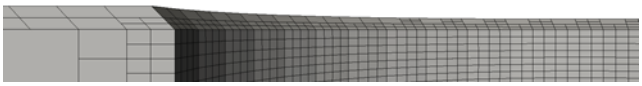

Figure 6.3: Numerical mesh in the solid domain at the cavity opening

The input heat flux, which is part of the boundary condition on the solid side of the heater surface, was only implemented at the horizontal plane at the top of the solid substrate and neglected at the fluid-solid interface inside the cavity in accordance to the experiment. As outlined in section 5.1.2, the power of the laser beam during the first 10 ms of the simulation after the very first nucleation is modeled by increasing the input heat flux at the heater surface with a circular Gaussian distribution around the nucleation site. In the simulations discussed in this section, this modeling causes a deviation of the simulations to the experiment. In reality the laser beam is focused on the cavity and causes a three-dimensional temperature increase in the fluid inside the cavity and in the solid material surrounding it. Contrarily, in the simulations a two-dimensional section of the heater surface around the cavity mouth experiences a rise in input heat flux. However, since the actual heat distribution in the solid and fluid volume due to the laser is not known, it is not possible to implement a proper volumetric distribution of the heat input due to laser power in the simulation. As in the simulations presented in chapter 5, the laser power

is $P_{\text{Laser}} = 177\,\text{mW}$ and the variance of the circular Gaussian distribution around the cavity is $\sigma = 30\,\mu\text{m}$.

The simulations start with a vapor nucleus or a vapor column inside the cavity and no pre-heating phase is included in the simulations. The simulations were conducted at a system pressure of 0.54 bar or a saturation temperature of 39.7 °C, respectively. The fluid inside the cavity and the solid domain hold a superheat at the start of the simulation, which is defined as $\Delta T_{\text{w,0}}$ in the respective case. Because the top plane of the fluid domain has a distance of only 300 µm to the heated wall, it is assumed, that it is situated within the thermal boundary layer rather than in the subcooled bulk fluid. Due to the lack of information on the temperature profile in the thermal boundary layer for all combinations of superheated wall and subcooled bulk, the temperature at the top plane is set to saturation temperature throughout all simulations with a linear temperature increase between wall and top plane (see figure 6.2 (b)).

The variation of initial vapor distribution is depicted in figure 6.4. For the simulation of initial bubbles, the three shown positions are chosen for the vapor nuclei; the positions will be called by the numbers 1, 2 and 3 as in figure 6.4 (a) in the following. The initial superheat of the solid and the fluid inside the cavity is varied between 0 K and 6.5 K. Furthermore, in simulations using a nucleus at position 1, the input heat flux is varied between $0.5\,\text{W/cm}^2$ and $1\,\text{W/cm}^2$ and simulations with the laser on and off are performed. For the simulations of successive bubbles it is assumed, that a previous bubble has left the cavity and a column of residual vapor is left inside the cavity (6.4 (b)). Simulations of the cavity filled with vapor up to a height of 110 µm, 170 µm and 230 µm are performed. In those simulations, only the initial superheat is varied between 0.5 K and 6.5 K. Table 6.2 gives an overview over all varied parameters.

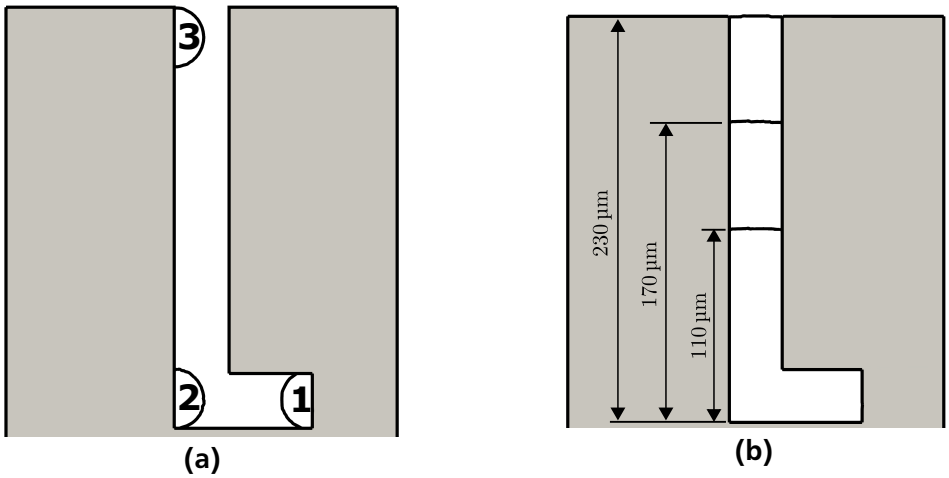

Figure 6.4: Initial position of the liquid-vapor interface: (a) Initial position of the vapor nucleus in the initial bubble simulations, (b) level of vapor filling the cavity in the simulations of successive bubbles

Nucleus position / vapor height	1	2	3	110 µm	170 µm	230 µm
Laser	on/off	on		off		
$\dot{q}_{\text{in}}[\text{W/cm}^2]$	0.5 - 1	1				
$\Delta T_{\text{w,0}}$ [K]	0 - 6.5	0.5 - 6.5				

Table 6.2: Parameter range for the nucleation study

6.1.2 Results

Initial bubbles

Variation of nucleus position

Figure 6.5 (a) shows the evolution of the equivalent bubble diameter for different starting positions of the vapor nucleus at the maximal wall superheat of 6.5 K and activated laser. The development for position 1 and 2 is very similar, with the growth from position 2 being slightly faster during the first 10 µs. This deviation is caused by the fact that the input heat flux including the laser power is implemented at the top surface of the cavity and therefore causes a temperature gradient between the cavity mouth and the lower part of the numerical domains. Since the bubble starting at position 1 first has to grow through the horizontal part of the cavity, which is most distant from the temperature maximum at the top surface, less evaporation takes place during the first few microseconds. However, in both cases the growth starts relatively slowly and accelerates later on, while in case of the nucleus at position 3 the growth starts slightly faster but slows down in a later stage.

The hydrodynamic difference in bubble growth between nucleus positions 1 and 3 is depicted in figure 6.6 for an initial wall superheat 0f 0 K. Note, that this is not the case evaluated in figure 6.5 (a), where the initial wall superheat in 6.5 K. In case of growth from the low positions, the liquid vapor interface barely touches the wall in the vertical section of the cavity, but instead a thin liquid film forms between the wall and the interface causing strong evaporation. On the other hand, in case of growth from the high position 3 the vapor closes the cavity opening very early leaving only a very short liquid-vapor interface for the liquid inside the cavity to evaporate. Instead, the majority of evaporation takes place outside the cavity at the horizontal wall strongly superheated by the laser heat flux. This superheat is the reason for the faster bubble growth in case 3 in the early stage of the simulation. However, the bubble soon grows into regions of lower superheat, which causes bubble growth to slow down compared to cases 1 and 2 later on.

Initial superheat and laser

Figure 6.5 (b) and (c) compare bubble growth for different initial wall superheats as well as for the laser turned on and off in 1.5 K, 3.5 K and 6.5 K wall superheat cases. In all cases, bubble growth starts from a nucleus at position 1. Apparently, depending on the wall superheat, it takes the bubble longer to grow through the horizontal section of the cavity. Exactly in that moment, when the bubble grows around the corner and reaches the vertical part of the cavity, an escalating growth begins independent of the initial superheat. The three-phase contact line does not completely move around the corner, so in the vertical part of the cavity the thin liquid film forms and causes strong evaporation.

The laser does not have an impact during the growth phase inside the cavity in all depicted cases (the bubbles leaves the cavity at an equivalent diameter of approximately 0.05 mm), because the wall and the liquid inside the cavity do not get heated by the source at the top surface during the short observed time period. Again, this phenomenon strongly depends on the modeling of the heat input due to the laser power and it can be assumed that if the laser directly heated up the liquid inside the cavity (as it probably does in the experiment), there would be an observable impact. In the performed simulations the laser has only an effect as soon as the bubble leaves the cavity and grows through the thermal boundary layer, which has been significantly heated by the input heat flux increased by the laser.

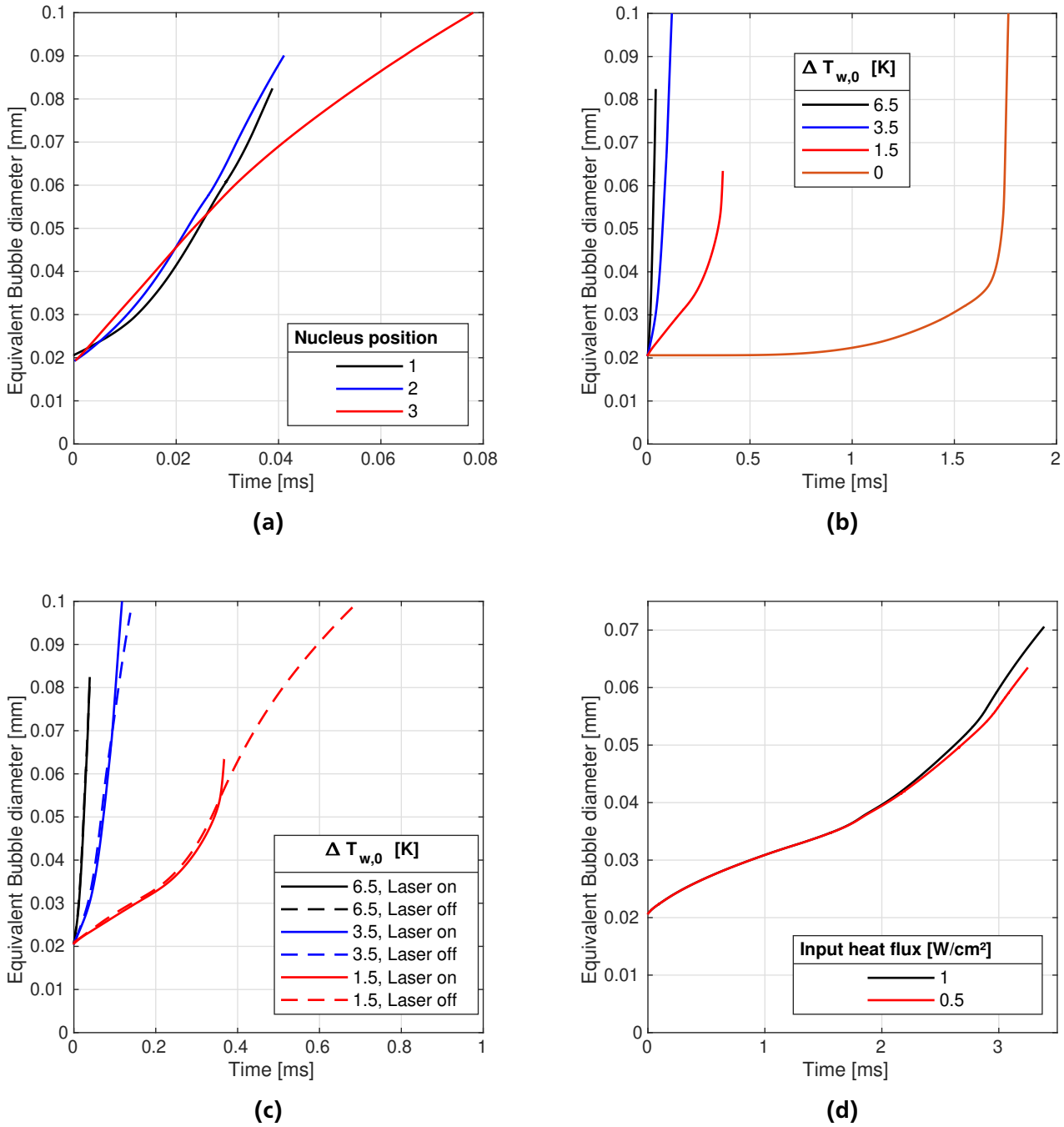

Figure 6.5: Evolution of bubble diameters for initial bubbles with (a) different nucleus positions at 6.5 K superheat, (b) nucleus at position 1 and different superheats with laser on, (c) nucleus at position 1 and different superheats and laser statuses, (d) nucleus at position 1, 0.5 K superheat, laser off and different input heat fluxes

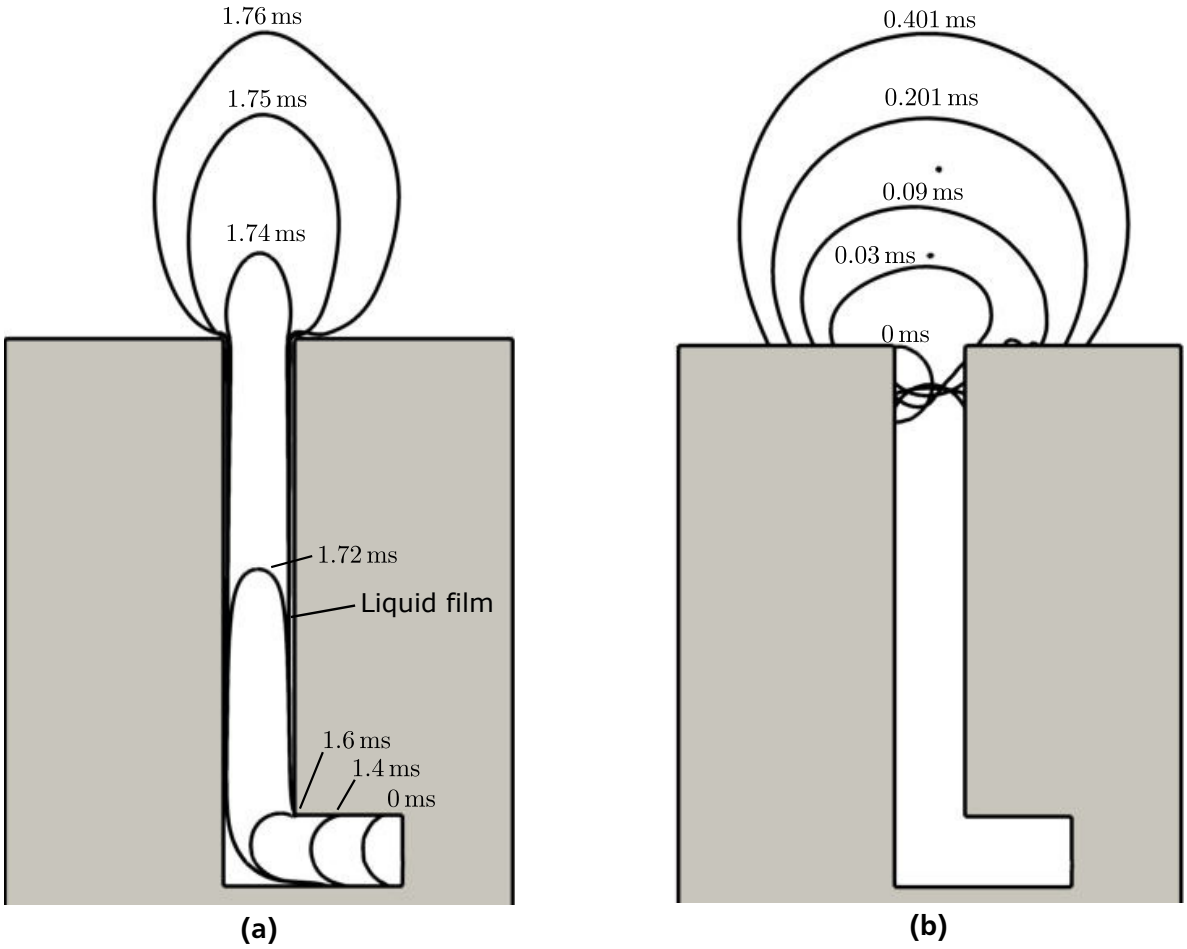

Figure 6.6: Liquid-vapor interfaces at 0 K initial superheat and different timesteps for nuclei at position (a) 1 and (b) 3

Input heat flux

Figure 6.5 (d) shows the impact of the input heat flux at the top surface without increase by the laser. Similar to the impact of the laser power, the input heat flux of the resistance heater has no observable effect on bubble growth while the bubble is inside the cavity. A deviation can be observed as soon as the bubble leaves the cavity, since the liquid above the heated wall has a higher temperature in case of a higher input heat flux. In opposition to the impact of the laser power, this phenomenon can be assumed to be in good accordance with the experiment and without a significant modeling error, since the permanent input heat flux from the resistance heater is in fact implemented on the top horizontal surface only.

Bubble shape outside the cavity

The growth rate of the bubble inside the cavity, which is determined by the amount of latent heat provided to the process and mainly influenced by the initial temperature of the surrounding material, has a significant impact on the bubble shape outside the cavity for cases with a starting nucleus at the bottom of the cavity. Figure 6.7 shows, that for high initial wall superheats the bubble gets strongly folded as soon as it exits the cavity. The reason for this hydrodynamic phenomenon is a circulating flow of the liquid around the bubble after it has been pushed out of the cavity by the fast growing bubble.

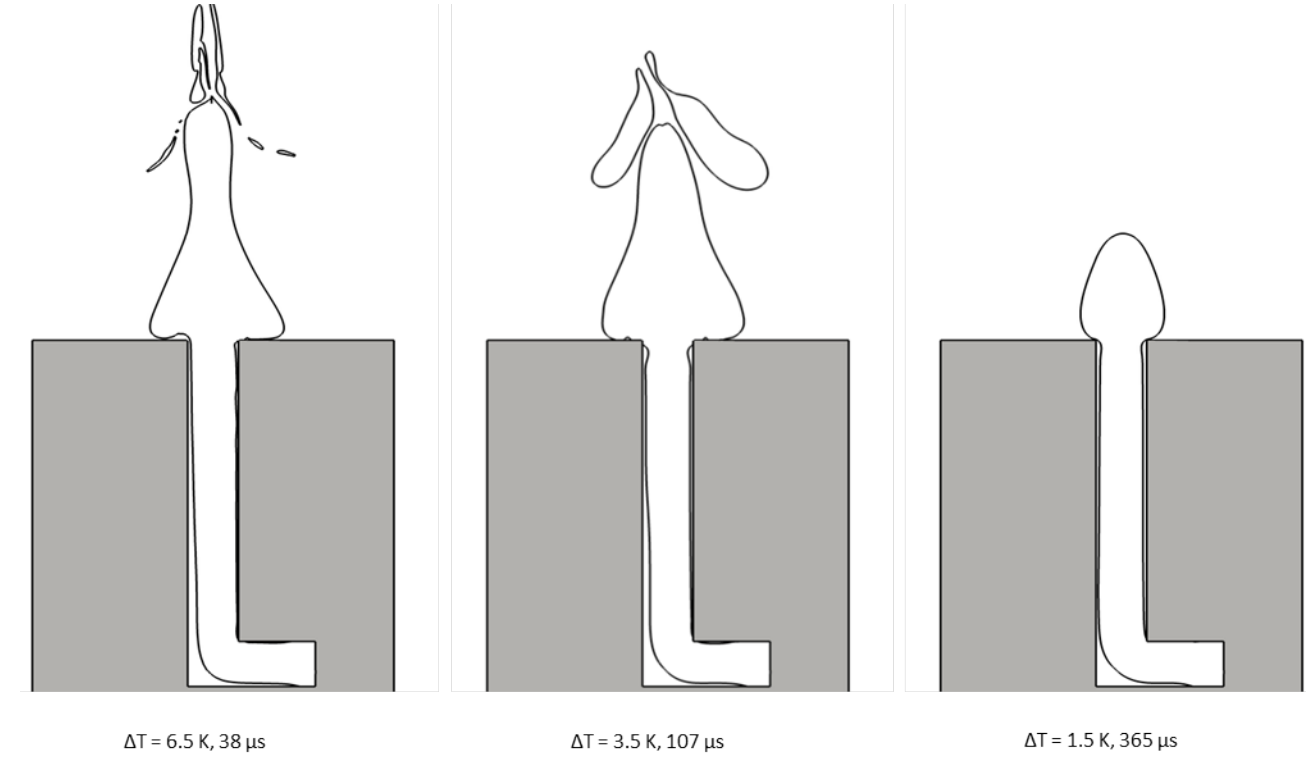

Figure 6.7: Liquid-vapor interfaces at exit of the bubble out of the cavity for nuclei at position 1 and different initial superheats

Furthermore, parts of the bubble get torn off and detach due to the strong inertia force caused by the rapid growth in the vertical part of the cavity. This observation is in good qualitative agreement to Multiscale Boiling experiments, see e.g. section 5.3. For a relatively low initial wall superheat of 1.5 K, the bubble takes almost ten times as long to grow out of the cavity and inertia only causes a slight upwards stretching of the bubble.

Deformation of the thermal boundary layer outside the cavity

In the simulations of the boiling cell presented in chapter 5, the nucleation process is modeled by creating a bubble instantaneously on top of the heater surface within the thermal boundary layer. That way, the liquid around the bubble has the same temperature profile as before the nucleation; the thermal boundary layer is not affected by the nucleation process. However, it is very likely that in reality the growth of the bubble out of the cavity alters the shape of the thermal boundary layer in a way, that the following growth process of the bubble above the wall is influenced. A deviation in the thermal boundary layer surrounding the bubble after nucleation is discussed as one of a number of possible reasons for the different evaporation rates between simulation and experiment in section 5.3.

Figure 6.8 shows the isothermes and the velocity vectors in the vicinity of the bubble opening at different timesteps of the bubble growth from position 1 at a moderate initial wall superheat of 1.5 K and with the laser turned on. The liquid pushed out of the cavity by the growing bubble induces a velocity field, which drags the thermal boundary layer, heated up to over 80 °C by the laser, upwards. As the bubble exits the cavity, a significant part of it is covered by isothermes of 50 °C and higher, which corresponds to a superheat of over 10 K. The simulation time conducted is too short to study further effects of bubble hydrodynamics on the more upper parts of the thermal boundary layer. However, even in less than the

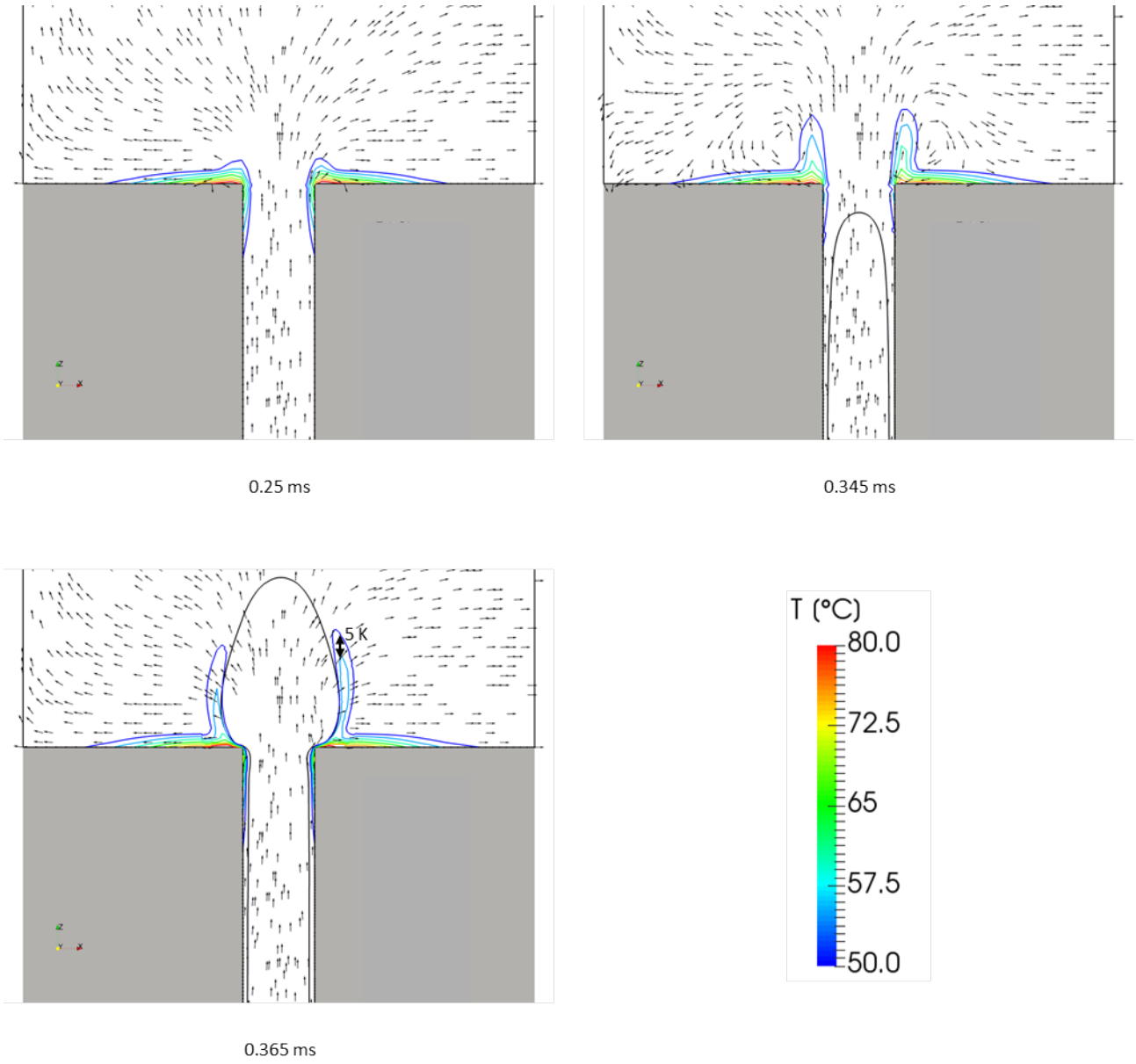

Figure 6.8: Liquid-vapor interface, isothermes and velocity vectors during bubble growth out of the cavity from position 1 at 1.5 K initial superheat

first half millisecond the temperature field is significantly deformed by the flow field resulting from the bubble growth out of the cavity. Hence, the larger part of the bubble hull is surrounded by strongly superheated liquid. It has to be examined in future investigations with longer simulation times, how pronounced this effect persists in later stages, and how pronounced it is, if not only the top horizontal surface but the whole liquid inside the cavity is heated by the laser. However, it can already be assumed, that a bubble after nucleation is covered by liquid of higher temperature than it is modeled in the boiling cell simulations of the present thesis.

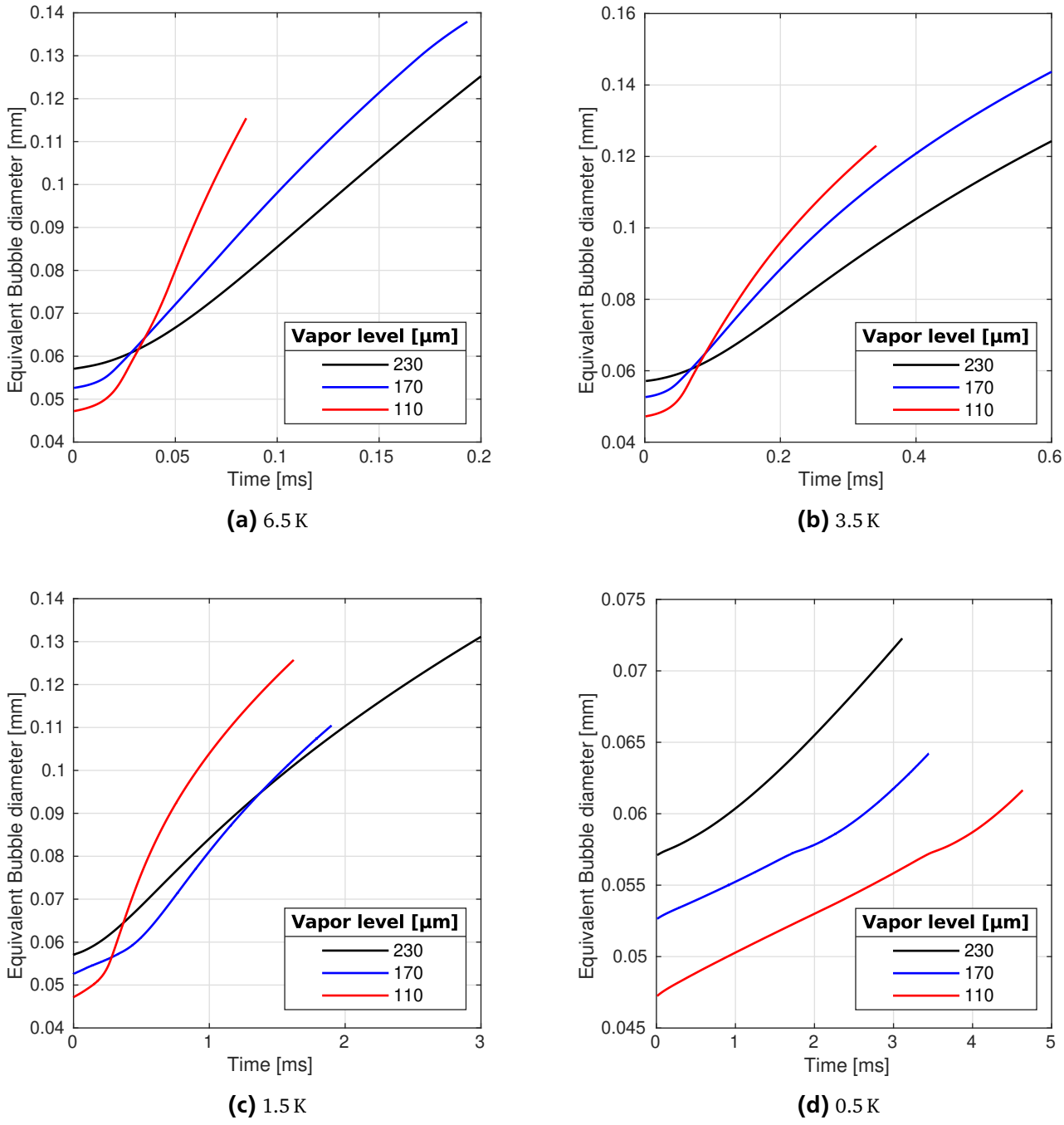

(a) 6.5 K **(b)** 3.5 K

(c) 1.5 K **(d)** 0.5 K

Figure 6.9: Evolution of bubble diameters for successive bubbles with different initial vapor levels inside the cavity and (a) 6.5 K superheat (b) 3.5 K superheat, (c) 1.5 K superheat, (d) 0.5 K superheat

Successive bubbles

The emergence of successive bubbles from residual vapor after the detachment was modeled by starting simulations with the cavity initially filled with vapor levels as depicted in figure 6.4 (b).

Figure 6.9 shows, that the influence of the vapor level inside the cavity on the growth process depends strongly on the initial superheat of the wall and the liquid. If the cavity is completely filled at start, only a modest acceleration in bubble growth can be noticed as soon as the bubble has left the cavity. This phenomenon can be observed for all studied initial superheats. In case of the cavity initially filled with low levels of vapor, a strong acceleration in bubble growth begins early after the beginning of the simulation, resulting in larger bubble diameters for lower intial vapor levels. This effect is pronounced more strongly in case of high initial superheats and completely disappears in case of the minimal superheat of 0.5 K.

The reason for this phenomenon is again a liquid film remaining between the wall and the liquid-vapor interface in case of combinations of high superheats and low initial vapor levels. Figure 6.10 depicts this behaviour for 1.5 K and 0.5 K initial superheat. In case of the minimal initial superheat the wall inside

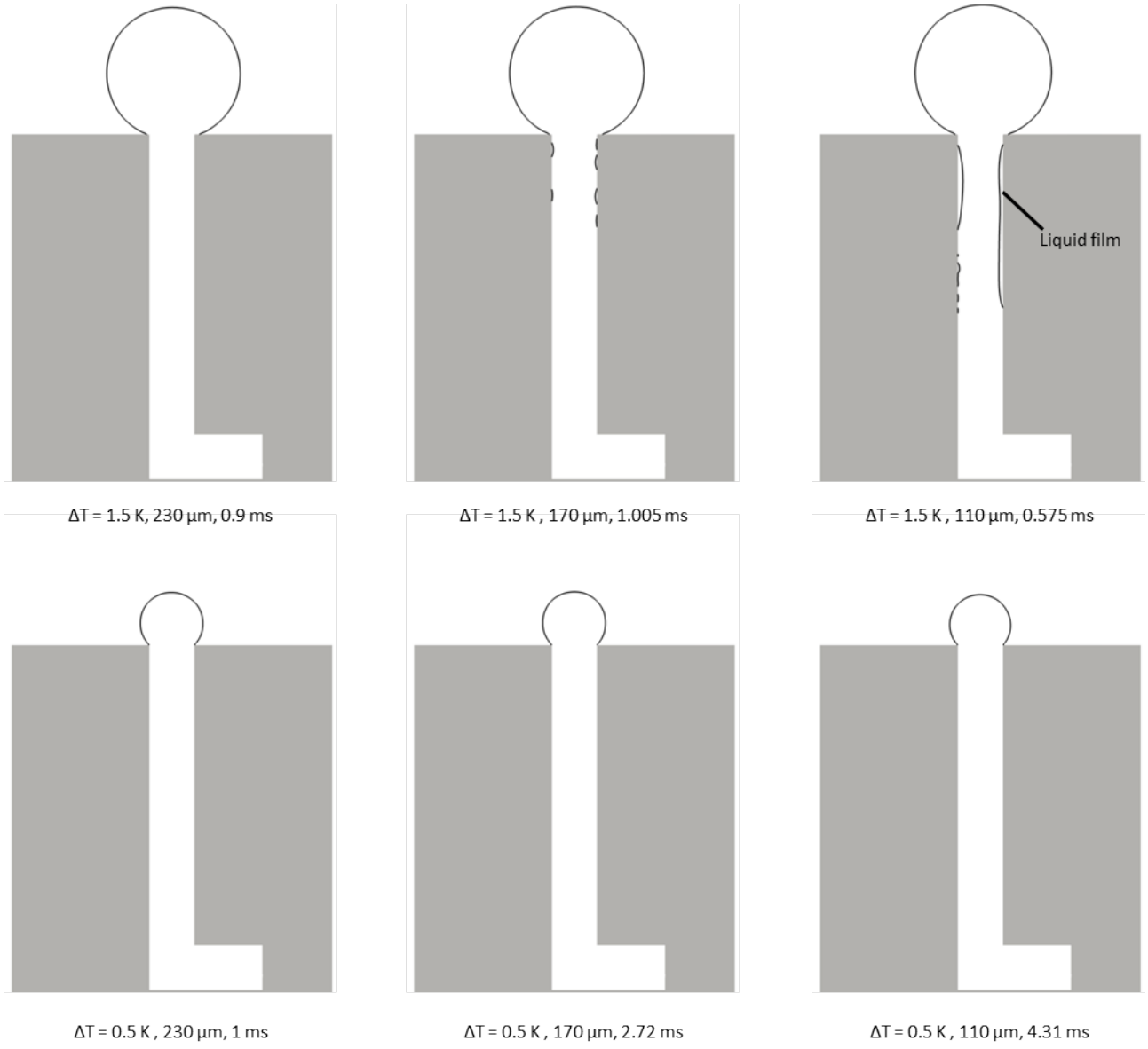

Figure 6.10: Liquid-vapor interfaces at exit of successive bubbles out of the cavity for different initial vapor levels and different initial superheats

the cavity gets completely dewetted throughout the growth process independent of the initial vapor level, since the inertia forces during the first stage of bubble growth inside the cavity are low and the three-phase contact line can move up the wall alongside the moving interface. However, parts of the wall remain wetted even for a moderate superheat of 1.5 K. The latter in turn is even more pronounced, if the initial vapor level is lower. Here, the first stage of growth inside the cavity is so rapid, that the contact line occasionally remains stuck and does not follow the rapidly moving interface sufficiently, resulting in the formation of the thin liquid film. This effect is even more pronounced for higher initial superheats. Furthermore, as the liquid film has formed, the evaporation rate at it is higher in case of a higher wall temperature next to it, resulting in the very high evaporation rates, which can be seen in figure 6.9 (a) and (b).

6.2 Investigations of bubble detachment at regular circular cavities

Additional to the simulations of the nucleation process, the detachment of a vapor bubble from a cavity of 30 µm diameter due to a shear flow in microgravity was examined. Because of high computational effort and long simulation times until detachment in case of the low flow velocities of the Multiscale Boiling experiment, detachment diameters were obtained for higher flow velocities and a dimensionless correlation was deduced. Furthermore the state of the cavity after detachment as an active nucleation site was investigated dependent on cavity depth and flow velocity.

6.2.1 Setup and Procedure

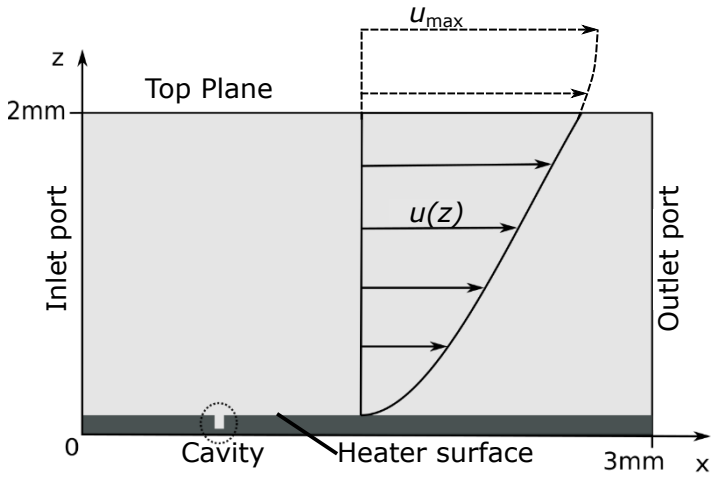

Figure 6.11: Numerical domains and velocity profile

The numerical setup again complies with that outlined in chapter 5, with the two numerical meshes representing a larger cutout of the Multiscale Boiling test cell than in the simulations presented in the prior section 6.1. Figure 6.11 shows the fluid and the solid computational domains and the boundary conditions. The latter comply with table 6.1 with the sole difference, that the velocity at the inlet port is not zero but a velocity profile is imposed as boundary condition. As in the simulations of the complete boiling cell, the velocity field at the inlet is modeled as an ideal laminar Poiseuille profile (see equation 5.1) with a theoretical maximal flow velocity at a channel height of 2.5 mm. Since the flow channel is only covered up to a height of 2 mm, the velocity profile is cut off at the top plane and a zero gradient boundary condition is imposed there for velocity. Although the domains represent only a small cutout

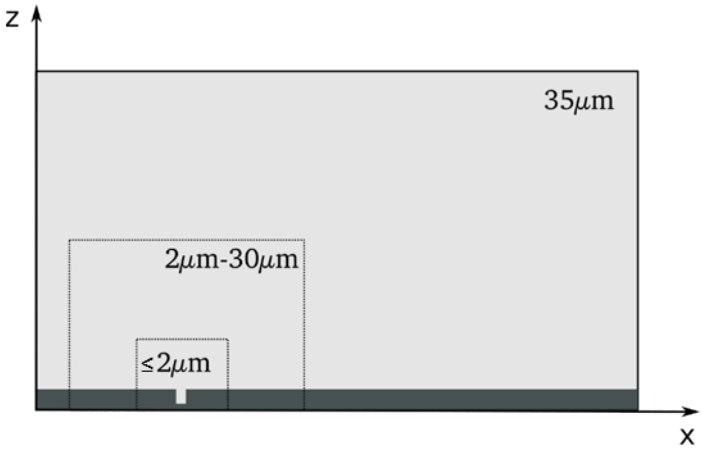

Figure 6.12: Areas of different mesh resolutions

of the test cell, it is apparent that the spatial dimensions of the fluid domain are still relatively large compared to the cavity. This accounts for the estimated large expansion of a bubble before detachment due to the lack of buoyancy.

In order to cover the bubble physics inside the cavity appropriately, the resolution of the base mesh is again set to 2 µm inside and in the vicinity of the cavity, as shown in figure 6.12. There is an exception for cavities of 3 µm depth, here the finest resolution of the base mesh before adaptive refinement is 1.25 µm. Two levels of adaptive refinement are imposed in the vicinity of the liquid-vapor interface during a running simulation, which results in a finest mesh resolution of ≤0.5 µm. In order to reduce the overall number of cells, the resolution of the base mesh distant from the cavity is enlarged up to 35 µm. A continuous spatial transition between the fine and the coarse mesh is realized by the O-grid functionality of ICEM CFD™ hexa meshing. Figure 6.12 depicts the areas of different mesh resolutions. With those settings the fluid mesh at the beginning of a simulation counts approximately 600 000 cells, the solid mesh approximately 400 000. Although the investigated volume represents only a fraction of the Multiscale Boiling test cell studied in chapter 5, the cell count in the base mesh is an order of magnitude higher due to the finer resolution demanded to resolve the cavity. Throughout the simulations the number of cells in the fluid grew to approximately 2 million.

In this subset of the investigation, all simulations were conducted at a system pressure of 0.9 bar, which corresponds to a saturation temperature of 53.53 °C. The bulk fluid was set to saturation temperature in order to accelerate bubble growth. The input heat flux was $\dot{q}_{\text{in}} = 1\,\text{W}/(\text{cm}^2)$ throughout all simulations and the initial wall temperature was set to 57.53 °C or 4 K superheat, respectively, in order to abbreviate the pre-heating phase and ensure a fast bubble growth out of the cavity in the beginning of the simulation. In contrast to the boiling cell simulations, no bubble creation process was conducted during running simulations, but a vapor volume was placed inside the cavity during pre-processing of the simulation, as depicted in figure 6.13.

Cavities of 30 µm diameter and of 3 µm, 25 µm and 50 µm depth were studied in order to investigate the influence of the depth on bubble growth and on the ability of the cavity to hold residual vapor after bubble detachment for different flow velocities. Additionally a velocity study was conducted for all three cavities in order to examine the influence of flow velocity on bubble growth and the correlation between bubble diameter, velocity and detachment time. Table 6.3 shows the range of the studied parameters. Velocities in this study are at least one order of magnitude higher than in the boiling cell

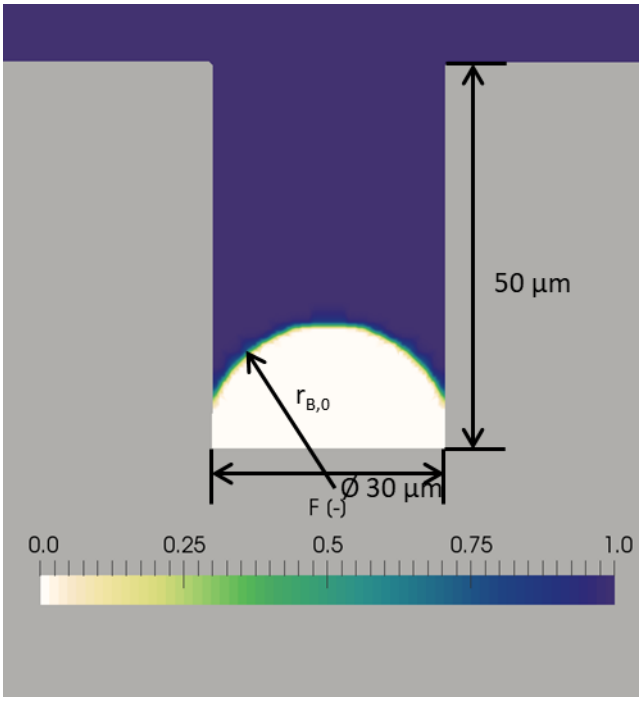

Figure 6.13: Distribution of the volume fraction field inside the 50 µm cavity at the beginning of the simulation

Cavity depth [µm]	3	25	50
Max. flow velocity [m/s]	0.15 - 1	0.15 - 1	0.1 - 10

Table 6.3: Band of examined maximal flow velocities in the middle of the flow channel for each of the three investigated cavities

simulations presented in chapter 5. The simulation of a bubble growing out of the cavity to a size, where it gets deformed by the shear flow and eventually detaches from the cavity, would demand unacceptable simulation times for flow velocities within the range of the Multiscale Boiling experiment. The lower the maximal flow velocity in the center of the channel is, the larger a bubble has to grow until it reaches zones of the flow channel, where the velocity is sufficient to drag the bubble downstream. This makes it computationally very expensive to simulate this numerical setup with low flow velocities. For the 50 µm cavity a wide range of even higher flow velocites has been studied in order to deduce a dimensionless relation between the maximal flow velocity and the bubble diameter at detachment. This correlation will be analysed and it will be discussed how suitable it is to transfer the results of high velocity cases to low flow velocities.

6.2.2 Results

Cavity depth study

In this section, the influence of the cavity depth on the process of detachment is presented. Figure 6.14 shows both the 25 µm cavity and the 50 µm cavity shortly after the detachment of the first bubble for a maximal flow velocity $u_{\max} = 1\,\mathrm{m/s}$. In both cases, detachment occurs approximately 12 ms after the start of the simulation. However, only the 50 µm cavity holds residual vapor and thus stays an active nucleation site.

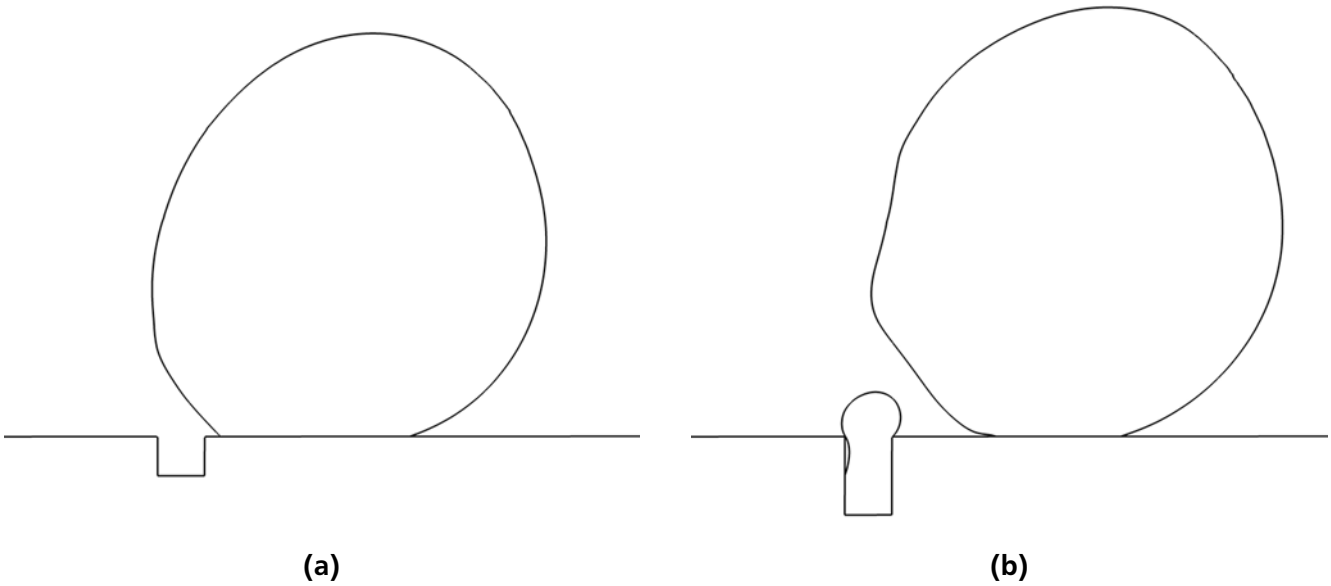

(a) (b)

Figure 6.14: Bubbles shortly after detachment for $u_{\max}$ = 1 m/s (a) at the 25 µm cavity at 12.1 ms, (b) at the 50 µm cavity at 11.9 ms

In case of the 3 µm cavity the bubble growth process reacts very sensible to the initial curvature of the liquid-vapor interface set at the beginning of the simulation. Figure 6.15 shows the two different interface curvatures investigated: If the initial vapor phase is modeled as a circle segment with a radius $r_{\mathrm{B},0} = 50\,\mu\mathrm{m}$, the surface tension force at the interface deviates strongly from its equilibrium state and the interface contracts very fast, striving towards a state of minimal surface tension force. This phenomenon has already been observed in the setup of the boiling cell simulations in chapter 5, depicted in figure 5.6. The result is the forming of a vapor bubble 0.1 ms after simulation start, which shortly detaches and attaches again to the horizontal part of the surface inside the cavity. As the upstream part of the cavity is not covered by vapor anymore, the shear flow intrudes the shallow cavity and drags the bubble out of it after only 1.5 ms, as depicted in figure 6.16 (a) and (b). If, on the other hand, the initial vapor phase is modeled as a circle segment with $r_{\mathrm{B},0} = 25\,\mu\mathrm{m}$ and thus twice the curvature at the interface, a stable bubble growth out of the cavity very similar to the cases of the deeper cavities can be observed (figure 6.16 (c)). A simulation time of only 8.2 ms could be achieved in this case. Thus it could not be observed, if the 3 µm cavity holds residual vapor after detachment. However, since even the 25 µm cavity gets completely washed out, it is most likely that the even shallower 3 µm cavity will not hold any remaining vapor as well.

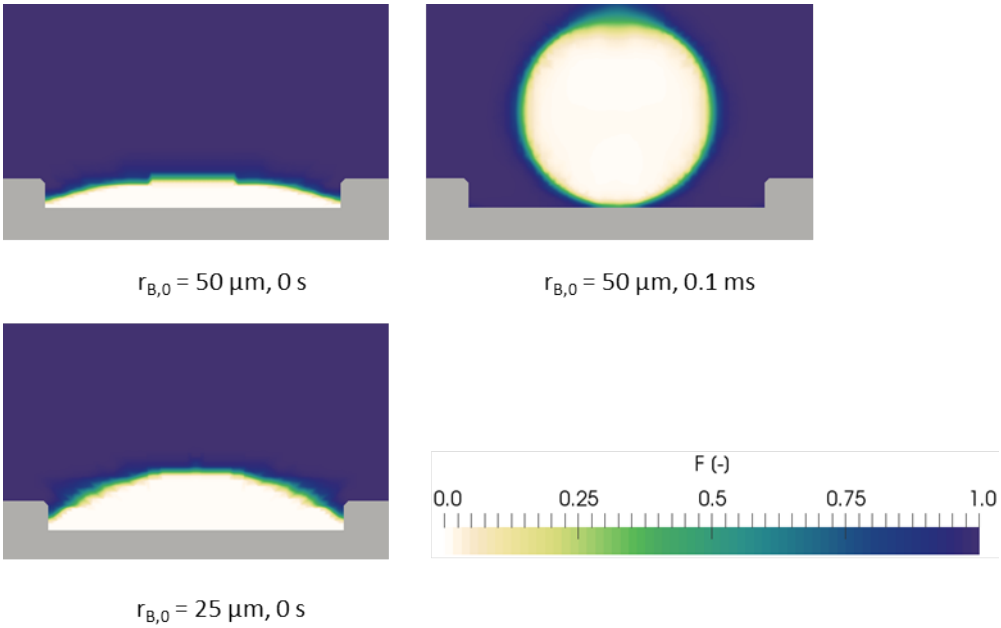

Figure 6.15: Volume fraction field in the beginning of the simulation inside the 3 µm cavity, with low (top) and high (bottom) initial curvature. In case of low curvature, the vapor volume rapidly contracts towards a bubble, which shortly detaches from the surface

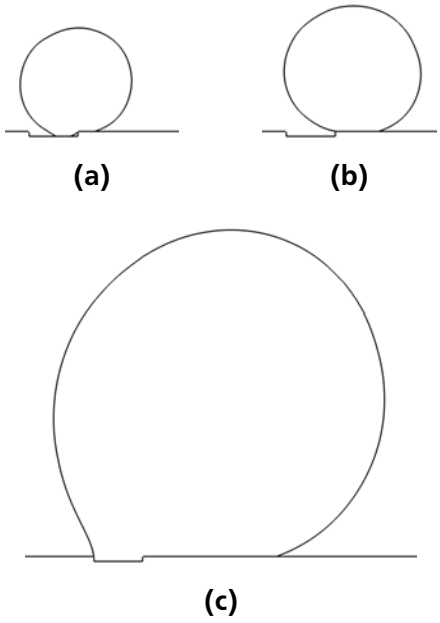

Figure 6.16: Bubbles at the 3 µm cavity for $u_{\max}$ = 1 m/s (a) in case of low initial curvature ($r_{B,0}$ = 50 µm) at 1 ms, (b) in case of low initial curvature ($r_{B,0}$ = 50 µm) at 1.5 ms, (c) in case of high initial curvature ($r_{B,0}$ = 25 µm) at 8.2 ms

Figure 6.17 shows the evolution of equivalent bubble diameter over time for the three different cavities and for the two variants of interface setup at the 3 µm cavity. The cavity depth does not have a big impact on the growth rate. Just in the very beginning of the growth phase, a rapid evaporation takes place until the interface reaches the opening of the cavity. Therefore, the growth of bubble volume is

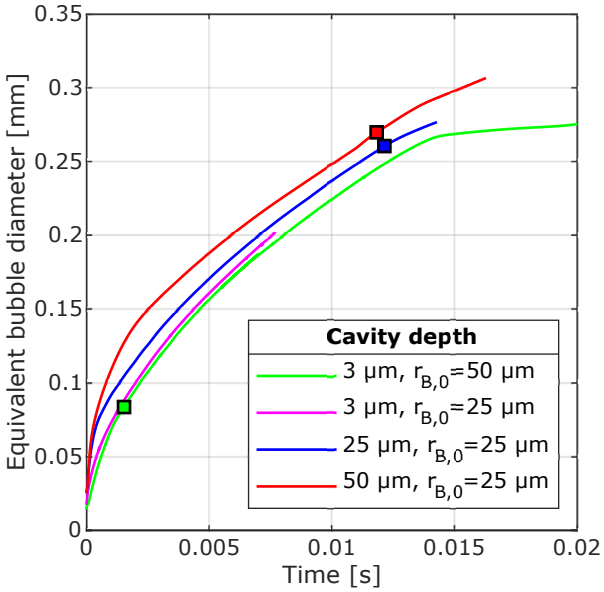

Figure 6.17: Evolution of the equivalent bubble diameter for different cavity depths at $u_{\max}$ = 1 m/s. In case of detachment, the corresponding timestep is marked with a square

slightly stronger in the beginning for deeper cavities.

The results show, that cavity depth does not have a large influence on the timestep of detachment. Furthermore, a minimal depth appears to be necessary for a cavity to hold residual vapor and stay active. This is valid for the investigated flow velocity of $u_{\max} = 1\,\mathrm{m/s}$ in the middle of the flow channel. As the following section will show, it was not possible to provoke detachments at lower flow velocities at the more shallow cavities due to heavily extended simulation times. Finally, cavity depth appears not to have a great influence on the bubble growth rate.

Influence of Flow velocity

For all three cavities the impact of flow velocity on the growth rate and the detachment was studied, the results are shown in figure 6.18. Note, that the results for the 3 µm cavity shown in figure 6.18 (a) are all taken from cases with low initial interface curvature. It is apparent, that for all cavities the flow velocity has no significant impact on the growth rate during the early stages of bubble growth, even after detachment from the cavity. This shows a contrast to the results of the boiling cell simulations presented in section 5.2.3, where a large impact of flow velocity on the overall hydrodynamics could be observed. This difference is partly caused by the fact, that in the present section only a very early stage of bubble growth is examined, and each bubble has to grow sufficiently high into the flow channel for the shear flow to have a significant impact. A second difference is, that the influence of flow velocity on the wall temperature and the temperature distribution in the thermal boundary layer are not taken into account here. While in the simulations presented in section 5.2.3 a very long pre-heating time of at least 10 s was imposed and a temperature distribution throughout the solid and the liquid could even out, in the present setup a constant wall and liquid temperature is assumed. This way, the indirect influence of flow velocity on bubble growth trough convective heat flow during the pre-heating time is denied. Therefore, it is found, that a pure hydrodynamic impact of flow velocity on bubble growth is not given at least

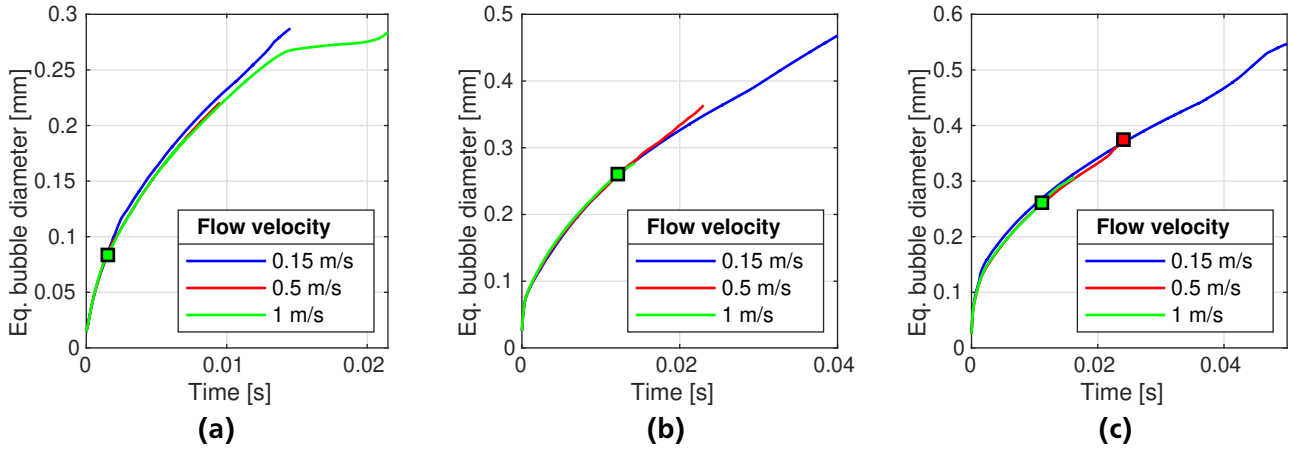

Figure 6.18: Evolution of equivalent bubble diameters (a) at the 3 μm cavity, (b) at the 25 μm cavity and (c) at the 50 μm cavity for different maximal flow velocities. In case of detachment from the cavity, the corresponding timestep is marked with a square

during early growth stages.

In 3-D calculations with a mesh resolution sufficient to take the physics at the cavity into account, it was not possible to achieve bubble detachment within a reasonable simulation time for velocities in the scale of the Multiscale Boiling experiment. Even for the investigated velocities in most cases no detachment could be achieved apart from 1 m/s for all cavities and 0.5 m/s in case of the 50 μm cavity. Therefore, a dimensionless correlation is developed in order to transfer the results of bubble detachment diameter gained at high flow velocities to low velocities.

The Reynolds number of a flow can be interpreted as the ratio between inertia forces and viscous forces:

$$Re = \frac{uL}{\nu}. \tag{6.1}$$

L is a characteristic length of the underlying problem. If the overflowed vapor bubble in the flow channel of the discussed problem is assumed spherical, which is valid during the majority of time between nucleation and detachment, a bubble Reynolds number can be introduced:

$$Re_B = \frac{\bar{u}_B h_B}{\nu_l}. \tag{6.2}$$

with the flow velocity $\bar{u}_B$ averaged over the bubble height h_B and the kinematic viscosity of the flowing liquid ν_l. This is not the Reynolds number of the shear flow in the rectangular flow channel, but the Reynolds number of the flow around a spherical vapor bubble. It presents the ratio between the inertial forces causing the bubble to move downstream and finally detach from the cavity, and the viscous forces attaching it to the cavity. Since the flow velocity increases with increasing distance from the lower wall, the averaged flow velocity around the bubble $\bar{u}_B$ depends on the diameter of the bubble and of course on the maximal flow velocity of the Poiseuille flow in the center of the channel. It can be calculated according to figure 6.19 by integrating equation 5.1 in the direction normal to the wall between zero (wall) and the distance of the bubble cap from the wall h_B and dividing it through h_B again afterwards:

$$\bar{u}_B = \frac{4u_{max}\int_0^{h_B}\left(1-\frac{z}{h}\right)\frac{z}{h}\,dz}{h_B}. \tag{6.3}$$

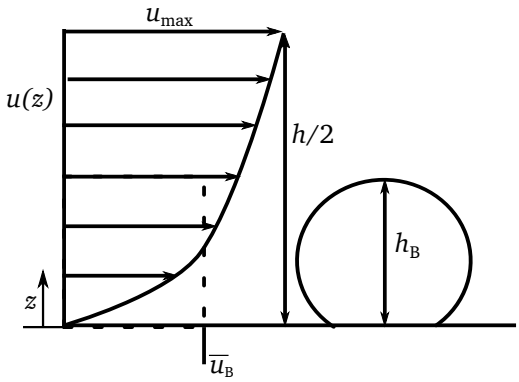

Figure 6.19: Deduction of the bubble averaged velocity $\bar{u}_B$ for the bubble Reynolds number

In equation 6.3 h is the height of the rectangular flow channel, which is $h = 5\,\text{mm}$ in case of the Multi-scale Boiling test cell.

In case of a spherical bubble with a low contact angle the bubble height is approximately its diameter:

$$h_B \approx d_B \tag{6.4}$$

Equation 6.3 can then be altered to

$$\bar{u}_B = \frac{4u_{max}\int_0^{d_B}\left(1-\frac{z}{h}\right)\frac{z}{h}\,dz}{d_B} \tag{6.5}$$

which results in

$$\bar{u}_B = 4u_{max}\left(\frac{d_B}{2h} - \frac{{d_B}^2}{3h^2}\right) \tag{6.6}$$

Putting equation 6.6 into equation 6.2 one gets:

$$Re_B = \frac{4u_{max}\left(\frac{{d_B}^2}{2h} - \frac{{d_B}^3}{3h^2}\right)}{\nu_l} \tag{6.7}$$

In order to verify, if the so deduced bubble Reynolds number is a suitable dimensionless correlation between maximal flow velocity and bubble detachment diameter, a detachment study with flow velocities ranging from $u_{max} = 0.5\,\text{m/s}$ up to $u_{max} = 10\,\text{m/s}$ was conducted at the 50 µm cavity. Actually, for such high velocities the assumption of a complete laminar shear flow does not hold true anymore. However, the simulations are not supposed to examine the flow physics in case the flow velocities were actually that high, but to check, if a consistent relation between the maximal flow velocity in the channel center and the bubble detachment diameter can be observed for the assumptions, which were made for low flow velocities. Hence, the assumption of a laminar flow has been maintained throughout the simulation campaign.

Figure 6.20 shows the evolution of the bubble Reynolds numbers over time for different maximal flow velocities and the timesteps of bubble detachment from the cavity highlighted with black squares. For very high flow velocities a deviation towards higher bubble Reynolds numbers at detachment can be observed. However, for the range between $u_{max} = 5\,\text{m/s}$ and $u_{max} = 0.5\,\text{m/s}$ a relatively narrow range of

bubble Reynolds numbers between 79 and 90 is observed, with a tendency towards 90 for decreasing flow velocities. Hence, for the given configuration the Reynolds number at the departing bubble appears almost constant and it seems promising to estimate the bubble detachment diameter for a given flow velocity profile.

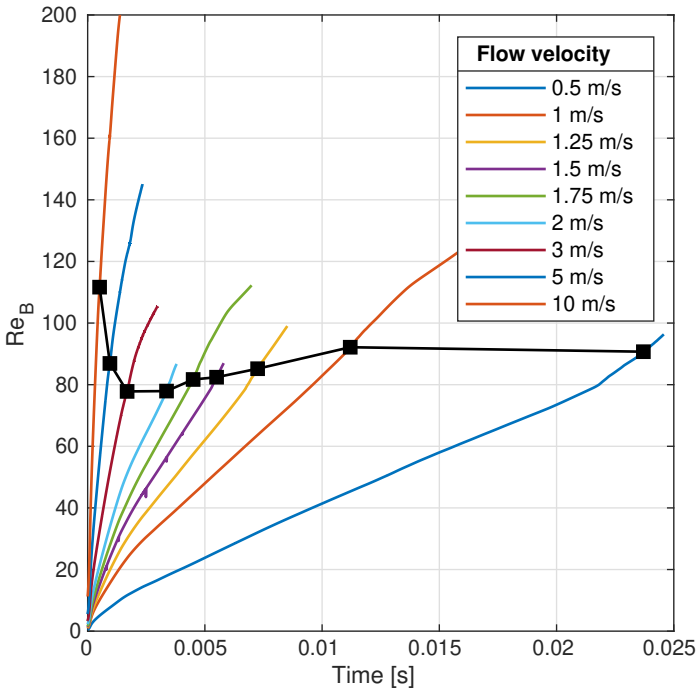

Figure 6.20: Evolution of bubble Reynolds numbers for different velocities at the 50 µm cavity. The timesteps of detachment are marked and connected

Equation 6.7 can be reformulated to:

$$d_B{}^3 - \frac{3}{2} h d_B{}^2 + \frac{3}{4} \nu_l h^2 \frac{Re_B}{u_{max}} = 0 \tag{6.8}$$

For the channel height of the Multiscale Boiling test cell flow channel $h = 5\,\text{mm}$ and a constant kinematic viscosity of the liquid $\nu_l = 2.87{\cdot}10^{-7}\,\text{m}^2/\text{s}$, equation 6.8 reads

$$d_B{}^3 - 7.5 \cdot 10^{-3}\text{m}\; d_B{}^2 + 5.38 \cdot 10^{-12} \frac{\text{m}^4}{s} \frac{Re_B}{u_{max}} = 0. \tag{6.9}$$

If we assume a bubble Reynolds number $Re_B = 90$ at detachment and the maximal flow velocity $u_{max} = 0.0375\,\text{m/s}$ from the reference case in chapter 5, equation 6.9 has one negative solution, one solution beyond the height of the flow channel, and one physical solution at

$$d_{B(Re=90, u_{max}=0.0375\,\text{m/s}, \nu_l = 2.87{\cdot}10^{-7}\,\text{m}^2/s)} \approx 1.46\,\text{mm}.$$

Since the simulations in chapter 5 were conducted for a different system pressure, the kinematic viscosity is different there. With a liquid kinematic viscosity $\nu_l = 3.25{\cdot}10^{-7}\,\text{m}^2/\text{s}$, the physical solution of equation 6.9 is

$$d_{B(Re=90, u_{max}=0.0375\,\text{m/s}, \nu_l = 3.25{\cdot}10^{-7}\,\text{m}^2/s)} \approx 1.57\,\text{mm}.$$

If the postulation of an approximately constant bubble Reynolds number at detachment from the cavity held true for low flow velocities and changing values of viscosity, the bubble from the reference case in chapter 5 would detach from the cavity at a diameter of around 1.6 mm. However, in future investigations this postulation should be verified by at least one simulation with a flow velocity in this order of magnitude and adapted viscosity, and it should be validated by experiments.

7 Summary, conclusions and outlook

In this work, numerical simulations of subcooled nucleate boiling in a laminar shear flow under microgravity conditions were conducted. The simulations were intended as addition to the Multiscale Boiling experiment, which is running aboard ISS since July 2019. Therefore, the simulations were strongly orientated to a complex experimental setup. For the simulations a CFD solver was employed, which is implemented in the OpenFOAM framework and which has been developed over the last decade towards a powerful tool to cover complex two-phase flows including phase change. The governing equations are solved with a finite-volume approach, the liquid-vapor interface is captured by a Volume-of-Fluid method and explicitly reconstructed. An evaporation model is implemented into the solver as well as a subgrid model to account for evaporation at the three-phase contact line. Transient heat transfer with the solid substrate is taken into account. For this work, this solver has been adapted further to account for specific design features of the according experiment.

In this chapter, the observations regarding methodological approach, impact of process parameters and of material properties in the boiling cell simulations and observations regarding the cavity simulations are summarized and design implications for an optimized heat transfer coefficient are given. At the end of each subsection, the most striking conclusions are listed. Finally, the main conclusions of the present work are given. The chapter concludes with an outlook to possible future research in the concerned field.

7.1 Simulations of flow boiling under microgravity conditions in the Multiscale Boiling test cell

7.1.1 Methodological approach

Accompanying the experiments conducted during the Multiscale Boiling project, numerical simulations of the evaporating two-phase flow were conducted, taking the geometry of the whole boiling cell and the solid substrate into account. The results of those simulations were presented in chapter 5. Due to the extremely small length scale of the cavity, which serves as nucleation site in the experiment, the cavity was not part of the numerical grid in this study.

Simulations of successive vapor bubbles in a shear flow, with bubble nuclei originating at a sole nucleation spot inside the boiling cell, were executed. The setup and operation of the numerical simulations were strongly orientated towards the according experiments: Every simulation started with a single phase flow for a defined pre-heating time for the thermal boundary layer above the heated wall to develop. The nucleation of the very first bubble was accompanied by an increase of the input heat flux by the power of a laser beam, which is employed in the experiment to activate the nucleation site. Subsequent bubbles would nucleate, as soon as the prior bubbles gave space at the defined nucleation spot and a defined wall superheat was reached. The proper determination of the wall superheat necessary for a subsequent bubble to nucleate turned out challenging. For the present thesis, the superheat was estimated employing a model from Hsu [39] for the incipience of boiling at natural cavities in a flow field. This approach has uncertainties regarding the thickness of the thermal boundary layer as well as the cavity geometry. The particular depth of the cavity used in the Multiscale Boiling experiment could not be covered by this model. The estimated superheat of 7 K necessary for a nucleation site to be active turned out to be too restricted compared to experimental results as well as compared to simulations of

the nucleation process in the second part of the present thesis.

Due to the lack of the cavity in the numerical grid, the nucleation process was modeled by creating a bubble nucleus on top of the heated wall in one discrete timestep. Therefore the impact of the growth process of the bubble out of the cavity on the thermal boundary layer above the heated wall could not be covered. Simulations of the nucleation process, however, showed, that this influence cannot be neglected. The flow out of the cavity has the potential to thicken the superheated thermal boundary layer in the vicinity of the cavity, leaving a larger part of the developing bubble covered by superheated liquid. Furthermore, the hydrodynamic interaction between a bubble continuously growing out of the cavity and other bubbles already present on the heater surface is neglected. Instead, the creation of a successive bubble must be postponed until all bubbles present on the surface are distant enough from the nucleation site, so that the creation process of the successive bubble does not cause a non-physical cut-out of any old bubble. The latter two modeling errors decrease with decreasing diameter of the created bubble nucleus, which is limited by the smallest grid size.

Additionally, inertia driven bubble detachment after explosive evaporation inside the cavity is not covered by this method, but it has been observed in the experiment as well as in the nucleation simulations. Specifically, in one experiment chosen as validation run, the very first bubble showed immediate detachment, coalesced with a series of successive bubbles during the detached state while moving downstream, and got attached to the surface again. A second bubble could then stably grow at the nucleation site. Such complex flow and evaporation patterns could not be reproduced by the numeric approach in action.

In two simulations, which were directly compared to according experimental runs, the deviations still turned out large. Bubble volumes calculated from black and white pictures were compared to the simulations. Additional to the mentioned modeling errors in the simulations, several uncertainties on the experimental side were discussed. The most striking deviation between simulations and experiments regarding bubble growth was the strive towards an equilibrium bubble volume determined by evaporation at the bubble foot and condensation at the bubble cap in the simulations, whereas in the evaluated experimental runs bubbles tend to grow until they leave the boiling cell.

Conclusions regarding the methodological approach can be summarized as follows:

- The numerical model is able to reproduce the specific setup of the Multiscale Boiling experiment in detail and to cover most of the hydrodynamic and heat transfer phenomena, which could be observed in experiments.
- The method of estimation of the wall superheat necessary for successive nucleations is too imprecise and the value chosen throughout all boiling cell simulations turned out too high in several cases.
- Neglecting the hydrodynamic impact of the nucleation process both on the thermal boundary layer above the heated wall and on other bubbles present on the heater surface has a distorting effect on the results.

7.1.2 Impact of process parameters

As basis for parameter studies a reference case was defined using intermediate values from the experimental parameter range. In this reference case, the very first bubble gained an equilibrium volume determined by evaporation at the bubble foot and condensation to the subcooled bulk fluid at the bubble

cap. After the nucleation of a successive bubble, that second bubble grew and merged with the very first bubble eventually. This process repeated several times. The share of contact line heat flow in the total evaporation heat flow was between 50 % and 60 % throughout the process and thus considerably higher as values in literature obtained under earth gravity conditions (e.g. [53] and [104]). The reason for this difference is the absence of natural convection and the reduced bubble growth dynamics in a 0-g environment, which under earth gravity conditions contribute significantly to the evaporation at the bubble hull.

In the wall underneath the moving contact line a significant temperature drop could be observed, which rapidly recovered due to the large thermal capacity of the substrate. This outcome is in good agreement with experimental observations from literature, e.g. Fischer and co-workers ([24], [25]).

Based on the reference case, a parameter study was performed studying the impact of flow velocity, input heat flux, pre-heating time, and subcooling. An increased flow velocity causes the thermal boundary layer above the wall to be thinner and, due to enhanced convective heat transfer, the wall superheat at the nucleation site to be lower. Therefore each bubble grows to a smaller volume and the waiting time between subsequent nucleations gets longer. It is more likely, that subsequent bubbles will not coalesce and that the enhanced latent and sensible heat transfer at the bubble foot of several bubbles add up. Low flow velocities on the other hand cause the very first bubble to grow larger and prevent the nucleation of subsequent bubbles, because the very first bubble blocks the nucleation site for a longer time.

High input heat flux as well as increased pre-heating time cause the very first bubble to grow to a larger equilibrium volume compared to the reference case. As soon as the very first bubble is dragged downstream sufficiently to give space at the nucleation site for further nucleations, a cycle of rapidly nucleating bubbles begins. Those bubbles coalesce immediately with the very first bubble, letting it grow infinitely beyond its equilibrium size. This phenomenon does not occur to the observed extent in boiling studies under earth gravity conditions, since at a specific diameter the bubble would detach due to buoyancy. Due to the surface tension force at the bubble foot of the smaller bubbles, which counteracts the pressure driven flow of the coalescence with the major bubble, very often parts of the small bubble get torn off during coalescence, stay attached to the surface and form a new growing bubble. This way, a complex pattern of flow and bubble growth emerges on the heater surface with several small bubbles surrounding the growing major bubble. Although the effect of increased input heat flux and increased pre-heating time on bubble growth is qualitatively very similar, it is more pronounced for an increased input heat flux by a factor of approximately 1.5 in terms of the observed bubble volume.

An increase in subcooling causes the very first bubble to grow to a smaller equilibrium volume and makes subsequent nucleation less likely, depending on the nucleation superheat criterion. A decrease in subcooling or saturated boiling cause the formation of several very large bubbles, which eventually coalesce. The pattern is similar to that of high input heat flux cases, but slower and with extended growth of each bubble before coalescence.

The heat transfer coefficient underneath a bubble decreases with increasing bubble size due to an increasing share of the evaluated area being covered by vapor. It is concluded that a parameter choice promoting the formation of one or few large bubbles causes a decline in heat transfer coefficient. This includes low flow velocity, low subcooling, high input heat flux and long pre-heating time. On the other hand, parameters causing many small bubbles with sufficient distance not to coalesce appear advantageous in terms of an enhanced heat transfer coefficient. This includes high flow velocity, high subcooling and low to moderate input heat flux. In the present studies, the nucleation of successive bubbles was very reluctant in the high flow velocity and high subcooling cases, causing only few bubbles being present on the heater surface at the same time. However, the estimated superheat criterion for the nucleation of

successive bubbles was rather conservative and turned out to be chosen too high for the experimental configuration with a very deep cavity, which provides for stable boiling at moderate wall superheats. The observed number of successive bubbles in those cases is very likely underestimated. For this configuration, a recommendation for high flow velocities and high subcooling combined with low to moderate input heat flux can be given in order to achieve enhanced heat transfer. For boiling surfaces typically employed for industrial applications with natural bumps, scratches and imperfections serving as nucleation sites, a higher wall temperature might be necessary and most probably moderate flow velocities and subcooling levels should be imposed.

From the reference case and from the results of the parameter study on process parameters, following conclusions are drawn:

- The share of contact line heat flow in total evaporation heat flow is higher under microgravity conditions compared to 1-g due to the absence of natural convection and to reduced bubble growth dynamics.
- Low flow velocity, low subcooling, high input heat flux and long pre-heating time cause a decrease in heat transfer coefficient in the influence zone of vapor bubbles, because a larger share of the evaluated area is covered by vapor instead of liquid.
- High flow velocity, high subcooling and low to moderate input heat flux promote the emergence of a number of small, not coalescing bubbles and therefore an increasing heat transfer coefficient.

7.1.3 Impact of material properties

Additional to process parameters, selected material properties of the working fluid as well as the solid substrate were varied and their impact on the boiling process was studied. When the thermal conductivity of the liquid is increased, bubble growth is enhanced until a turning point, when a further increase in thermal conductivity causes decreasing growth rates. This turning point depends on other parameters, e.g. on input heat flux. The heat transfer coefficient, however, shows an stable increase for increasing thermal conductivity over the studied value range.

If the increase in liquid thermal conductivity is combined with a variation of input heat flux or pre-heating time, the different impact between those two parameters on bubble growth increases further. The combination of increased thermal conductivity of the working fluid and high input heat flux causes explosive bubble growth, which can cause inertia driven detachment of the initial bubble. The speed of bubble growth brings the Volume-of-Fluid based numerical approach to its limits, since it causes the formation of multiple three-phase contact lines on the heated surface within the foot of the growing bubble out of numerical artifacts.

For the solid substrate the thermal conductivity as well as the specific heat capacity of the material were varied to values lower than the physical values. A lowering of one of the values always causes enhanced bubble growth and higher contact line and sensible heat flow to the fluid, with more impact in case of lowered heat capacity. The influence of both properties on the heat transfer coefficient were compared to an empirical prediction from literature, which had been drawn from a series of boiling experiments. Although the setup of those experiments was in some way different from the experimental and numerical setup in the Multiscale Boiling project, and although those experiments were conducted under earth gravity conditions, the results were found to be in good agreement with the prediction in case of a single bubble. However, as soon as the highly dynamic pattern of nucleating and merging bubbles begins, accompanied by unlimited growth of the initial bubble, the influence of the varied material

properties diminishes, as the heat transfer coefficient decreases with increasing bubble size.

The following conclusions are drawn from the variation of liquid and solid material properties:

- Increasing the liquid thermal conductivity up to a specific value causes increased bubble growth. Increasing it beyond this value causes decreasing bubble growth again. The heat transfer coefficient, however, always increases for increasing liquid thermal conductivity.
- The different quantitative impact of input heat flux and pre-heating time on bubble growth is amplified by an increased liquid thermal conductivity.
- Decreasing the solid thermal conductivity as well as the solid heat capacity causes enhanced bubble growth and a decreasing heat transfer coefficient, the latter in good agreement with an empirical correlation from literature.

7.2 Simulations of boiling from different types of cavities under microgravity conditions

Additional to the simulation of the whole boiling cell, nucleation inside the complex shaped cavity of the Multiscale Boiling experiment was investigated as well as studies of bubble detachment from cylindrical cavities under microgravity conditions due to a shear flow.

The simulations of nucleation inside the cavity of the Multiscale Boiling experiment showed a strong dependency of the evaporation process on the initial superheat of the wall as well as on the starting position of the vapor nucleus. If the nucleus is positioned at the bottom of the cavity, combined with a sufficiently high wall superheat, a thin liquid film forms between the wall and the liquid-vapor interface, which causes strong evaporation rates and fast bubble growth both inside and outside the cavity. For very high initial wall superheats, the growth is fast enough to cause partial detachment of vapor outside the cavity, which could also be observed in the experiment. In contrast, if the nucleus is positioned near the cavity opening, no liquid film forms and the growth rate slows down after nucleation.

Simulations of successive bubble nucleations starting from a vapor column in the Multiscale Boiling cavity showed a similar behavior: In case of a low vapor column, combined with a sufficiently high wall temperature, a liquid film formed at the wall of the cavity causing strong bubble growth outside the cavity. However, for low wall superheats the influence of the vapor column height was neglectable.

Furthermore it was shown, that the velocity field resulting from the growth of the bubble out of the cavity significantly alters the temperature field in the vicinity of the cavity opening. The thermal boundary layer is stretched perpendicular to the wall, leaving a larger part of the bubble outside the cavity surrounded by liquid of high temperature, than in the simulations of chapter 5.

In the detachment studies the depth of the cavity did not show a significant impact on growth rate and detachment diameter or detachment time, respectively. However, for the cavities with a depth smaller than 50 µm, no residual vapor stayed inside the cavities, but the cavities were flooded by liquid and inactive after detachment.

Investigating the correlation between flow velocity in the channel and the detachment diameter, employing flow velocities typical for the Multiscale Boiling experiment, simulation times were unacceptably large. A dimensionless correlation was deduced in order to transfer the detachment diameters obtained for higher flow velocities to lower velocity cases. For this similarity approach, the Reynolds number of

the flow around the vapor bubble was chosen as dimensionless number. This bubble Reynolds number showed almost constant values at detachment over a wide range of flow velocities, despite deviations at very high velocities. This could make the approach a useful tool to estimate bubble detachment diameter under microgravity conditions.

Conclucions drawn from the cavity simulations are as follows:

- If nucleation starts from a nucleus sitting at the cavity bottom or from a low vapor column, combined with a sufficiently high wall superheat, a thin liquid film forms between the liquid-vapor interface and the wall, causing very strong evaporation.
- The growth process in the cavity has a significant impact on bubble hydrodynamics and on the thermal boundary layer outside the cavity.
- Cavity depth does not have a significant impact on the detachment diameter.
- A cavity must have a minimum depth in order to hold residual vapor and stay active after detachment.

7.3 Main conclusions

Summarizing the results from the entire work, following main conclusions are drawn:

- In order to increase the heat transfer coefficient in the area affected by vapor bubbles, a recommendation is given to choose process parameters, which cause numerous small bubbles with sufficient distance to each other not to coalesce. Those parameters are: High flow velocity, high subcooling and low to moderate input heat flux and pre-heating time, respectively.
- High input heat flux, long pre-heating time and low subcooling cause rapid nucleation of successive bubbles and coalescence with the very first bubble. The latter grows very large in those cases, correlated with a decreasing heat transfer coefficient.
- The different impact on bubble growth between input heat flux and pre-heating time is amplified, if the thermal conductivity of the liquid increases.
- Decreasing thermal conductivity or heat capacity of the solid substrate causes the heat transfer coefficient underneath a single bubble to decrease in quantitative agreement with empirical predictions from literature. It also promotes a pattern of rapid nucleation and coalescence, causing the formation of a very large bubble and an even lower heat transfer coefficient.
- If inside the cavity, which serves as nucleation site, the bubble nucleus is at a low position and the wall superheat is sufficiently high, a liquid film based evaporation mechanism causes a very high evaporation rate and therefore bubble growth, which should not be neglected in numerical nucleation models.

7.4 Outlook

In future numerical studies of the Multiscale Boiling experiments and subsequent experimental projects on boiling in microgravity, it would be interesting to transfer findings from the nucleation process to the macroscopic simulations of the boiling cell. E.g. it is imaginable, that during the creation process of a bubble nucleus the thermal boundary layer around the created bubble is manipulated in a way, that

it matches with the temperature field resulting from nucleation simulations. For this purpose, further investigations of the nucleation process inside the cavity have to be conducted, with extended simulation time and specifically customized initial conditions of the temperature field.

Additionally, the fit between experiment and simulation should be enhanced by adapting the numerical setup. For this, the reasons for the deviations must be understood in more detail. Experimental data on temperatures at the solid-liquid boundary as well as detailed information on the flow field inside the test cell and especially in the vicinity of the nucleation site are desirable for this purpose.

Furthermore, the Multiscale Boiling experiment provides experimental data on the influence of an electrical field on the boiling process. In future investigations, it would be of great interest to implement a method in the numerical solver, which accounts for the force of the electrical field on the fluid and to compare the results to the experiment.

Bibliography

[1] H. Abarajith, V. Dhir, G. Warrier, and G. Son. Numerical simulation and experimental validation of the dynamics of multiple bubble merger during pool boiling under microgravity conditions. *Annals of the New York Academy of Sciences*, 1027:235–258, 2004.

[2] E. Aktinol and V. Dhir. Numerical simulation of nucleate boiling phenomenon coupled with thermal response of the solid. *Microgravity Science and Technology*, 24:255–265, 2012.

[3] E. Aktinol, G. Warrier, and V. Dhir. Single bubble dynamics under microgravity conditions in the presence of dissolved gas in the liquid. *International Journal of Heat and Mass Transfer*, 79:251–268, 2014.

[4] Q. Bai and V. Dhir. Numerical simulation of bubble dynamics in the presence of boron in the liquid. *Proceedings of 2001 ASME International Mechanical Engineering Congress and Exposition*, 2001.

[5] S. Batzdorf. *Heat transfer and evaporation during single drop impingement onto a superheated wall*. PhD thesis, TU Darmstadt, 2015.

[6] R. Behle. *Determination of the flow profile in an experimental setup for pool boiling in weightlessness*. Master's thesis, TU Darmstadt, 2020.

[7] E. Berberović, I. Roisman, S. Jakirlić, and C. Tropea. Inertia dominated flow and heat transfer in liquid drop spreading on a hot substrate. *International Journal of Heat and Fluid Flow*, 32(4):785–795, 2011.

[8] J. Brackbill, D. Kothe, and C. Zemach. A continuum method for model surface tension. *Journal of Computational Physics*, 100:335–354, 1992.

[9] V. P. Carey. *Liquid-Vapor Phase-Change Phenomena: An Introduction to the Thermophysics of Vaporization and Condensation Processes in Heat Transfer Equipment*. 1. Taylor & Francis, 1992.

[10] R. Cole. Bubble frequencies and departure volumes at subatmosperic pressures. *AIChE Journal*, 13(4):779–783, 1967.

[11] C. Colin, O. Kannengieser, W. Bergez, M. Lebon, J. Sebilleau, M. Sagan, and S. Tanguy. Nucleate pool boiling in microgravity: Recent progress and future prospects. *Comptes Rendus Mecanique*, 345:21–34, 2017.

[12] P. Delgoshaei and J. Kim. Microscale heat transfer measurements during subcooled pool boiling of pentane: Effect of bubble dynamics. *Proceedings of the 14th International Heat Transfer Conference*, 2010.

[13] F. Demiray and J. Kim. Microscale heat tranfer measurements during pool boiling of fc-72: Effect of subcooling. *International Journal of Heat and Mass Transfer*, 47:3257–3268, 2004.

[14] V. Dhir, G. Warrier, and E. Aktinol. Numerical simulation of pool boiling: A review. *Journal of Heat Transfer*, 135(6):1–17, 2013.

[15] V. Dhir, G. Warrier, E. Aktinol, D. Chao, J. Eggers, W. Sheredy, and W. Booth. Nucleate pool boiling experiments (npbx) on the international space station. *Microgravity Science and Technology*, 24(5):307–325, 2012.

[16] P. Di Marco. Influence of force fields and flow patterns on boiling heat transfer performance: A review. *Journal of Heat Transfer*, 134, 2012.

[17] J. Dietl. *Numerical Simulation of Pool Boiling from Reentrant Type Structured Surfaces*. PhD thesis, TU Darmstadt, 2015. http://tuprints.ulb.tu-darmstadt.de/4653.

[18] J. Ervin, H. Merte JR., R. Keller, and K. Kirk. Transient pool boiling in microgravity. *International Journal of Heat and Mass Transfer*, 35:659–674, 1992.

[19] A. Esmaeeli and G. Tryggvason. Computations of film boiling. part i: Numerical method. *International Journal of Heat and Mass Transfer*, 47:5451–5461, 2004.

[20] A. Esmaeeli and G. Tryggvason. Computations of film boiling. part ii: Multi-mode film boiling. *International Journal of Heat and Mass Transfer*, 47:5463–5476, 2004.

[21] A. Esmaeeli and G. Tryggvason. A front tracking method for computations of boiling in complex geometries. *International Journal of Multiphase Flow*, 30:1037–1050, 2004.

[22] R. Fedkiw, T. Aslam, B. Merriman, and S. Osher. A non-oscillatory eulerian approach to interfaces in multimaterial flows (the ghost fluid method). *Journal of Computational Physics*, 152:457–492, 1999.

[23] S. Fischer. *Experimental Investigation of Heat Transfer during Evaporation in the Vicinity of Moving Three-Phase Contact Lines*. PhD thesis, TU Darmstadt, 2015.

[24] S. Fischer, S. Herbert, A. Sielaff, E. Slomski, P. Stephan, and M. Oechsner. Experimental investigation of nucleate boiling on a thermal capacitive heater under variable gravity conditions. *Microgravity Science and Technology*, 24(3):139–146, 2012.

[25] S. Fischer, S. Herbert, E. Slomski, P. Stephan, and M. Oechsner. Local heat flux investigation during pool boiling single bubble cycles under reduced gravity. *Heat Transfer Engineering*, 35(5):482–491, 2014.

[26] B. Franz, A. Sielaff, and P. Stephan. Numerical investigation of successively nucleating bubbles during subcooled flow boiling of fc-72 in microgravity. *Microgravity Science and Technology*, 35(27), 2021.

[27] W. Fritz. Berechnung des maximalvolumens von dampfblasen. *Physikalische Zeitschrift*, 36:379–384, 1936.

[28] T. Fuchs. *Numerische Analyse transienter Wärmetransport- und Wärmespeicherungsmechanismen in Heizwand und Fluid beim Blasensieden eines binären Gemisches.* PhD thesis, Technische Universität Darmstadt, 2008.

[29] T. Fuchs, J. Kern, and P. Stephan. A transient nucleate boiling model including microscale effects and wall heat transfer. *Journal of Heat Transfer*, 128:1257–1265, 2006.

[30] A. Georgoulas and M. Marengo. Numerical simulation of pool boiling: The effects of initial thermal boundary layer, contact angle and wall superheat. *Proceedings of 14th UK Heat Transfer Conference, Edinburgh, UK*, 2015.

[31] D. Gorenflo. *VDI-Wärmeatlas, Chapter H2: Behältersieden (Sieden in freier Konvektion)*, volume 11. Verein Deutscher Ingenieure, Springer Verlag, Berlin, Heidelberg, 2013.

[32] D. Gründing, M. Smuda, T. Antritter, M. Fricke, D. Rettenmaier, F. Kummer, P. Stephan, H. Marschall, and D. Bothe. A comparative study of transient capillary rise using direct numerical simulations. *Applied Mathematical Modelling*, 86:142 – 165, 2020. http://www.sciencedirect.com/science/article/pii/S0307904X20302134.

[33] S. Hardt and F. Wondra. Evaporation model for interfacial flows based on a continuum-field representation of the source terms. *Journal of Computational Physics*, 227:5871–5895, 2008.

[34] F. Harlow and J. Welch. Numerical calculation of time-dependent viscous incompressible flow of fluid with free surface. *The Physics of Fluids*, 8(12):2182–2189, 1965.

[35] C. Henry and J. Kim. A study of the effects of heater size, subcooling, and gravity level on pool boiling heat transfer. *International Journal of Heat and Fluid Flow*, 25:262–273, 2004.

[36] S. Herbert, T. Gambaryan-Roisman, and P. Stephan. Influence of the governing dimensionless parameters on heat transfer during single drop impingement onto a hot wall. *Colloids and Surfaces, A: Physicochemical and Engineering Aspects*, 432:57–63, 2013.

[37] C. Hirt, A. Amsden, and J. Cook. An arbitrary lagrangian-eulerian computing method for all flow speeds. *Journal of Computational Physics*, 14:227–253, 1974.

[38] C. Hirt and B. Nichols. Volume of fluid (vof) method for the dynamics of free boundaries. *Journal of Computational Physics*, 39:201–225, 1981.

[39] Y. Y. Hsu. On the size range of active nucleation cavities on a heating surface. *Journal of Heat Transfer*, 84(3):207–213, 1962.

[40] G. Huber, S. Tanguy, M. Sagan, and C. Colin. Direct numerical simulation of nucleate pool boiling at large microscopic contact angle and moderate jakob number. *International Journal of Heat and Mass Transfer*, 113:662–682, 2017.

[41] K. Ibrahem, M. Abd Rabbo, T. Gambaryan-Roisman, and P. Stephan. Experimental investigation of evaporative heat transfer characteristics at the 3-phase contact line. *Experimental Thermal and Fluid Science*, 34:1036–1041, 2010.

[42] K. Ibrahem, M. Abd Rabbo, T. Gambaryan-Roisman, and P. Stephan. Experimental investigation of micro-scale heat transfer at an evaporating moving 3-phase contact line. *Proceedings of the 14th International Heat Transfer Conference*, 2010.

[43] J. N. Israelachvili. Chapter 13 - van der waals forces between particles and surfaces. In J. N. Israelachvili, editor, *Intermolecular and Surface Forces (Third Edition)*, pages 253 – 289. Academic Press, San Diego, third edition edition, 2011.

[44] R. Issa, A. Gosman, and A. Watkins. The computation of compressible and incompressible recirculating flows by a non-iterative implicit scheme. *Journal of Computational Physics*, 62(1):66 – 82, 1986.

[45] M. Jakob and W. Fritz. Versuche über den verdampfungsvorgang. *Forschung auf dem Gebiet des Ingenieurwesens*, 2:435–447, 1931.

[46] D. Juric and G. Tryggvason. Numerical simulations of phase change in microgravity. *Heat Transfer in Microgravity Systems*, 1996.

[47] D. Juric and G. Tryggvason. Computations of boiling flows. *International Journal of Multiphase Flow*, 24:387–410, 1998.

[48] D. Kenning, T. Kono, and M. Wienecke. Investigation of boiling heat transfer by liquid crystal thermography. *Experimental Thermal and Fluid Science*, 25:219–229, 2001.

[49] D. Kenning and Y. Yan. Pool boiling heat transfer on a thin plate: Features revealed by liquid crystal thermography. *International Journal of Heat and Mass Transfer*, 39:3117–3137, 1996.

[50] J. Kern. *Modell und numerische Berechnung des Wärmeübergangs beim Blasensieden binärer Gemische*. PhD thesis, Technische Universität Darmstadt, 2001.

[51] J. Kern and P. Stephan. Investigation of decisive mixture effects in nucleate boiling of binary mixtures using a theoretical model. *Journal of Heat Transfer*, 125:1116–1122, 2003.

[52] J. Kern and P. Stephan. Theoretical model for nucleate boiling heat and mass transfer of binary mixtures. *Journal of Heat Transfer*, 125:1106–1115, 2003.

[53] J. Kim. Review of nucleate pool boiling bubble heat transfer mechanisms. *International Journal of Multiphase Flow*, 35:1067–1076, 2009.

[54] C. Kunkelmann. *Numerical Model and Investigation of Boiling Phenomena*. PhD thesis, TU Darmstadt, 2011.

[55] C. Kunkelmann, K. Ibrahem, N. Schweizer, S. Herbert, P. Stephan, and T. Gambaryan-Roisman. The effect of three-phase contact line speed on local evaporative heat transfer: Experimental and numerical investigation. *International Journal of Heat and Mass Transfer*, 55:1896–1904, 2012.

[56] C. Kunkelmann and P. Stephan. Cfd simulation of boiling flows using the volume-of-fluid method within openfoam. *Numerical Heat Transfer, Part A: Applications*, 56:631–646, 2009.

[57] C. Kunkelmann and P. Stephan. Modification and extension of a standard volume-of-fluid solver for simulating boiling heat transfer. *Proceedings of ECCOMAS CFD, Lisbon, Portugal*, 2010.

[58] C. Kunkelmann and P. Stephan. Numerical simulation of the transient heat transfer during nucleate boiling of refrigerant hfe-7000. *International Journal of Refrigeration*, 33:1221–1228, 2010.

[59] S. Kühnemund. *Anpassung eines Versuchsstandes zur Untersuchung des Blasensiedens in Schwerelosigkeit mit anschließender Parameterstudie*. Master's thesis, TU Darmstadt, 2019.

[60] H. Lee and H. Merte JR. Pool boiling mechanisms in microgravity. *Proceedings of the Engineering Foundation Conference on Microgravity Fluid Physics and Heat Transfer, Hawai*, 1999.

[61] W. Lee and G. Son. Numerical simulation of boiling enhancement on a microstructured surface. *International Communications in Heat and Mass Transfer*, 38(2):168–173, 2011.

[62] W. Lee, G. Son, and H. Yoon. Numerical study of bubble growth and boiling heat transfer on a microfinned surface. *International Communications in Heat and Mass Transfer*, 39(1):52–57, 2012.

[63] D. Li and V. Dhir. Numerical study of single bubble dynamics during flow boiling. *Journal of Heat Transfer*, 129:864–876, 2007.

[64] N. Linder. *Numerical Simulation of Complex Wetting*. PhD thesis, TU Darmstadt, 2015.

[65] N. Linder, A. Criscione, I. Roisman, H. Marschall, and C. Tropea. 3d computation of an incipient motion of a sessile drop on a rigid surface with contact angle hysteresis. *Theoretical and Computational Fluid Dynamics*, 29:373–390, 2015.

[66] J. López and J. Hernández. Analytical and geometrical tools for 3d volume of fluid methods in general grids. *Journal of Computational Physics*, 227(12):5939 – 5948, 2008.

[67] I. Malenkov. The frequency of vapor-bubble seperation as a function of bubble size. *Fluid Mechanics - Soviet Research*, 1:36–42, 1972.

[68] R. Marek and J. Straub. Analysis of the evaporation coefficient and the condensation coefficient of water. *International Journal of Heat and Mass Transfer*, 44(1):39 – 53, 2001.

[69] B. B. Mikic and W. M. Rohsenow. A new correlation of pool-boiling data including the effect of heating surface characteristics. *Journal of Heat Transfer*, 91(2):245–250, 1969.

[70] S. Moghaddam and K. Kiger. Physical mechanisms of heat transfer during single bubble nucleate boiling of FC-72 under saturation conditions-I. experimental investigation. *International Journal of Heat and Mass Transfer*, 52:1284–1294, 2009.

[71] S. Moghaddam and K. Kiger. Physical mechanisms of heat transfer during single bubble nucleate boiling of FC-72 under saturation conditions-II. theoretical analysis. *International Journal of Heat and Mass Transfer*, 52:1295–1303, 2009.

[72] A. Mukherjee and V. Dhir. Study of lateral merger of vapor bubbles during nucleate pool boiling. *Journal of Heat Transfer*, 126, 2004.

[73] A. Mukherjee and S. Kandlikar. Numerical study of single bubbles with dynamic contact angle during nucleate pool boiling. *International Journal of Heat and Mass Transfer*, 50:127–138, 2007.

[74] J. Myers, V. Yerramilli, S. Hussey, G. Yee, and J. Kim. Time and space resolved wall temperature and heat flux measurements during nucleate boiling with constant heat flux boundary conditions. *International Journal of Heat and Mass Transfer*, 48:2429–2442, 2005.

[75] I. Nejati, A. Sielaff, B. Franz, M. Zimmermann, P. Hänichen, K. Schweikert, J. Krempel, P. Stephan, A. Martin, H. Scheerer, T. Engler, and M. Oechsner. Experimental investigation of single bubble nucleate boiling in microgravity. *Microgravity Science and Technology*, 32:597–607, 2020.

[76] S. Nukiyama. The maximum and minimum values of the heat q transmitted from metal to boiling water under atmospheric pressure. *Journal of the Japan Society of Mechanical Engineers*, 7:367–374, 1934.

[77] J. Okajima and P. Stephan. Numerical simulation of liquid film formation and its heat transfer through vapor bubble expansion in a microchannel. *International Journal of Heat and Mass Transfer*, 136:1241–1249, 2019.

[78] S. Osher and J. Sethian. Fronts propagating with curvature dependent speed: Algorithms based on hamilton-jacobi formulations. *Journal of Computational Physics*, 79:12–49, 1988.

[79] A. Pattamatta, M. Freystein, and P. Stephan. A parametric study on phase change heat transfer due to taylor-bubble coalescence in a square minichannel. *International Journal of Heat and Mass Transfer*, 76:16–32, 2014.

[80] R. Raj, C. Kunkelmann, P. Stephan, J. Plawsky, and J. Kim. Contact line behavior for a highly wetting fluid under superheated conditions. *International Journal of Heat and Mass Transfer*, 55:2664–2675, 2012.

[81] D. Rettenmaier. *Numerical Simulation of Shear Driven Wetting*. PhD thesis, TU Darmstadt, 2019.

[82] D. Rettenmaier, D. Deising, Y. Ouedraogo, G. E., H. De Gersem, D. Bothe, C. Tropea, and H. Marschall. Load balanced 2d and 3d adaptive mesh refinement in openfoam. *SoftwareX*, 10, 2019.

[83] F. Schommartz. *Simulation des Keimprozesses von Dampfblasen aus einer Kavität in Schwerelosigkeit*. Bachelor's thesis, TU Darmstadt, 2020.

[84] R. Schrage. *A theoretical study of interface mass transfer*. Columbia University Press, 1953.

[85] K. Schweikert, A. Sielaff, and P. Stephan. Heat flux during dip-coating of a superheated substrate. *InterfacialPhenomena and Heat Transfer*, 7:269–281, 2019.

[86] K. Schweikert, A. Sielaff, and P. Stephan. On the transition between contact line evaporation and microlayer evaporation during the dewetting of a superheated wall. *International Journal of Thermal Sciences*, 145, 2019.

[87] N. Schweizer. *Multi-scale investigaiton of nucleate boiling phenomena in microgravity*. PhD thesis, Technische Universität Darmstadt, 2010.

[88] N. Schweizer and P. Stephan. Experimental study of bubble behavior and local heat flux in pool boiling under variable gravitational conditions. *Multiphase Science and Technology*, 21:329–350, 2009.

[89] M. Schäfer. *Computational Engineering*. Springer Verlag, 2006.

[90] L. E. Scriven. On the dynamics of phase growth. *Chemical Engineering Science*, 10:1–13, 1959.

[91] B. Shu. *Numerische Simulation des Blasensiedens mit Volume-Of-Fluid- und Level-Set-Methode*. PhD thesis, Technische Universität Darmstadt, 2009.

[92] R. Siegel. Effects of reduced gravity on heat transfer. *Advances in Heat Transfer*, 4:143–228, 1967.

[93] A. Sielaff. *Experimental Investigation of Single Bubbles and Bubble Interactions in Nucleate Boiling*. PhD thesis, TU Darmstadt, 2014.

[94] C. Sodtke, J. Kern, N. Schweizer, and P. Stephan. High resolution measurements of wall temperature distribution underneath a single vapour bubble under low gravity conditions. *International Journal of Heat and Mass Transfer*, 49:1100–1106, 2006.

[95] G. Son and V. Dhir. Numerical simulation of saturated film boiling on a horizontal surface. *Journal of Heat Transfer*, 119(3):525–533, 1997.

[96] G. Son and V. Dhir. Numerical simulation of film boiling near critical pressures with a level set method. *Journal of Heat Transfer*, 120:183–192, 1998.

[97] G. Son and V. Dhir. A level set method for analysis of film boiling on an immersed solid surface. *Numerical Heat Transfer, Part B*, 52:153–177, 2007.

[98] G. Son, V. Dhir, and N. Ramanujapu. Dynamics and heat transfer associated with a single bubble during nucleate boiling on a horizontal surface. *Journal of Heat Transfer*, 121:623–631, 1999.

[99] E. space research and technology centre. *Multiscale Boiling (RUBI) Experiment Scientific Requirements*. Technical report 3, European Space Agency, 2019.

[100] F. Stechowsky. *Simulation des Blasenwachstums und -abrisses an einer Kavitaet in Schwerelosigkeit*. Bachelor's thesis, TU Darmstadt, 2019.

[101] K. Stephan and M. Abdelsalam. Heat-transfer correlations for natural convection boiling. *International Journal of Heat and Mass Transfer*, 23:73–87, 1980.

[102] P. Stephan and C. Busse. Analysis of the heat transfer coefficient of grooved heat pipe evaporator walls. *International Journal of Heat and Mass Transfer*, 35:383–391, 1992.

[103] P. Stephan and J. Hammer. A new model for nucleate boiling heat transfer. *Wärme- und Stoffübertragung*, 30:119–125, 1994.

[104] P. Stephan and J. Kern. Evaluation of heat and mass tranfer phenomena in nucleate boiling. *International Journal of Heat and Fluid Flow*, 25:140–148, 2004.

[105] P. Stephan, A. Sielaff, S. Fischer, J. Dietl, and S. Herbert. A contribution to the basic understanding of nucleate boiling phenomena: Generic experiments and numerical simulations. *Thermal Science and Engineering*, 21(2):39–57, 2013.

[106] S. Tanguy, M. Sagan, B. Lalanne, F. Couderc, and C. Colin. Benchmarks and numerical methods for the simulation of boiling flows. *Journal of Computational Physics*, 264:1–22, 2014.

[107] J. Thome, V. Dupont, and A. Jacobi. Heat transfer model for evaporation in microchannels. part i: presentation of the model. *International Journal of Heat and Mass Transfer*, 47:3375–3385, 2004.

[108] G. Tryggvason, B. Bunner, A. Esmaeeli, D. Juric, N. Al-Rawahi, W. Tauber, J. Han, S. Nas, and Y.-J. Jan. A front-tracking method for the computations of multiphase flow. *Journal of Computational Physics*, 169:708–759, 2001.

[109] S. Unverdi and G. Tryggvason. A front-tracking method for viscous, incompressible, multi-fluid flows. *Journal of Computational Physics*, 100:25–37, 1992.

[110] A. Urbano, S. Tanguy, and C. Colin. Direct numerical simulation of nucleate boiling in zero gravity conditions. *International Journal of Heat and Mass Transfer*, 143, 2019.

[111] A. Urbano, S. Tanguy, G. Huber, and C. Colin. Direct numerical simulation of nucleate boiling in micro-layer regime. *International Journal of Heat and Mass Transfer*, 123:1128–1137, 2018.

[112] T. Voskuilen. Mesh balancing. https://github.com/tgvoskuilen/meshBalancing, 2014. Accessed: 2020-07-29.

[113] E. Wagner, C. Sodtke, N. Schweizer, and P. Stephan. Experimental study of nucleate boiling heat transfer under low gravity conditions using tlcs for high resolution temperature measurements. *Heat and Mass Transfer*, 42:875–883, 2006.

[114] E. Wagner, P. Stephan, O. Koeppen, and H. Auracher. High resolution temperature measurements at moving vapor/liquid and vapor/liquid/solid interfaces during bubble growth in nucleate boiling. *Proceedings to 4th International Berlin Workshop on Transport Phenomena with Moving Boundaries*, 2007.

[115] C. H. Wang and V. K. Dhir. On the gas entrapment and nucleation site density during pool boiling of saturated water. *Journal of Heat Transfer*, 115(3):670 – 679, 1993.

[116] P. Wayner, Y. Kao, and L. LaCroix. The interline heat-transfer coefficient of an evaporating wetting film. *International Journal of Heat and Mass Transfer*, 19:487–492, 1976.

[117] S. Welch. Local simulation of two-phase flows including interface tracking with mass transfer. *Journal of Computational Physics*, 121:142–154, 1995.

[118] S. Welch. Direct simulation of vapor bubble growth. *International Journal of Heat and Mass Transfer*, 12:1655–1666, 1998.

[119] S. Welch and T. Rachidi. Numerical computation of film boiling including conjugate heat transfer. *Numerical Heat Transfer, Part B*, 42:35–53, 2002.

[120] S. Welch and J. Wilson. A volume of fluid based method for fluid flows with phase change. *Journal of Computational Physics*, 160:662–682, 2000.

[121] H. Weller, G. Tabor, H. Jasak, and C. Fureby. A tensorial approach to computaional continuum mechanics using object-orientated techniques. *Computers in Physics*, 12:620–631, 1998.

[122] J. Wu and V. Dhir. Numerical simulations of the dynamics and heat transfer associated with a single bubble in subcooled pool boiling. *Journal of Heat Transfer*, 132, 2010.

[123] J. Wu, V. Dhir, and J. Qian. Numerical simulation of subcooled nucleate boiling by coupling level-set method with moving-mesh method. *Numerical Heat Transfer, Part B*, 51:535–563, 2007.

[124] N. Zuber. Nucleate boiling. the region of isolated bubbles and the similarity with natural convection. *International Journal of Heat and Mass Transfer*, 6:53–78, 1963.

List of Figures

List of Tables

A Material Properties

Property	Value	Unit
p_{sat}	0.5	bar
t_{sat}	37.7	°C
σ	$9.911 \cdot 10^{-3}$	N/m
Δh_{v}	89.767	kJ/kg
ρ_{l}	1653.91	kg/m^3
ρ_{v}	7.02	kg/m^3
c_{l}	1069.23	J/(kgK)
$c_{p,\mathrm{v}}$	857.93	J/(kgK)
ν_{l}	$3.32 \cdot 10^{-7}$	m^2/s
ν_{v}	$14 \cdot 10^{-7}$	m^2/s
λ_{l}	$54.2 \cdot 10^{-3}$	W/(m K)
λ_{v}	$7.65 \cdot 10^{-3}$	W/(m K)

Table A.1: Fluid properties of FC-72 at saturation, $p = 0.5$ bar

Property	Value	Unit
p_{sat}	0.54	bar
t_{sat}	39.7	°C
σ	$9.735 \cdot 10^{-3}$	N/m
Δh_{v}	89.228	kJ/kg
ρ_{l}	1650.18	kg/m^3
ρ_{v}	7.06	kg/m^3
c_{l}	1072.31	J/(kgK)
$c_{p,\mathrm{v}}$	860.86	J/(kgK)
ν_{l}	$3.254 \cdot 10^{-7}$	m^2/s
ν_{v}	$13.1 \cdot 10^{-7}$	m^2/s
λ_{l}	$54.1 \cdot 10^{-3}$	W/(m K)
λ_{v}	$7.75 \cdot 10^{-3}$	W/(m K)

Table A.2: Fluid properties of FC-72 at saturation, $p = 0.54$ bar

Property	Value	Unit
p_{sat}	0.9	bar
t_{sat}	53.53	°C
σ	$8.53 \cdot 10^{-3}$	N/m
Δh_{v}	85.392	kJ/kg
ρ_{l}	1625.4	$\mathrm{kg/m^3}$
ρ_{v}	12.1	$\mathrm{kg/m^3}$
c_{l}	1093.7	J/(kgK)
$c_{p,\mathrm{v}}$	880.72	J/(kgK)
ν_{l}	$2.87 \cdot 10^{-7}$	$\mathrm{m^2/s}$
ν_{v}	$7.92 \cdot 10^{-7}$	$\mathrm{m^2/s}$
λ_{l}	$52.5 \cdot 10^{-3}$	W/(m K)
λ_{v}	$8.5 \cdot 10^{-3}$	W/(m K)

Table A.3: Fluid properties of FC-72 at saturation, $p = 0.9$ bar

Property	Value	Unit
ρ	4890	$\mathrm{kg/m^3}$
c	410	J/(kgK)
λ	10.9	W/(m K)

Table A.4: Properties of Barium Fluoride $\mathrm{BaF_2}$

B Correlation coefficients for the contact line model

The regression polynomial of the microzone model follows the rule:

$$\Phi(\Delta T, u_{\mathrm{cl}}) = \sum_{\mathrm{i}=1}^{N} a_{\Phi,T,i} \Delta T^{1/i} \cdot \sum_{\mathrm{j}=0}^{M} a_{\Phi,u,j} \left(u_{\mathrm{cl}} \Delta T^{b_\Phi} \right)^j \tag{B.1}$$

	0	1	2	3	4	5	6	7
$a_{Q,T,i}$	-	-0.436	95.941	-1286.774	4703.661	-6272	2759.87	-
$a_{Q,u,j}$	1	-2.014	8.657	-29.935	59.199	-64.146	35.514	-7.843
b_Q	-0.263							
$a_{\Theta,T,i}$	-	-7.894	2318.409	-35325.133	136558.946	-187885.573	84360.737	-
$a_{\Theta,u,j}$	1	17.209	-110.39	321.848	736.044	-7054.173	15837.654	-11823.62
b_Θ	-0.888							
$a_{\delta,T,i}$	-	6.312	-8.369	9.976	-0.00034	0.00043	-0.00019	-
$a_{\delta,u,j}$	1	3.829	-2.143	7.838	-11.741	10.051	-3.315	0.215
b_δ	-0.144							

Table B.1: Correlation coefficients for FC-72 in the range of 5 K < ΔT < 20 K and -0.2 m/s < u_{cl} < 2 m/s